

# Coherence in Molecular Photoionization

PhD thesis

David Ayuso Molinero

Supervisors:

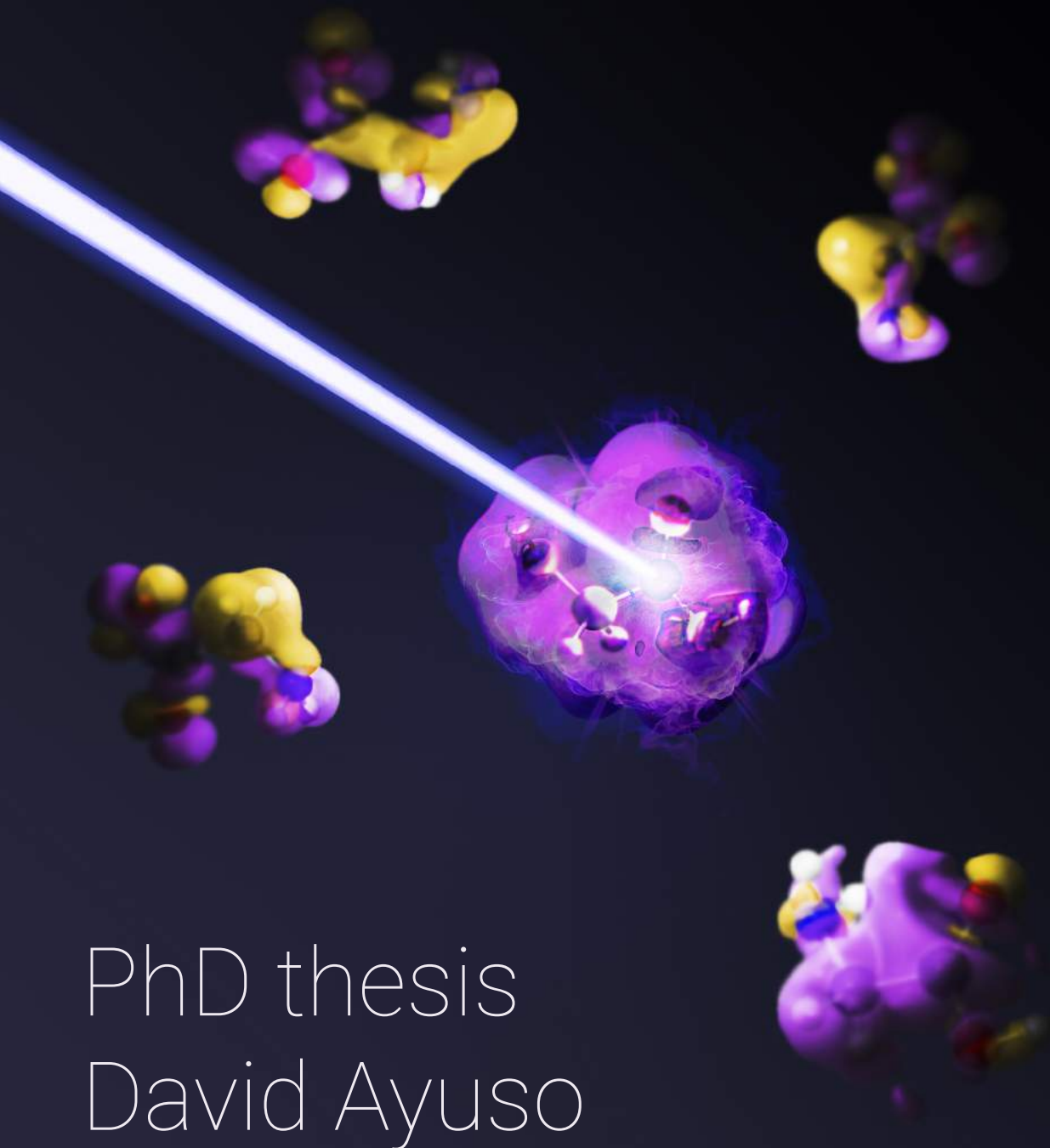
- Alicia Palacios Cañas
- Fernando Martín García



FACULTAD DE  
CIENCIAS

December 2015

# Coherence in Molecular Photoionization



PhD thesis  
David Ayuso

# Abstract

We present a theoretical study of light-induced phenomena in gas-phase molecules, exploring the physical phenomena arising in two distinct contexts: using synchrotron radiation and ultrashort laser pulses. This work has been done in close collaboration with Piero Decleva (Università degli Studi di Trieste).

We first present our work on inner-shell photoionization of diatomic (CO) and small polyatomic (CF<sub>4</sub>, BF<sub>3</sub>) molecules at high photoelectron energies performed in collaboration with the experimental groups of Edwin Kukk (Turku University), Catalin Miron (Synchrotron SOLEIL), Kiyosi Ueda (Synchrotron SPring-8) and Thomas Darrah Thomas (Oregon State University). The combination of state-of-the-art Density Functional Theory (DFT)-like calculations, capable to describe photoionization accounting for the nuclear degrees of freedom, together with high-resolution third-generation synchrotron facilities, has enabled the investigation of non-Franck-Condon effects observable in vibrationally resolved photoionization measurements. We demonstrate that the nuclear response to intramolecular electron diffraction is observable and can be used to obtain structural information. As a proof-of-principle, by using the DFT calculations as an analysis tool to fit the experimental data, we have accurately determined the equilibrium distance of the CO molecule and the bond contraction that takes place upon C 1s ionization. This is a surplus of photoelectron spectroscopy with respect to more conventional spectroscopic techniques, which usually can only provide structural information of neutral molecular species. Furthermore, we have explored the different phenomenon arising when an electron is emitted from a delocalized orbital: multicenter emission. The results on molecular fluorine coming from our numerical simulations are in good qualitative agreement with those pro-

---

vided by the simple formula proposed by Cohen and Fano in the sixties.

We have employed the same DFT-based methodology together with time-dependent first-order perturbation theory and a reduced density matrix formalism to report the first demonstration of purely electron dynamics in a biological molecule: the amino acid phenylalanine, in collaboration with the experimental groups of Mauro Nisoli (Politecnico di Milano), Luca Poletto (Istituto Nazionale di Fotonica - Consiglio Nazionale delle Ricerche) and Jason Greenwood (Queen's University). The use of attosecond pulses in combination with novel detection techniques has enabled the capture of purely electron motion at its intrinsic time scale. Because of their wide energy bandwidth, attosecond pulses are ideal sources to generate coherent superpositions of states, triggering an ultrafast electronic response that can be later tracked with attosecond resolution. Our theoretical study enabled to interpret the experimental findings in terms of charge migration, thus confirming the first observation of purely electron dynamics in a biomolecule. The work presented here has been extended to treat the amino acids glycine and tryptophan, which has allowed the investigation of radical substitution effects in the charge migration mechanism.

# Resumen

Esta tesis doctoral constituye un estudio teórico de procesos ultrarrápidos que ocurren en moléculas aisladas cuando son expuestas a radiación electromagnética. En particular, hemos investigado los fenómenos físicos que surgen en dos contextos diferentes: (i) cuando la energía de los fotones incidentes está bien definida, como ocurre en experimentos que hacen uso de radiación sincrotrón, y (ii) cuando la duración de la interacción radiación-materia es extremadamente corta, lo cual es posible gracias al desarrollo de pulsos láser ultra-cortos, del orden de tan solo unos pocos cientos de attosegundos ( $1 \text{ as} = 10^{-18} \text{ s}$ ). Este trabajo ha sido supervisado por Fernando Martín y Alicia Palacios (Universidad Autónoma de Madrid), y ha sido realizado en estrecha colaboración con Piero Decleva (Università degli Studi di Trieste) y con varios grupos experimentales de distintos países, como se indica a continuación.

En primer lugar, presentamos un estudio sobre fotoionización de capa interna de moléculas diatómicas (CO) y poliatómicas (CF<sub>4</sub>, BF<sub>3</sub>) con radiación sincrotrón a altas energías del fotoelectrón, que ha sido realizado en colaboración con los grupos experimentales de Edwin Kukk (Turku University), Catalin Miron (Synchrotron SOLEIL), Kiyosi Ueda (Synchrotron SPring-8) y Thomas Darrah Thomas (Oregon State University). El uso de instalaciones sincrotrón de tercera generación, en combinación con técnicas de detección avanzadas de alta resolución en energía, nos ha permitido observar claras violaciones del principio de Franck-Condon (FC) en espectros fotoelectrónicos resueltos vibracionalmente. Nuestro trabajo teórico, basado en la aplicación de la Teoría del Funcional de la Densidad (DFT, del inglés, Density Functional Theory) para describir procesos de fotoionización en sistemas multielectrónicos, ha sido esencial para guiar

---

las campañas experimentales, así como para interpretar los resultados de las mismas. Para ello, ha sido necesario tener en cuenta en nuestras simulaciones computacionales los grados de libertad adicionales debidos al movimiento nuclear. Nuestro estudio conjunto demuestra que las violaciones del principio de FC observadas son consecuencia de un fenómeno de difracción electrónica: cuando se emite un electrón desde una región bien localizada en el centro de una molécula poliatómica, como el orbital 1s del átomo de carbono en la molécula CF<sub>4</sub>, éste puede ser difractado por los átomos circundantes, originando interferencias constructivas y destructivas en los espectros fotoelectrónicos. La respuesta nuclear al fenómeno de difracción electrónica es observable, y los espectros fotoelectrónicos contienen información estructural del sistema. Sin embargo, la extracción de esta información puede llegar a ser todo un desafío. En esta tesis doctoral proponemos un método de determinación estructural, basado en el uso de cálculos DFT como herramienta de análisis para el ajuste de datos experimentales. Como prueba de concepto, hemos determinado con precisión, y simultáneamente, la distancia de equilibrio de la molécula de CO y la contracción de enlace que tiene lugar tras la extracción de un electrón del orbital 1s del átomo de carbono. Nuestro método presenta una clara ventaja frente a técnicas espectroscópicas más convencionales que, en general, tan solo son capaces de proporcionar información estructural de la especie neutra.

Cuando el electrón no se emite desde una región bien localizada en el centro de la molécula, sino desde un orbital deslocalizado entre varios átomos, tiene lugar un fenómeno físico diferente: emisión multicéntrica. Nuestras simulaciones en la molécula de flúor muestran que este fenómeno es experimentalmente observable en espectros fotoelectrónicos, y nuestros resultados coinciden, de forma cualitativa, con los predichos por la sencilla fórmula propuesta por Cohen y Fano en los años 60.

Poder observar y controlar el movimiento de los electrones en moléculas biológicas es uno de los principales objetivos de la ciencia de attosegundos (attociencia). El uso de pulsos laser ultra-cortos permite inducir corrientes electrónicas ultra-rápidas en la materia mediante la creación de superposiciones coherentes de autoestados del sistema. Además, estos pulsos tienen la duración adecuada para

visualizar las corrientes creadas con la resolución temporal requerida. En colaboración con los grupos experimentales de Mauro Nisoli (Politecnico di Milano), Luca Poletto (Istituto Nazionale di Fotonica Consiglio Nazionale delle Ricerche) y Jason Greenwood (Queen's University), hemos reportado la primera observación de dinámica puramente electrónica en una molécula biológica: el amino ácido fenilalanina. Esto ha sido posible gracias a la creación y aplicación de pulsos laser de tan solo 300 attosegundos de duración, en combinación con novedosas técnicas de detección de fragmentos iónicos doblemente cargados (formados tras la ionización de la biomolécula). La migración de carga observada precede cualquier reordenamiento estructural y es la base de un gran número de procesos biológicos. Nuestras simulaciones computacionales, basadas en DFT junto con teoría de perturbaciones a primer orden y un formalismo de matriz de densidad reducida, han sido esenciales en la interpretación de los hallazgos experimentales en términos de migración de carga ultra-rápida. Para ello, ha sido necesario describir de forma precisa la interacción de la molécula con el pulso laser empleado en los experimentos, así como la respuesta molecular inducida. Nuestro trabajo ha revelado, de manera inequívoca, que las variaciones de carga observadas se deben única y exclusivamente al movimiento ondulatorio de los electrones en la biomolécula. Hemos descubierto que la migración de carga desde un extremo a otro del amino ácido tarda entre 3 y 4 femtosegundos ( $1 \text{ fs} = 10^{-15} \text{ s}$ ). Merece la pena sealar que, hasta entonces, ningún trabajo teórico había sido capaz de describir el proceso de ionización por un pulso de attosegundos y el posterior reordenamiento electrónico en una molécula compleja, de relevancia biológica.

En esta tesis doctoral presentamos un estudio completo que incluye los amino ácidos glicina y triptófano. Esto nos ha permitido generalizar los resultados obtenidos a otras moléculas biológicas, así como investigar cómo afecta la sustitución del radical al mecanismo de migración de carga ultra-rápida en un amino ácido. Nuestros resultados demuestran que, modificando las características el pulso laser (amplitud y fase de sus componentes espectrales) es posible modificar la respuesta electrónica inducida, permitiendo controlar a la carta el movimiento de los electrones en sistemas de relevancia biológica.





# Publications

The work presented in this PhD thesis has lead to the following publications peer reviewed journals (inverse chronological order):

7. **Ultrafast Charge Dynamics in an Amino Acid Induced by Attosecond Pulses.** F. Calegari, D. Ayuso, A. Trabattoni, L. Belshaw, S. De Camillis, F. Frassetto, L. Poletto, A. Palacios, P. Decleva, J. B. Greenwood, F. Martín, and M. Nisoli. *IEEE Journal of Selected Topics in Quantum Electronics* **21**, 5, 8700512 (2015). Attached in appendix [G](#).
6. **Vibrationally Resolved B 1s Photoionization Cross Section of BF<sub>3</sub>.** D. Ayuso, M. Kimura, K. Kooser, M. Patanen, E. Plésiat, L. Argenti, S. Mondal, O. Travnikova, K. Sakai, A. Palacios, E. Kukk, P. Decleva, K. Ueda, F. Martín and C. Miron. *The Journal of Physical Chemistry A* **119**, 5971-5978 (2015). Attached in appendix [B](#).
5. **Ultrafast electron dynamics in phenylalanine initiated by attosecond pulses.** F. Calegari, D. Ayuso, A. Trabattoni, L. Belshaw, S. De Camillis, S. Anumula, F. Frassetto, L. Poletto, A. Palacios, P. Decleva, J. B. Greenwood, F. Martín and M. Nisoli. *Science* **346**, 6207, 336 (2014). Attached in appendix [F](#).
4. **Vibrationally resolved C 1s photoionization cross section of CF<sub>4</sub>.** M. Patanen, K Kooser, L. Argenti, D. Ayuso, M. Kimura, S. Mondal, A. Palacios, K. Sakai, O. Travnikova, P. Decleva, E. Kukk, E. Plésiat, C. Miron K. Ueda and F Martín. *Journal of Physics B: Atomic, Molecular and Optical Physics* **47**, 124032 (2014). Attached in appendix [C](#).

- 
3. **Dissociative and non-dissociative photoionization of molecular fluorine from inner and valence shells.** D. Ayuso, A. Palacios, P. Decleva and F. Martín. *Journal of Electron Spectroscopy and Related Phenomena* **195**, 320-326 (2014). Attached in appendix [E](#).
  2. **Intramolecular photoelectron diffraction in the gas phase.** K. Ueda, C. Miron, E. Plésiat, L. Argenti, M. Patanen, K. Kooser, D. Ayuso, S. Mondal, M. Kimura, K. Sakai, O. Travnikova, A. Palacios, P. Decleva, E. Kukk, and F. Martín. *The Journal of Chemical Physics* **139**, 124306 (2013). Attached in appendix [A](#).
  1. **Effects of molecular potential and geometry on atomic core-level photoemission over an extended energy range: The case study of the CO molecule.** E. Kukk, D. Ayuso, T. D. Thomas, P. Decleva, M. Patanen, L. Argenti, E. Plésiat, A. Palacios, K. Kooser, O. Travnikova, S. Mondal, M. Kimura, K. Sakai, C. Miron, F. Martín, and K. Ueda. *Physical Review A* **88**, 033412 (2013). Attached in appendix [D](#).

# Acknowledgements

I would like to express my gratitude to the people that have made this work possible:

- To Alicia, for guiding me during these four years, for her constant support and her very useful advice.
- To Fernando, for giving me the opportunity to join this wonderful group, for his support and for being a constant source of inspiration.
- To Piero, for being so accessible, for his clear explanations, for his support and for being the perfect host every time I had the opportunity to visit him in Trieste.
- To the experimental collaborators I had the opportunity to work with, in Milan, Belfast, Oregon, Turku, Sendai and Saint Malo, for allowing me to be part of amazing projects.
- To Álvaro, Oriana, Lara and Darek, for all the good moments shared during these four years and for their constant support.
- To Inés, Jesús, Luca, Sergio and Selma, for their useful advice and for sharing a bit of their knowledge with me.
- To my office mates, and to everyone in the department, because it has been wonderful to spend these four years with them.
- And to my family and friends, and to Steven.

---

The research leading to these results has received funding from European Union's Seventh Framework Programme (FP7/2007-2013) projects ERC-AdG-XChem (GA 290853) and MC-IRG ATTOTREND (GA 268284).

# Contents

<b>Introduction</b>	<b>15</b>
<b>Theory</b>	<b>29</b>
<b>1 Light-matter interaction</b>	<b>29</b>
1.1 Time-dependent Schrödinger equation . . . . .	29
1.2 Time-dependent perturbation theory . . . . .	32
1.3 Photoionization cross section . . . . .	35
<b>2 Molecular structure</b>	<b>37</b>
2.1 The molecular Hamiltonian . . . . .	37
2.1.1 The Born-Oppenheimer approximation . . . . .	38
2.2 Evaluation of electronic states . . . . .	42
2.2.1 Density functional theory . . . . .	42
2.2.2 Static-exchange DFT . . . . .	44
2.2.3 Time-dependent DFT . . . . .	52
2.3 Inclusion of the nuclear motion . . . . .	53
2.3.1 The nuclear Hamiltonian . . . . .	54
2.3.2 Evaluation of vibrational eigenstates . . . . .	56
2.3.3 Vibrationally resolved cross sections . . . . .	57
<b>3 Electron dynamics initiated by attosecond pulses</b>	<b>59</b>
3.1 Wave packet dynamics . . . . .	59
3.2 Evolution of the ionic subsystem . . . . .	63

---

<b>Results</b>	<b>69</b>
<b>4 Interferences in molecular photoionization</b>	<b>69</b>
4.1 Intramolecular scattering in inner-shell photoionization . . . . .	70
4.2 Photoionization of F <sub>2</sub> : multicenter emission . . . . .	77
4.3 Conclusions . . . . .	78
<b>5 Ultrafast electron dynamics in aminoacids</b>	<b>79</b>
5.1 Evaluation of electronic states . . . . .	85
5.2 Photoionization cross sections . . . . .	88
5.3 Ultrafast electron dynamics initiated by attosecond pulses . . . . .	92
5.3.1 Fourier analysis on the amino group . . . . .	97
5.3.2 Fourier analysis on different atoms . . . . .	103
5.3.3 Comparison with the experiment: Gabor profiles . . . . .	107
5.3.4 What about molecular conformation? . . . . .	109
5.4 Time-evolution of the full electron system . . . . .	113
<b>Conclusions</b>	<b>115</b>
<b>Conclusiones</b>	<b>119</b>
<b>Appendices</b>	<b>125</b>
<b>A</b> Intramolecular photoelectron diffraction in the gas phase	<b>125</b>
<b>B</b> Vibrationally resolved B1s photoionization cross section of BF <sub>3</sub>	<b>133</b>
<b>C</b> Vibrationally resolved C1s photoionization cross section of CF <sub>4</sub>	<b>147</b>
<b>D</b> Effects of molecular potential and geometry on atomic core-level photoemission over an extended energy range: The case study of the CO molecule	<b>157</b>

<b>E</b> Dissociative and non-dissociative photoionization of molecular fluorine from inner and valence shells	<b>167</b>
<b>F</b> Ultrafast electron dynamics in phenylalanine initiated by attosecond pulses	<b>177</b>
<b>G</b> Ultrafast charge dynamics in an amino acid induced by attosecond pulses	<b>203</b>
<b>Bibliography</b>	<b>217</b>





# Introduction

Chemical reactions occur as a result of bond breaking and formation, a dynamical process that, in general, is initiated by changes in the electronic structure of a molecule and followed by the subsequent nuclear rearrangement. The study of the dynamics associated to the nuclei belongs to the realm of femtochemistry, a well-established field that for more than twenty years has been able to capture and even control the nuclear motion in chemical reactions and intramolecular processes [1, 2]. The field obtained an important recognition in 1999, when Ahmed Zewail was awarded the Nobel prize in Chemistry “for his studies of the transition states of chemical reactions using femtosecond spectroscopy” [3]. One of the most common techniques to investigate the dynamics of a chemical reaction constitutes the well-known pump-probe spectroscopy: a short pulse of light (pump) is used to induce a process in a molecular target and, after some time, the dynamical response of the system is monitored with a second pulse (probe). By performing measurements with different time delays between the two pulses, it is possible to take “snapshots” of a chemical reaction. Of course, the duration of the light pulses employed needs to be (at least) of the same order of magnitude (or shorter) than the dynamics to observe. For instance, in order to monitor a process of charge transfer mediated by the nuclear motion in organic molecules [4], pulses in the femtosecond time domain were needed. This is the reason why purely electron motion, occurring in the attosecond time domain, has remained hidden from direct experimental observation until very recently, when pulses with durations as short as a few tens of attoseconds became available.

---

## Attosecond science

The experimental demonstration of attosecond pulses was achieved in 2001 [5, 6] using high harmonic generation (HHG) techniques, which opened a new era of time resolved experiments. HHG is a non-linear process occurring when an atomic or molecular gas is irradiated with an intense femtosecond laser, usually a Ti:sapphire laser with a central wavelength of 800 nm. The target will then emit XUV light with frequencies that are high odd multiples of the driving field [7, 8]. An interpretation of this phenomenon was given in 1993 [9] by Paul Corkum by means of a three-step model. Due to the distortion of the Coulomb potential generated by the strong IR field, the electron is ionized by tunneling through the electric barrier (see fig. 1). Then (second step), the electron is accelerated by the laser field and driven back towards the parent ion. In the last step, the recombination, the energy that the electron has accumulated during its journey is released as an energetic XUV or X-ray photon [9]. Since the first step (tunnel ionization) is a non-linear process that requires the absorption of several photons, it is more likely to occur at the maxima of the laser field, when the tunneling picture is valid. Thus, electrons are released and recombined in ultrashort intervals, leading to the formation attosecond laser pulses [10].

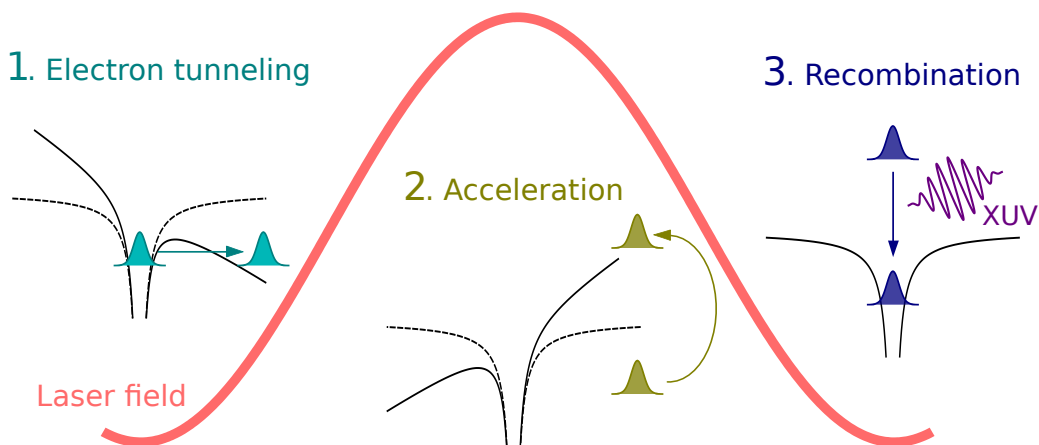


Figure 1: Schematic representation of the three-step model [9] for HHG: (1) tunnel ionization, (2) acceleration by the driving field and (3) recombination with the parent ion.

According to the three-step model, an attosecond pulse is generated every

half a cycle of the driving femtosecond pulse, which leads to the production of attosecond pulse trains (APTs) rather than single attosecond pulses (SAPs). A lot of work has been directed towards the generation of SAPs [11]. The first SAP was produced in 2001 by the group of Ferenc Krausz by using the selection of cutoff harmonics generated with a 7 fs IR pulse [5]. This short duration made that the highest harmonics were produced only during one half-cycle, thus generating a SAP. In order to characterize a SAP, one can use a co-propagating IR laser pulse by means of the attosecond streak camera [12]: the photoelectron emitted by the XUV pulse is driven by the presence of the IR field and its momentum is modified in a extent that depends on the relative time delay between the two pulses. The first fully-characterized few-cycle SAP was generated in 2006 in the group of Mauro Nisoli [13], with a duration of 130 as and a central frequency of 35 eV. Only two years later, an even shorter pulse was produced, with duration of 80 as and 80 eV of central energy [14]. To date, the shortest XUV pulses ever produced and characterized were 67 as-long and their central energy was 90 eV [15].

These impressive achievements have enabled the real-time observation and control of electron motion in atoms, molecules and condensed phases [16, 11, 17, 18]. The observation of the femtosecond Auger decay in krypton in 2002 was the first application of isolated attosecond pulses [19]. This demonstration was followed by other important experimental results in the field of ultrafast atomic physics, such as the real-time observation of electron tunneling [20] and the measurement of temporal delays of the order of a few tens of attoseconds in the photoemission of electrons from different atomic orbitals of neon [21] and argon [22]. The unprecedented time resolution offered by attosecond pulses has also allowed quantum mechanical electron motion and its degree of coherence to be measured in atoms by using attosecond transient absorption spectroscopy [23]. Attosecond techniques have also been applied in the field of ultrafast solid-state physics, with the measurement of delays in electron photoemission from crystalline solids [24] and the investigation of the ultrafast field-induced insulator-to-conductor state transition in a dielectric [25].

The application of attosecond techniques to molecules offers the possibility of investigating primary relaxation processes, which involve electronic and nu-

---

clear degrees of freedom and their coupling [26, 27, 28, 29, 30]. In the case of large molecules (e.g., biologically relevant molecules), prompt ionization by attosecond pulses may produce ultrafast charge migration along the molecular skeleton, preceding any nuclear rearrangements. This phenomenon has been predicted by various authors [31, 32, 33, 34, 35], whose work was stimulated by pioneering experiments performed by R. Weinkauff, E. W. Schlag and collaborators on fragmentation of peptide chains [36, 37, 38]. Ultrafast electron dynamics evolving on an attosecond or few-femtosecond temporal scale can determine the subsequent relaxation pathways of a molecule [30]. The process is induced by sudden generation of an electronic wave packet, which moves across the molecular chain and induces a site selective reactivity, which is related to charge localization in a particular site of the molecule [31]. Although the study of complex molecules is challenging, a formative measurement of the amino acid phenylalanine has shown that ionization by a short APT leads to dynamics on a temporal scale of a few tens of femtoseconds. This has been interpreted as the possible signature of ultrafast electron transfer inside the molecule [39]. Even though picosecond and femtosecond pulses are suitable for the investigation of nuclear dynamics, the study of electronic dynamics with these pulses has been made possible by slowing down the dynamics through the use of Rydberg electron wave packets [40]. However, in order to study the electron wave packet dynamics in the outer-valence molecular orbitals, relevant to most chemical and biological systems, attosecond pulses are required.

Despite the impressive progress made in the last decades, attosecond pulses generated via HHG still have two main constraints: their relatively low intensities, which can make some attosecond pump-probe experiments quite challenging, and the limited range of photon energies in which they can be produced. These limitations are overcome in the recently operating XUV/X-ray free-electron laser (FEL) facilities, which can already produce bright few-femtosecond pulses based on synchrotron light.

## **Synchrotron light**

Synchrotron radiation is emitted when charged particles moving at velocities close to the speed of light are forced to change direction by a magnetic field, as dictated

by the fundamental laws of electrodynamics [41]. The first observation of artificial synchrotron light occurred at the General Electric Research Laboratory in New York in 1947 [42], opening a new era of accelerator-based light sources. Synchrotron light sources rapidly evolved ever since through up to four different generations [43].

The so-called first-generation light sources were high-energy physics facilities where synchrotron radiation was generated as a byproduct. The interest for the use of synchrotron light increased over the years, motivating a series of pioneering advances. The most important was the development of storage rings [44], the basis for all of today's synchrotrons. A storage ring is a type of circular accelerator in which the beam of particles can circulate at a fixed energy during several hours, providing stable beam conditions and reducing the radiation hazard. In 1975, the Synchrotron Radiation Source (SRS) at the Daresbury Laboratory in the UK, the first synchrotron exclusively designed to the production of light, began to be constructed [45, 46]. It became operational in 1981 [47], the same year as the BESSY synchrotron [48] in Berlin, giving birth to the second-generation light sources. Over the years, some facilities that were originally developed to high-energy physics, such as the HASYLAB (Hamburger Synchrotronstrahlungslabor) at DESY, or the Stanford Synchrotron Radiation Laboratory at the SLAC National Accelerator Laboratory at Stanford, were upgraded to second-generation status and gradually started to dedicate more operating time to light production.

The development of insertion devices [49] led to the advent of third-generation light sources. Insertion devices are arrays of magnets with alternating polarity that, located into the straight sections of the storage rings, generate very bright beams and allow to shift the light spectrum towards higher photon energies. These devices were quickly incorporated into existing the synchrotron facilities. Third-generation facilities, designed with insertion devices in place from the beginning, saw the light in the 90s. The first of them was the European Synchrotron Radiation Facility (ESRF), located in Grenoble, France, which started operating in 1994 [50, 51].

To date, there are more than 50 dedicated second- and third-generation light

---

sources all over the world serving many areas of science. The BESSY II in Berlin, the ELETTRA in Trieste, the National Synchrotron Light Source in the USA, Spring-8 in Japan or SOLEIL in France are just a few examples. All of them present similar structures, with a storage ring having many ports connected to the beamlines, which are small stations where the experiments are performed. The configuration of the different beamlines, however, can be more different, depending on the kind of experiments they have been designed for.

Synchrotron radiation spans a wide energy range, from infrared light up to hard X-rays. It is characterized by its high brightness, being orders of magnitude brighter than that produced in conventional light sources. Synchrotron light is also highly polarized (linearly, circularly or elliptically), tunable, collimated (consisting of almost parallel rays) and concentrated over a small area. These properties make of synchrotron radiation one of the most important and universal research tools, with a steadily increasing number of applications [43, 52, 53].

The brightness of the light beams produced these facilities and the use of efficient X-ray monochromators [54] have brought unprecedented energy resolution to X-ray spectroscopy. This has led to major advances in X-ray absorption spectroscopy (XAS) that include the development of the near edge X-ray absorption fine structure spectroscopy (NEXAFS) and the X-ray absorption fine-structure spectroscopy (EXAFS) [55, 56] techniques. In addition to conventional XAS, ion-yield spectroscopy techniques, in which the yield of ionic fragments is recorded as a function of the photon energy, can provide useful information about photodissociation dynamics occurring in highly excited states [57, 58]. By recording fragmentation yields for different ejection angles one can also gain information about the symmetry of the states involved in the fragmentation dynamics [59].

Photoelectron spectroscopy has allowed to measure core-hole lifetime widths of molecular species [60, 61, 62] as well as their corresponding vibrational structures [63]. Recent work [64] has demonstrated that high-resolution resonant photoelectron spectroscopy can be applied to image molecular potentials of excited states and to identify new states that are invisible in conventional photoelectron spectroscopy techniques. The combination of high-resolution photoelectron spectroscopy with normal Auger electron spectroscopy has allowed to obtain in-

formation about potential energy curves of two-hole states in diatomic molecules [65]. By recording photoelectrons, Auger electrons and ionic fragments in coincidence, it has been possible to get a deeper insight into the Auger decay process [66, 67, 68, 69, 70, 71].

The application of angle-resolved photoelectron spectroscopy to gas-phase molecules can reveal structural details about the target. By measuring the photoemission intensity over a hemispherical region, it has been possible to reconstruct molecular orbital densities of large  $\pi$ -conjugated molecules [72]. When an electron is emitted from an inner shell of a molecule, the outgoing wave can be coherently scattered by the surrounding atomic constituents. Therefore, molecular-frame photoelectron angular distributions (MFPADs) are sensitive to molecular potentials and can thus be used to image molecular structures. MFPADs can be measured by registering photoelectrons in coincidence with ions [73] or with Auger electrons [74, 75]. It has been shown that in the case of small polyatomic molecules in which the central atom is bonded to hydrogens, such as  $\text{CH}_4$ , photoelectrons with low kinetic energy are emitted along the chemical bonds [76, 77, 78]. Although this assumption is no longer true when hydrogens are replaced by heavier fluorine atoms [78], MFPADs can still retrieve information about the tridimensional structure of the molecular target. Measuring MFPADs requires the use of rather sophisticated coincidence setups with high angular resolution and high detection efficiency [79, 80], which are not always available or applicable. Alternatively, recent work on the photoionization of diatomic and small polyatomic molecules by synchrotron radiation [81, 82] has shown that, under some circumstances, photoelectron spectra integrated over electron ejection angle can also be a valuable tool for structural determination.

Free-electron lasers (FELs) constitute the fourth generation of light sources, being able to generate ultrashort and ultrabright pulses of coherent light by using powerful linear accelerators which are several kilometers long. The underlying principle behind FELs is the self-amplified spontaneous emission (SASE). As in third-generation facilities, FELs make use of insertion devices to generate synchrotron light. This radiation interacts with the oscillating electrons, making them drift into microbunches, which are separated by a distance that is equal to one radiation wavelength. Through this interaction, the electrons start to emit

---

coherent light. The emitted radiation can reinforce itself, leading to high beam intensities and laser-like properties.

The first FEL to become operational was the Tesla Test Facility in Hamburg in 2000, that was replaced by FLASH in 2005, the first soft X-ray FEL [83], where the first experiments on coherent diffractive imaging were performed [84, 85, 86] by means of the so-called diffraction-before-destruction [87] technique. In 2009, the Linac Coherent Light Source (LCLS) in Stanford became the first hard X-ray FEL, improving the resolution of coherent diffractive imaging experiments [88, 89]. Other FEL facilities such as FERMI [90] (2010), at the Elettra Sincrotrone in Trieste, or SACLA (2011), embedded in the Spring-8 complex [91], have recently become operational, and new facilities are being designed or under construction.

## Theoretical methods

Advances in synchrotron- and HHG-based light sources have opened the door for structural determination of single isolated molecules, as well as for imaging and even controlling electron and nuclear dynamics, with exciting applications in physics, chemistry and biology. In order to guide and to understand these new generation of experiments, theoretical calculations are crucial. As we have seen, the development of high-resolution third-generation synchrotron light sources enabled the application of traditional photoelectron X-ray diffraction techniques to small molecules in the gas phase. However, solid theoretical support combining state-of-the-art calculations with the use of simple models was needed to understand and interpret the diffraction patterns arising in the photoelectron spectra. Moreover, theoretical predictions have guided and motivated a large number of attosecond experiments, such as the recent observation of ultrafast charge migration in a biomolecule [92]. The first theoretical prediction of charge migration in complex systems came from Lorenz S. Cederbaum and J. Zobeley more than 15 years ago [32], demonstrating that electron correlation can drive purely electron dynamics in a sub-femtosecond time scale, faster than the onset of the nuclear motion. Over the years, they have investigated this phenomenon in a large number of organic molecules, ranging from small amino acids such as glycine [93, 94] to larger systems containing aromatic rings [95], using *ab initio* approaches that accurately account for electron correlation. Charge migration has become a hot



topic, attracting the interest of a number of researchers and giving rise to exciting theoretical predictions [96]. In 2006, Françoise Remacle and Raphael D. Levine showed that a positive hole could migrate from the amino to the carboxyl terminal of a tetrapeptide in just one and a half femtosecond [31] by using Density Functional Theory. These predictions have motivated recent experimental observations [39, 92, 97] with attosecond pulses generated via HHG as well as the design of noble experiments based on FELs [98]. In these theoretical works, the initial wave packet was prepared by removing an electron from a given molecular orbital, creating a hole in the electronic structure of the molecule. Then, since the ionized state is not a stationary state of the ionic Hamiltonian but a linear superposition of several of them, the hole moves through the molecular skeleton with a velocity that is dictated by the energy spacing between the interfering states. Although approaches accounting for the interaction with experimentally realistic attosecond pulses have been recently developed [99, 100, 101, 92, 97], the evaluation of electronic wave packets in the continuum is still challenging, especially in the case of complex molecules.

The so-called fixed-nuclei approximation has been assumed in the works above mentioned. Although it is a reasonable approach because the nuclear motion usually comes into play in a longer time scale, some influence cannot be completely excluded. For instance, it has been shown that stretching a few picometers of carbon bonds can occur in a few femtoseconds and can modify the charge dynamics in organic molecules [95]. Semi-classical approaches have been recently applied to the description of coupled electron-nuclear dynamics in complex molecules. An implementation of the Ehrenfest method within the Complete Active Space Self Consistent Field (CASSCF) formalism has allowed to explore the damper effect of the nuclear dynamics in the charge migration mechanism [102, 103, 104]. Another recent work [105] has shown that attosecond hole migration in a benzene cation can survive the nuclear motion for more than 10 fs. However, despite these advances, a full description of charge migration in a complex molecule including the nuclear degrees of freedom in which the photoionization step is properly accounted for is yet to be done.

The theoretical description of electron and nuclear dynamics in which all degrees of freedom are fully correlated is very difficult even for the case of small mo-

---

lecules. In this context, the multi-configurational time-dependent Hartree-Fock (MCTDHF) method [106, 107, 108, 109, 110, 111, 112, 113] has been proved to be a powerful tool. Also, approaches based on Density Functional Theory (DFT) can be very useful because of their good compromise between accuracy and computational effort. Our group, in collaboration with Piero Decleva in Trieste, is pioneer in the use of the static-exchange DFT method and a more elaborate time-dependent version together with new approaches to include the nuclear motion at the Born-Oppenheimer level in diatomic molecules [81, 82, 114, 115, 116] and for the symmetric stretching mode in molecules with a small number of atoms [117, 118, 119, 120, 121, 122], finding very good agreement with recent experimental results obtained with synchrotron radiation. These studies have been partially developed during this PhD thesis. Nevertheless, it should be mentioned that the inclusion of more vibrational degrees of freedom while keeping a reliable description of electron correlation remains a challenge.

## Outline

The aim of this work is to investigate light-induced phenomena in simple isolated systems, with especial emphasis in the theoretical description of processes that can be traced and manipulated using synchrotron radiation and ultrafast laser pulses. In particular, we have focused on the investigation of (1) photoionization of small molecules using methods that account for both nuclear and electronic degrees of freedom, and (2) ultrafast electron dynamics in larger molecules initiated by attosecond XUV pulses. All the work presented in this PhD thesis has been done in collaboration with Piero Decleva, from Università degli Studi di Trieste.

The theoretical methods employed in this work are described in chapters 1, 2 and 3. Chapter 1 reviews the general concepts to treat light-matter interaction. How to apply these concepts to the special case of molecules interacting with synchrotron radiation and attosecond pulses is presented in chapters 2 and 3. In this work we have employed the static-exchange DFT method, developed by Mauro Stener, Piero Decleva and collaborators, briefly described in chapter 2, to evaluate bound and continuum electronic stationary states. The nuclear motion has been accounted for within the Born-Oppenheimer approximation in the case of diatomic and small polyatomic molecules. This has allowed

for the computation of vibrational excitations upon ionization and the investigation of non-Franck-Condon effects. Results are presented in chapters 4 and 5. Chapter 4 is devoted to our study of small molecules with synchrotron radiation, while chapter 5 is focused on the investigation of electron dynamics upon photoionization with ultrashort pulses in amino acids.

We have first investigated the interferences arising in the photoionization of small molecules ( $\text{BF}_3$ ,  $\text{CF}_4$ ,  $\text{CO}$  and  $\text{F}_2$ ) at high photoelectron energies by analyzing the role of the nuclear motion. In collaboration with the experimental groups of Edwin Kukk (Turku University), Catalin Miron (Synchrotron SOLEIL), Kiyosi Ueda (Synchrotron SPring-8) and Thomas Darrah Thomas (Oregon State University), we have found evidence of intramolecular scattering occurring in the inner-shell photoionization of  $\text{CO}$ ,  $\text{CF}_4$  and  $\text{BF}_3$  imprinted the collective vibrational excitation that accompanies 1s ionization from the C ( $\text{CO}$ ,  $\text{CF}_4$ ) or the B ( $\text{BF}_3$ ) atom at high photoelectron energies. The ratios between vibrationally resolved photoionization cross sections ( $\nu$ -ratios) show pronounced oscillations as a function of the photon energy which are the fingerprint of electron diffraction by the surrounding atomic centers and therefore carry information of the molecular target as well as of the ionization process. As a proof of principle, we have illustrated how to retrieve the structural information encoded in the  $\nu$ -ratios by determining the internuclear distances of the  $\text{CO}$  molecule and of the core-hole species generated upon C 1s ionization. A different scenario occurs when the electron is emitted not from a well confined region in the molecule but from a delocalized orbital. In these situations, double (triple...) slit-like interferences are expected to arise. We have investigated this phenomenon in the  $\text{F}_2$  molecule, where, due to symmetry, the orbitals are delocalized between the two atomic centers. By analyzing the role of the nuclear motion upon photoabsorption, we have found experimentally measurable evidence of double slit-like interferences in the angle-integrated photoelectron spectra. All these results are summarized in chapter 4 and the published manuscripts are attached in appendices A, B, C, D and E.

We then move to more complex molecules, where we restrict ourselves to frozen nuclei, although applying time-dependent treatments for electron dynamics. Ultrashort light pulses can create coherent superpositions of electronic states, trigge-

---

ring electron motion at a speed that is determined by the energy spacing between the interfering states. We have investigated the ultrafast electronic response of large biological systems to attosecond XUV pulses, in collaboration with the experimental groups of Mauro Nisoli (Politecnico di Milano), Luca Poletto (Istituto Nazionale di Fotonica - Consiglio Nazionale delle Ricerche) and Jason Greenwood (Queen's University). Our study, presented in chapter 5 and in appendices F and G, includes the amino acids glycine, phenylalanine and tryptophan, with the aim of understanding the influence of the different radicals in the charge migration mechanism. For each molecule, we have evaluated the electronic wave packet generated by an attosecond XUV pulse by means of the static-exchange DFT method and time-dependent first-order perturbation theory. The Fourier analysis of the hole density over different portions of the molecule reveals ultrafast beatings that are in very good agreement with the oscillations found in a XUV/NIR pump-probe experiment where the yield of different fragments is measured as a function of the pump-probe time delay.

# Theory



# Chapter 1

## Light-matter interaction

The aim of this chapter is to review the general concepts on light-matter interaction and the expressions that we employ to describe the behavior of atomic and molecular systems in an electromagnetic field. We focus on the interaction with “weak” radiation, which can be accurately described using perturbative approaches.

### 1.1 Time-dependent Schrödinger equation

The evolution of a quantum system is fully determined by the time-dependent Schrödinger equation (TDSE) [123]:

$$i\hbar \frac{\partial}{\partial t} \Phi(t) = \hat{H}(t) \Phi(t) \quad (1.1)$$

where  $\Phi(t)$  is the wave function of the system and  $\hat{H}(t)$  is the Hamiltonian operator. For the sake of simplicity, nor spatial or spin coordinates are explicitly indicated here. The formal solution of the TDSE is given by

$$\Phi(t) = U(t_0, t) \Phi(t_0) \quad (1.2)$$

where  $U(t_0, t) = e^{-\frac{i}{\hbar} \int_{t_0}^t \hat{H}(\tau) d\tau}$  is the so-called evolution operator, which propagates the wave function from an initial time  $t_0$  to  $t$ ,  $\hbar$  being the reduced Planck constant. Eqs. 1.1 and 1.2 are general and, in principle, applicable to any sys-

tem. Our goal is to investigate the behavior of matter upon interaction with bright light. Specifically, we are interested in exploring molecular targets subject to ultrashort laser pulses and synchrotron radiation. These light sources are usually intense enough so that one can describe the flux of photons as a continuum variable, i.e., by means of Maxwell equations [41, 123]. Furthermore, magnetic interactions are usually weak in these contexts and light can be modeled as an oscillating electric field. Neglecting spin orbit couplings, mass polarization and relativistic effects, the Hamiltonian operator of a set of  $N$  charged particles may be written as

$$\hat{H}(t) = \underbrace{\sum_{i=1}^N \left[ \frac{\mathbf{p}_i^2}{2m_i} + \sum_{j=1}^N \frac{q_i q_j}{|\mathbf{r}_i - \mathbf{r}_j|^2} \right]}_{\hat{H}_0} + \underbrace{\sum_{i=1}^N q_i \mathbf{r}_i \mathbf{E}(t)}_{\hat{V}(t)} \quad (1.3)$$

where  $\mathbf{r}_i$ ,  $\mathbf{p}_i$ ,  $m_i$  and  $q_i$  are the position, momentum, mass and charge of the  $i$ -th particle, respectively, and  $\mathbf{E}(t)$  is the electric field of the electromagnetic wave in the dipole approximation [41, 123], which neglects the spatial dependence of the field across the system. This is usually a good approach for long and medium wavelength fields and for small atomic systems as long as the wavelength is significantly larger than the dimensions of the system. For our purposes, it is convenient to split  $\hat{H}$  into two parts (see eq. 1.3): the field-free Hamiltonian,  $\hat{H}_0$ , and a term accounting for the interaction with the radiation,  $\hat{V}(t)$ . Note that the interaction term in eq. 1.1 has been written in the length gauge.

## Spectral methods

Even though eq. 1.1 does not have an exact analytical solution in most cases, it can be solved, for instance, by defining an initial wave function in a grid of points and then propagate it numerically. However, grid-based methods are typically expensive since one has to use large numbers of grid points in order to get accurate results. In quantum chemistry, it is more efficient to use spectral methods, in which the wave function is expanded onto a complete basis set of functions. Of course, the efficiency and accuracy here depend on the adequate choice of the basis set for the particular problem. It is usually a good approach to use the eigenstates



of the field-free Hamiltonian, which are the solutions of the the eigenvalue problem given by

$$\hat{H}_0\phi_k = E_k\phi_k \quad (1.4)$$

where  $\phi_k$  are the eigenfunctions of  $\hat{H}_0$ , which form a complete basis set, and  $E_k$  are the corresponding eigenvalues. The total wave function can be expanded as

$$\Phi(t) = \sum_k c_k(t)\phi_k \quad (1.5)$$

where the time dependence is contained in the spectral coefficients  $c_k(t)$ , which satisfy

$$c_k(t) = \langle\phi_k|\Phi(t)\rangle \quad (1.6)$$

due to the orthogonality of the basis. Inserting the spectral expansion of the wave function (eq. 1.5) into the TDSE (eq. 1.1), we obtain

$$i\hbar\frac{\partial}{\partial t}\sum_k c_k\phi_k = \sum_k c_k[E_k + \hat{V}(t)]\phi_k \quad (1.7)$$

where we have made use of eq. 1.4. By left-side projecting onto  $\langle\phi_n|$  and applying the orthogonality relation  $\langle\phi_i|\phi_j\rangle = \delta_{ij}$ , eq. 1.7 reads

$$i\hbar\frac{d}{dt}c_n(t) = c_n(t)E_n + \sum_k c_k\langle\phi_n|\hat{V}(t)|\phi_k\rangle \quad (1.8)$$

We have obtained a set of coupled equations that describe the time-evolution of the spectral coefficients. A more compact version of eq. 1.8 can be obtained by performing the change of variables

$$c_n(t) = \tilde{c}_n(t)e^{-iE_n t/\hbar} \quad (1.9)$$

where  $\tilde{c}_n(t)$  are the coefficients in the interaction picture [123], which are equivalent to those in the Schrödinger picture  $c_n(t)$  except for the corresponding stationary phases. Applying eq. 1.9 to the coefficients in eq. 1.8 and multiplying

both sides of eq. 1.8 by  $e^{iE_n t/\hbar}$ , we obtain

$$i\hbar \frac{d}{dt} \tilde{c}_n(t) = \sum_k \tilde{c}_k(t) e^{i\omega_{nk}t} \langle \phi_n | \hat{V}(t) | \phi_k \rangle \quad (1.10)$$

where we have introduced the Bohr angular frequency  $\omega_{nk} = \frac{E_n - E_k}{\hbar}$ . This set of coupled equations is completely general and rigorously equivalent to eq. 1.1. The coupling between different states arises from the existence of the external potential  $\hat{V}(t)$ , which relates the evolution of  $\tilde{c}_n(t)$  to that of all the other coefficients. In general, eq. 1.10 can be solved numerically by breaking the time domain into small steps  $\{t_1, t_2, \dots\}$  and the set  $\{\tilde{c}_n(t_j)\}_n$  is obtained from  $\{\tilde{c}_n(t_{j-1})\}_n$  through iterative procedures [124, 17, 125]. However, this approach might become computationally expensive in some situations. If the external potential  $\hat{V}(t)$  is weak, the time-evolution of the wave function can be evaluated more efficiently making use of perturbation theory, as we explain in the next section.

## 1.2 Time-dependent perturbation theory

Perturbation theory provides a useful approach to solve the TDSE when the field applied to the system is weak and therefore  $\hat{V}(t)$  can be treated as a perturbation. Under this assumption, the set of coefficients  $\tilde{c}_n(t)$  hardly vary in time and their zero-th order solution is given by their initial values:

$$\tilde{c}_n^{(0)}(t) \simeq \tilde{c}_n(0) \quad (1.11)$$

Solutions of higher order ( $r > 0$ ) can be evaluated using the recurrence relation

$$i\hbar \frac{d}{dt} \tilde{c}_n^{(r)}(t) = \sum_k \tilde{c}_k^{(r-1)}(t) e^{i\omega_{nk}t} \langle \phi_n | \hat{V}(t) | \phi_k \rangle \quad (1.12)$$

which enables to obtain the  $r$ -th order solution from the  $(r - 1)$ -th order one. We are interested in situations in which non linear processes are negligible and can thus be accurately described using **first-order perturbation theory**, which approximates the exact wave function to its first-order solution. If the system is assumed to be in the ground state at  $t = 0$ , that is,  $\tilde{c}_n(0) = \delta_{0n}$ , the zero-th order

solution is given by  $\tilde{c}_n^{(0)}(t) = \delta_{0n}$ . Inserting it into the right side of eq. 1.12, we can evaluate the first-order solution

$$i\hbar \frac{d}{dt} \tilde{c}_n^{(1)}(t) \simeq e^{i\omega_{n0}t} \langle \phi_n | \hat{V}(t) | \phi_0 \rangle \quad (1.13)$$

By integrating in time and making use of the initial condition  $\tilde{c}_n(0) = \delta_{0n}$  we obtain:

$$\tilde{c}_n^{(1)}(t) \simeq \delta_{0n} - \frac{i}{\hbar} \int_0^t e^{i\omega_{n0}\tau} \langle \phi_n | \hat{V}(\tau) | \phi_0 \rangle d\tau \quad (1.14)$$

In our particular case  $\hat{V}(t) = \boldsymbol{\mu} \mathbf{E}(t)$ , where  $\boldsymbol{\mu} = \sum_n q_n \mathbf{r}_n$  is the dipole moment operator. Then, for  $n \neq 0$ , we have

$$\tilde{c}_n^{(1)}(t) = -\frac{i}{\hbar} \langle \phi_n | \boldsymbol{\mu}_\epsilon | \phi_0 \rangle \int_0^t e^{i\omega_{n0}\tau} \mathbf{E}(\tau) d\tau \quad (1.15)$$

where  $\boldsymbol{\mu}_\epsilon = \hat{\boldsymbol{\epsilon}} \boldsymbol{\mu}$  is the component of the dipole operator along  $\hat{\boldsymbol{\epsilon}}$ , the polarization direction of the field and  $\mathbf{E}(t) = E(t) \hat{\boldsymbol{\epsilon}}$ . Eq. 1.15 can provide accurate values of the time-dependent coefficients upon interaction with an ultrashort laser pulse provided only linear effects come into play. We can retrieve the set of coefficients in the Schrödinger picture using using eq. 1.9. The corresponding transition probabilities are given by the square of the spectral amplitudes:

$$P_{n \leftarrow 0}(t) = |c_n(t)|^2 = |\tilde{c}_n(t)|^2 \quad (1.16)$$

where one can use  $c_n(t)$  or  $\tilde{c}_n(t)$  since they are equal except for a stationary phase.

### The special case of a sinusoidal perturbation

Let us consider the case of monochromatic light in the dipole approximation, i.e.,

$$\mathbf{E}(t) = E_0 \sin(\omega t) \hat{\boldsymbol{\epsilon}} = \frac{E_0}{2} \left[ e^{i\omega t} - e^{-i\omega t} \right] \hat{\boldsymbol{\epsilon}} \quad (1.17)$$

where  $\omega$  is the frequency of the radiation. This is a reasonable approach to model an experiment with synchrotron radiation, where the photon energy is well defined

[43]. Inserting eq. 1.17 into eq. 1.15, we obtain:

$$\tilde{c}_n^{(1)}(t) = -\frac{i}{2\hbar} \langle \phi_n | \boldsymbol{\mu}_\epsilon | \phi_0 \rangle \int_0^t \left[ e^{i(\omega_{n0} + \omega)\tau} - e^{i(\omega_{n0} - \omega)\tau} \right] d\tau \quad (1.18)$$

$$= -\frac{i}{2\hbar} \langle \phi_n | \boldsymbol{\mu}_\epsilon | \phi_0 \rangle \left[ \frac{1 - e^{i(\omega_{n0} + \omega)t}}{\omega_{n0} + \omega} - \frac{1 - e^{i(\omega_{n0} - \omega)t}}{\omega_{n0} - \omega} \right] \quad (1.19)$$

By making use of eq. 1.16 we can evaluate the transition probability:

$$P_{n \leftarrow 0}(t) = |\tilde{c}_n|^2(t) = \frac{2}{4\hbar^2} |\langle \phi_n | \boldsymbol{\mu}_\epsilon | \phi_0 \rangle|^2 \left| \frac{1 - e^{i(\omega_{n0} + \omega)t}}{\omega_{n0} + \omega} - \frac{1 - e^{i(\omega_{n0} - \omega)t}}{\omega_{n0} - \omega} \right|^2 \quad (1.20)$$

For a fixed value of  $t$ , the transition probability is a function of  $\omega$  having two pronounced maxima for  $\omega = \omega_{n0}$  and  $\omega = -\omega_{n0}$  due to the two terms inside the bracket. The first term, which maximizes for  $\omega = -\omega_{n0}$ , accounts for transitions from the initial to lower energy states occurring through induced photoemission. Here we seek to describe excitations that take place upon photoabsorption from the ground state. These are accounted for in the second term, which maximizes for  $\omega = \omega_{n0}$ . Removing the induced photoemission term in eq. 1.20 and making use of the identity  $e^{i\alpha} - 1 = 2ie^{i\alpha/2} \sin(\alpha/2)$ , we obtain:

$$P_{n \leftarrow 0}(t) = \frac{2}{\hbar^2} |\langle \phi_n | \boldsymbol{\mu}_\epsilon | \phi_0 \rangle|^2 \frac{\sin^2([\omega_{n0} - \omega]t/2)}{(\omega_{n0} - \omega)^2} \quad (1.21)$$

We are interested in finding the transition probability upon a long-time interaction. In the limit  $t \rightarrow \infty$ , the function  $\frac{\sin^2(\alpha t/2)}{\alpha^2}$  can be approximated by  $\frac{\pi t}{2} \delta(\alpha)$ . Then, in the long-time limit, we have:

$$P_{n \leftarrow 0}(t) = \frac{\pi^2 t}{2\hbar^2} |\langle \phi_n | \boldsymbol{\mu}_\epsilon | \phi_0 \rangle|^2 \delta(\omega_{n0} - \omega) \quad (1.22)$$

Note that this limit corresponds to the case of perfectly monochromatic light, where the photon energy is well defined and given by  $\hbar\omega$ . Therefore, a transition from the ground to an excited state  $n$  will only occur if  $\omega = \omega_{n0}$ . The transition rate, i.e., the transition probability per unit of time can be obtained by integrating over a range of frequencies  $(\omega_1, \omega_2)$  containing  $\omega_{n0}$  and derivating with respect to

time:

$$\Gamma_{n\leftarrow 0} = \frac{d}{dt} \int_{\omega_1}^{\omega_2} P_{n\leftarrow 0}(t) d\omega = \frac{\pi^2}{2\hbar^2} |\langle \phi_n | \boldsymbol{\mu}_\epsilon | \phi_0 \rangle|^2 \quad (1.23)$$

Although transition rates are experimentally measurable quantities, in practice, it is more convenient to measure photoionization cross sections since they are independent of the experimental conditions, as we explain in the next section.

### 1.3 Photoionization cross section

The cross section is defined as the hypothetical surface of effective interaction between a flux of particles and their targets. In the particular case of photoionization, it refers to the probability of an electron to be emitted from the target upon interaction with the field. The cross section corresponding to a transition from the ground state  $\Phi_0$  to a final  $\Phi_n$  state is given by [123]:

$$\sigma = \frac{\Gamma_{n\leftarrow 0}}{F} \quad (1.24)$$

where  $F$  is the flux of photons per unit of area and time, which is related to the amplitude of the electric field  $E_0$  according to

$$F = \frac{E_0^2 c}{8\pi\hbar\omega} \quad (1.25)$$

and  $c$  is the speed of light. Inserting 1.23 and 1.25 into 1.24, we obtain the photoionization cross section for a given orientation of the system with respect to the field:

$$\sigma_\epsilon = \frac{4\pi^2\omega}{\hbar c} |\langle \phi_n | \boldsymbol{\mu}_\epsilon | \phi_0 \rangle|^2 \quad (1.26)$$

As can be seen in eq. 1.26, the cross section does not depend on the parameters of the field. For this reason, it is a very useful quantity to compare results obtained under different experimental conditions.

#### Randomly oriented targets

In the case of randomly oriented molecules, the total cross section can be retrieved by averaging incoherently over three orthogonal directions of  $\epsilon$ , let us call them

$x$ ,  $y$  and  $z$ :

$$\sigma = \frac{\sigma_x + \sigma_y + \sigma_z}{3} \quad (1.27)$$

Eq. 1.27 allows to reproduce experimental results in which targets without spherical symmetry are not aligned with the field.

# Chapter 2

## Molecular structure

The present chapter describes the methodology employed to include the electronic and nuclear degrees of freedom in the theoretical description of molecular photoionization. Ionization of molecules is more complex than in the case of atoms because of the lack of spherical symmetry and due to the added degrees of freedom of the nuclear motion. Thus, one has to assume certain approximations that simplify the full problem which, as the number of degrees of freedom increases, becomes computationally intractable. In this work we have evaluated the electronic structure of the molecules we have investigated using methods based on the Density Functional Theory (DFT), which can account for electronic exchange and correlation effects in medium and large size systems using reasonable computational resources. The nuclear motion has been included at the Born-Oppenheimer level in the case of diatomic and small polyatomic molecules, allowing to evaluate vibrationally resolved photoionization cross sections.

### 2.1 The molecular Hamiltonian

The Hamiltonian operator representing the energy of the electrons and the nuclei in a molecule, the field-free molecular Hamiltonian, can be written as [126]:

$$\hat{H} = \hat{T}_e + \hat{T}_N + \hat{V}_{ee} + \hat{V}_{eN} + \hat{V}_{NN} \quad (2.1)$$

where:

- $T_e = -\frac{1}{2} \sum_{i=1}^N \frac{1}{m_e} \nabla_i^2$  is the kinetic energy of the  $N$  electrons,
- $\hat{T}_N = -\frac{1}{2} \sum_{i=1}^M \frac{1}{M_\alpha} \nabla_\alpha^2$  is the kinetic energy of the  $M$  nuclei,
- $\hat{V}_{ee} = \sum_{i=1}^N \sum_{j>i}^N \frac{e^2}{|\mathbf{r}_i - \mathbf{r}_j|}$  is the electrostatic repulsion between electrons,
- $\hat{V}_{eN} = -\sum_{i=1}^N \sum_{\alpha=1}^M \frac{Z_\alpha e^2}{|r_i - \mathbf{R}_\alpha|}$  is the attraction between electrons and nuclei,
- $\hat{V}_{NN} = \sum_{\alpha=1}^M \sum_{\beta>\alpha}^M \frac{Z_\alpha Z_\beta e^2}{|\mathbf{R}_\alpha - \mathbf{R}_\beta|}$  is the repulsion energy term between nuclei,

$\mathbf{r}_i$  and  $\mathbf{R}_\alpha$  stand for the coordinates of the electron  $i$  and nuclei  $\alpha$ , respectively,  $m_e$  and  $e$  are the mass and the absolute value of the charge of the electron, and  $M_\alpha$  and  $Z_\alpha$  are the mass and the atomic number of the nuclei  $\alpha$ . In order to find the eigenstates of  $\hat{H}$ , which constitute the set of stationary solutions of the molecular system, one can take advantage of the fact that since nuclei are more massive than the light electrons, their motion is slower, as we explain in the following.

### 2.1.1 The Born-Oppenheimer approximation

Since the electromagnetic forces acting on electrons and nuclei have similar intensity, one might assume their momenta to be of the same magnitude. Then, as the nuclei are significantly heavier, they must accordingly have much smaller velocities. Based on this idea, Max Born and J. Robert Oppenheimer proposed a way to decouple electron and nuclear dynamics by splitting the total wave function into two parts [127]. Within the Born-Oppenheimer approximation, the stationary states of the full-system can be written as product of an electronic stationary state  $\Psi_n(\bar{\mathbf{x}}, \bar{\mathbf{R}})$ , depending on both the electronic and the nuclear coordinates, and a nuclear stationary state  $\chi_{n\nu}(\bar{\mathbf{R}})$ , which only depends on the nuclear degrees of freedom:

$$\Phi_{n\nu}(\bar{\mathbf{x}}, \bar{\mathbf{R}}) = \Psi_n(\bar{\mathbf{x}}, \bar{\mathbf{R}}) \chi_{n\nu}(\bar{\mathbf{R}}) \quad (2.2)$$



where  $n$  and  $\nu$  are indexes (in general, sets of indexes) over the electronic and nuclear eigenstates labeling the vibronic state  $\Phi_{n\nu}(\bar{\mathbf{x}}, \bar{\mathbf{R}})$ , where  $\bar{\mathbf{x}} = (\mathbf{x}_1, \dots, \mathbf{x}_N)$  is a vector containing the spin and spatial coordinates of all electrons and  $\bar{\mathbf{R}} = (\mathbf{R}_1, \dots, \mathbf{R}_M)$  contains all nuclear spatial coordinates (nuclear spin coordinates have been dropped). Electronic stationary states satisfy the electronic time-independent Schrödinger equation:

$$\left[ \underbrace{\hat{T}_e + \hat{V}_{ee} + \hat{V}_{eN} + \hat{V}_{NN}}_{\hat{H}_e} \right] \Psi_n(\bar{\mathbf{x}}, \bar{\mathbf{R}}) = E_n(\bar{\mathbf{R}}) \Psi_n(\bar{\mathbf{x}}, \bar{\mathbf{R}}) \quad (2.3)$$

where  $\hat{H}_e$  is the electronic Hamiltonian and  $E_n(\bar{\mathbf{R}})$  is the energy of the electronic state  $n$ , which depends on the nuclear coordinates  $\bar{\mathbf{R}}$ . Eq. 2.3 can be solved parametrically in a grid of nuclear geometries. By doing so, one obtains the potential energy surfaces  $E_n(\bar{\mathbf{R}})$  in which the nuclei move. Note that, in each electronic calculation, the nuclear repulsion energy term ( $\hat{V}_{NN}$  in eq. 2.3) is just a constant value and thus its only effect is increasing the electronic eigenvalue. The nuclear stationary states  $\chi_{n\nu}$  associated to a given electronic state  $n$  can be obtained by solving nuclear time-independent Schrödinger equation:

$$\left[ \underbrace{T_N + E_n(\bar{\mathbf{R}})}_{\hat{H}_N} \right] \chi_{n\nu}(\bar{\mathbf{R}}) = E_{n\nu} \chi_{n\nu}(\bar{\mathbf{R}}) \quad (2.4)$$

where  $E_{n\nu}$  is energy of the vibronic state defined by the quantum numbers  $n$  and  $\nu$ . The Born-Oppenheimer approximation assumes that  $\Phi_{n\nu}(\bar{\mathbf{x}}, \bar{\mathbf{R}})$  varies very smoothly with  $\bar{\mathbf{R}}$  and therefore that the electrons rearrange instantaneously as the nuclei move. This assumption is valid as long as the energy spacing between electronic states, i.e.,  $E_n(\bar{\mathbf{R}}) - E_{n-1}(\bar{\mathbf{R}})$ , is sufficiently large and, in a photoionization process, as long as the photoelectron is not emitted very slowly, that is, with very low kinetic energy. The Born-Oppenheimer approximation provides a powerful tool for the accurate evaluation of vibronic stationary states of diatomic and small polyatomic molecules, and also of larger systems in situations in which reduced-dimensionality models are applicable.

## Potential energy curves

As already indicated, the eigenvalues of eq. 2.3, when solved in a grid of molecular geometries, constitute a set of potential energy surfaces (PESs) or curves (PECs) in the monodimensional case. In this work we have employed the static-exchange DFT method and also the more elaborate time-dependent DFT to evaluate the electronic stationary states of the molecules we have investigated, as we explain in section 2.2. Although these methods can accurately describe transitions to the electronic continuum, essential in order to describe photoionization, the energy values they provide might not be accurate enough in some situations. In general, *ab initio* multi-reference methods can produce accurate PESs of medium-size systems [126]. In the case of a core-hole species, the situation is more challenging since one needs to develop specific approaches to avoid the variational collapse of the wave function while keeping a good description of electron correlation [128, 129]. We have investigated the role of the nuclear motion in the photoionization of diatomic (CO, F<sub>2</sub>) and small polyatomic (BF<sub>3</sub>, CF<sub>4</sub>) molecules under conditions in which only one vibrational mode is active. In these situations, the harmonic and the Morse approximations provide a good alternative for the evaluation of the PECs:

- **The harmonic oscillator** models an ideal system that when taken away from the equilibrium position  $R_{eq}$  experiences a restoring force that is proportional to the extent of the displacement. It allows to write the potential energy as

$$E(R) = \frac{1}{2}m\omega^2(R - R_{eq})^2 \quad (2.5)$$

where  $m$  is the mass of the system,  $\omega$  is the angular frequency and  $R$  is the nuclear coordinate. This simple formula can provide a good representation of the PEC around the equilibrium geometry, but it cannot describe molecular dissociation since it does not take into account the anharmonicity of the chemical bonds. Consequently, it allows to evaluate low-energy stationary eigenstates with accuracy [118, 120], but it should not be used to describe the high-energy region.

- **The Morse potential** [130] provides a valid description of the PEC in a larger range of internuclear distances in terms of a simple analytical formula

that takes into account the anharmonicity of the chemical bonds:

$$V(R) = V(R_{eq}) + D_e \left[ 1 - e^{\alpha(R-R_{eq})} \right]^2 \quad (2.6)$$

where  $R_{eq}$  is the equilibrium distance,  $D_e$  is the depth of the potential energy well and  $\alpha$  is a parameter controlling its width. The Morse parameters are related to the usual spectroscopic ones (the oscillator strength,  $\omega_e$ , and the anharmonicity parameter,  $\omega_e x_e$ ) by the formulas

$$D_e = \frac{\omega_e^2}{4\omega_e x_e} - \frac{\omega_e x_e}{4} \simeq \frac{\omega_e^2}{4\omega_e x_e} \quad (2.7)$$

$$\alpha = \sqrt{\frac{k_e}{2D_e}} \quad (2.8)$$

Although eq. 2.6 was designed for studying diatomic molecules, it can still provide accurate results for the totally-symmetric stretching mode of small polyatomics [82, 118, 119, 122].

### The fixed-nuclei approximation

Some purely electronic processes can occur before the onset of the nuclear motion and can thus be described in the framework of the fixed-nuclei approximation (FNA), in which the nuclei are assumed to remain frozen at their equilibrium positions ( $\bar{\mathbf{R}} = \bar{\mathbf{R}}_{eq}$ ). Within the FNA, electronic stationary states satisfy:

$$\left[ \underbrace{\hat{T}_e + \hat{V}_{ee} + \hat{V}_{eN} + \hat{V}_{NN}}_{\hat{H}_e} \right] \Psi_n(\bar{\mathbf{x}}, \bar{\mathbf{R}}_{eq}) = E_n(\bar{\mathbf{R}}_{eq}) \Psi_n(\bar{\mathbf{x}}, \bar{\mathbf{R}}_{eq}) \quad (2.9)$$

The fixed-nuclei approximation can provide accurate values of total photoionization cross sections (see, for instance [131, 132, 133]) when the variation of the electronic structure with the internuclear distances is smooth around the Franck-Condon region. The FNA has also been successfully applied to time-dependent problems in large systems. For instance, most theoretical work on charge migration [32, 93, 31, 94, 99, 96] relies on the validity of the FNA to propagate electronic wave packets. Of course, its applicability depends on the characteristics of each particular problem and, in general, the nuclear motion is expected to

play a role in the femtosecond time domain.

## 2.2 Evaluation of electronic states

As we discussed, the electronic eigenvalue problem given in eq. 2.3 does not have an exact analytical solution in most cases. A widely used approach is given by the Hartree–Fock (HF) method, that can provide a first approximation to the “exact” ground state solution in terms of a Slater determinant constructed from HF molecular orbitals, which are obtained within the mean field approximation through a self consistent field procedure. However, it is well known that HF solutions are usually rather poor since the mean field approximation cannot describe electron correlation properly [126]. Post-HF methods manage this problem by expanding the total wave function as a linear combination of Slater determinants (electronic configurations), being able to yield accurate solutions for the ground and for excited states of few-electron systems. Yet, the number of configurations one might need to include in the expansion to reach the desired accuracy can make these methods extremely costly. In this sense, DFT constitutes a useful alternative to *ab initio* methods, providing an excellent compromise between accuracy and computational effort for medium and large size systems [134].

### 2.2.1 Density functional theory

Density functional theory (DFT) is widely used in physics, chemistry and materials science to investigate the ground state electronic structure of atoms, molecules and condensed phases. According to DFT, the energy (or any other observable) of a many-electron system in the ground state can be determined by using functionals which solely depend on the electron density. The most essential concepts of the method are given here; for a deeper insight, see, for instance [134], [135] or [136].

DFT is supported on the theorems proposed by Pierre Hohenberg and Walter Kohn in 1964 [137], namely:

1. “Any observable of a stationary non-degenerate ground state can be calculated, exactly in theory, from the electron density of the ground state”.

2. “The electron density of a non-degenerate ground state can be calculated, exactly in theory, determining the density that minimizes the energy of the ground state”.

The use of the electron density  $\rho(\mathbf{r})$  instead of the wave function  $\Psi(\mathbf{x}_1, \dots, \mathbf{x}_N)$  is the foundation of DFT. Both entities are related through the equation:

$$\rho(\mathbf{r}) = N \int \dots \int |\Psi(\mathbf{x}, \mathbf{x}_2 \dots d\mathbf{x}_N)|^2 ds d\mathbf{x}_2 \dots d\mathbf{x}_N \quad (2.10)$$

where  $\mathbf{x}_i = \mathbf{r}_i s_i$  gathers the spatial  $\mathbf{r}_i$  and spin  $s_i$  coordinates of the  $i$ -th electron <sup>1</sup>. In 1965, Walter Kohn and Lu Jeu Sham provided a systematical approach to evaluate the ground state electron density of a many-body system by introducing the so-called Kohn-Sham equation [138].

### The Kohn-Sham equation

The Kohn-Sham equation is the time-independent Schrödinger equation of a fictitious system of non-interacting particles that generates the same density as a given system of interacting particles. It can be written as

$$\left[ -\frac{\hbar^2}{2m_e} \nabla^2 + V_{\text{eff}}(\mathbf{r}) \right] \phi_i(\mathbf{x}) = \epsilon_i \phi_i(\mathbf{x}) \quad (2.11)$$

where  $\phi_i$  are the so called Kohn-Sham orbitals,  $\epsilon_i$  are the corresponding energies and  $V_{\text{eff}}$  the fictitious effective potential in which the non-interacting particles move:

$$V_{\text{eff}}(\mathbf{r}) = -\sum_{\alpha=1}^M \frac{e^2 Z_{\alpha}}{|\mathbf{r} - \mathbf{R}_{\alpha}|} + V_H[\rho(\mathbf{r})] + V_{XC}[\rho(\mathbf{r})] \quad (2.12)$$

where  $V_H$  is the Hartree (Coulomb) potential:

$$V_H[\rho(\mathbf{r}_i)] = e^2 \int \frac{\rho(\mathbf{r}')}{|\mathbf{r} - \mathbf{r}'|} d\mathbf{r}' \quad (2.13)$$

---

<sup>1</sup>For the sake of simplicity, the parametric dependence on the nuclear coordinates has been dropped.

and  $V_{XC}$  is the exchange-correlation potential:

$$V_{XC}[\rho(\mathbf{r})] = \frac{\delta E_{XC}}{\delta \rho} \quad (2.14)$$

$E_{XC}$  is the exchange-correlation energy. If the exact forms of  $E_{XC}$  and  $V_{XC}$  were known, the Kohn-Sham strategy would provide the exact ground state energy. Unfortunately, this is not the case and the exchange-correlation energy (potential) needs to be approximated through empirical formulations. The central goal of modern DFT is finding better approximations to these two quantities. As the particles of the Kohn-Sham system are non-interacting fermions, the ground state wave function can be written as a Slater determinant of the lowest energy solutions of eq. 2.11:

$$\Psi(\mathbf{x}_1, \mathbf{x}_2, \dots, \mathbf{x}_N) = \frac{1}{\sqrt{N!}} \begin{vmatrix} \phi_1(\mathbf{x}_1) & \phi_2(\mathbf{x}_1) & \cdots & \phi_N(\mathbf{x}_1) \\ \phi_1(\mathbf{x}_2) & \phi_2(\mathbf{x}_2) & \cdots & \phi_N(\mathbf{x}_2) \\ \vdots & \vdots & \ddots & \vdots \\ \phi_1(\mathbf{x}_N) & \phi_2(\mathbf{x}_N) & \cdots & \phi_N(\mathbf{x}_N) \end{vmatrix} \quad (2.15)$$

By using eq. 2.10, we can evaluate the ground state electron density:

$$\rho_0(\mathbf{r}) = \sum_{i=1}^N |\psi_i(\mathbf{r})|^2 \quad (2.16)$$

where  $\psi_i(\mathbf{r})$  is the spatial part of the spin orbital  $\phi_i(\mathbf{x})$ , that is,  $\phi_i(\mathbf{x}) = \psi_i(\mathbf{r})\alpha(s)$  or  $\phi_i(\mathbf{x}) = \psi_i(\mathbf{r})\beta(s)$ . In practice, since the Kohn-Sham Hamiltonian depends on the Kohn-Sham orbitals (solutions of the eigenvalue problem) through the electron density, they are numerically found by performing a self-consistent field procedure.

### 2.2.2 Static-exchange DFT

Standard DFT methods can accurately represent the electronic ground state of many-electron systems. In order to describe photoionization processes one also needs to describe the electronic continuum. In this work we have employed the static-exchange DFT method [139, 140, 141, 142, 143], developed by Mauro Stener,

Piero Decleva and collaborators, to evaluate transitions to continuum states. The method makes use of the Kohn-Sham formalism to describe bound states and of the Galerkin approach to evaluate photoelectron wave functions in the field of the corresponding Kohn-Sham density. Over the last decades, this methodology has provided accurate values of photoionization cross sections of small molecules as well as of medium and large size systems within the fixed-nuclei approximation [140, 144, 145, 146, 147, 148], from small diatomic molecules such as  $N_2$  to fullerenes. More recently, the method was extended in collaboration with the group of Fernando Martín to include the nuclear degrees of freedom, successfully evaluating vibrationally resolved cross sections of diatomic [81, 114, 115, 116, 121] and small polyatomic [117, 82, 118, 119, 120, 122] molecules, providing results which are in good agreement with experimental data. In this section we explain the most relevant characteristics of the method.

### Electronic states within the static-exchange approximation

The static-exchange DFT method makes use of single Slater determinants to define bound and excited (continuum) electronic states, ensuring that the Pauli exclusion principle is fulfilled. The ground state wave function may be written as

$$\Psi_0(\mathbf{x}_1, \mathbf{x}_2, \dots, \mathbf{x}_n) = \left| \phi_1 \phi_2 \dots \phi_N \right| \quad (2.17)$$

where  $N$  is the number of electrons,  $\phi_i(\mathbf{x}) = \psi_i(\mathbf{r})\alpha(s)$  if  $i$  is odd and  $\phi_i(\mathbf{x}) = \psi_i(\mathbf{r})\beta(s)$  if  $i$  is even. For a closed-shell system,  $\psi_1(\mathbf{r}) = \psi_2(\mathbf{r}), \dots, \psi_{N-1}(\mathbf{r}) = \psi_N(\mathbf{r})$ . Continuum states are defined by promoting one electron from a bound spin orbital  $\phi_\alpha$  to a continuum orbital  $\phi_{\varepsilon lh}$  with kinetic energy  $\varepsilon$  and angular quantum numbers  $l$  and  $h$ , and can be written as

$$\Psi_{\alpha\varepsilon lh}(\mathbf{x}_1, \mathbf{x}_2, \dots, \mathbf{x}_n) = \left| \phi_1 \phi_2 \dots \phi_{\alpha-1} \phi_{\varepsilon lh} \phi_{\alpha+1} \dots \phi_N \right| \quad (2.18)$$

Bound and continuum orbitals are expanded in a multicentric basis set of B-splines, as we explain as follows.

### Multicentric B-spline basis set

Traditional basis sets make use of Gaussian or Slater type orbital functions, which provide fast convergence for the lowest bound states with a reduced number of basis functions [126]. However, these expansions are not adequate for the description of the rapidly oscillating continuum states, since numerical linear dependences rapidly come up as the basis set is increased due to the large overlap between functions with different centers. In this context, basis sets of B-spline functions, which are piecewise polynomials, constitute a very powerful tool [142]. B-spline functions are very flexible and due to its local nature they can describe accurately both bound and continuum orbitals without running into numerical dependencies [142]. The present method evaluates bound and continuum orbitals in a multicentric basis set of B-splines, using symmetry-adapted [149] linear combinations of real spherical harmonics with origin over different positions in the molecule:

- A large one-center expansion (OCE) over the center of mass provides an accurate description of the long-range behavior of the continuum states.
- Small expansions, called off-centers (OC), located over the non-equivalent nuclei, complement the OCE. They improve dramatically the convergence of the calculation, allowing to reduce the angular expansion in the OCE, since they can effectively describe the Kato cusps [150] at the nuclear positions.

In the case of symmetric molecules, a large amount of computational effort can be saved by making use of point group symmetry and dividing the three-dimensional space into equivalent regions. The basis set elements may be written as

$$\xi_{nlh\lambda\mu}^p = \sum_{q \in \Lambda_p} \frac{1}{r_q} B_n^\kappa(r_q) \underbrace{\sum_m b_{mlh\lambda\mu}^q Y_{lm}(\theta_q, \varphi_q)}_{X_{lh\lambda\mu}^p(\theta_q, \varphi_q)} \quad (2.19)$$

where  $\Lambda_p$  represents a shell of equivalent centers ( $p = 0$  refers to the OCE),  $q$  runs over the centers in the shell,  $n$  is an index over the B-spline functions  $B_n^\kappa$ , whose order is  $\kappa = 10$ ,  $\lambda\mu$  are the indexes of the irreducible representation (see [143]),  $h$  runs over the linearly independent angular functions, which are constructed as linear combinations of real spherical harmonics associated to a fixed angular quantum number  $l$ , and the coefficients  $b_{mlh\lambda\mu}^q$  are determined by symmetry [149],



defining the so called symmetry-adapted spherical harmonics  $X_{lh\lambda\mu}^p$ , which are invariant under the symmetry operations of a given point group. For instance, in the case of  $\text{BF}_3$  (in the ground state equilibrium geometry),  $p = 1$  would represent the shell of equivalent F atoms ( $q = 1, 2, 3$  since there are 3 equivalent F atoms) and no more OC expansions would be required since the OCE would be located at the B atom (center of mass).

In each center  $q$ , the B-spline expansion reaches a maximum value  $R_{\text{max}}^p$ , which can be different for non-equivalent centers (different value of  $p$ , see eq. 2.19). A large value of  $R_{\text{max}}^0$  is required in the OCE in order to provide a good description of the oscillatory behavior of the continuum states. One can control the overlap between the basis elements, avoiding running into linear dependences, by keeping small OC expansions ( $R_{\text{max}}^{p>0} \simeq 1$  a.u.) since the Kato cusps are usually well localized at the atomic positions. Angular expansions are truncated so  $l$  takes values up to a maximum  $l_{\text{max}}^p$ , which can also be different for the non-equivalent centers. In general, one can keep small values of  $l_{\text{max}}$  in the OCs to complement the OCE in the description of the bound states, but a large angular expansion is usually required in the OCE, especially in the case of complex molecules and for the evaluation of continuum states with high kinetic energy.

### Evaluation of bound orbitals

There are several quantum chemistry packages available which can efficiently perform DFT calculations. In this work, we have employed the Amsterdam Density Functional (ADF) program [151, 152, 153] to evaluate the ground state electron density of the molecules we have investigated using a double or a triple  $\zeta$ -polarization plus basis set (taken from the ADF library). Electronic exchange and correlation effects have been accounted for with the VWN [154] local density approximation functional in some cases, or with the LB94 [155], depending on the characteristics of particular problem. Besides providing a reliable description of bound states, these two functionals have been found to be suitable for the description of the long range behavior of the continuum states. The electron density provided by the ADF calculation is projected into a multicentric B-spline basis set like the one described in the previous section. Then, the correspon-

ding Hamiltonian  $\mathbf{H}$  and overlap  $\mathbf{S}$  matrices are constructed:

$$H_{nn'lw'hh'\lambda\mu}^{pp'} = \langle \xi_{nlh\lambda\mu}^p | H | \xi_{n'l'h'\lambda\mu}^{p'} \rangle \quad (2.20)$$

$$S_{nn'lw'hh'\lambda\mu}^{pp'} = \langle \xi_{nlh\lambda\mu}^p | \xi_{n'l'h'\lambda\mu}^{p'} \rangle \quad (2.21)$$

By definition, both  $\mathbf{H}$  and  $\mathbf{S}$  are symmetric matrices. Since the OC expansions cannot overlap,  $H_{nn'lw'hh'\lambda\mu}^{pp'}$  and  $S_{nn'lw'hh'\lambda\mu}^{pp'}$  are zero if  $p \neq p'$ , unless  $p = 0$  or  $p' = 0$  (elements of the OCE). By solving the eigenvalue problem given by the secular equation

$$\mathbf{H}\mathbf{c} = \varepsilon\mathbf{S}\mathbf{c} \quad (2.22)$$

we obtain the set coefficients  $\mathbf{c}$  that define the bound orbitals in the B-spline basis. Of course, both the basis set employed in the ADF calculation and the B-spline basis set need to be dense enough so the two calculations provide the same sets of orbitals.

### Evaluation of continuum orbitals

The continuum spectrum of an operator constitutes a family of eigenfunctions whose eigenvalues are a continuum variable. The set of discrete solutions of eq. 2.22 whose energy is higher than the ionization threshold can be interpreted as a representation of the continuum, but with a different (arbitrary) normalization condition:  $\varphi(R_{\max}^0) = 0$ , and normalized at the same level as the bound states: to a Kronecker delta. Of course, the characteristics of these solutions depend on the numerical expansion and one needs to use a dense basis set and a large value of  $R_{\max}^0$  so their asymptotic behavior is properly represented. In order to compute measurable quantities such as photoionization cross sections, one has to set the proper normalization of the continuum states: to a Dirac delta, and impose the adequate scattering boundary conditions, in the case of a molecule, of a multichannel problem. Here we have employed the Galerkin [142] approach to evaluate photoelectron states at different energies and the correct boundary conditions have been imposed to the solutions, as we explain in this section.

**The Galerkin approach.** The present method can yield the continuum wave function at any photoelectron energy using a fixed basis set. The traditional

eigenvalue problem given by eq. 2.22 does not admit non-trivial solutions ( $\mathbf{c} \neq \mathbf{0}$ ) for an arbitrary value of energy  $\varepsilon$ . However, one can obtain approximate solutions by finding the coefficients that minimize the residual vector ( $\mathbf{H}\mathbf{c} - \varepsilon\mathbf{S}\mathbf{c}$ ), with  $\mathbf{c} \neq \mathbf{0}$  by solving the eigenvalue problem

$$\mathbf{A}(\varepsilon)\mathbf{c} = a\mathbf{c} \quad (2.23)$$

where  $\mathbf{A}(\varepsilon) = \mathbf{H} - \varepsilon\mathbf{S}$ . The eigenfunctions corresponding to the lowest eigenvalues  $a_0, a_1, \dots$  can be taken as approximate solutions with energy  $\varepsilon$  if their eigenvalues are close to zero. It has been observed that, for  $n$  partial waves, one can always find a set of  $n$  eigenvalues  $\{a_i\}_{i=1}^n$  whose moduli are sufficiently small and well separated from the others, provided that the basis set is dense and flexible enough. Due to the lack of boundary conditions,  $\mathbf{A}(\varepsilon)$  is not a Hermitian matrix and therefore its eigenvalues  $a_i$  and eigenvectors  $\mathbf{c}_i$  are, in general, complex. Nonetheless since  $\mathbf{A}(\varepsilon)$  is real they appear in conjugate pairs, i.e., for each pair  $(a, \mathbf{c})$  that satisfies 2.23, so does  $(a^*, \mathbf{c}^*)$ . This later property makes possible to avoid complex representations just by taking  $\Re(\mathbf{c})$  and  $\Im(\mathbf{c})$  as independent solutions. Although these solutions do not satisfy the adequate boundary conditions of a multichannel scattering problem, they constitute a complete set and therefore can be combined to provide linear combinations that do. In the next lines we explain how the Galerkin solutions can be renormalized so they accurately describe an electron being scattered from the molecular potential.

**Renormalization of continuum sates.** Photoelectron wave functions describe a particle being ejected from an atom or a molecule. Therefore, they must be solutions of the scattering Schrödinger equation

$$\hat{H}_{sc}\varphi^-(\mathbf{r}) = \varepsilon\varphi^-(\mathbf{r}) \quad (2.24)$$

where  $\hat{H}_{sc}$  is the scattering Hamiltonian:

$$\hat{H}_{sc} = -\frac{1}{2}\nabla^2 - U_\alpha(\mathbf{r}) \quad (2.25)$$

and  $U_\alpha(\mathbf{r})$  is the potential generated by the residual ion. In our case, electronic exchange and correlation effects are included in the potential through the use of

a functional. At long distances, the ionic potential can be approximated by that of a positive charge, i.e.:

$$\lim_{r \rightarrow \infty} U_{\alpha}(\mathbf{r}) = \frac{1}{r} \quad (2.26)$$

where  $r = |\mathbf{r}|$ . The scattering Hamiltonian (eq. 2.24) does not admit analytical eigenfunctions in the case of complex potentials. However, as  $r$  increases, it tends to the Coulomb Hamiltonian,  $\hat{H}_c$ :

$$\lim_{r \rightarrow \infty} H_{sc} = H_c = -\frac{1}{2}\nabla^2 - \frac{1}{r} \quad (2.27)$$

which does have analytical solutions: the regular  $F_{\varepsilon l}(r)$  and the irregular  $G_{\varepsilon l}(r)$  Coulomb functions. At long distances, they can be written as

$$F_{\varepsilon l}(r) = \sqrt{\frac{2}{\pi k}} \frac{1}{r} \sin(kr - l\frac{\pi}{2} - \eta \log 2kr + \sigma_l) \quad (2.28)$$

$$G_{\varepsilon l}(r) = \sqrt{\frac{2}{\pi k}} \frac{1}{r} \cos(kr - l\frac{\pi}{2} - \eta \log 2kr + \sigma_l) \quad (2.29)$$

where  $k$  is the momentum and  $\sigma_l$  is the Coulomb phase shift:

$$\sigma_l = \arg \Gamma(l + 1 + i\eta) \quad (2.30)$$

and  $\Gamma$  is the Euler's Gamma function. The asymptotic boundary conditions of the photoelectron scattering wave functions can be written in terms of the Coulomb functions:

$$\varphi_{\varepsilon lh}^- = F_{\varepsilon l}(r)X_{lh} + \sum_{l'} \pi K_{ll'} G_{\varepsilon l}(r)X_{l'h} \quad (2.31)$$

where the  $\mathbf{K}$  matrix is related to the usual scattering matrix  $\mathbf{S}$  [156] by

$$I - i\pi\mathbf{K} = (I + i\pi\mathbf{K})\mathbf{S} \quad (2.32)$$

The set of continuum states provided by the Galerkin approach in the basis set of B-splines, however, satisfy arbitrary boundary conditions of the form:

$$\varphi_{\varepsilon lh} = \sum_{l'} a_{ll'} F_{\varepsilon l'}(r)X_{l'h} + \sum_{l'} \pi K_{ll'} G_{\varepsilon l}(r)X_{l'h} \quad (2.33)$$

where the sets of coefficients  $\{a_{ll'}\}$  and  $\{b_{ll'}\}$  can be obtained by comparing the radial part of the wave functions  $\varphi_{\epsilon lh}$  and its first derivatives at  $r = R_{\max}$  with those of the Coulomb functions. They define two matrices  $\mathbf{A}$  and  $\mathbf{B}$  that can be used to obtain the correct wave functions:

$$\varphi_{\epsilon lh}^- = \mathbf{A}^{-1} \varphi_{\epsilon lh} \quad (2.34)$$

The resulting wave functions  $\varphi_{\epsilon lh}^-$  have the proper  $K$ -matrix normalization, with  $\pi \mathbf{K} = -\mathbf{A}^{-1} \mathbf{B}$ .

### Dipole-transition matrix elements

As explained in the previous chapter, in order to evaluate the electronic wave packet generated in a molecule upon ionization by ultrashort laser pulses (eq. 1.15) or to compute photoionization cross sections (eq. 1.24), the dipole-transition matrix elements are required. Here we indicate how to evaluate the element corresponding to a transition from the electronic ground state  $\Psi_0$  (eq. 2.17) to a continuum state  $\Psi_{\alpha \epsilon lh}$  (eq. 2.18) upon interaction with linearly polarized light. In our description of the wave function, the residual ion remains frozen (static-exchange approximation), which reduces the problem to the calculation of the coupling between the bound orbital where the electron is taken from  $\phi_\alpha$  and the continuum orbital where is promoted to  $\phi_{\epsilon lh}$ , that is,

$$\mu_\epsilon^{\alpha \epsilon lh} = \langle \Psi_{\alpha \epsilon lh}(\bar{\mathbf{x}}) | \boldsymbol{\mu}_\epsilon^e(\bar{\mathbf{r}}) | \Psi_0(\bar{\mathbf{x}}) \rangle = \langle \phi_{\epsilon lh}(\mathbf{r}) | \boldsymbol{\epsilon} \mathbf{r} | \phi_\alpha(\mathbf{r}) \rangle \quad (2.35)$$

where  $\boldsymbol{\epsilon}$  is the polarization vector of the electric field. Dipole transition elements can be used to evaluate cross sections.

### Photoionization cross section within the fixed-nuclei approximation

Making use of eqs. 1.26 and 2.35 and summing incoherently over all photoelectron symmetries (all possible values of  $l$  and  $h$ ), we can evaluate total photoionization cross sections in the framework first-order perturbation theory within the

fixed-nuclei approximation:

$$\sigma_{\epsilon\alpha}(\varepsilon) = \frac{4\pi^2\omega}{\hbar c} \sum_{lh} |\mu_{\epsilon}^{\alpha\epsilon lh}|^2 \quad (2.36)$$

As indicated in section 1.3, for the case of randomly oriented molecules, one needs to compute  $\sigma_{\epsilon\alpha}$  for three orthogonal directions of the polarization vector of the field  $\epsilon$  and then average the results incoherently.

### 2.2.3 Time-dependent DFT

An improvement of the static-exchange DFT method described in the previous section in order to describe the coupling between different photoionization channels is the time-dependent DFT approach. The method uses many concepts from the static-exchange version. Here we present the most relevant concepts, for a more complete description, see [157].

The linear response of the electron density to an external field can be evaluated using the scheme proposed by Zangwill and Soven by defining an effective self-consistent field potential:

$$V_{\text{SCF}}(\mathbf{r}, \omega) = V_{\text{EXT}}(\mathbf{r}, \omega) + \delta V(\mathbf{r}, \omega) \quad (2.37)$$

where  $\omega$  is the frequency of the radiation,  $V_{\text{EXT}}(\mathbf{r}, \omega)$  is the external dipole potential and  $\delta V(\mathbf{r}, \omega)$  is the induced potential, which is given by the sum of the Hartree and exchange-correlation screening due to the redistribution of the electrons:

$$\delta V_{\text{SCF}}(\mathbf{r}, \omega) = \int \frac{\delta(\mathbf{r}, \omega)}{|\mathbf{r} - \mathbf{r}'|} d\mathbf{r}' + \left. \frac{\partial V_{XC}}{\partial \rho} \right|_{\rho=\rho(\mathbf{r})} \delta\rho(\mathbf{r}, \omega) \quad (2.38)$$

$\rho(\mathbf{r})$  is the unperturbed electron density and  $\delta(\mathbf{r}, \omega)$  denotes the induced density in the adiabatic local density approximation [158], which can be expressed in terms of the dielectric susceptibility  $\chi$  and the self-consistent field potential:

$$\delta\rho(\mathbf{r}, \omega) = \int \chi(\mathbf{r}, \mathbf{r}', \omega) V_{\text{SCF}}(\mathbf{r}', \omega) d\mathbf{r}' \quad (2.39)$$

By inserting eq. 2.39 into eq. 2.38, we obtain:

$$\delta V(\mathbf{r}, \omega) = \iint K(\mathbf{r}, \mathbf{r}') \chi(\mathbf{r}, \mathbf{r}', \omega) V_{\text{SCF}}(\mathbf{r}, \omega) d\mathbf{r} d\mathbf{r}' \quad (2.40)$$

where  $K(\mathbf{r}, \mathbf{r}')$  represents the Hartree and exchange-correlation kernel:

$$K(\mathbf{r}, \mathbf{r}') = \frac{1}{|\mathbf{r} - \mathbf{r}'|} + \delta(\mathbf{r} - \mathbf{r}') \left. \frac{V_{\text{XC}}}{d\rho'} \right|_{\rho'=\rho(\mathbf{r})} \quad (2.41)$$

Eq. 2.40 is solved with respect to  $\delta V(\mathbf{r}, \omega)$  in a basis set of B-splines basis as the one employed in the static-exchange DFT approach and the adequate boundary conditions for the photoelectron wave functions are imposed. Then, the electronic dipole-transition matrix elements are evaluated using  $V_{\text{SCF}}$  instead of the dipole operator. The time-dependent DFT method can accurately describe interchannel coupling effects and autoionization resonances at the linear-response level. For this reason, it is more suitable than the static-exchange version for the description of correlation effects due to the coupling between different ionization channels.

## 2.3 Inclusion of the nuclear motion

The nuclear motion may play an important role in molecular photoionization since the energy of the incident photon is usually distributed between electrons and nuclei. In general, molecules undergo vertical transitions upon photoionization because the electronic emission occurs suddenly and the nuclei have no time to rearrange. This can lead to (several) vibrational excitations in the parent ion, thus generating superpositions of vibronic states  $\sum_{\nu} c_{n\nu} \chi_{n\nu}(\bar{\mathbf{R}})$ , where  $\chi_{n\nu}(\bar{\mathbf{R}})$  are the (final) vibrational wave functions,  $\nu$  and  $n$  being the vibrational and electronic quantum numbers, respectively, and the expansion coefficients  $c_{n\nu}$  are approximately given the overlaps with the initial wave function  $\chi_0(\bar{\mathbf{R}})$ , i.e., the Franck-Condon factors  $\langle \chi_{n\nu}(\bar{\mathbf{R}}) | \chi_0(\bar{\mathbf{R}}) \rangle$ . Vibrational excitations in the parent ion are experimentally observable even in the case of inner-shell photoionization, thanks to the advent of the third generation of synchrotron radiation sources and high-energy-resolution detection techniques [43]. Of course, in order to describe these situations, the nuclear degrees of freedom must be taken into account. Here we present a method for including the nuclear motion at the Born-Oppenheimer

level applicable to diatomic molecules and to small polyatomics in situations in which only one vibrational mode is active.

### 2.3.1 The nuclear Hamiltonian

Within the Born-Oppenheimer approximation, the nuclear Hamiltonian (see eq. 2.4) of a **diatomic AB molecule** in a given electronic state  $n$  can be written as

$$\hat{H}_N = -\frac{1}{2M}\nabla_{\mathbf{R}_{\text{CM}}}^2 - \underbrace{\frac{1}{2\mu}\nabla_R^2 + E_n(R)}_{\hat{H}_{\text{int}}} \quad (2.42)$$

where  $M$  and  $\mu$  are the total and the reduced mass of the system, respectively,  $R$  is the relative distance between the two nuclei,  $\mathbf{R}_{\text{CM}}$  is the position of the center of mass and  $E_n$  is the potential energy curve associated to the electronic state  $n$  in the Born-Oppenheimer approximation. In this formulation, it is clear that the total kinetic energy is composed by a translational motion of the center of mass (first term in the left side of eq. 2.42) and an internal motion (second term). The translational motion is not quantized and just contributes to the total energy by adding a constant energy to the eigenvalues. For this reason, here we will focus on finding the eigenstates of the internal Hamiltonian  $\hat{H}_{\text{int}}$ , which in polar coordinates is given by

$$\hat{H}_{\text{int}} = -\frac{\hbar}{2\mu}\left(\frac{\partial^2}{\partial R^2} + \frac{2}{R}\frac{\partial}{\partial R}\right) + \frac{\hat{L}^2}{2\mu R^2} + E_n(R) \quad (2.43)$$

where  $\hat{L}^2$  is the square of the total angular momentum operator. The eigenfunctions of  $\hat{H}_{\text{int}}$  can be written as a product of a radial part  $\chi_{n\nu}(R)$ , describing the vibrational motion, and a spherical harmonic  $Y_l^m(\theta, \phi)$  that accounts for the molecular rotation. Since the rotational energy is significantly smaller than the vibrational quantum, we can neglect this term and describe the nuclear motion in terms of vibrational states  $\chi_\nu(R)$ , which are the eigenfunctions of the vibrational Hamiltonian:

$$\hat{H}_{\text{vib}}(R) = -\frac{\hbar}{2\mu}\left(\frac{\partial^2}{\partial R^2} + \frac{2}{R}\frac{\partial}{\partial R}\right) + E_n(R) \quad (2.44)$$



Vibrational eigenfunctions can be written as

$$\chi_{n\nu}(R) = \frac{\zeta_{n\nu}(R)}{R} \quad (2.45)$$

which simplifies the eigenvalue problem to

$$\left[ -\frac{\hbar}{2\mu} \frac{\partial^2}{\partial R^2} + E_n(R) \right] \zeta_{n\nu}(R) = E_{n\nu} \zeta_{n\nu}(R) \quad (2.46)$$

Vibrational eigenstates are evaluated in a basis set of B-spline functions, as we explain in section 2.3.2.

**Polytomic molecules.** The motion of a set of particles can be decomposed into translation and rotation of the center of mass and vibration of its particles. A  $n$ -particle system has  $3n - 5$  vibrational degrees of freedom (vibrational modes) if it is linear and  $3n - 6$  otherwise [134]. A complete description of molecular vibration within the Born-Oppenheimer approximation would require including in the total wave function the corresponding vibrational eigenfunctions depending on all vibrational degrees of freedom. In this work we have investigated inner shell photoionization of polyatomic  $AB_n$  molecules, A being the central atom and B the surrounding atomic centers, symmetrically displaced around A. Recent experimental data [159, 160] has shown that, in this scenario, the totally symmetric stretching mode (TSSM), that in which the B atoms move symmetrically towards A, is the most affected by the structural rearrangement that accompanies core ionization. For this reason, in this work we have restricted nuclear motion to the TSSM coordinate. The dynamics of the B atoms along the TSSM can be understood in terms of a virtual particle moving in a monodimensional well  $V(R)$ , defined by the  $n$  chemical bonds, with a reduced mass<sup>2</sup>  $\mu = 3M_B$ . Then, eq. 2.43 remains valid with  $R = |\mathbf{R}_B - \mathbf{R}_A|$ , the TSSM coordinate.

---

<sup>2</sup>The mass of the central atom ( $m_A$ ) does not contribute to  $\mu$  since it remains frozen along the TSSM coordinate.

### 2.3.2 Evaluation of vibrational eigenstates

Vibrational eigenstates are evaluated by solving the eigenvalue problem given by eq. 2.46 in a basis set of B-splines

$$\zeta(R)_{n\nu} = \sum_{i=1}^{N_{\max}} c_{n\nu i} B_i(R) \quad (2.47)$$

where  $n$  and  $\nu$  are the electronic and vibrational quantum numbers, respectively, and  $i$  is an index going over the  $N_{\max}$  B-spline functions  $B_i$ , which are defined up to a value of  $R_{\max}$ . The corresponding secular equation in its matrix form,  $\mathbf{H}\mathbf{c} = E\mathbf{S}\mathbf{c}$ , where  $\mathbf{H}$  and  $\mathbf{S}$  are the Hamiltonian and the overlap matrices in the B-spline basis set, is solved using a standard diagonalization procedure. Since B-spline functions are piecewise polynomials, the elements of  $\mathbf{H}$  and  $\mathbf{S}$  are computed exactly using a Gauss-Legendre integration method.

#### Bound states

The resolution of the secular equation provides an orthonormal set of stationary states. Those whose energy is lower than the molecular dissociation limit constitute the bound part of the spectrum. Of course, the number of bound states and the energy spacing depends on the shape of the potential well (depth and width) and on the reduced mass of the system, but not on the parameters of the B-spline expansion, provided the basis set has been wisely chosen.

#### Continuum states

The stationary solutions of the secular equation with energy higher than the dissociation limit constitute a discretized representation of the vibrational continuum with the arbitrary boundary condition  $\chi(R_{\max}) = 0$ . As in the case of the electronic states (section 2.2.2), the number of continuum states and their energy spacing depend on the parameters of the numerical expansion and one needs to employ a large value of  $R_{\max}$  and a dense grid of B-splines so the asymptotic behavior of the continuum wave functions can be properly described. However, the situation here is more simple since this is a mono-channel scattering problem and the adequate normalization of the true continuum states  $\chi_{E\nu}$  can be set

by multiplying the solutions coming from the diagonalization procedure by a factor:

$$\chi_{E_\nu} = \sqrt{\rho(E_\nu)}\chi_\nu \quad (2.48)$$

where  $\rho_{E_\nu}$  is the density of states [142]. Working with discretized states in a box,  $\rho(E_\nu)$  can be approximated by

$$\rho(E_\nu) = \left| \frac{\partial E(\nu')}{\partial \nu'} \right|_{\nu'=\nu} \simeq \frac{2}{E_{\nu+1} - E_{\nu-1}} \quad (2.49)$$

which has been proved to be a good approximation [142].

### 2.3.3 Vibrationally resolved cross sections

Let us consider a transition from the ground state  $\Phi_{0\nu}(\mathbf{x}, R)$ , with  $\nu = 0$ , to a state  $\Phi_{\alpha\varepsilon lh\nu'}(\mathbf{x}, R)$  in which an electron has been emitted from the  $\alpha$  molecular orbital with  $\varepsilon$  kinetic energy and  $lh$  symmetry, leaving the residual ion in the  $\alpha\nu$  vibronic state. These are Born-Oppenheimer states and can be written as

$$\Phi_{0\nu}(\mathbf{x}, R) = \Psi_0(\mathbf{x}, R)\chi_{0\nu}(R) \quad (2.50)$$

$$\Phi_{\alpha\varepsilon lh\nu'}(\mathbf{x}, R) = \Psi_{\alpha\varepsilon lh}(\mathbf{x}, R)\chi_{\alpha\nu'}(R) \quad (2.51)$$

The corresponding dipole transition matrix element upon interaction with linearly polarized light is given by:

$$\mu_\epsilon^{\alpha\varepsilon lh\nu' \leftarrow 0\nu} = \int \langle \Phi_f(\mathbf{x}, R) | \mu_\epsilon | \Phi_i(\mathbf{x}, R) \rangle dR \quad (2.52)$$

where  $\mu_\epsilon$  is the total dipole operator ( $\hat{\epsilon}$  is the polarization vector of the field), which is the sum of two contributions:

$$\mu_\epsilon = \underbrace{\hat{\epsilon} \sum_n \mathbf{r}_n}_{\mu_\epsilon^{\text{elec}}} + \underbrace{\hat{\epsilon} \sum_\alpha Z_\alpha \mathbf{R}_n}_{\mu_\epsilon^{\text{nuc}}} \quad (2.53)$$

Inserting eqs. 2.50, 2.51 and 2.53 into eq. 2.52, we have

$$\begin{aligned} \mu_{\epsilon}^{\alpha\epsilon lh\nu'\leftarrow 0\nu} &= \int \underbrace{\langle \Psi_{\alpha\epsilon lh}(\mathbf{x}, R) | \mu_{\epsilon}^{\text{elec}} | \Psi_0(\mathbf{x}, R) \rangle}_{\mu_{\epsilon}^{\alpha\epsilon lh\leftarrow 0}} \chi_{\alpha\nu'}(R) \chi_{0\nu}(R) dR \\ &+ \int \langle \Psi_{\alpha\epsilon lh}(\mathbf{x}, R) | \Psi_0(\mathbf{x}, R) \rangle \chi_{\alpha\nu'}(R) \mu_{\epsilon}^{\text{nuc}} \chi_{0\nu}(R) dR \end{aligned}$$

where the second term is zero due to the orthogonality of electronic states. Then, the vibronic dipole-transition matrix element can be written as

$$\mu_{\epsilon}^{\alpha\epsilon\nu'lh\leftarrow 0\nu} = \int \mu_{\epsilon}^{\alpha\epsilon lh\leftarrow 0} \chi_{\alpha\nu'}(R) \chi_{0\nu}(R) dR \quad (2.54)$$

An expression for the photoionization cross section upon interaction with monochromatic light is obtained inserting eq. 2.54 into eq. 1.26 and summing incoherently over all photoelectron symmetries (all values of  $l$  and  $h$ ):

$$\sigma_{\epsilon}^{\alpha\nu'}(\epsilon) = \frac{4\pi^2\omega}{\hbar c} \sum_{lh} \left| \int \mu_{\epsilon}^{\alpha\epsilon lh\leftarrow 0} \chi_{\alpha\nu'}(R) \chi_{0\nu}(R) dR \right|^2 \quad (2.55)$$

where  $\omega$  is the photon energy, which is related to the photoelectron energy  $\epsilon$  through the equation  $\epsilon = \hbar\omega - E_{\alpha}^{\nu\nu'}$ , where  $E_{\alpha}^{\nu\nu'} = E_{\alpha\nu'} - E_{0\nu}$  is the energy required to produce the ion in the  $\alpha\nu'$  vibronic state. For the case of randomly oriented molecules, one can compute  $\sigma_{\epsilon}^{\alpha\nu'}$  for three orthogonal directions of  $\hat{\epsilon}$  and then the results incoherently (eq. 1.27).

## Chapter 3

# Electron dynamics initiated by attosecond pulses

The development of attosecond technology has enabled the real-time observation of electron motion in atoms, molecules and solids [11]. Experimentally, it is now possible to generate laser pulses of durations of a few tens of attoseconds. These durations are of the order of the period of revolution of the first Bohr orbit, which is 150 attoseconds, thus opening the way to track and to manipulate electron dynamics at its natural time scale. Due to their wide spectral bandwidth, attosecond pulses create coherent superpositions of electronic states, inducing an ultrafast response in the target. In this chapter we present a method to evaluate the electronic wave packet generated in a molecule upon attosecond ionization and the subsequent charge redistribution, applying the concepts that have been previously introduced in chapters 1 and 2.

### 3.1 Wave packet dynamics

Attosecond XUV pulses can efficiently ionize molecules from several shells, creating coherent superpositions of electronic states, i.e., electronic wave packets. In general, the ultrafast electronic response to prompt ionization can be described in the framework of the fixed-nuclei approximation since it usually precedes the onset of the nuclear motion. In this work we have employed the static-exchange Density Functional Theory method, explained in section 2.2.2, to evaluate the

electronic structure of molecules. The electronic wave packet generated by attosecond ionization can be written as:

$$\Phi(\bar{\mathbf{x}}, t) = c_0(t)\Psi_0(\bar{\mathbf{x}}) + \sum_{\alpha lh} \int c_{\alpha\epsilon lh}(t)\Psi_{\alpha\epsilon lh}(\bar{\mathbf{x}})d\epsilon \quad (3.1)$$

where  $\bar{\mathbf{x}} = (\mathbf{x}_1, \dots, \mathbf{x}_N)$  stands for the spatial and spin coordinates of the  $N$  electrons in the molecule,  $\Psi_0(\bar{\mathbf{x}})$  is the electronic ground state,  $\Psi_{\alpha\epsilon lh}(\bar{\mathbf{x}})$  represents a continuum state in which an electron has been promoted from the  $\alpha$  orbital to a continuum orbital with kinetic energy  $\epsilon$  and angular quantum numbers  $l$  and  $m$  and the time-dependence of the wave function is included in the spectral coefficients  $c_0$  and  $c_{\alpha lh}$ , which satisfy the normalization condition:

$$|c_0(t)|^2 + \sum_{\alpha lh} \int |c_{\alpha\epsilon lh}(t)|^2 d\epsilon = 1 \quad (3.2)$$

At  $t = 0$  the system is assumed to be in the ground state, i.e.,  $|c_0(0)|^2 = 1$  and  $c_{\alpha\epsilon lh}(0) = 0$ . If the attosecond pulse is weak, most of the population will remain in the ground state, i.e.,  $|c_0(t)|^2 \simeq 1$ , and the time-dependent coefficients can be evaluated using first-order perturbation theory, as explained in section 1.2. We can thus make use of eq. 1.15 to evaluate the continuum spectral coefficients which, for our particular case, reads:

$$c_{\alpha\epsilon lh}(t) = -\frac{i}{\hbar} \langle \Psi_{\alpha\epsilon lh}(\bar{\mathbf{x}}) | \boldsymbol{\mu}_\epsilon | \Psi_0(\bar{\mathbf{x}}) \rangle e^{-\frac{i}{\hbar}(E_\alpha + \epsilon)t} \int_0^t E(\tau) e^{\frac{i}{\hbar}(E_\alpha + \epsilon - E_0)\tau} d\tau \quad (3.3)$$

where  $\hat{\boldsymbol{\epsilon}}$  is the polarization direction of the electric field  $\mathbf{E}$  and  $E_\alpha$  is the energy of an ion with a hole in the  $\alpha$  molecular orbital. After the interaction with the pulse ( $t > T$ ), the integral in eq. 3.3 can be substituted by the Fourier transform of the electric field  $\mathcal{F}_{\{\mathbf{E}\}}$ :

$$c_{\alpha\epsilon lh}(t > T) = -\frac{i}{\hbar} \langle \Psi_{\alpha\epsilon lh}(\bar{\mathbf{x}}) | \boldsymbol{\mu}_\epsilon | \Psi_0(\bar{\mathbf{x}}) \rangle e^{-\frac{i}{\hbar}(E_\alpha + \epsilon)t} \mathcal{F}_{\{\mathbf{E}\}} \left( \frac{E_\alpha + \epsilon - E_0}{\hbar} \right) \quad (3.4)$$

where the dependence on time is that of the stationary phases  $e^{-\frac{i}{\hbar}(E_\alpha + \epsilon)t}$  as the wave packet evolves freely. The interferences between the spectral components of the wave packet can be imprinted in different observables.

### Electron density

As explained in section 2.2.2, we employ a discretization technique to describe the electronic continuum. The perturbed part of the time-dependent wave function, that is, the part of the wave function that does not contain the ground state (see eq. 3.1), can be approximated by:

$$\Phi^{\text{pert}}(\bar{\mathbf{x}}, t) \simeq \sum_{\alpha n l h} \tilde{c}_{\alpha n l h}(t) \Psi_{\alpha \varepsilon n l h}(\bar{\mathbf{x}}) \quad (3.5)$$

where the integral has been replaced by a discrete sum,  $n$  is an index on the discretized photoelectron energies  $\varepsilon_n$  and the coefficients of the discretized expansion  $\tilde{c}_{\alpha n l h}$  are related those in eq. 3.1 by:

$$\tilde{c}_{\alpha n l h} = \frac{c_{\alpha l h}(\varepsilon_n)}{\sqrt{D_n}} \quad (3.6)$$

where  $D_n$  is the density of states [142], which, as discussed in section 2.3.2, can be approximated as  $D_n \simeq \frac{2}{\varepsilon_{n+1} - \varepsilon_{n-1}}$ . The time-dependent electron density can be evaluated by inserting eq. 3.5 into eq. 2.10:

$$\rho(\mathbf{r}) = N \int \dots \int \left| \sum_{\alpha n l h} \tilde{c}_{\alpha n l h}(t) \Psi_{\alpha \varepsilon n l h}(\bar{\mathbf{x}}) \right|^2 d s d \mathbf{x}_2 \dots d \mathbf{x}_N \quad (3.7)$$

where  $N$  is the number of electrons in the neutral molecule. After some rearrangement, eq. 3.7 can be written as:

$$\begin{aligned} \rho(\mathbf{r}) &= N \sum_{\alpha n l h} |\tilde{c}_{\alpha n l h}(t)|^2 \int \dots \int |\Psi_{\alpha \varepsilon n l h}(\bar{\mathbf{x}})|^2 d s d \mathbf{x}_2 \dots d \mathbf{x}_N \\ &+ N \sum_{\substack{m n' l' h h' \\ (n l h) \neq (n' l' h') \\ \text{same spin}}} \sum_{\alpha} \left[ \tilde{c}_{\alpha n l h}^*(t) \tilde{c}_{\alpha n' l' h'}(t) \right] \int \dots \int \Psi_{\alpha \varepsilon n l h}(\bar{\mathbf{x}})^* \Psi_{\alpha \varepsilon n' l' h'}(\bar{\mathbf{x}}) d s d \mathbf{x}_2 \dots d \mathbf{x}_N \\ &+ N \sum_{\substack{\alpha \alpha' \\ \alpha \neq \alpha' \\ \text{same spin}}} \sum_{n l h} \left[ \tilde{c}_{\alpha n l h}^*(t) \tilde{c}_{\alpha' n l h}(t) \right] \int \dots \int \Psi_{\alpha \varepsilon n l h}(\bar{\mathbf{x}})^* \Psi_{\alpha' \varepsilon n l h}(\bar{\mathbf{x}}) d s d \mathbf{x}_2 \dots d \mathbf{x}_N \end{aligned} \quad (3.8)$$

where we have taken into account that for  $\alpha \neq \alpha'$  and  $(n, l, h) \neq (n', l', h)$

$$\int \dots \int \Psi_{\alpha \varepsilon_n l h}(\bar{\mathbf{x}})^* \Psi_{\alpha' \varepsilon_{n'} l' h'}(\bar{\mathbf{x}}) d s d \mathbf{x}_2 \dots d \mathbf{x}_N = 0 \quad (3.9)$$

Eq. 3.8 can be simplified by making use of the following relations:

- The integral of the absolute square of a stationary state is given by

$$\int \dots \int |\Psi_{\alpha \varepsilon_n l h}(\bar{\mathbf{x}})|^2 d s d \mathbf{x}_2 \dots d \mathbf{x}_N = \frac{1}{N} \left( \sum_{\substack{\alpha' \\ \alpha' \neq \alpha}} |\varphi_{\alpha'}(\mathbf{r})|^2 + |\varphi_{\varepsilon_n l h}(\mathbf{r})|^2 \right) \quad (3.10)$$

- If  $(n, l, h) \neq (n', l', h')$ , then

$$\int \dots \int \Psi_{\alpha \varepsilon_n l h}(\bar{\mathbf{x}})^* \Psi_{\alpha' \varepsilon_{n'} l' h'}(\bar{\mathbf{x}}) d s d \mathbf{x}_2 \dots d \mathbf{x}_N = \frac{1}{N} \varphi_{\varepsilon_n l h}(\mathbf{r}) \varphi_{\varepsilon_{n'} l' h'}(\mathbf{r}) \quad (3.11)$$

- If  $\alpha \neq \alpha'$ , then

$$\int \dots \int \Psi_{\alpha \varepsilon_n l h}(\bar{\mathbf{x}})^* \Psi_{\alpha' \varepsilon_n l h}(\bar{\mathbf{x}})^* d s d \mathbf{x}_2 \dots d \mathbf{x}_N = -\frac{1}{N} \varphi_{\alpha}(\mathbf{r}) \varphi_{\alpha'}(\mathbf{r}) \quad (3.12)$$

provided the ionic substates  $\alpha$  and  $\alpha'$  have the same spin, otherwise the integral given in 3.12 is zero.

Making use of these properties (eqs. 3.10, 3.11 and 3.12), eq. 3.8 can be simplified to:

$$\begin{aligned} \rho(\mathbf{r}, t) = & \sum_{\alpha n l h} |\tilde{c}_{\alpha n l h}(t)|^2 \left( \sum_{\alpha'} |\varphi_{\alpha'}(\mathbf{r})|^2 + |\varphi_{\varepsilon_n l h}(\mathbf{r})|^2 \right) \\ & + \sum_{\substack{n n' l' h h' \\ \text{same spin}}} \sum_{\alpha} \left[ \tilde{c}_{\alpha n l h}^*(t) \tilde{c}_{\alpha n' l' h'}(t) \right] \varphi_{\varepsilon_n l h}(\mathbf{r}) \varphi_{\varepsilon_{n'} l' h'}(\mathbf{r}) \\ & - \sum_{\substack{\alpha \alpha' \\ \text{same spin}}} \sum_{n l h} \left[ \tilde{c}_{\alpha n l h}^*(t) \tilde{c}_{\alpha' n l h}(t) \right] \varphi_{\alpha}(\mathbf{r}) \varphi_{\alpha'}(\mathbf{r}) \end{aligned} \quad (3.13)$$

We can see that the electron density is the sum of three contributions. The first term is a stationary term that does not depend on time. The second is constructed



using continuum orbitals and thus describes the emission of the photoelectron wave. The third term, built from bound (Kohn-Sham) orbitals, accounts for the charge redistribution along the molecular skeleton. The evaluation of the full electron density might become tedious in some situations due to the large number of continuum orbitals one may need to employ to describe the photoelectron wave (term 2 in eq. 3.7). An alternative approach to evaluate the ultrafast charge redistribution occurring in the residual ion upon attosecond ionization is to employ the reduced density matrix of the ionic subsystem, as we explain in the next section.

## 3.2 Evolution of the ionic subsystem

We seek to analyze the evolution of the hole generated in the molecular target upon attosecond ionization. The residual ion is an open system that remains coupled to the emitted electron. Therefore, it can be fully characterized in terms of its reduced density matrix, whose elements can be constructed from the spectral coefficients (eqs. 3.3 and 3.4):

$$\gamma_{\alpha\alpha'}^{(\text{ion})}(t) = \sum_{lh} \int c_{\alpha\epsilon lh}(t) c_{\alpha'\epsilon lh}^*(t) d\epsilon \quad (3.14)$$

where the double sum runs over the ionic states from which the electron has been emitted with the same spin. The trace of the reduced density matrix contains the population of each ionic state and the off-diagonal terms provide the coherence between pairs of states. In the case of ionization with monochromatic light, all off-diagonal terms would be zero (except those involving degenerate states) since the parent ion would be in an incoherent superposition of states. This is the situation one would expect to find in experiment with synchrotron radiation where the energy of the incident photons is well defined [43]. Due to their wide spectral bandwidths, attosecond XUV pulses can generate coherent superpositions of electronic states, allowing to investigate ultrafast dynamics with the required time resolution [11].

### Electron density of the residual ion

The reduced density matrix (eq. 3.14) contains all the information about the ionic subsystem and therefore can retrieve any observable depending on its coordinates. In particular, the time-dependent electron density is given by:

$$\rho^{(\text{ion})}(\mathbf{r}, t) = \sum_{\alpha} \gamma_{\alpha\alpha}^{(\text{ion})}(t) \sum_{\alpha'} |\varphi_{\alpha'}(\mathbf{r})|^2 - \sum_{\substack{\alpha\alpha' \\ \text{same} \\ \text{spin}}} \gamma_{\alpha\alpha'}^{(\text{ion})}(t) \varphi_{\alpha}(\mathbf{r}) \varphi_{\alpha'}(\mathbf{r}) \quad (3.15)$$

Where the first term is time-independent since the trace of the reduced density matrix is constant. By comparing eq. 3.15 with the electron density of the full system including the photoelectron (eq. 3.7) we can see that the former contains all the terms describing the ultrafast dynamics occurring in the parent ion upon ultrafast ionization. Only the terms describing the photoelectron emission, i.e., those containing continuum orbitals  $\varphi_{\varepsilon_n lh}(\mathbf{r})$ , are not included in eq. 3.15.

### Hole density

An interesting observable is the density of the hole generated upon ionization, defined by Lorenz S. Cederbaum and coworkers [32] as the difference between the electron density of the ion,  $\rho^{(\text{ion})}(\mathbf{r}, t)$ , and that of the (initial) neutral molecule,  $\rho_0(\mathbf{r})$ , which does not depend on time:

$$Q(\mathbf{r}, t) = \rho_0(\mathbf{r}) - \rho^{(\text{ion})}(\mathbf{r}, t) = \sum_{\substack{\alpha\alpha' \\ \text{same} \\ \text{spin}}} \gamma_{\alpha\alpha'}^{(\text{ion})}(t) \varphi_{\alpha}(\mathbf{r}) \varphi_{\alpha'}(\mathbf{r}) \quad (3.16)$$

where the ground state density is given by

$$\rho_0(\mathbf{r}) = \sum_{\alpha} \varphi_{\alpha}^2(\mathbf{r}) \quad (3.17)$$

and we have assumed that the reduced density matrix of the ionic subsystem is normalized to unity, i.e.,

$$\sum_{\alpha} \gamma_{\alpha\alpha}^{(\text{ion})} = 1$$

Fluctuations in the hole density might arise if several ionic states are populated coherently, that is, if off-diagonal elements of the reduced density matrix are not zero. Although, up to now, no experiment has been able to measure the hole density of an isolated molecule directly, the ultrafast charge redistribution accompanying sudden ionization can be imprinted in observables that are experimentally accessible. For instance, some fragmentation channels may be sensitive to the localization of the hole created in the molecule upon attosecond ionization [92, 97].



# Results



## Chapter 4

# Interferences in molecular photoionization

X-rays can ionize matter from their inner and valence shells, producing short-wavelength electrons that can be diffracted by the surrounding atomic centers. Consequently, scattered photoelectrons convey structural information about the system, which can be extracted by fitting experimental photoelectron spectra to analytical formulas. Based on this principle, the NEXAFS (near-edge X-ray absorption fine structure) and the EXAFS (extended X-ray absorption fine structure) techniques [161, 162] can retrieve structural information of crystals and of bulk amorphous materials [163, 164, 165, 166, 167, 168, 169], where the relatively low intensity of standard X-rays is compensated by the large number of particles in the sample. However, obtaining structural information of isolated molecules is more difficult because of the low densities of the gas phase. To overcome this difficulty, in addition to the development of the gas-phase EXAFS technique [170, 171, 172], other methods are being explored. One of them takes advantage of the high brightness of the X-ray free electron lasers (XFEL), which can take time-resolved “pictures” through the so-called photoelectron holography [173]. However, its practical applications are still very limited due to the complexity and large dimensions of the recently operating XFEL facilities. A more traditional method consists of measuring molecular-frame photoelectron angular distributions in photoionization with synchrotron radiation [174, 175, 76, 77]. Also, recent work on diatomic molecules [176, 81, 82, 114] has shown that even the

angle-integrated photoelectron spectra might be a valuable tool for structural determination. Here we present an overview of our most significant results on photoionization of diatomic ( $\text{CO}$ ,  $\text{F}_2$ ) and small polyatomic ( $\text{BF}_3$ ,  $\text{CF}_4$ ) molecules with synchrotron radiation. We show that the interferences arising between different ionization paths may encode structural information that can be extracted by analyzing the role of the nuclear motion. This chapter constitutes only a summary of the work attached in appendices [A](#), [B](#), [C](#), [D](#) and [E](#), performed in collaboration with Piero Decleva (Università degli Studi di Trieste) and with the experimental groups of Catalin Miron (Synchrotron SOLEIL), Kiyosi Ueda (Synchrotron SPring-8), Edwin Kukk (University of Turku) and Thomas Darrah Tomas (University of Oregon).

## 4.1 Intramolecular scattering in inner-shell photoionization

We have investigated inner-shell photoionization of small molecules, where an electron is ejected from a  $1s$  orbital of a first-row atom. Fig. 4.1 shows the photoelectron spectra of  $\text{CO}$ ,  $\text{BF}_3$  and  $\text{CF}_4$  taken at photon energies of 425, 383 and 518 eV, respectively, at PLEIADES beamline [177] at SOLEIL Synchrotron. The experimental spectrum of  $\text{BF}_3$  and  $\text{CF}_4$  (fig. 4.1) shows several vibrational excitation peaks in the the totally-symmetric stretching mode (TSSM), which is the most affected by the electronic rearrangement accompanying core ionization [159, 160]. Potential energy curves of the electronic ground state and of the core-hole species generated upon C  $1s$  and B  $1s$  ionization of  $\text{CO}$ ,  $\text{CF}_4$  and  $\text{BF}_3$ , respectively, are shown in fig. 4.2, as well as the relevant vibrational eigenfunctions. They have been evaluated using the harmonic ( $\text{CF}_4$ ) and the Morse ( $\text{CO}$ ,  $\text{BF}_3$ ) approximations using reliable spectroscopic parameters available in the literature ( $\text{CO}$ : [178, 179],  $\text{CF}_4$ : [180, 160],  $\text{BF}_3$ : [181, 182, 183, 184, 159]). Photoionization of  $\text{BF}_3$  leads to a large progression of vibrational levels  $\nu'$ , reaching up to  $\nu' = 7$ , as a consequence of the favorable Franck-Condon (FC) overlap between the initial and several final-state vibrational wave functions due to the large bond contraction accompanying core-ionization ( $\Delta R_{\text{BF}} = -0.110$  a.u. [159]). The progression is limited to only two vibrational levels in the spectrum of  $\text{CF}_4$  because the potential



energy curves of the neutral and the ionic species (fig. 4.2) are very similar in the region close to the equilibrium geometry ( $\Delta R_{\text{CF}} = -0.0115$  a.u. [160]). The spectrum of CO shows an intermediate situation: 4 vibrational excitations in the only vibrational mode of the parent ion ( $\Delta R_{\text{CO}} = -0.0932$  a.u. [178], see fig. 4.2).

Fig. 4.3 shows the vibrationally resolved C 1s and B 1s photoionization cross sections of CO, CF<sub>4</sub> and BF<sub>3</sub>, respectively, as a function of the photon energy. They have been calculated as explained in section 2.3.3, using the static-exchange Density Functional Theory (DFT) method within the Born-Oppenheimer approximation, and in the case of BF<sub>3</sub> and CF<sub>4</sub> the nuclear motion has been restricted to the TSSM coordinate. In good agreement with the spectrum shown in fig. 4.1, we observe a large progression of vibrational excitations upon B 1s ionization of BF<sub>3</sub>,  $\nu' = 2$  and  $\nu' = 3$  being the dominant contributions in the entire energy range. Only the low-lying vibrational eigenstates or the parent ion are excited in C 1s ionization of CO and CF<sub>4</sub>, as experimentally found. In all cases, we can distinguish that the photoionization cross sections (fig. 4.3) exhibit sharp increases near the ionization threshold due to the presence of shape resonances [185, 186, 187]. The origin of these structures can be understood in terms of a quasi-bound state embedded in the electronic continuum as a consequence to the existence of a small barrier in the molecular potential. More subtle structures arise at higher energies due to photoelectron diffraction by the surrounding atomic centers (O in CO, F in BF<sub>3</sub> and CF<sub>4</sub>). However, the rapid decrease of the cross sections with the photon energy usually washes out scattering effects in the high-energy region. A better analysis can be performed by taking ratios between vibrationally resolved cross sections ( $\nu$ -ratios), since the decay is the same for each vibrational component. Experimentally, presenting the cross sections as  $\nu$ -ratios is advantageous since certain calibration problems that one would face in case of absolute cross sections can be avoided.

Fig. 4.4 shows the experimental and theoretical  $\nu$ -ratios as a function of the photoelectron momentum. For the three systems, the  $\nu$ -ratios are calculated taking the largest contribution as a reference, which is  $\nu' = 0$  for CO and CF<sub>4</sub> and  $\nu' = 2$  for BF<sub>3</sub>. The shape resonances appear now as even sharper structures close to the ionization threshold. At higher energies, the  $\nu$ -ratios exhibit pronounced oscillations superimposed to a nearly flat background which are a consequence of

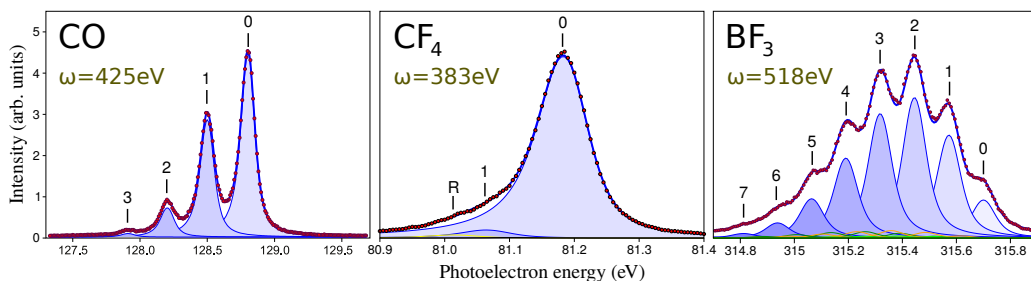


Figure 4.1: Photoelectron spectra of CO (left), CF<sub>4</sub> (center) and BF<sub>3</sub> (right) taken SOLEIL at  $h\nu = 425$ , 383 and 518 eV, respectively. Experimental results: red circles. Thick blue line: fit of the experimental data. Thin blue lines enclosing shaded areas: vibrational progression associated with the symmetric stretching mode. Other thin lines: contribution of other modes resulting from recoil. Peak labels indicate the vibrational quantum numbers of the core-hole species.

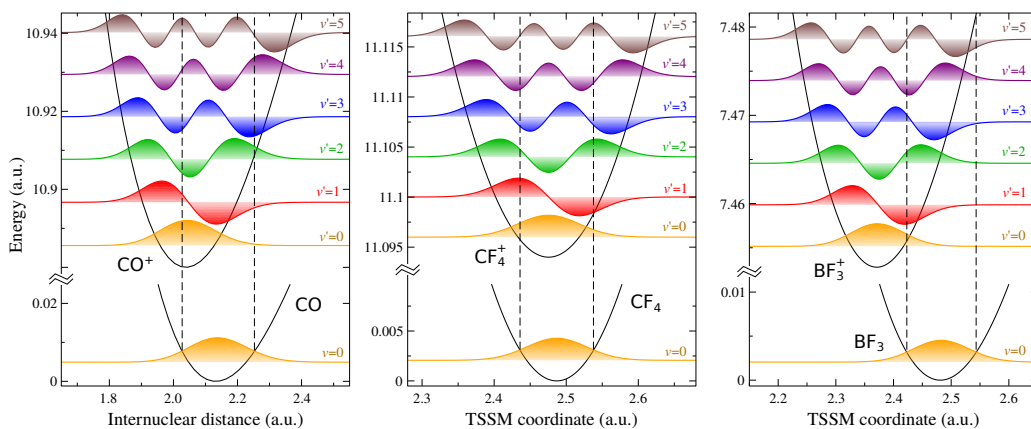


Figure 4.2: Potential energy curves of the electronic ground state of CO (left), CF<sub>4</sub> (center) and BF<sub>3</sub> (right) and of the core-hole species generated upon C 1s (CO and CF<sub>4</sub>) and B 1s (BF<sub>3</sub>) ionization along the internuclear distance of CO and the TSSM coordinate of CF<sub>4</sub> and BF<sub>3</sub>. They have been constructed using reliable spectroscopic parameters available in the literature (CO: [178, 179], CF<sub>4</sub>: [180, 160], BF<sub>3</sub>: [181, 182, 183, 184, 159]). The relevant vibrational eigenstates are shown: the ground state of the neutral molecules (orange) and the low-lying states of the core-hole species (different colors), as well as the corresponding FC regions (dashed black lines).

intramolecular scattering. The periodicity of the oscillations is  $2k_e R$ , where  $k_e$  is the photoelectron momentum and  $R$  the distance between emitting and diffracting

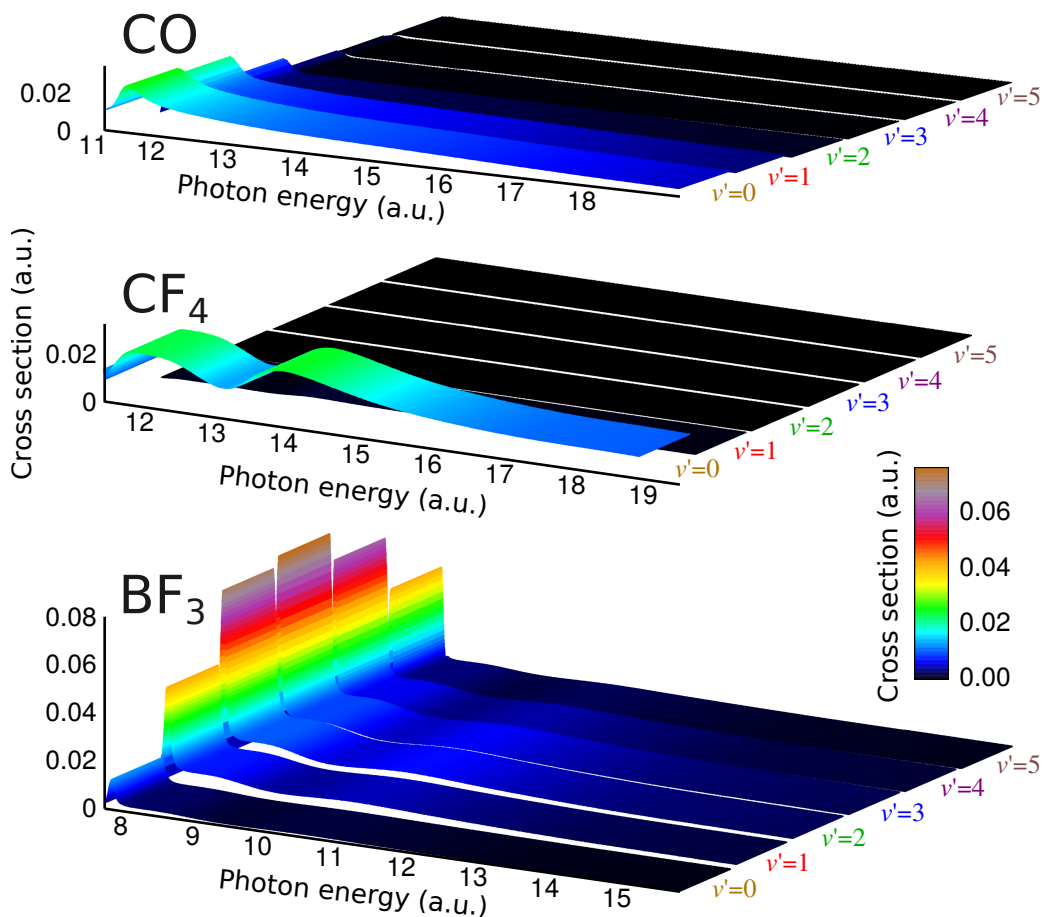


Figure 4.3: Vibrationaly resolved C 1s photoionization cross section of CO (upper figure) and CF<sub>4</sub> (center) and B 1s photoionization cross section of BF<sub>3</sub> (lower figure). The nuclear motion in the polyatomic molecules BF<sub>3</sub> and CF<sub>4</sub> has been restricted to the TSSM.

atoms, as in the well known EXAFS equation [188]. Our interpretation in terms of intramolecular scattering is supported by the good agreement with a first Born model [82] (see appendices A and B).

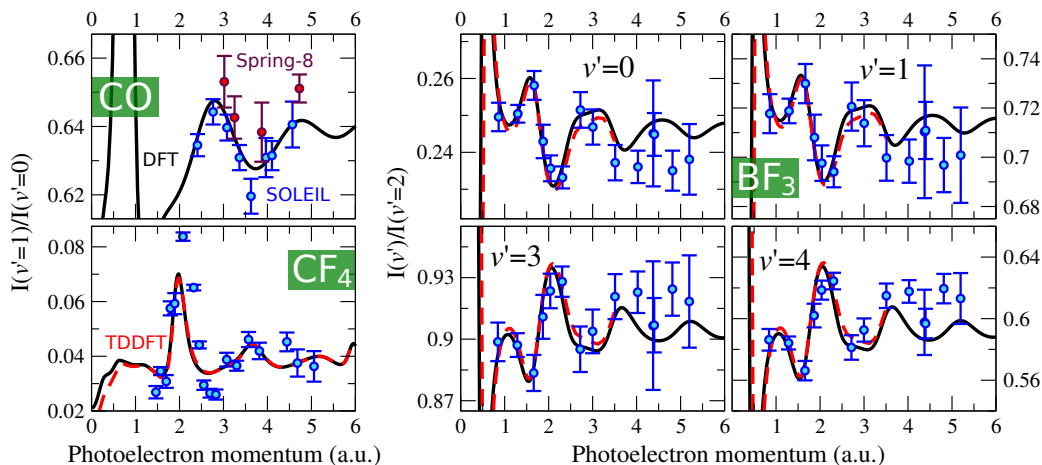


Figure 4.4: Ratios between inner-shell vibrationally resolved photoionization cross sections of CO (upper left), CF<sub>4</sub> (lower left) and BF<sub>3</sub> (right), shown in fig. 4.3. Circles with error bars: experimental data including statistical errors taken at SOLEIL and Spring-8. Black dashed lines: results from the static-exchange DFT calculations. Red full lines: results of the TDDFT calculations (BF<sub>3</sub> and CF<sub>4</sub>). Horizontal dashed-dotted lines: ratios predicted by the FC approximation.

The agreement between theory and experiment is very good in all cases. The excellent agreement between the results provided by the static-exchange and the time-dependent DFT methods indicates that interchannel coupling does not play an important role in core-ionization and that therefore one can rely on the former to interpret the experimental findings. In the case of BF<sub>3</sub>, the overall shape of the  $\nu$ -ratios is very similar for all  $\nu \geq 3$ ; for  $\nu' = 0$  and  $\nu' = 1$ , the oscillations are essentially identical but appear inverted. The reason is that all vibrational contributions are referred to  $\nu' = 2$ . If we choose  $\nu' = 4$  instead, then the first four  $\nu$ -ratios would be inverted. The same behavior is observed in CO and CF<sub>4</sub>. These results suggest that, for a given molecule, all  $\nu$ -ratios carry the same structural information. In fact, as discuss in appendices A and B, the information contained in each individual  $\nu$ -ratio can be gathered in a generalized  $\nu$ -ratio. In the case of BF<sub>3</sub>, where the vibrational progression reaches up to  $\nu' = 7$ , the use of a generalized  $\nu$ -ratio is very useful because it improves dramatically the statistical significance of the experimental data.

### Extracting structural information

As the oscillatory patterns found in the  $\nu$ -ratios are due to intramolecular scattering, they convey structural information about the system. In appendix D, we present a systematical approach for extracting this information. As a proof of principle, we have applied it to the simultaneous determination of the internuclear distance of CO ( $R = R_{\text{CO}}$ ) and the bond contraction ( $\Delta R = R_{\text{CO}^+} - R_{\text{CO}}$ ) upon C 1s ionization. Fig. 4.5 illustrates of how the  $\nu$ -ratio  $I(\nu' = 1)/I(\nu' = 0)$  changes when  $R$  and  $\Delta R$  are modified independently. Since the bond contraction sets the overlap between the initial and the final vibrational wave functions, the  $\nu$ -ratios are shifted vertically when varying  $\Delta R$  (left panel in fig. 4.5). This effect is very sensitive because the FC overlap is strongly affected by small modifications of  $\Delta R$ , as can be seen in fig. 4.2. When  $R$  is modified (right panel in fig. 4.5), the periodicity of the high-energy oscillations changes because they are due to intramolecular scattering and therefore depend on the distance between the emitting (C) and diffracting (O) centers.

We have performed a  $\chi$ -square minimization procedure in order to find the values of  $R$  and  $\Delta R$  that provide the theoretical  $\nu$ -ratio that is in best agreement with the experimental points measured at SOLEIL and Spring-8 (fig. 4.6). These values are  $R = 2.09 \pm 0.03$  a.u and  $\Delta R = -0.0945 \pm 0.00014$  a.u. Details of the fitting procedure can be found in appendix D. The  $\nu$ -ratios computed using these values and those taken from the literature [178, 179]:  $R_{\text{lit}} = 2.1322$  a.u. and  $\Delta R_{\text{lit}} = -0.0932$  a.u. are shown in fig. 4.6 as well as the experimental points. We note that the literature values lay inside the confidence intervals provided by the method. The  $\chi$ -square function of the fit is shown in 4.6 as a function of  $R$  and  $\Delta R$ , as well as the and the isocurves that determine the bidimensional confidence regions for different confidence levels. Due to the lack of local minima in the  $\chi$ -square function, we note that the fitting procedure always converges to the same values, regardless the initial guess.

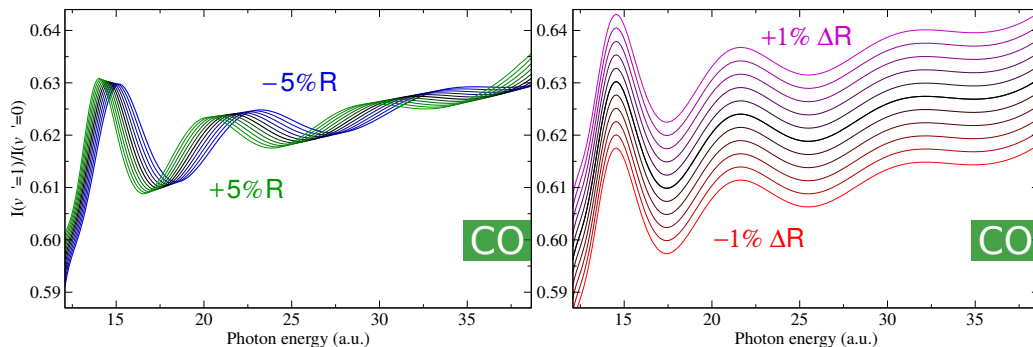


Figure 4.5: Vibrational branching ratio  $I(\nu' = 1)/I(\nu' = 0)$  corresponding to C 1s photoionization of CO calculated using the bibliographic values of  $R$  and  $\Delta R$  [178, 179] (both panels: black lines), increasing/decreasing  $R$  in steps of 1% (left panel: green and blue lines) and increasing/decreasing  $\Delta R$  in steps of 0.2% (right panel: pink and red lines).

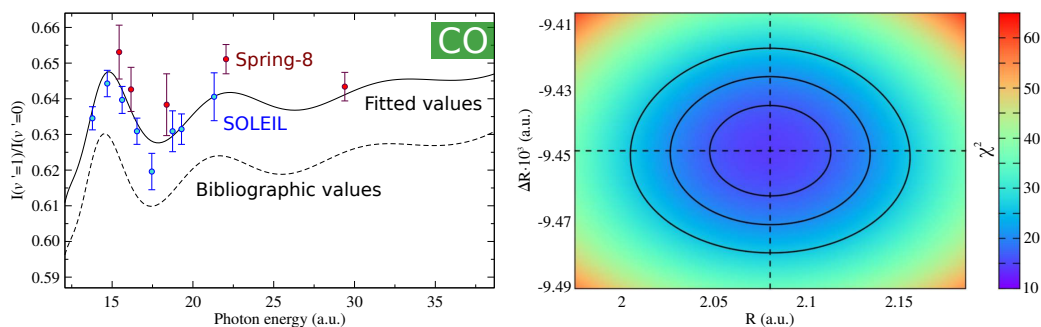


Figure 4.6: Left panel: vibrational branching ratio  $I(\nu' = 1)/I(\nu' = 0)$  corresponding to C 1s photoionization of CO measured at Spring-8 (red points) and SOLEIL (blue points) and calculated using the bibliographic values of  $R$  and  $\Delta R$  [178, 179] (dashed black line) and those that provide the best agreement with the experimental points (full black line). The optimum values of  $R$  and  $\Delta R$  have been obtained by performing a  $\chi^2$  minimization procedure. Right panel:  $\chi^2$  function as a function of  $R$  and  $\Delta R$ . The black lines correspond to the limits of the confidence regions for confidence levels: 68.3% ( $1\sigma$ ), 95.4% ( $2\sigma$ ) and 99.7% ( $3\sigma$ ).

## 4.2 Photoionization of $F_2$ : multicenter emission

Young’s double slit interferences are expected to arise when an electronic wave is coherently emitted from two (several) atomic centers. As found by Cohen and Fano in the sixties [189], these interferences are imprinted in the angle-integrated photoelectron spectra of homonuclear diatomic molecules. This phenomenon has attracted the interest of various authors [190, 176, 191, 192, 81, 117, 114] in the last few years. We have investigated multicenter emission effects in the fluorine molecule by analyzing dissociative and non-dissociative ionization from inner and valence shells. Here we present a brief summary of our work, which is explained in detail in appendix E.

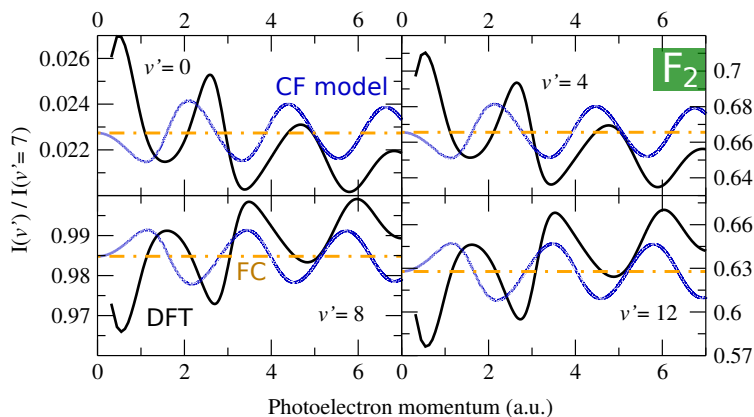


Figure 4.7: Ratios between vibrationally resolved  $3\sigma_g$  photoionization cross sections photoionization of  $F_2$ . Black lines: DFT theory; blue dashed lines: Cohen-Fano model; orange dashed lines: FC values.

Fig. 4.7 shows some  $\nu$ -ratios corresponding to ionization from the  $3\sigma_g$  orbital as a function of the photoelectron momentum. We have chosen  $\nu' = 7$  as the common denominator because it constitutes the largest contribution to the total cross section. As in fig. 4.4, the  $\nu$ -ratios show pronounced oscillations around the FC value as a function of the photoelectron momentum. However, in this case they are not due to photoelectron diffraction but to multicenter emission as the electron is ejected from an orbital that is delocalized between the two fluorine atoms. In order to confirm this assumption, we have extended formula developed by Cohen and Fano in the sixties [189] to account for the vibrational motion,

as is [81]. The results of the model are included in fig. 4.7, where we can see that the agreement with the static-exchange theory is very good. As discussed in appendix E, the agreement is not so good in the case of  $1\pi_g$  and  $1\pi_u$  ionization because  $\pi$  orbitals concentrate most of the electron density outside the molecular axis. However, even in those situations, the amplitudes and periodicities of the oscillations predicted by the Cohen-Fano formula are close to the ones provided by the static-exchange DFT theory. Only the phases are not properly described.

### 4.3 Conclusions

In summary, we have found measurable evidence of intramolecular scattering and multicenter emission occurring in the photoionization of small molecules at high photoelectron energies. The details of the work presented here can be found in appendices A, B, C, D and E. When an electron is emitted from a very localized region of a molecule, such as the C 1s (B 1s) orbital in CO or CF<sub>4</sub> (BF<sub>3</sub>), features due to photoelectron diffraction are expected to arise, whereas in the case of ionization from a delocalized orbital, like those in F<sub>2</sub>, one should expect to observe Cohen-Fano-like interferences. Vibrationally resolved photoelectron spectroscopy allows to detect these high-energy interferences in an elegant and consistent way, because (i) the problem of the rapid decrease of the ionization probability with the photon energy can be avoided by monitoring the ratios between vibrationally resolved cross sections, and (ii) the effect of the interferences manifest differently in different final vibrational states. The combination of state-of-the-art DFT-like calculations and high-resolution third-generation synchrotron facilities has enabled to explore these non-Franck-Condon effects both theoretically and experimentally, demonstrating that the nuclear response to intramolecular electron diffraction / multicenter emission is observable and can provide structural information of both the neutral molecule and the ionized species.



## Chapter 5

# Ultrafast electron dynamics in aminoacids

Intramolecular charge transfer is the trigger of important chemical and biological processes, such as photosynthesis [193], cellular respiration [194] or DNA damage [195]. The study of charge transfer within isolated complex molecules was pioneered by R. Weinkauff and coworkers in the 90s [36, 37, 38]. They were able to track the motion of a positive hole generated upon ionization through up to 12 sigma bonds of a tetrapeptide by analyzing light absorption shifts. However, the time resolution in their experiments was limited by the durations of the pulses they employed, that were around 200 ns. One decade later, by using femtosecond pulses, they could measure how long it took for a positive charge to move from the phenyl to the amino group in the PENNA molecule:  $(80 \pm 20)$  fs [4]. In their paper, they suggested that the charge transfer was probably mediated by the nuclear motion through a conical intersection. Motivated by the pioneering work of R. Weinkauff and collaborators [36, 37, 38], Lorenz S. Cederbaum and coworkers demonstrated that electron correlation can drive ultrafast charge dynamics in a time scale that is faster than the onset of the nuclear motion [32]. This phenomenon has been referred to as charge migration to distinguish it from charge transfer mediated by nuclear motion and, over the last two decades, it has been widely investigated in a large number of molecules of biological interest [31, 32, 33, 34, 35, 93, 94].

The application of attosecond technology to the study of complex molecules has led to the experimental demonstration of charge migration in a biomolecule: the amino acid phenylalanine [92, 97]. The  $\alpha$ -amino acids consist of a central carbon atom ( $\alpha$  carbon) linked to an amino group ( $-\text{NH}_2$ ), a carboxyl group ( $-\text{COOH}$ ), a hydrogen atom and a side chain (R), which in the case of phenylalanine is a benzyl group. A two-color pump-probe technique was used in the experiment. Charge dynamics were initiated by isolated XUV sub-300-as pulses, with photon energy in the spectral range between 15 and 35 eV and probed by 4-fs, waveform-controlled visible/near infrared (VIS/NIR, central photon energy of 1.77 eV) pulses (see appendices F and G). Ionization induced by the attosecond pulse occurred in a sufficiently short time interval to exclude substantial electron rearrangement during the excitation process. The yield for the production of doubly charged immonium ions was measured as a function of the time delay between the attosecond pump pulse and the VIS/NIR probe pulse. Fig. 5.1a shows the results on a 100-fs time scale. The experimental data display a rise time of  $(10 \pm 2)$  fs and an exponential decay with time constant of  $(25 \pm 2)$  fs (this longer relaxation time constant is in agreement with earlier experimental results reported in [39]). Fig. 5.1b shows a 25-fs-wide zoom of the pump-probe dynamics, obtained by reducing the delay step between pump and probe pulses from 3 to 0.5 fs. An oscillation of the dication yield is clearly visible. For a better visualization, fig. 5.1c shows the same yield after subtraction of an exponential fitting curve. The data have been fitted with a sinusoidal function of frequency 0.234 PHz (corresponding to an oscillation period of 4.3 fs), with lower and upper confidence bounds of 0.229 and 0.238 PHz, respectively (see appendices F and G). The ultrafast oscillations in the temporal evolution of the dication yield cannot be related to nuclear dynamics, which usually come into play on a longer temporal scale, ultimately leading to charge localization in a particular molecular fragment. Therefore, these measurements constitute the first experimental observation of purely electron dynamics in a biomolecule.

In order to verify that the observed oscillations are not related to any nuclear dynamics, we have calculated the vibrational frequencies and the corresponding periods of phenylalanine by means of Density Functional Theory (DFT) using the B3LYP functional [196, 197] and a 6-311+g(3df,2p) basis set, implemented in the

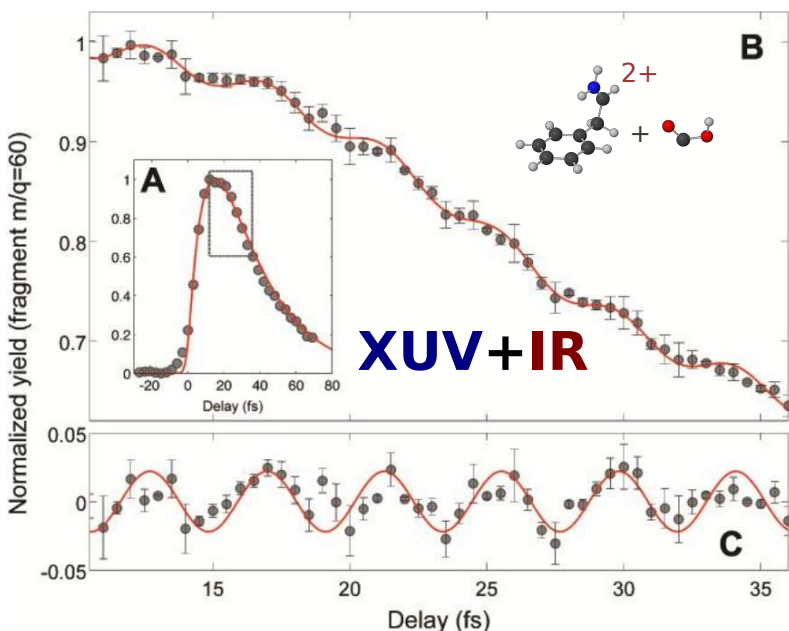


Figure 5.1: Experimental data from the group of Mauro Nisoli. (A) Yield of doubly charged immonium ion (mass/charge = 60) as a function of pump-probe delay, measured with 3-fs temporal steps. The red line is a fitting curve with an exponential rise time of 10 fs and an exponential relaxation time of 25 fs. (B) Yield of doubly charged immonium ion versus pump-probe delay measured with 0.5-fs temporal steps, within the temporal window shown as dotted box in (A). Error bars show the standard error of the results of four measurements. The red line is the fitting curve given by the sum of the fitting curve shown in (A) and a sinusoidal function of frequency 0.234 PHz (4.3-fs period). (C) Difference between the experimental data and the exponential fitting curve displayed in (A). Red curve is a sinusoidal function of frequency 0.234 PHz

quantum chemistry package Gaussian 09 [198]. The results are given in table 5.1. Our calculations show that the highest vibrational frequency is 0.11 PHz, which corresponds to a period of 8.9 fs, associated with X-H stretching modes, whereas skeleton vibrations are even slower, so that one can rule out that the observed beatings are due to vibrational motion. In any case, some influence of the nuclear motion cannot be completely excluded, because, for example, stretching of the order of a few picometers of carbon bonds can occur in a few femtoseconds, and this could modify the charge dynamics [95, 102].

Mode	Freq. (PHz)	Period (fs)	Mode	Freq. (PHz)	Period (fs)
1	0.0011	894.8	33	0.0335	29.8
2	0.0013	740.7	34	0.0342	29.2
3	0.0020	499.2	35	0.0353	28.3
4	0.0031	319.9	36	0.0355	28.2
5	0.0057	174.2	37	0.0362	27.6
6	0.0069	145.3	38	0.0365	27.4
7	0.0074	134.5	39	0.0373	26.8
8	0.0088	113.9	40	0.0388	25.8
9	0.0114	88.0	41	0.0399	25.1
10	0.0123	81.6	42	0.0403	24.8
11	0.0125	79.8	43	0.0410	24.4
12	0.0146	68.4	44	0.0413	24.2
13	0.0148	67.6	45	0.0421	23.8
14	0.0170	59.0	46	0.0446	22.4
15	0.0181	55.2	47	0.0446	22.4
16	0.0191	52.5	48	0.0459	21.8
17	0.0193	51.7	49	0.0486	20.6
18	0.0214	46.7	50	0.0493	20.3
19	0.0220	45.5	51	0.0500	20.0
20	0.0232	43.1	52	0.0544	18.4
21	0.0234	42.8	53	0.0907	11.0
22	0.0256	39.0	54	0.0916	10.9
23	0.0260	38.5	55	0.0929	10.8
24	0.0266	37.7	56	0.0946	10.6
25	0.0276	36.2	57	0.0947	10.6
26	0.0283	35.3	58	0.0950	10.5
27	0.0299	33.5	59	0.0952	10.5
28	0.0300	33.3	60	0.0956	10.5
29	0.0302	33.1	61	0.1050	9.5
30	0.0304	32.9	62	0.1070	9.3
31	0.0315	31.7	63	0.1125	8.9
32	0.0331	30.2			

Table 5.1: Frequencies (PHz) and periods (fs) of the vibrational modes of phenylalanine.

---

Fig. 5.2 shows an energy-level diagram of the electronic states of singly charged phenylalanine ( $\text{phe}^+$ ) accessible by the XUV pulse, all the states of doubly-charged phenylalanine ( $\text{phe}^{++}$ ) and those of the system doubly-charged immonium + carboxyl. The energies of the latter two systems have been evaluated within the static-exchange approximation, which is accurate enough to provide a qualitative picture of the full process. As can be seen, one can go from a highly excited state of  $\text{phe}^+$  to the lowest states of the  $\text{phe}^{++}$  or the dissociated system by absorbing just a few VIS/NIR photons (photon energy around 1.77 eV). Of course, one cannot know how likely this transition will be, but one can unambiguously say that the process only requires absorption of very few VIS/NIR photons. Even if these transitions were unlikely, e.g., due to unfavorable overlap between initial and final orbitals, the transition should be much more likely than others involving many photons even with favorable overlap. Since the HOMO orbital of phenylalanine is substantially localized on the amino group, ionization by the VIS/NIR pulse is expected to occur from this part of the molecule. Therefore, the removal of the second electron is sensitive to charge localization on the amino group.

In order to understand the origin of the ultrafast oscillations shown in fig. 5.1, we have evaluated the electronic wave packet generated in phenylalanine upon ionization by an attosecond pulse similar to that used in the experiment and the subsequent evolution of the electron density. We aim to understand the influence of different radicals, so we have performed a systematical study including the amino acids glycine and tryptophan. For the evaluation of the ionization amplitudes and the wave packet dynamics, we have employed the static-exchange DFT method within the formalism of time-dependent first-order perturbation theory, as explained in chapter 3. The most stable conformers of glycine [199], phenylalanine [200] and tryptophan [201] are depicted in fig. 5.3. It is well known that, even at room temperature, amino acids present several conformations due to their structural flexibility. In the case of phenylalanine, 37 conformers have been theoretically found [200]. This chapter is organized as follows: first, we give the details about the evaluation of the electronic stationary states and show the relevant molecular orbitals of the three amino acids (section 5.1) and the corresponding photoionization cross sections (section 5.2), restricting the analysis to the most stable

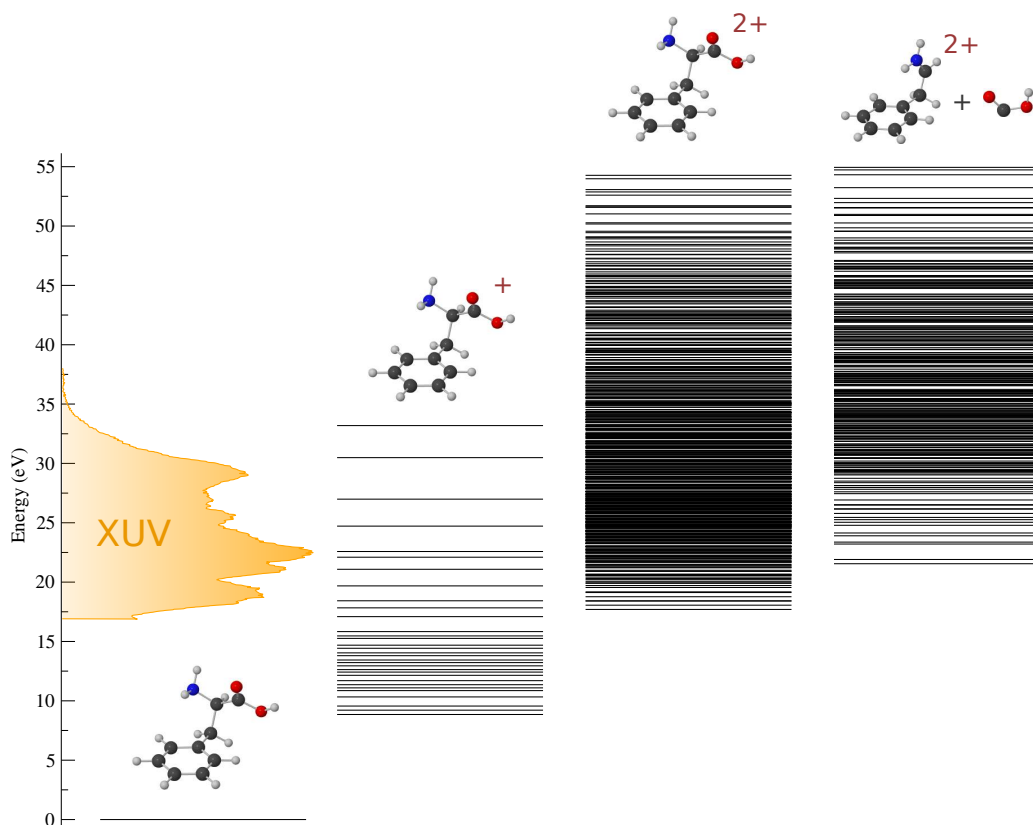


Figure 5.2: Energy level diagram containing the states of singly charged phenylalanine populated by the XUV pulse, whose energy distribution is included as a shadowed area in the axis bar, the states of doubly-charged phenylalanine and those of the system doubly-charged immonium + neutral carboxyl.

conformers at the temperature of the experiment presented in fig. 5.2. Then, we analyze the wave packet dynamics initiated by an attosecond pulse similar to that used in the experiment (section 5.3), performing a Fourier analysis of the electron density on different portions of the molecules and comparing our results with experimental data and with previous theoretical work, when available. We conclude by exploring the effect of molecular conformation (section 5.3.4) and the role of the photoelectron emission dynamics (section 5.4) in the charge migration mechanism.

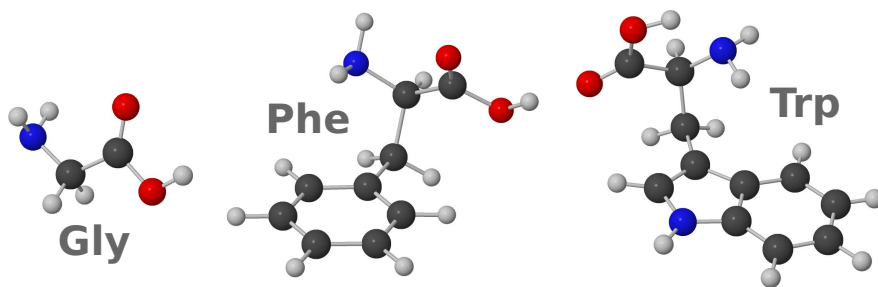


Figure 5.3: Geometry of the most abundant conformers of glycine [199], phenylalanine [200] and tryptophan [201] at 430 K, the temperature of the pump-probe experiment presented in fig. 5.1.

## 5.1 Evaluation of electronic states

We employ Slater determinants to represent electronic stationary states, as explained in section 2.2. The corresponding bound (Kohn-Sham) and continuum orbitals have been evaluated in a basis set of B-splines and spherical harmonics. In particular, we used a large one-center expansion (OCE) of a variable number of B-spline functions, from 118 in glycine to 135 in tryptophan, enclosed in a sphere of 30 a.u. with origin in the center of mass, using spherical harmonics up to an angular momentum of  $l = 20$  (see eq. 2.19). The OCE was complemented with small off centers, located at the atomic positions, with sizes varying from 0.2 to 1.6 a.u., larger for the heavier nuclei since they accumulate more electron density. The angular expansion in each off-center was limited to  $l = 2$ . The LB94 [155] functional was employed to account for electronic exchange and correlation effects. An initial guess for the electronic density of the three amino acids was generated with the Amsterdam Density Functional (ADF) package [151, 152, 153] using a double  $\zeta$ -polarization plus (DZP) basis set in the case of glycine and a triple  $\zeta$ -polarization plus (TZP) [134] for the more complex amino acids phenylalanine and tryptophan. Since it is well known that the LB94 functional overestimates the molecular orbital eigenvalues, the first ionization potential of glycine was calculated using the outer-valence Green's function (OVGF) [202] method implemented in Gaussian09 [198], which can provide accurate values of the ionization potentials of the outer-valence shells. Then, the DFT/LB94 eigenvalues were shifted according to the energy difference between the first IP provided by the OVGF method

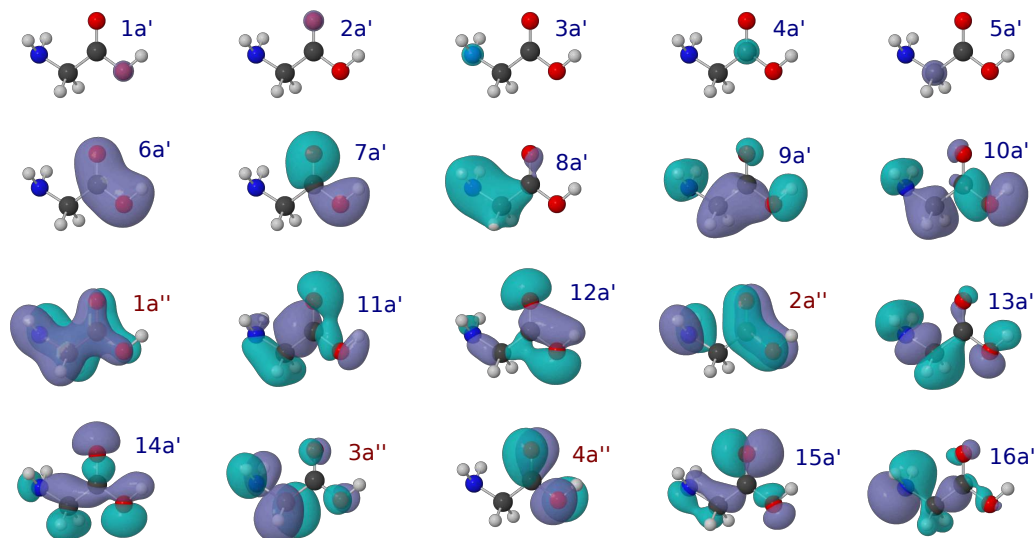


Figure 5.4: Occupied Kohn-Sham orbitals of neutral glycine. They have been calculated using the LB94 [155] functional in a basis set of B-spline functions, as explained in the text.

and the DFT/LB94 calculation. In order to obtain reliable values of the ionization energies of phenylalanine and tryptophan, we have employed the VWN [154] local density approximation functional within the Slater transition state procedure [203] using ADF with a TZP basis set. The molecular geometries were previously optimized at the DFT/B3LYP [196, 197] level in a 6311+g(3df,2p) basis set (6-31+g(d) in the case of tryptophan) using Gaussian09 [198], starting from the approximate optimized geometries reported in [199, 200, 201].

Figs. 5.4, 5.5 and 5.6 show the occupied Kohn-Sham orbitals of the ground state of glycine, phenylalanine and tryptophan, respectively, which were used to evaluate the corresponding wave functions according to equations 2.17 and 2.18. Glycine has planar symmetry and therefore belongs to the  $C_s$  point group and its orbitals have either  $a'$  or  $a''$  symmetry. As can be seen in fig. 5.4,  $a'$  orbitals are symmetric with respect to reflection through the mirror plane and  $a''$  orbitals are antisymmetric and thus contain a nodal plane. Phenylalanine and tryptophan belong to the  $C_1$  point group because they are not invariant under any symmetry transformation except for the identity operation and therefore all their orbitals have A symmetry.



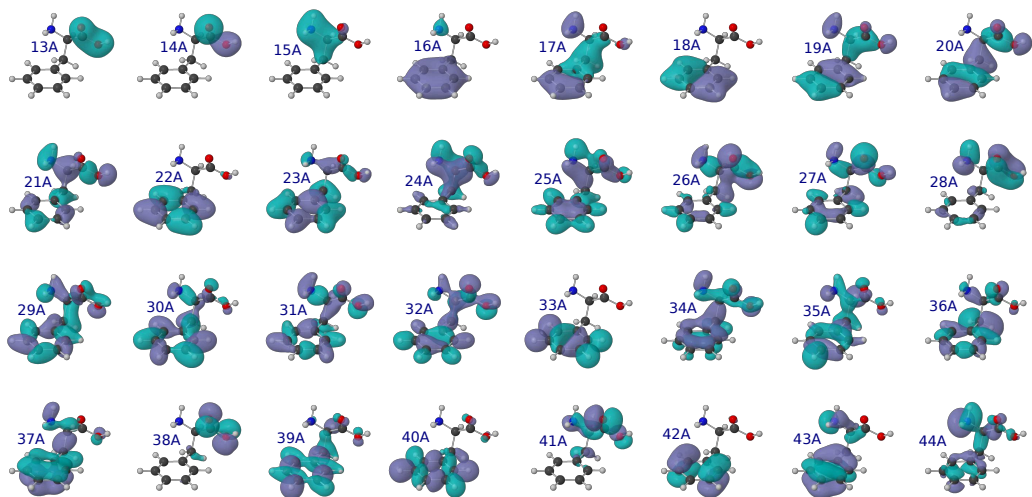


Figure 5.5: Same as fig. 5.4 for phenylalanine (core orbitals have been omitted).

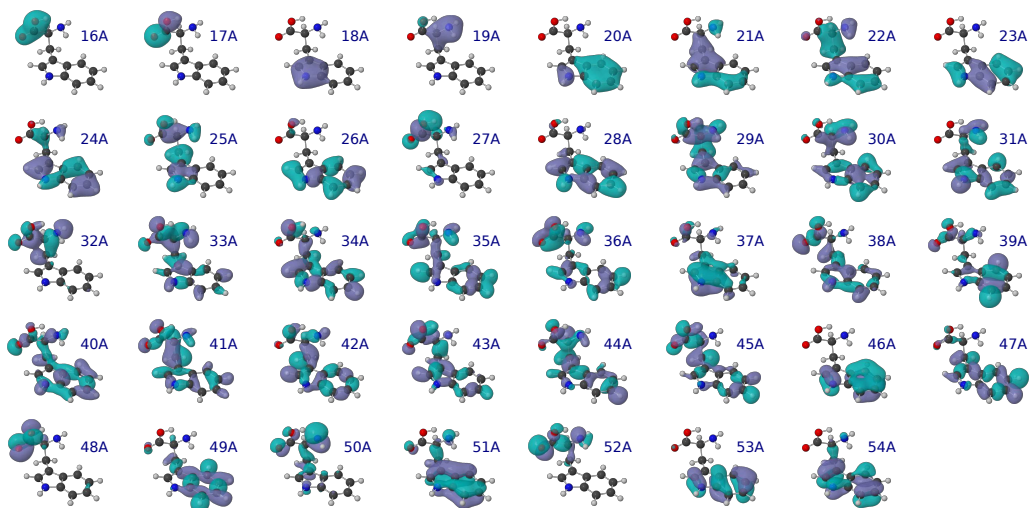


Figure 5.6: Same as fig. 5.4 for tryptophan (core orbitals have been omitted).

Neutral glycine, phenylalanine and tryptophan have 40, 88 and 108 electrons, respectively. Therefore, the corresponding electronic ground states constitute closed-shell systems that can be accurately described using 20, 44 and 54 molecular orbitals. Core orbitals are those constituted by the 1s orbitals of the “heavy” atoms (C, N and O). The energy required to remove an electron from a core orbital in these molecules ranges from around 290 eV in the case of C 1s to 400 eV for N 1s and 535 eV for O 1s. They are thus not accessible with usual attosecond pulses generated via HHG. Valence orbitals, with ionization potentials ranging from around 10 to 20 eV, are the easiest to ionize. They are highly delocalized, especially in phenylalanine and tryptophan since they contain an aromatic ring. Inner-valence orbitals present an intermediate situation, with ionization energies from around 20 to 35 eV. In order to describe the interaction with an XUV pulse, capable of ionizing from all valence and inner-valence shells, the corresponding ionization amplitudes need to be evaluated.

## 5.2 Photoionization cross sections

We have evaluated photoionization cross sections of glycine, phenylalanine and tryptophan from all valence and inner-valence shells in the framework of the fixed-nuclei approximation, as explained in section 1.3. The results are shown in figs. 5.7, 5.8 and 5.9 in the energy range accessible by the attosecond XUV pulse used in the experiment presented in fig. 5.1. The energy spectrum of the pulse is depicted in the figs. by a thick orange curve lying over a shaded area. As expected, the cross sections decay with the photon energy. In some ionic channels, we can see sharp structures near the threshold that can be understood in terms of shape resonances [185, 186, 187] due to the existence of small barriers in the complex molecular potentials. Unfortunately, the use of a single excitation approach prevents us from observing any possible signature coming from multiple (doubly, triply) excited electronic states of the molecule embedded in the ionization continuum.

From the figures, it is clear that the three molecules will be efficiently ionized from most valence and inner-valence shells upon interaction with the attosecond pulse. Only core electrons will remain unaffected. In fact, for any energy within

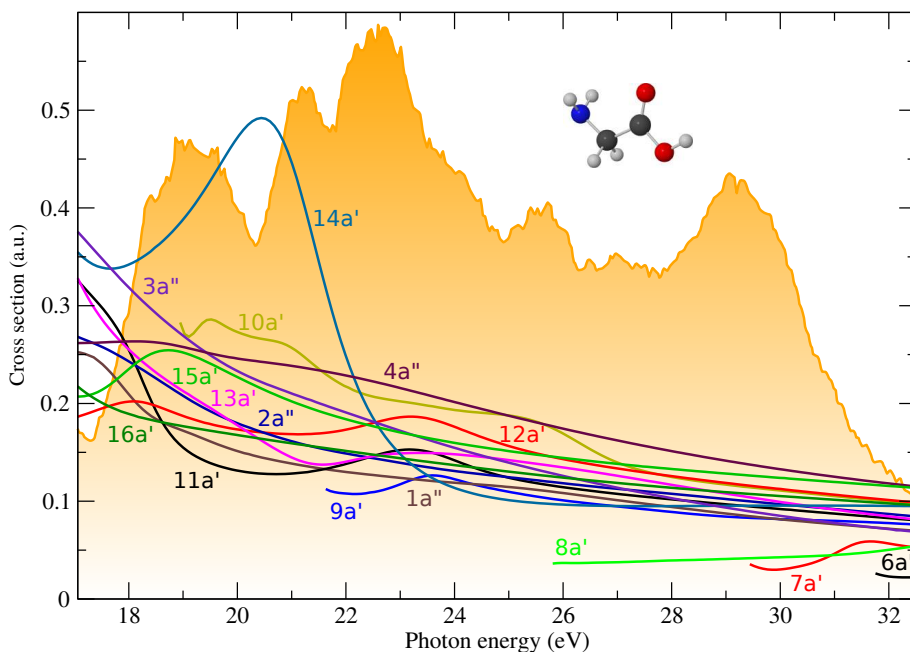


Figure 5.7: Photoionization cross sections of glycine from different molecular orbitals calculated using the static-exchange DFT method. Numbers and colors denote the molecular orbitals from where the electron is emitted in each case (fig. 5.4). The energy spectrum of the attosecond pulse employed in the experiment presented in fig. 5.1 is represented by a thick orange curve lying over a shaded area.

the bandwidth, we find similar contribution from different ionization thresholds. For instance, using (monochromatic) synchrotron radiation of 22 eV in phenylalanine, electrons would be ejected from orbitals 19A...44A and 33A would represent the largest contribution. This would lead to a very delocalized hole in the parent ion. However, monochromatic light would generate an incoherent superposition of ionic states and the hole would not migrate. Due to their broad energy bandwidths, attosecond pulses can generate coherent superpositions of electronic states, i.e., electronic wave packets, by emitting electrons with the same energy from different molecular orbitals and thus induce charge dynamics along the molecular skeleton. Note that this scenario differs from that considered in most previous works on charge migration [32, 93, 31, 94, 99, 96], where the initial hole is created in a given molecular orbital.

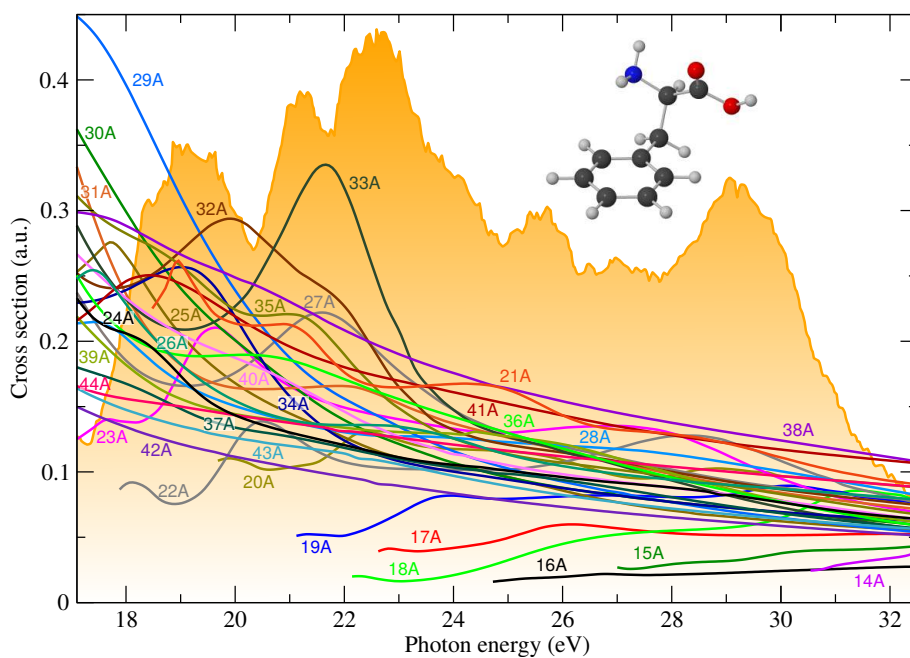


Figure 5.8: Same as fig. 5.7 for phenylalanine (orbitals are shown in fig. 5.5).

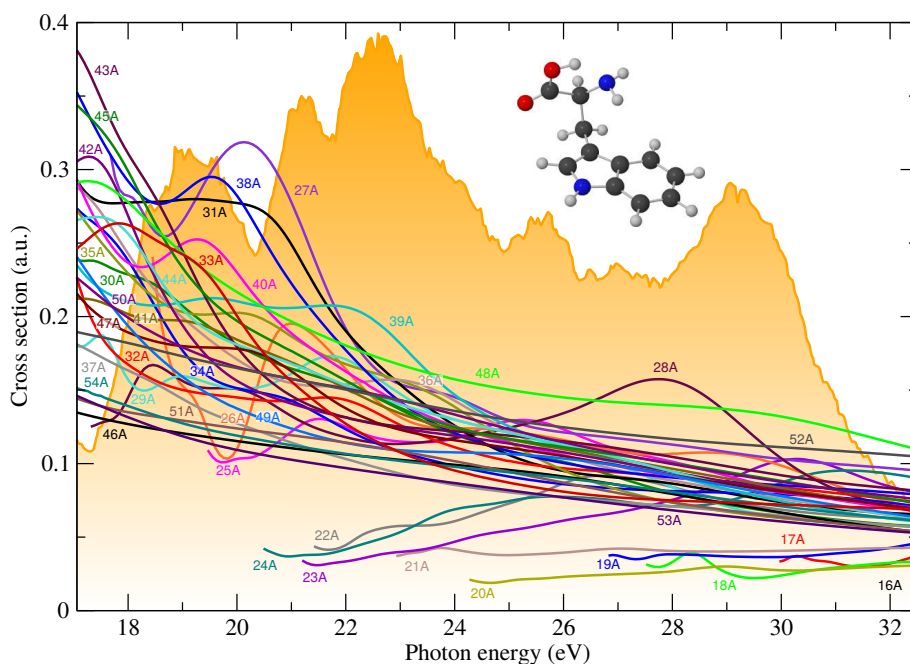


Figure 5.9: Same as fig. 5.7 for tryptophan (orbitals are shown in fig. 5.6).

### Comparison with experimental photoelectron spectra

In order to test the validity of our description of the ionization process, we have calculated the photoelectron spectra of phenylalanine for photon energies of 21.2 and 45 eV using the cross section values at those energies (shown in fig. 5.8) and the corresponding ionization potentials. Then, we have compared our results with synchrotron [204] and He(I) [205, 206] radiation spectra available in the literature. For the comparison with the experiments, we have convoluted our infinitely resolved lines with a Lorentzian function of 0.3-eV width at half maximum to account for the vibrational broadening and experimental energy resolution, which is rather limited in these and earlier experiments (the experiments cannot resolve the individual peaks). The comparison between theory and experiment is shown in fig. 5.10. As can be seen, the agreement is reasonably good. We no-

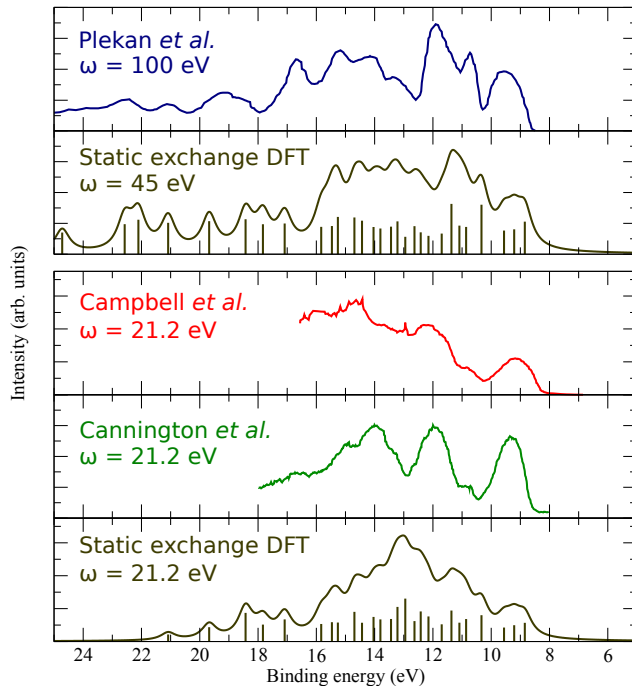


Figure 5.10: Comparison between the calculated photoelectron spectra of phenylalanine at 45 eV and 21.2 eV and the experimental spectra reported by Plekan *et al.* [204] at 100 eV and Campbell *et al.* [205] and Cannington *et al.* [206] at 21.2 eV

tice however that the experiment of Plekan *et al.* [204] was performed at a photon energy of 100 eV, which is substantially higher than ours. The other two earlier experiments [205, 206] were performed at a photon energy of 21.2 eV. Our results are in better agreement with the most recent experiment, especially for binding energies below 15 eV. This energy range includes the states that play an important role in the ultrafast charge dynamics initiated in the molecule by the attosecond pulse considered in this work (represented in fig. 5.8), as we show in section 5.3. The photoelectron spectrum is expected to be more sensitive to the choice of photon energy as we approach the threshold. The reason is that the ionization amplitudes can strongly vary with photon energy for values below 25 – 30 eV, while the variation becomes smoother for larger values, as can be seen in fig. 5.8. This is most likely the reason we find a better agreement between the high-energy spectra.

### 5.3 Ultrafast electron dynamics initiated by attosecond pulses

The first theoretical predictions of the possibility of observing ultrafast charge migration upon prompt ionization of an organic molecule can be attributed to Lorenz S. Cederbaum and collaborators [32]. In that work, an electronic wave packet is generated by sudden electron removal from a Hartree Fock (HF) molecular orbital of the difluoropropadienone molecule. Then, the hole generated in the electronic structure moves through the molecular skeleton because the prepared state is not a stationary state of the ionic Hamiltonian but a linear combination of several. Over the years, they have investigated charge migration in a large number of organic molecules (see, for instance [32, 93, 94, 96]). Here we consider a different scenario: (i) we are using an ultrashort pulse with a broad energy bandwidth to create an electronic wave packet in the parent ion, and (ii) we compute the scattering states to obtain the actual photoionization amplitudes.

In order to verify the validity of our time-propagation method, we have compared our results with those obtained by Kuleff, Breidbach and Cederbaum for the case of glycine [93]. To perform a meaningful comparison, we have started from the same initial wave function as in [93]. The corresponding HF orbitals ha-

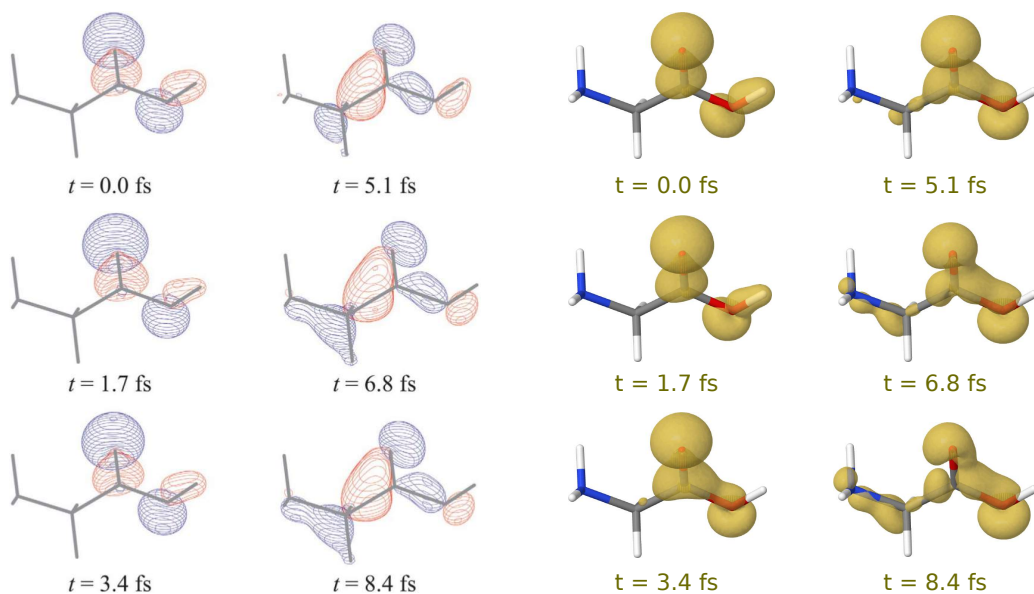


Figure 5.11: Time evolution of the hole generated in glycine upon sudden ionization from the  $11a'$  HF orbital. Left figure: natural charge orbitals calculated by A. Kuleff *et al.* [93] (the square of the natural orbitals provides the hole density). Reprinted with permission from [93]. Copyright 2005, AIP Publishing LLC. Right figure: hole density, evaluated using the present approach.

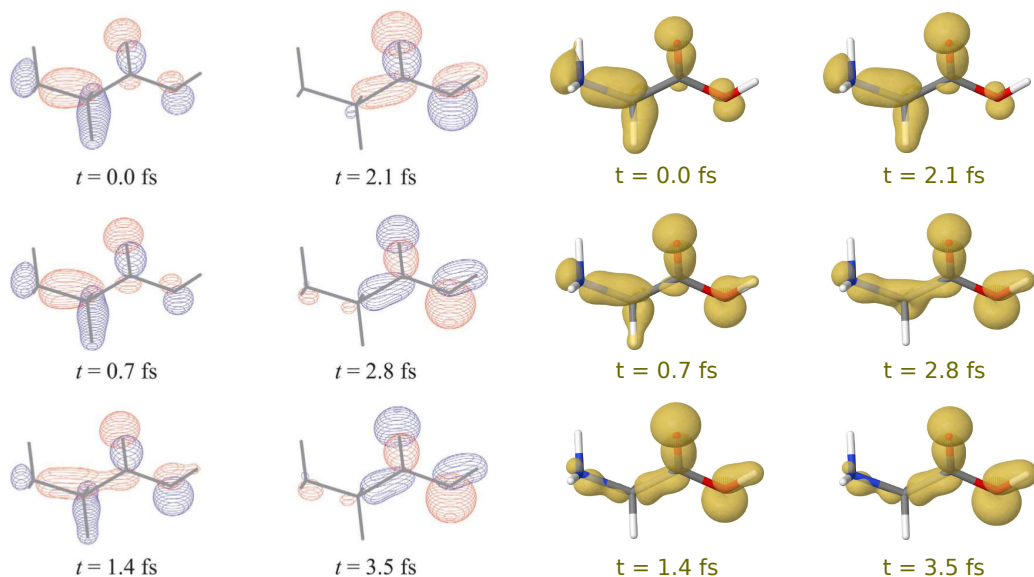


Figure 5.12: Same as fig. 5.11 for the case of sudden ionization from the  $14a'$  HF orbital of glycine. Left figure reprinted with permission from [93]. Copyright 2005, AIP Publishing LLC.

ve been evaluated using Gaussian 09 [198] with a DZP basis set. Then, to study the time evolution of the hole density, we have projected the initial state onto the Slater determinants built from the KS orbitals (shown in fig. 5.4) that we use to represent ionic stationary states. The projection leads to a coherent superposition of ionic states that is let evolve freely as dictated by the relative phases resulting from the corresponding energy differences. The evolution of the hole dynamics is shown in figs. 5.11 and 5.12 for the cases of sudden ionization from the 11a' and the 14a' HF orbitals, respectively. As can be seen, the agreement between our results and those previously reported [93] is quite satisfactory. In the latter reference, two-holes-one-particle (2h1p) configurations were explicitly included in the time propagation, so a direct comparison with their results provides an answer about the role played by those configurations, which are not included in our time propagation scheme. If we considered sudden ionization from the inner-valence HF orbitals of glycine instead, as in [94], the agreement would not be so spectacular because in that case 2h1p configurations play a role. However, these are not expected to be important in the dynamics studied here. The main reason is that a transition from the ground state to doubly-excited (shake-up) state is a two-electron process and therefore is less likely to occur via 1 photon absorption than a direct transition to a one-hole (1h) state.

In the following, we present our results on the time-evolution of the hole generated in the electronic structure of the amino acids glycine, phenylalanine and tryptophan upon interaction with an attosecond XUV pulse similar to that used in the experiment illustrated in fig. 5.1. As discussed in the previous section, attosecond pulses do not remove electrons from only one molecular orbital but from several of them, generating coherent superpositions of ionic states. Ionization amplitudes have been evaluated for all open channels (15 for glycine, 32 for phenylalanine and 39 for tryptophan) using the static-exchange DFT method [139, 140, 141, 142, 143] (see section 2.2.2), which has been thoroughly tested in systems of similar complexity, and time-dependent first-order perturbation theory (see section 1.2). From the ionization amplitudes, we have evaluated the reduced density matrices of the ionic subsystems using eq. 3.14. Then, the hole densities were calculated as the difference between the electronic densities of the neutral molecules, which do not depend on time, and the electronic densities of the



ions (eq. 3.16). Because in the experiments the molecules are not aligned, we performed calculations considering three orthogonal orientations with respect to the polarization vector of the attosecond pulse. The results were then averaged assuming randomly oriented molecules.

Figs. 5.13, 5.14 and 5.15 display snapshots of the relative variation of the hole density with respect to the time-averaged values for glycine, phenylalanine and tryptophan, respectively. In spite of the very delocalized nature of the hole densities resulting from the broadband XUV excitations, substantial redistributions take place on a sub-femtosecond scale. These charge dynamics cannot be associated with simple migrations between two sites of the molecules, as found in most previous theoretical work [32, 93, 31, 94, 96]. However, despite the complexity of the charge configuration calculated in a realistic (i.e., experimentally accessible) situation, the concept of charge migration is still valid.

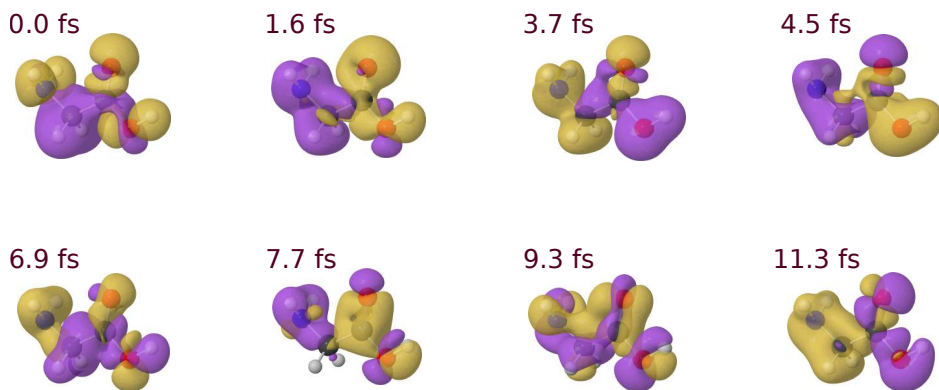


Figure 5.13: Relative variation of the hole density on glycine with respect to its time-averaged value as a function of time. Isosurfaces of the relative hole density are shown for cutoff values of  $10^{-4}$  a.u. (yellow) and  $-10^{-4}$  a.u. (purple). Time is with reference to the end of the XUV pulse (first snapshot).

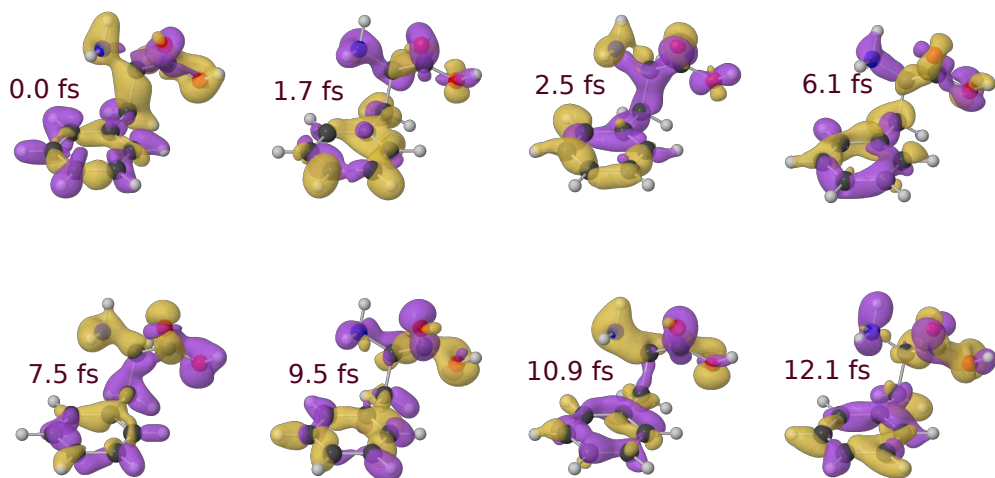


Figure 5.14: Same as fig 5.13 for phenylalanine.

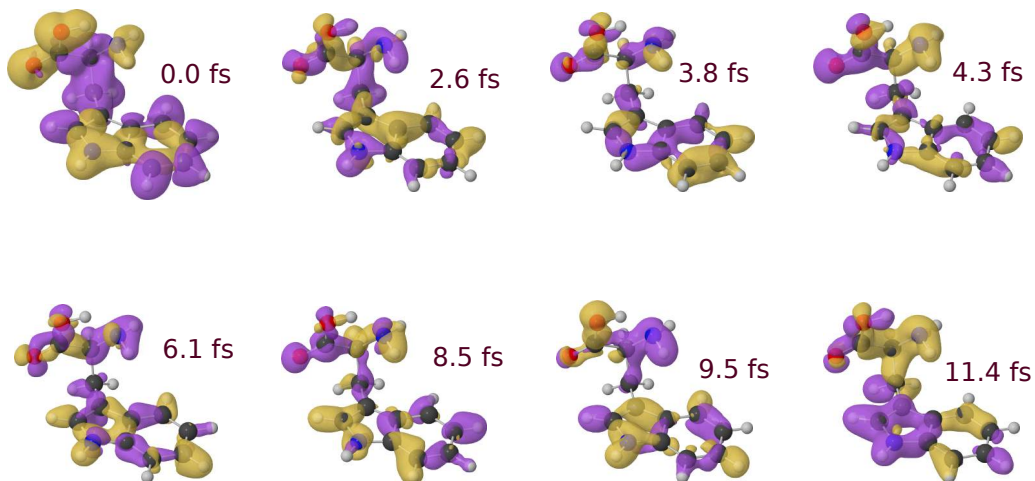


Figure 5.15: Same as fig 5.13 for tryptophan.

### 5.3.1 Fourier analysis on the amino group

In order to perform a more quantitative analysis of the charge dynamics, we have integrated the hole density around different portions of the molecule. Here we present our results on the amino group. In the case of phenylalanine, these results can be compared with the fragmentation yield of double-charged immonium presented in fig. 5.1 since, as already discussed, this signal is sensitive to hole localization on the amino group. A full analysis including different atomic centers is presented in section 5.3.2. Figs. 5.16, 5.17 and 5.18 show the Fourier power spectra of the hole density on the amino group of glycine, phenylalanine and tryptophan, respectively, for three orthogonal orientations of the molecules with respect to the polarization vector of the field (indicated in the figures) and for the case of randomly oriented molecules. The peaks appearing in the Fourier spectra provide information about the frequency and the intensity of the charge fluctuations observed in figs. 5.13, 5.14 and 5.15. As expected, the complexity of the spectra increases with the number electrons in the molecule as so does the number of 1h states are accessible by the pulse.

To better understand the observed dynamics, we have identified the ionic states that are responsible for the most important beatings (indicated in figs. 5.16, 5.17 and 5.18). Each beating frequency is given by the energy difference between the pair of states that originate it. The main interferences involve states with holes in orbitals that are delocalized between the amino group and another common part of the molecule, which allows charge migration between the two sites. Also, we can see that the dominant beatings involve states which are close in energy. In fact, the greater the energy spacing between two ionic states, the weaker the interference between them is expected to be. This can be easily understood in terms of the coherences between the ionic states populated by the attosecond pulse, which are given by the off-diagonal terms of reduced density matrix (see eq. 3.14). If the energy spacing  $\Delta E_{\alpha\alpha'} = |E_{\alpha} - E_{\alpha'}|$  between two ionic states  $\alpha$  and  $\alpha'$  is large, then the kinetic energy ranges in which the photoelectron is emitted when the two states are populated are very different and therefore the corresponding element in the reduced density matrix  $\gamma_{\alpha\alpha'}$  is small. If  $\Delta E_{\alpha\alpha'}$  were greater than the energy bandwidth of the pulse (and the two ionic states were accessible), they would be populated incoherently because the photoelectron

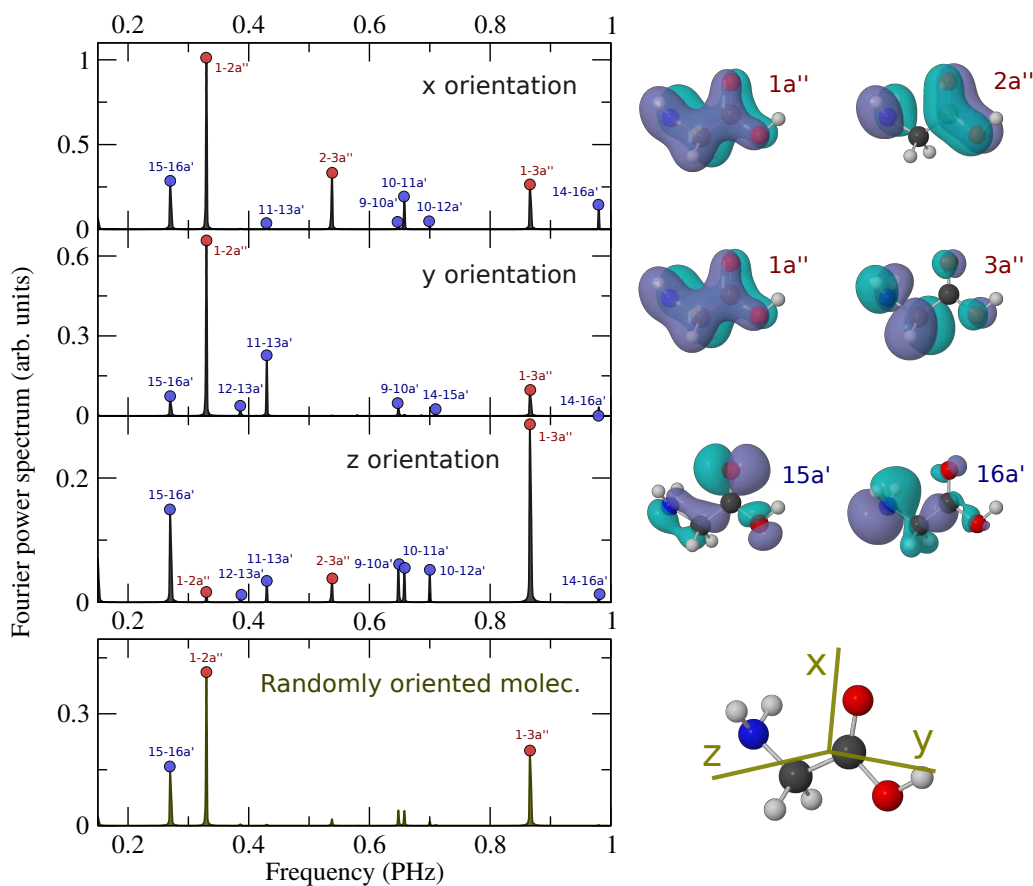


Figure 5.16: Fourier power spectra of the hole density integrated over the amino group of glycine. Results are shown for three orthogonal orientations of the molecule with respect to the polarization vector of the electric field associated to the attosecond XUV pulse and for the case of randomly oriented molecules. In order to obtain well resolved peaks in frequency, the hole density has been evaluated up to 500 fs. The states that give rise to the dominant peaks are indicated in the spectra by labels that denote the molecular orbitals where the holes have been created (molecular orbitals are shown in fig. 5.4).

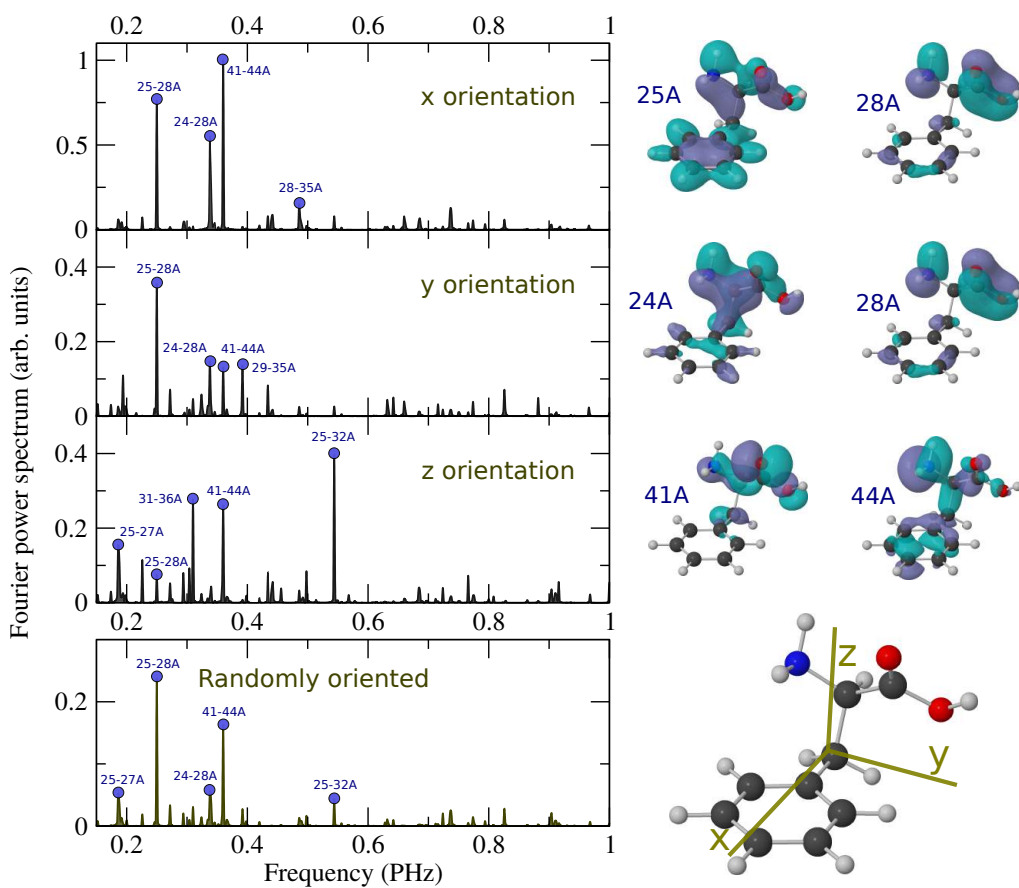


Figure 5.17: Same as fig. 5.16 for phenylalanine (molecular orbitals are shown in fig. 5.5).

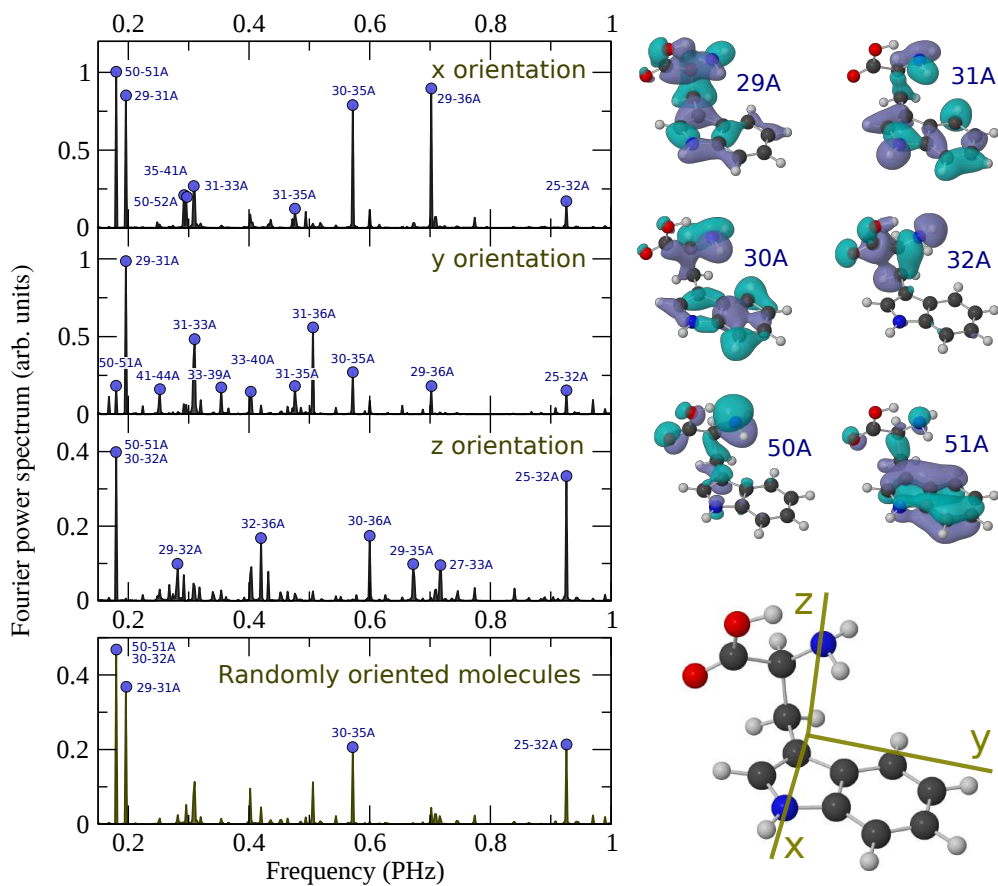


Figure 5.18: Same as fig. 5.16 for tryptophan (molecular orbitals are shown in fig. 5.6).

kinetic energy ranges would not overlap at all and therefore  $\gamma_{\alpha\alpha'}$  would be zero. Because of the large energy bandwidth of the attosecond pulse considered here, all 1h states are populated coherently, but coherences between states with similar energy are, in general, higher.

In the spectrum of glycine (fig. 5.16), we can only see interferences between states having the same symmetry because states with different symmetry are populated incoherently. The reason is that, for a given orientation of the field, electrons emitted from two orbitals ( $\alpha$ ,  $\alpha'$ ) with different symmetry have, in general, different symmetry and therefore the corresponding coherence term ( $\gamma_{\alpha\alpha'}$ ) is zero (see eq. 3.14). In the case of phenylalanine and tryptophan (figs. 5.17 and 5.18), although there are no strict selection rules due the lack of global symmetry elements, approximate selection rules will apply. For instance, one of the most intense beatings in the amino group of phenylalanine occurs between the states with holes in the 41A and the 44A orbitals, both having nodal planes that contain the C–N and the C=O bonds with very similar orientations.

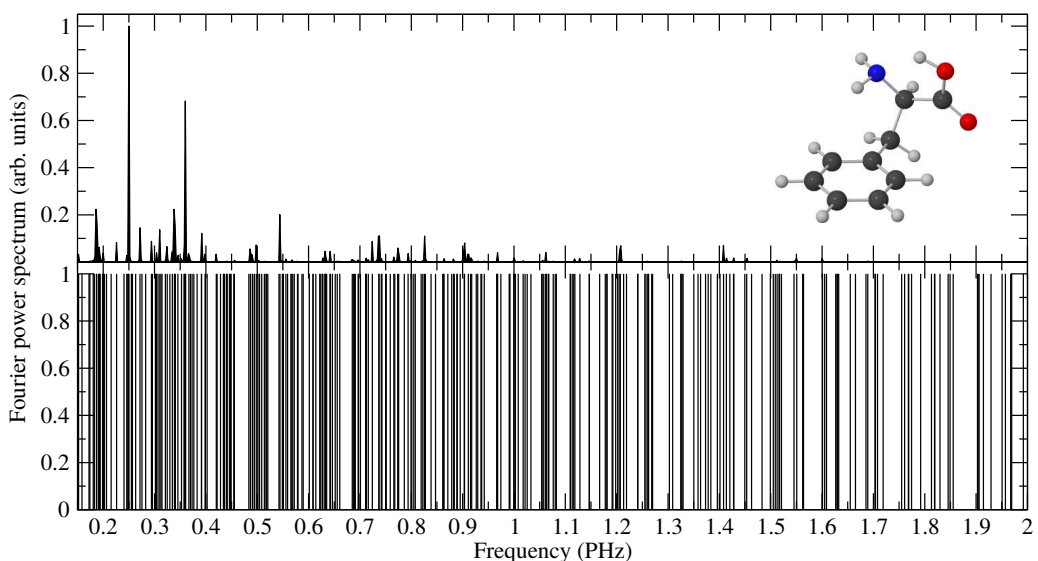


Figure 5.19: Fourier power spectra of the calculated hole density integrated over the amino group of phenylalanine. Upper panel: results from the actual calculation (as in the lower panel of fig. 5.17). Lower panel: results obtained by using an equal weight for all ionic states accessible by the XUV pulse.

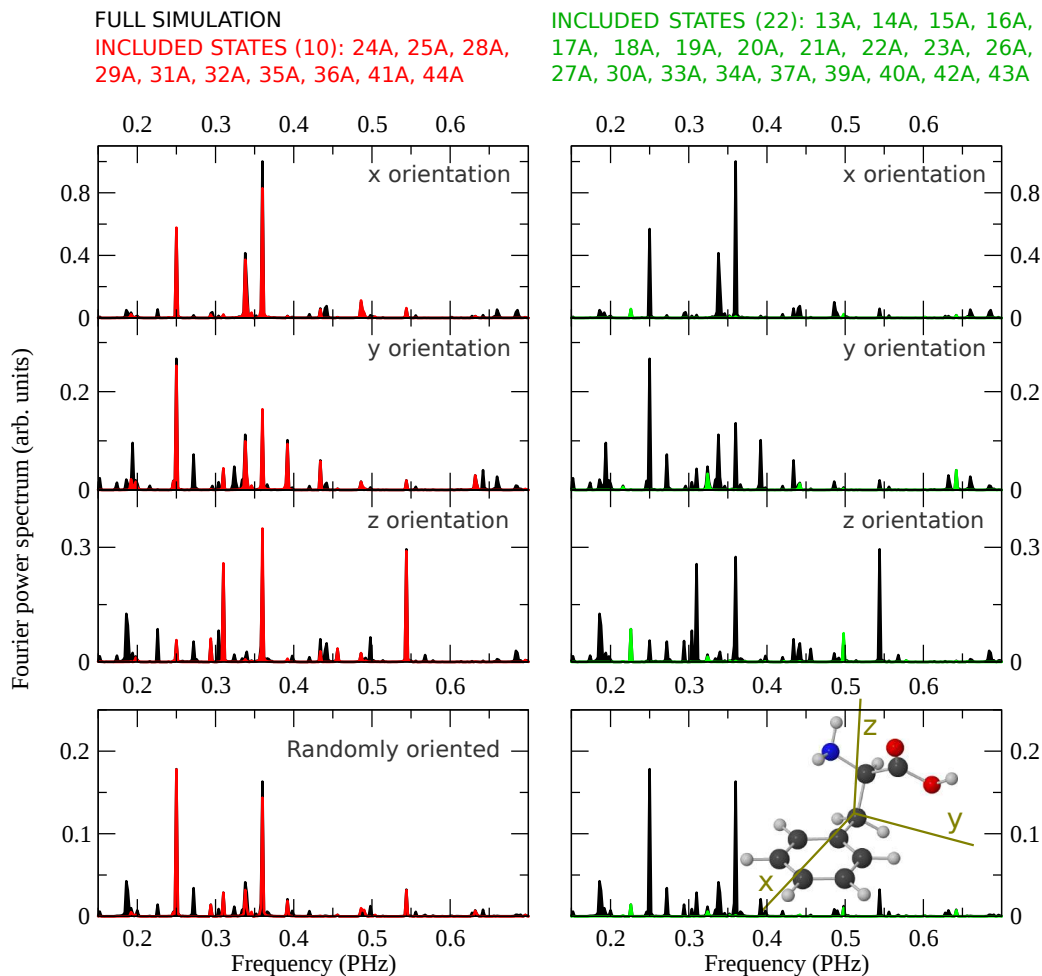


Figure 5.20: Fourier power spectra of the hole density integrated over the amino group of phenylalanine: results from the full calculation (black lines in all panels), from a calculation in which only the ionic states resulting from removing an electron from the 24A, 25A, 28A, 29A, 31A, 32A, 35A, 36A, 41A, and 44A orbitals are included (red lines on top of the black lines, left panels), and from a calculation in which all ionic states but the above mentioned ones are included (green curves on top of the black lines, right panels).

It is clear from the Fourier analysis presented here that the hole density not only provides information about energy spacings between different quantum states responsible of the electronic beatings, but also probes the specific dynamics generated by the attosecond pulse. This is further illustrated in fig. 5.19 for the



case of phenylalanine, in which the calculated Fourier spectrum is compared with a similar one containing all possible energy spacings with an equal weight. The dynamics of the electronic wave packet generation by the attosecond pulse is responsible for the fact that only a few beatings are observed. These depend on the dipole matrix elements (i.e., the ionizing transition induced by the XUV attosecond pulse) and the interference between the different amplitudes, which are imprinted in the time evolution of the hole density.

To illustrate that the observed dynamics in the amino group can almost be entirely explained in terms of some of the ionic states that are populated by the attosecond XUV pulse, we have carried out calculations for phenylalanine in which only ionic states resulting from removing an electron from the 24A, 25A, 28A, 29A, 31A, 32A, 35A, 36A, 41A, and 44A orbitals are included in the free propagation of the electronic wave packet. Conversely, we have also performed calculations in which all 1h states but the above mentioned are included. The results of these two calculations are shown and compared with the full calculations in fig. 5.20. As can be seen, the full spectrum is almost entirely reproduced by only including the above ten states. In contrast, the dynamics resulting from excluding these states is almost inexistent.

### 5.3.2 Fourier analysis on different atoms

Charge fluctuations on the amino group are most likely to be responsible for the observed beatings in the experimental results shown in 5.1. In order to perform a complete analysis of the charge modulations on different sites of the molecule, we have performed a Fourier analysis also on different atoms of the three amino acids. Figs. 5.21, 5.22 and 5.23 show the Fourier power spectra of the hole density integrated over various atoms of the three molecules. As expected, charge fluctuations occur with different frequencies on different atoms because they are due to interferences between different pairs of states. Indeed, it is a requirement for a beating to be observed on a specific site (atom) of the molecule that the two states involved contain a significant part of their hole localized on that particular site.

In the case of phenylalanine, beating frequencies in agreement with the experimental observations were observed when the charge density was integrated

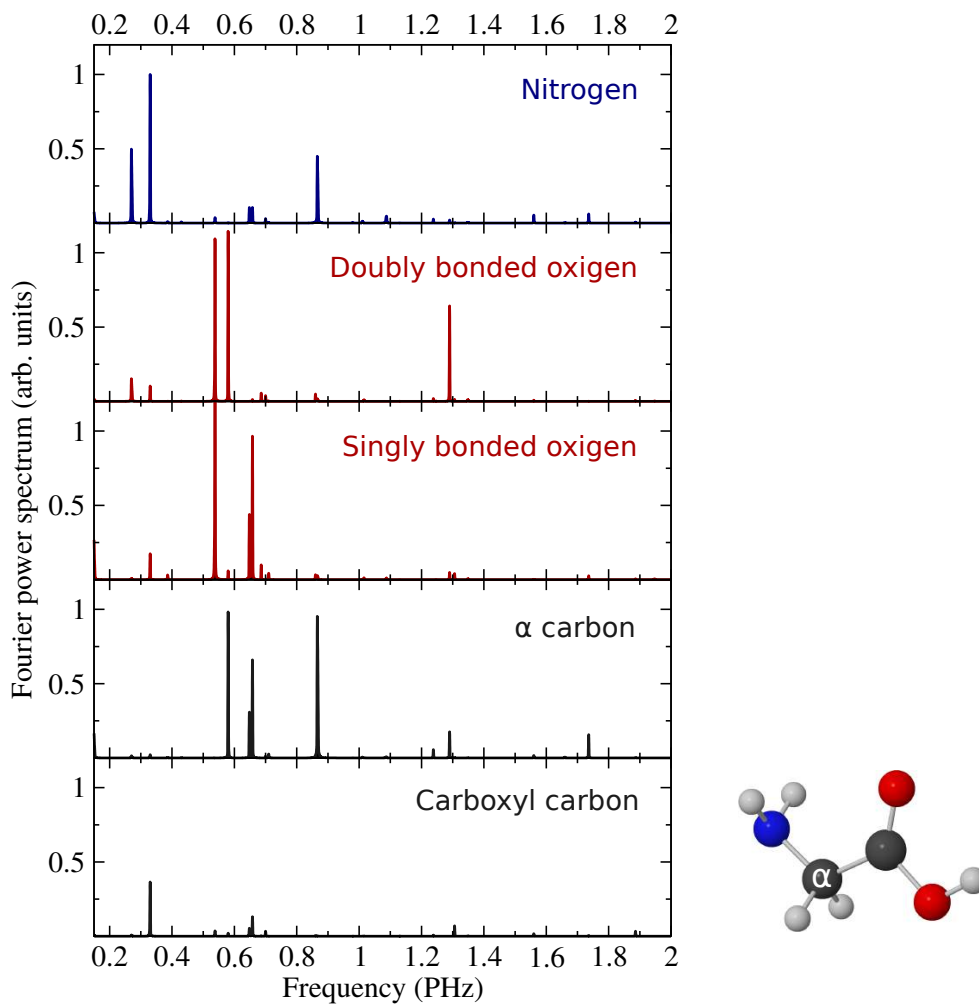


Figure 5.21: Fourier power spectra of the calculated hole density integrated over various atoms of glycine for the case of randomly oriented molecules. In order to obtain well resolved peaks in frequency, the hole density has been evaluated up to 500 fs.

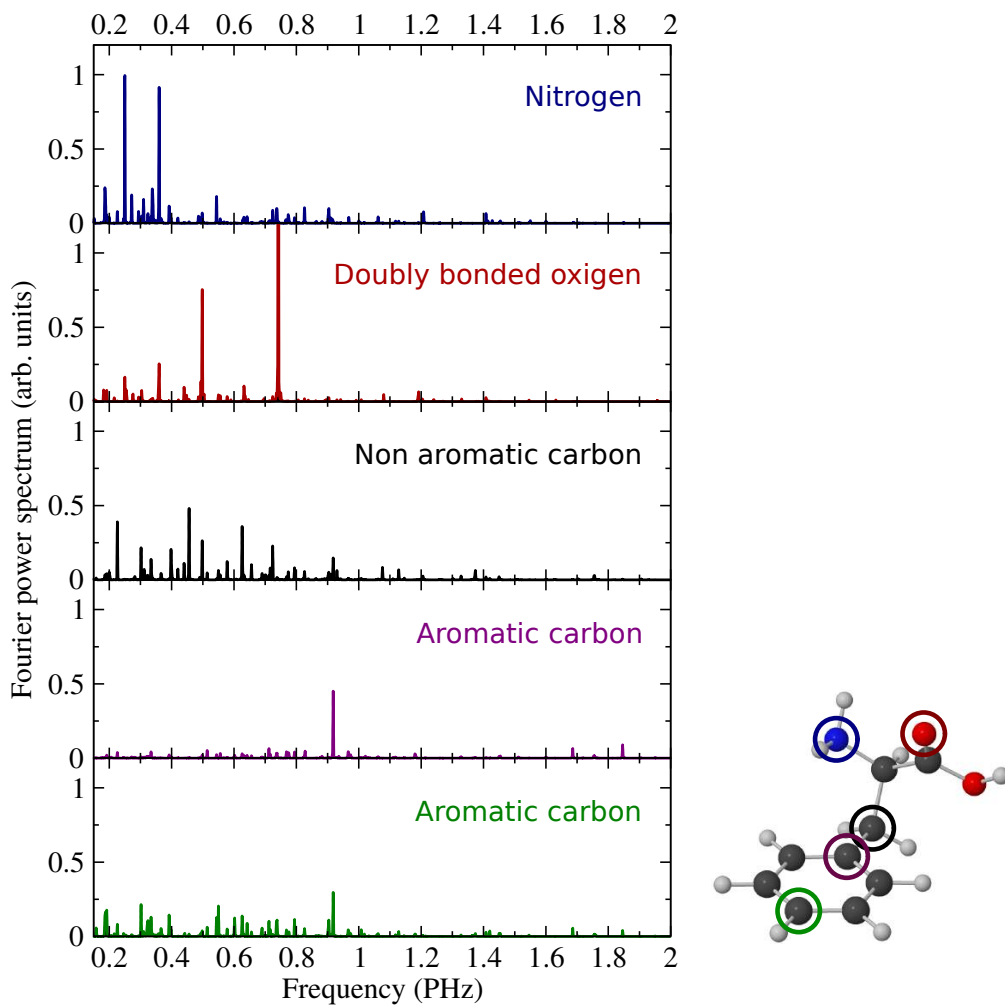


Figure 5.22: Same as 5.21 for phenylalanine.

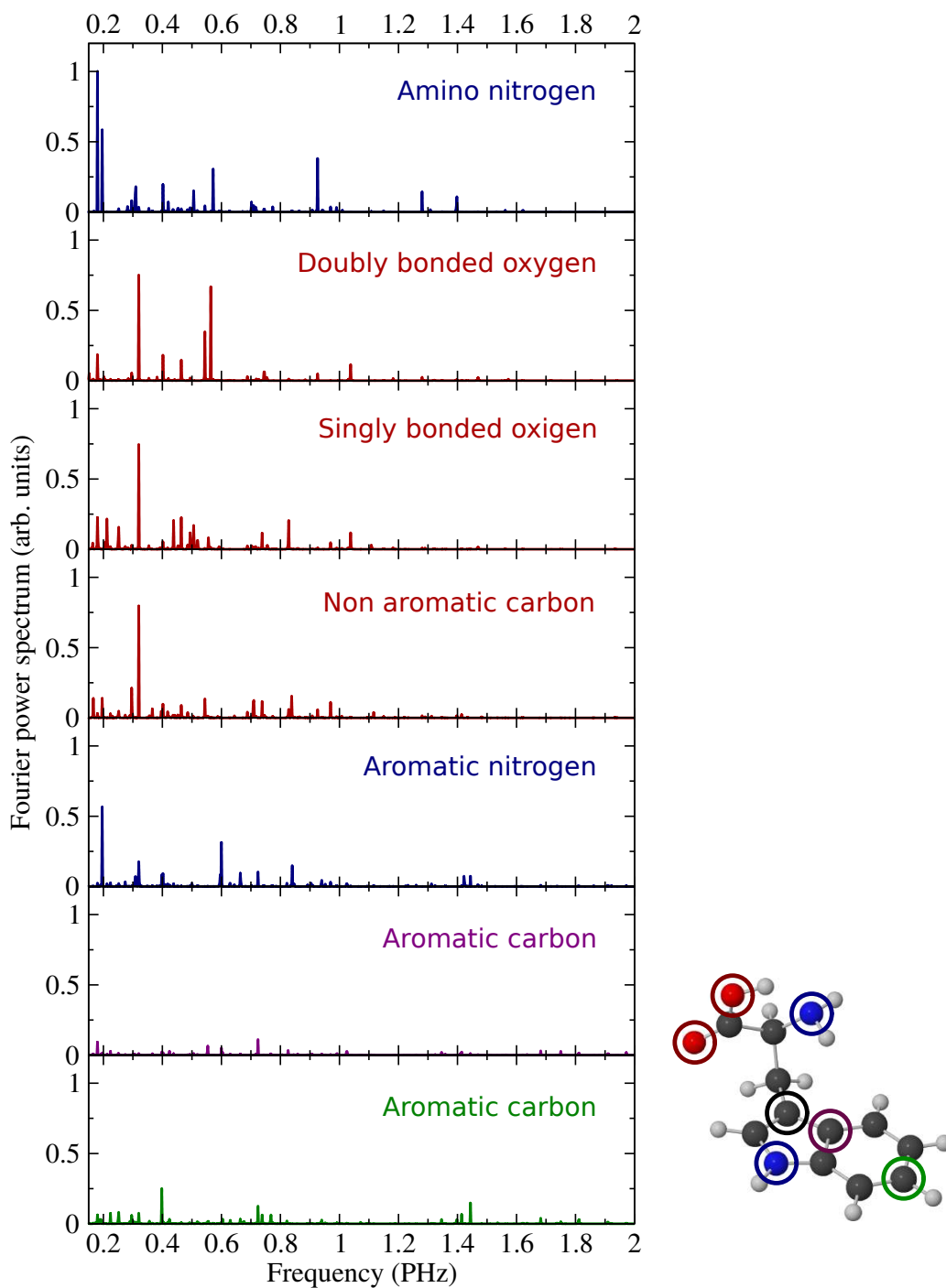


Figure 5.23: Same as 5.21 for tryptophan.

around the nitrogen atom in amino group. The hole densities at different positions do not show clear and clean frequency components, with the exception of the doubly bonded O atom in the carboxyl group. We note that the VIS/NIR probe pulse is not locally absorbed only by the amino group, but also by other sites of the molecule. However, the simulations indicate that the periodic modulations observed in the experiment are mainly related to the absorption of the probe pulse by the amino group.

### 5.3.3 Comparison with the experiment: Gabor profiles

The hole density on the amino group has been analyzed by using a sliding-window Fourier transform which, at the expense of frequency resolution, shows frequency and time information on the same plot. The same procedure has been applied to the fragmentation yield of doubly-charged immonium presented in fig. 5.1. Fig. 5.24 shows the resulting spectrograms in a temporal window up to 45 fs. The theoretical spectrogram presents a dominant peak around 0.25 PHz, which forms in about 15 fs and vanishes after about 35 fs, in close agreement with the results of the Fourier analysis of the experimental data. A higher frequency component is visible around 0.36 PHz in the delay intervals below 15 fs and above 30 fs. At short delays, this component favorably compares with the experimental observation of the frequency peak around 0.30 PHz in the same window of pump-probe delays. The good agreement between theory and experiment strongly supports the interpretation of the measured data in terms of charge migration. The temporal evolution of the main Fourier components is a consequence of the complex interplay among several beating processes initiated by the broadband excitation pulse. Despite the agreement with the experimental results, we cannot exclude that the nuclear dynamics, which are not included in the simulations, also play a role in the temporal evolution of the measured oscillation frequencies.

The good agreement between theory and experiment is rather remarkable in light of the fact that simulations do not take into account the interaction of the VIS/NIR probe pulse. The fact that the effects of the probe pulse are not included in the simulations can explain why the calculated intensities of the different beatings differ from the experimental ones. We note that the beating frequencies

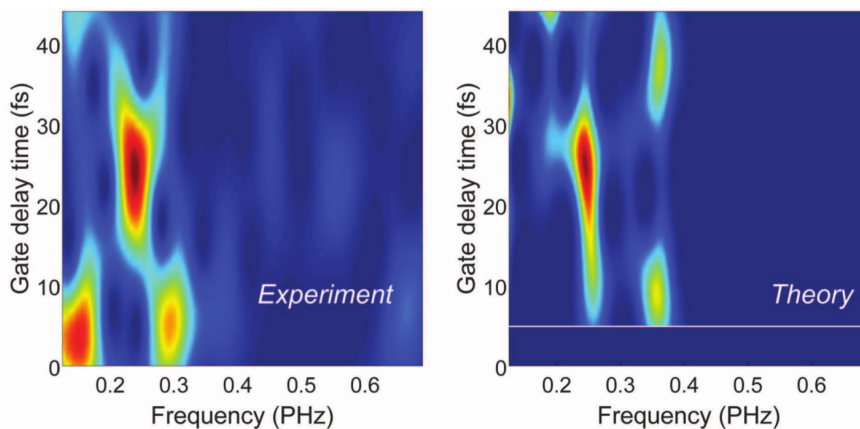


Figure 5.24: Fourier analysis of charge dynamics. Spectrograms calculated for the measured data of 5.1 (left panel) and for the calculated hole density integrated over the amino group of phenylalanine (right panel), shown in fig 5.14. The sliding window Fourier transforms have been calculated by using a Gaussian window function  $g(t - t_d) = e^{-(t-t_d)^2/t_0^2}$ , with  $t_0 = 10$  fs and peak at  $t_d$  (gate delay time). The theoretical spectrogram (right panel) was calculated considering an experimental temporal resolution of 3 fs.

have been observed experimentally even though the initial hole density is highly delocalized. An important result of the simulations is that the measured beating frequencies originate from charge dynamics around the amino group. This leads to the conclusion that the periodic modulations measured in the experiment are mainly related to the absorption of the probe pulse by the amino group. The mechanism that makes the probe pulse sensitive specifically to the charge density on this group is still not well understood. Moreover, we observe that, in spite of the large number of potential frequency beatings associated to the wave packet motion induced by the attosecond pulse, only a few ones manifest in the experiment, thus reducing the impact of the modulations introduced by the probe pulse in the analysis of the wave packet motion. These results can be seen as the first experimental confirmation that attosecond pulses and techniques are essential tools for understanding of dynamical processes on a temporal scale that is relevant for the evolution of crucial microscopic events at the heart of the macroscopic biological response of molecular complexes.

### 5.3.4 What about molecular conformation?

It is well known that amino acids exist in many conformations as a result of their structural flexibility. Typically, the energy barrier to interconversion between different conformers is small, of the order of a few kcal/mol, so that, even at room temperature, thermal energy is sufficient to induce conformational changes. Theoretical investigations have shown that such changes can affect the charge migration process [94]. In the case of phenylalanine, 37 conformers have been found by ab initio calculations [200], with a conformational distribution that depends on the temperature. However, in the experiment presented in fig. 5.1, performed at an average temperature of about 430 K, only six conformers are substantially present [200]. Figs. 5.25, 5.26 and 5.27 show the most stable conformations of glycine, phenylalanine and tryptophan at 430K. The relative populations of the conformers of phenylalanine have been calculated using statistical mechanics methods based on DFT/B3LYP quantum chemistry calculations of the geometries, energies, vibrational frequencies and rotational constants [200]. In the case of glycine [199, 207] and tryptophan [201], the relative populations were estimated assuming Boltzman distributions.

The ultrafast temporal evolution of the wave packet generated by the attosecond pump pulse has also been calculated for the most stable conformers of the three amino acids. The corresponding Fourier power spectra are shown in figs. 5.25, 5.26 and 5.27, together with the results for the thermal average obtained by taking into account the estimated populations (given in figs. 5.25, 5.26 and 5.27). We have found that, although the precise frequencies of the relevant peaks in the calculated Fourier spectra depend on the particular conformer, the spectrum of the most abundant conformer is very similar to that of the thermal average. In the case of the most populated conformers of phenylalanine (and therefore for the averaged results), the frequencies at which the dominant peaks appear are in good agreement with those observed experimentally.

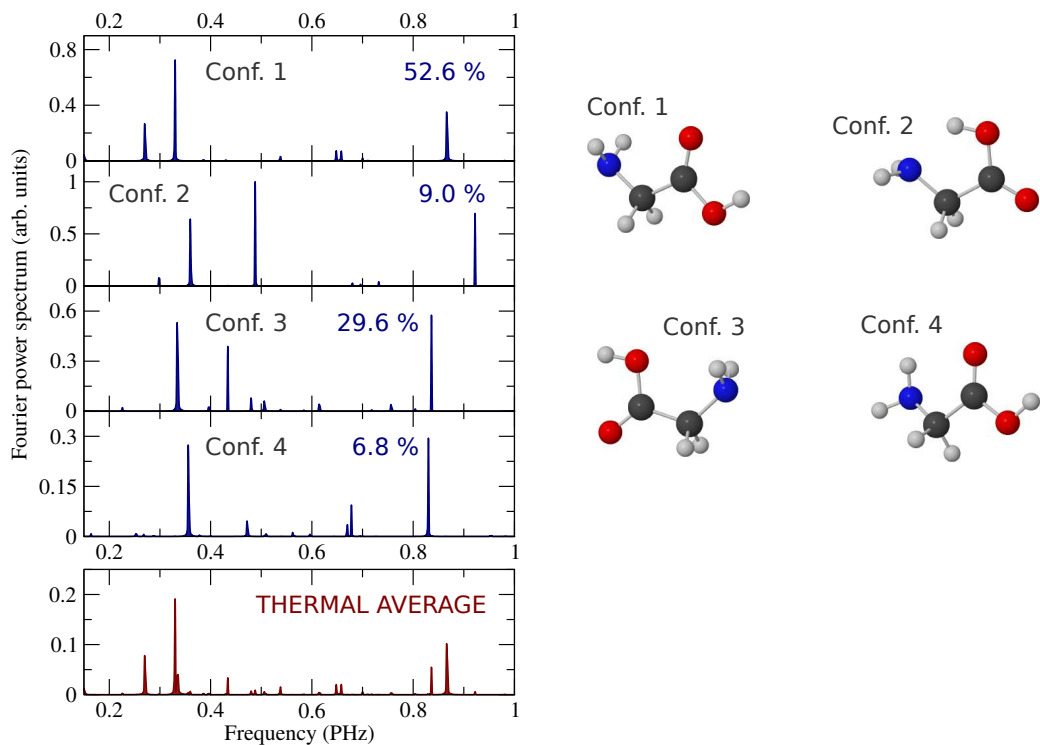


Figure 5.25: Fourier power spectra of the hole density on the amino group of the most abundant conformers of glycine at 430 K. The relative populations have been calculated assuming a Boltzman distribution. The lower panel shows the averaged results and the corresponding geometries are shown in the right.



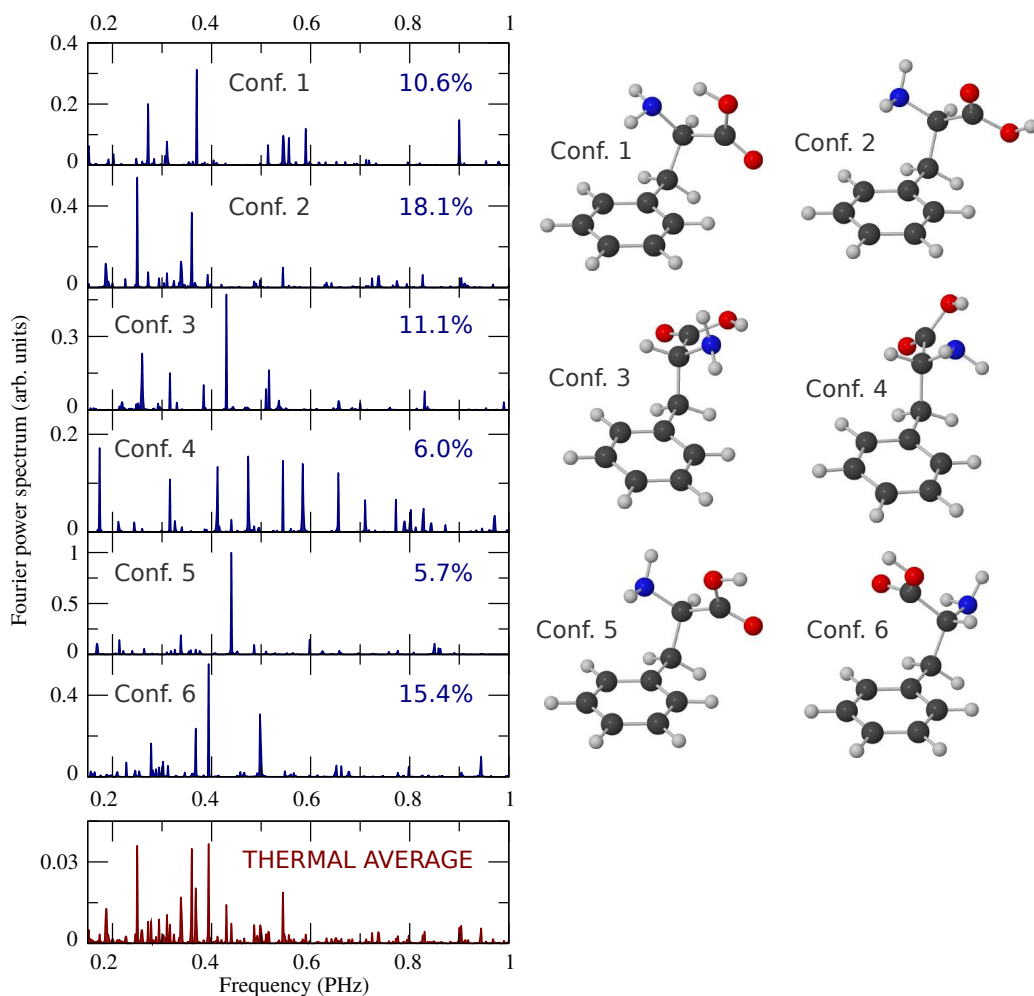


Figure 5.26: Same as fig. 5.25 for the most stable conformers of phenylalanine, rescaled with their relative weights for a better illustration. Their relative populations according to Huang *et al.* [200] are indicated.

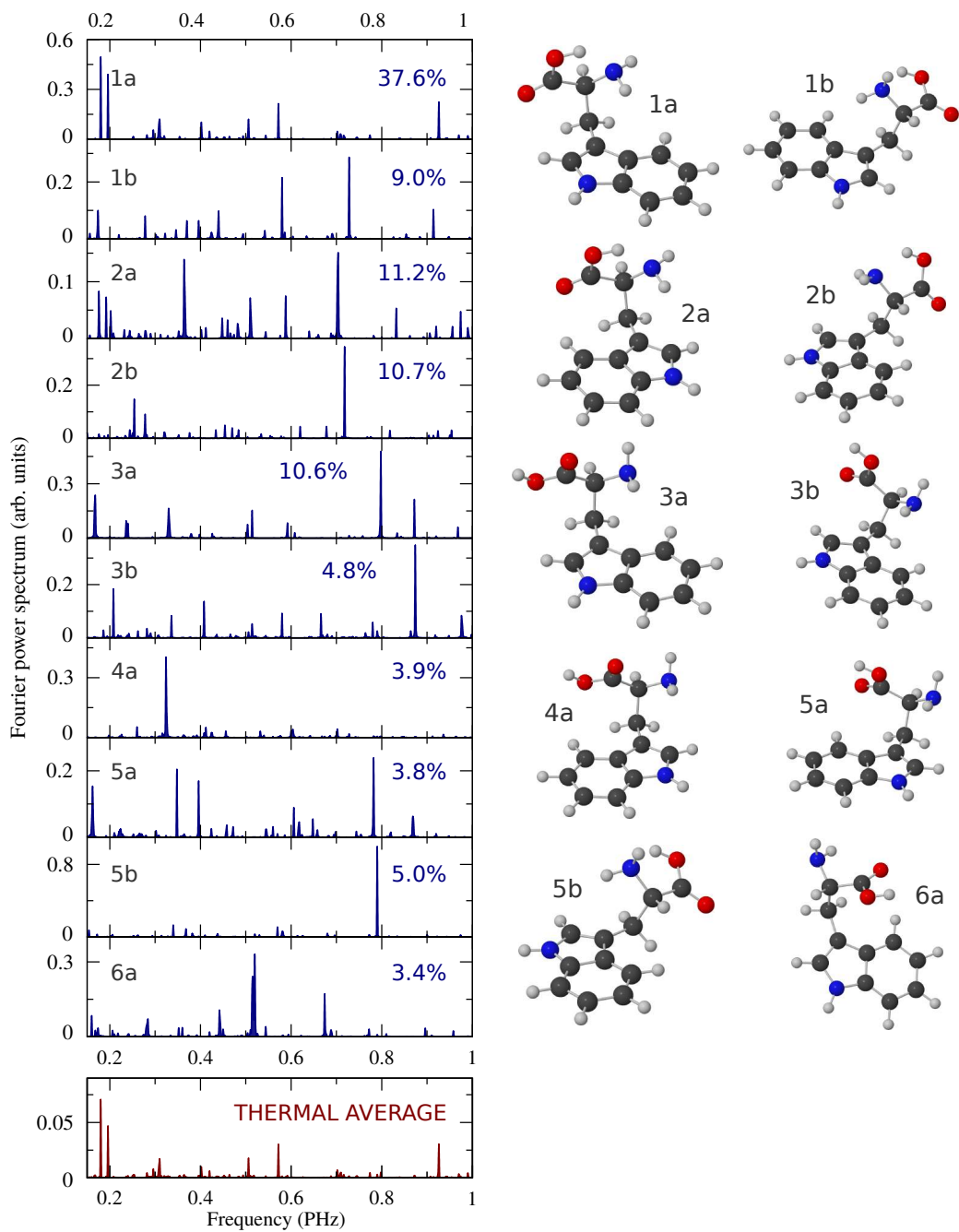


Figure 5.27: Same as fig. 5.25 for the most stable conformers of tryptophan. The relative populations have been calculated assuming a Boltzman distribution.

## 5.4 Time-evolution of the full electron system

The evaluation of the hole density generated upon ionization in terms of the reduced density matrix of the ionic subsystem has allowed to describe the ultrafast response of the parent ion to attosecond ionization. In order to analyze the time-evolution of the electronic wave packet created in the continuum, one needs to evaluate the electron density of the full system, including the photoelectron. This can be done by making use of eq. 3.13, which retrieves the electron density in terms of the the wave packet coefficients (see eq. 3.1) and the corresponding bound and continuum orbitals. We have analyzed the time-evolution of the electron density of the glycine molecule upon interaction with an attosecond pulse similar to that used in the experiment illustrated in fig. 5.1. Fig. 5.28 (rows 1 and 3) shows snapshots of the relative variation of the electron density of the full system for different times, from right after the interaction with the pulse to up to 1fs. For comparison, snapshots of the relative electron density of the residual ion, calculated using eq. 3.15 and the reduced density matrix of the ionic subsystem (eq. 3.15), are also shown in fig. 5.28 (rows 2 and 4). For analysis purposes, we have chosen a bigger cutoff value ( $10^{-3}$  a.u.) to generate the isosurfaces of the electron density than that employed in fig. 5.13 ( $10^{-4}$  a.u.). Note that positive values of the relative electron density (purple surfaces in fig. 5.28) correspond to negative values of the relative hole density (purple surfaces in fig. 5.13).

We can see in fig. 5.13 that at  $t = 0$  the molecule is surrounded by a bulky electronic cloud due to the presence of the photoelectron. This cloud gradually vanishes as the photoelectron wave is emitted and, at  $t = 0.7$  fs, the electron density of the full system is identical to that of the residual ion. These results justify the analysis of the ultrafast charge redistributions occurring in the system in terms of the electron density of the residual ion.

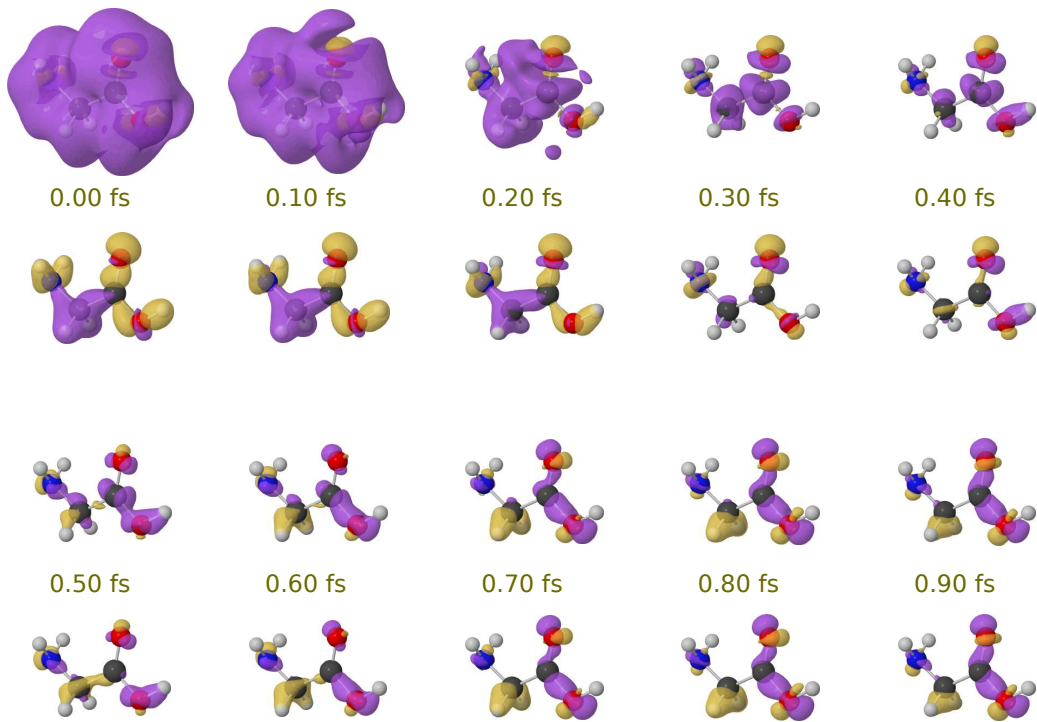


Figure 5.28: Relative variation of the electron density of glycine with respect to its time-averaged value as a function of time. Rows 1 and 3: dynamics of the full-system, containing all electrons. Rows 2 and 4: dynamics of the residual ion, calculated in terms of its reduced density matrix. Isosurfaces of the relative electron density are shown for cutoff values of  $10^{-3}$  a.u. (purple) and  $-10^{-3}$  (yellow). Time is with reference to the end of the XUV pulse.

# Conclusions

The advent of ultrabright light sources based on synchrotron radiation and ultrafast pulses based on high harmonic generation (HHG) opened the door to image molecular structures and to monitor and even control electron and nuclear dynamics in their intrinsic time scales. In this quest, theoretical modelling and numerical simulations have been probed to be fundamental in the design of new experimental schemes and to understand the complex outcomes of those. Methods based on the Density Functional Theory (DFT) provide an excellent compromise between accuracy and computational effort. In this work, we have employed the static-exchange DFT method to evaluate the electronic structure of molecules (from CO or F<sub>2</sub> up to large amino acids) in order to predict and to understand recent experiments performed in two well-defined contexts: using third-generation light sources and attosecond pulses generated via HHG. The development of high-resolution third-generation synchrotron facilities has enabled the investigation of vibrationally-resolved inner-shell photoionization in small molecules made of first-row atoms of the periodic table. In chapter 4 and in appendices A, B, C, D and E we have presented C 1s and B 1s vibrationally resolved photoionization cross sections of CO, CF<sub>4</sub> and BF<sub>3</sub>, which have been evaluated using the static-exchange and the time-dependent DFT methods including the nuclear motion at the Born-Oppenheimer level. By comparing our results with photoelectron spectra measured at SOLEIL and Spring-8 synchrotron light sources, we have found clear evidence of non-Franck-Condon effects that take place upon photoabsorption. When the de Broglie wave length of the photoelectron is comparable to the dimensions of the molecular target, i.e., for photon energies of the order of a few hundreds of eVs, the undulatory nature of the electron manifests as diffraction interferences by the surrounding atomic centers. These inter-

---

ferences are imprinted in the ratios between vibrationally resolved cross sections ( $\nu$ -ratios) as clear oscillations as a function of the photoelectron momentum. As a proof-of-principle, we have used the C 1s photoelectron spectra of CO to determine the internuclear distance of the neutral molecule and the bond contraction accompanying C 1s ionization. This is a surplus of photoelectron spectroscopy with respect to more conventional spectroscopic techniques, which usually can only provide structural information of neutral molecular species. Near the photoionization threshold, where the continuum waves are sensitive to the details of the molecular potentials, the cross sections show sharp features due to the presence of shape resonances. From the theoretical calculations, and the angular momentum decompositions, we have also confirmed the existence of confinement effects as those previously found in more simple molecules. In the future, molecules such as BF<sub>3</sub>, CF<sub>4</sub> or CO could provide an interesting workbench to study the photoelectron scattering phenomenon in a time-resolved (pump-probe) scheme using novel ultrahigh intensity photon sources like seeded FELs, which now become available.

We have also investigated deviations from the Franck-Condon approximation in the photoionization of molecular fluorine, by considering electron ejection from different molecular orbitals using the static-exchange DFT method. For the outermost shells, we have included the nuclear degrees of freedom, which has allowed us to describe dissociative and non-dissociative ionization channels. The photoionization cross sections show an oscillatory behavior as a function of the photoelectron momentum, which is the result of the coherent emission from two equivalent centers. The observed interference patterns are similar to those already explained by Cohen and Fano [189] in the early sixties. These interferences can be described by using very simple expressions that account for both the ratio between total photoionization cross sections associated to different orbitals and to the branching ratios between vibrationally resolved cross sections associated to the same electronic ionic state. Both effects were demonstrated in previous work [81] in other diatomic molecules, so the present work reinforces the general validity of those findings. The fact that there is a non-negligible probability of dissociation accompanying valence-ionization could be exploited experimentally to obtain molecular frame photoelectron angular distributions by using multi-coincidence techniques,

since detection of the charged atomic fragments provides information about the orientation of the molecule at the instant of ionization.

Since the generation of the first isolated attosecond pulses at the very beginning of the present century, tracing ultrafast phenomena using attosecond pump-probe techniques became a reality. The observation of charge migration in complex molecular structures and, in particular, in biologically relevant systems, is one of the main targets of attosecond science. Although charge migration was predicted in the late nineties by L. S. Cederbaum and coworkers, experimental evidence or reliable simulations of the electronic wave packet that could be created by an attosecond pulse were inexistent. In this work, we have investigated the electronic response of molecules of biological relevance, the amino acids glycine, phenylalanine and tryptophan, to attosecond ionization. We have found that attosecond pulses can induce ultrafast charge fluctuations over large regions of these complex molecules on a temporal scale that is much shorter than the vibrational response of the system. The work presented here differs from most previous theoretical work on charge migration, where charge dynamics is initiated by removing an electron from a given molecular orbital. Here, the use of the static-exchange DFT method in the framework of time-dependent first-order perturbation theory has allowed us to evaluate the actual wave packet generated upon attosecond ionization. Because of the broad energy spectrums of attosecond pulses, in a realistic experiment electrons are coherently emitted from various (many) molecular orbitals and thus the initial hole is highly delocalized along the molecular skeleton. The application of isolated attosecond pulses to prompt ionization of the amino acid phenylalanine has allowed the subsequent detection of ultrafast dynamics on a sub-4.5 femtosecond temporal scale, which is shorter than the vibrational response of the molecule. The good agreement with our numerical simulations of the temporal evolution of the electronic wave packet created by the attosecond pulse strongly supports the interpretation of the experimental data in terms of charge migration resulting from ultrafast electron dynamics preceding any nuclear rearrangement.





# Conclusiones

La llegada de fuentes de luz ultra-brillantes basadas en radiación sincrotrón y de pulsos láser ultra-cortos basados en la generación de altos armónicos (HHG, del inglés “high harmonic generation”) han abierto la puerta a la visualización de estructuras moleculares y al seguimiento e incluso el control de dinámica electrónica y nuclear en sus escalas de tiempo intrínsecas. El modelado teórico y las simulaciones numéricas han demostrado jugar un papel fundamental en el diseño de nuevos experimentos así como en la comprensión de los complejos resultados procedentes de los mismos. Los métodos basados en la Teoría del Funcional de la Densidad (DFT, del inglés “Density Functional Theory”) presentan un excelente compromiso entre precisión y esfuerzo computacional. En este trabajo hemos empleado el método “static-exchange DFT” para evaluar la estructura electrónica de moléculas (desde CO o F<sub>2</sub> hasta grandes amino ácidos) con el objetivo de predecir y comprender experimentos recientes realizados bajo condiciones bien diferenciadas: utilizando fuentes de luz de tercera generación y pulsos ultra-cortos basados en HHG. El desarrollo de instalaciones sincrotrón de última generación ha permitido la investigación de procesos de fotoionización de capa interna en moléculas pequeñas, constituidas por átomos del primer periodo de la tabla periódica, con resolución vibracional. En el capítulo 4 y en los apéndices A, B, C, D y E hemos presentado las secciones eficaces de fotoionización de capa interna de las moléculas CO, CF<sub>4</sub> y BF<sub>3</sub>, calculadas mediante el método “static-exchange DFT” y su versión dependiente del tiempo, incluyendo el movimiento nuclear a nivel de Born-Oppenheimer. La comparación de nuestros resultados teóricos con los espectros fotoelectrónicos medidos en los sincrotrones SOLEIL y Spring-8, nos ha permitido investigar desviaciones de la aproximación Franck-Condon en procesos de ionización de capa interna. Cuando la longitud

---

de onda de de Broglie del fotoelectrón es comparable a las dimensiones del sistema, es decir, cuando su energía cinética es del orden de unos cientos de eVs, la naturaleza ondulatoria del fotoelectrón produce interferencias de difracción intramolecular. Estas interferencias quedan impresas en los ratios entre secciones eficaces resueltas vibracionalmente ( $\nu$ -ratios), produciendo claras oscilaciones en función del momento del fotoelectrón. Como prueba de concepto, hemos utilizado espectros fotoelectrónicos de la molécula de CO para determinar la distancia internuclear de la especie neutra y la contracción del enlace que tiene lugar tras la extracción un electrón del orbital 1s del átomo de carbono. Cerca del umbral de ionización, donde las funciones del continuo son más sensibles a los detalles de los potenciales moleculares, las secciones eficaces presentan estructuras agudas debido a la presencia de resonancias de forma. La descomposición en momento angular ha permitido confirmar la existencia de efectos de confinamiento electrónico similares a los que ya se habían observado previamente en moléculas más simples. En el futuro, moléculas como BF<sub>3</sub>, CF<sub>4</sub> or CO podrían constituir un punto de referencia para el estudio del fenómeno de difracción fotoelectrónica mediante el uso de técnicas bombeo-sonda utilizando pulsos ultra-intensos de láseres de electrones libres.

También hemos investigado el origen de las desviaciones de la aproximación de Franck-Condon que tienen lugar en la fotoionización de la molécula de flúor, considerando emisión fotoelectrónica desde distintos orbitales. La inclusión del movimiento nuclear en el estudio de las capas más externas nos ha permitido describir canales de fotoionización disociativos y no disociativos. Como consecuencia de un proceso de emisión multicéntrica, las secciones eficaces de fotoionización presentan claras oscilaciones en función del momento del fotoelectrón. Los patrones de interferencia observados son similares a aquellos para los que Cohen y Fano [189] fueron capaces de dar una explicación teórica en los años 60. Estas interferencias pueden ser descritas de forma cualitativa mediante el uso de expresiones sencillas que permiten calcular ratios entre secciones eficaces totales correspondientes a diferentes canales iónicos así como entre secciones eficaces resueltas vibracionalmente asociadas al mismo canal. Estos efectos fueron previamente observados [81] en moléculas diatómicas más sencillas, así que este trabajo refuerza la validez general de esos hallazgos. El hecho de que exista una pro-

babilidad no despreciable de que la molécula de flúor disocie tras ser ionizada desde sus capas de valencia podría ser explotado para medir distribuciones angulares del fotoelectrón mediante el uso de técnicas de coincidencia múltiple, ya que la detección de fragmentos atómicos cargados proporciona información sobre la orientación de la molécula en el instante de la ionización.

La generación de pulsos de attosegundos a comienzos de este siglo ha permitido la observación y el seguimiento de procesos ultra-rápidos mediante el uso de técnicas bombeo-sonda. La observación de migración de carga en estructuras moleculares complejas y, en particular, en moléculas de relevancia biológica, es uno de los objetivos fundamentales de la ciencia de attosegundos. A pesar de que los procesos de migración de carga fueron predichos a finales de la década de los noventa por Lorenz S. Cederbaum y sus colaboradores, no existían pruebas experimentales sólidas ni estudios teóricos del paquete de ondas electrónico generado por un pulso de attosegundos. En este trabajo hemos investigado la respuesta electrónica de moléculas de relevancia biológica, los amino ácidos glicina, fenilalanina y triptófano, a la ionización ultra-rápida. Hemos descubierto que los pulsos de attosegundos pueden inducir fluctuaciones de carga ultra-rápidas, en una escala de tiempo que precede a la respuesta vibracional del sistema. Nuestro trabajo es distinto a otros estudios teóricos previos, donde la dinámica se inicia arrancando un electrón de un determinado orbital molecular. El uso del método “static-exchange DFT” en el marco de teoría de perturbaciones a primer orden ha permitido evaluar el paquete de ondas electrónico generado por un pulso de attosegundos. Debido sus anchos espectros energéticos, los pulsos de attosegundos son capaces de emitir fotoelectrones desde varios (muchos) orbitales moleculares de forma coherente, generando huecos que están completamente deslocalizados sobre el esqueleto molecular. La reciente aplicación de pulsos de attosegundos aislados a la ionización del aminoácido fenilalanina ha permitido la detección experimental de dinámica puramente electrónica. El buen acuerdo con nuestras simulaciones numéricas de la evolución temporal del paquete de ondas electrónico apoya firmemente la interpretación de los resultados experimentales en términos de migración de carga ultra-rápida que precede al movimiento nuclear.



# Appendices



## **Appendix A**

Intramolecular photoelectron  
diffraction in the gas phase





## Intramolecular photoelectron diffraction in the gas phase

K. Ueda,<sup>1,a)</sup> C. Miron,<sup>2</sup> E. Plésiat,<sup>3</sup> L. Argenti,<sup>3</sup> M. Patanen,<sup>2</sup> K. Kooser,<sup>4</sup> D. Ayuso,<sup>3</sup> S. Mondal,<sup>1</sup> M. Kimura,<sup>1</sup> K. Sakai,<sup>1</sup> O. Travnikova,<sup>2</sup> A. Palacios,<sup>3</sup> P. Decleva,<sup>5</sup> E. Kukuk,<sup>4</sup> and F. Martín<sup>3,6,b)</sup>

<sup>1</sup>*Institute of Multidisciplinary Research for Advanced Materials, Tohoku University, Sendai 980-8577, Japan*

<sup>2</sup>*Synchrotron SOLEIL, L'Orme des Merisiers, Saint-Aubin, BP 48, 91192 Gif-sur-Yvette Cedex, France*

<sup>3</sup>*Departamento de Química, Módulo 13, Universidad Autónoma de Madrid, 28049 Madrid, Spain*

<sup>4</sup>*Department of Physics and Astronomy, University of Turku, 20014 Turku, Finland*

<sup>5</sup>*Dipartimento di Scienze Chimiche, Università di Trieste, 34127 Trieste, and CNR-IOM, Trieste, Italy*

<sup>6</sup>*Instituto Madrileño de Estudios Avanzados en Nanociencia (IMDEA-Nanociencia), Cantoblanco, 28049 Madrid, Spain*

(Received 27 May 2013; accepted 5 August 2013; published online 27 September 2013)

We report unambiguous experimental and theoretical evidence of intramolecular photoelectron diffraction in the collective vibrational excitation that accompanies high-energy photoionization of gas-phase  $\text{CF}_4$ ,  $\text{BF}_3$ , and  $\text{CH}_4$  from the  $1s$  orbital of the central atom. We show that the ratios between vibrationally resolved photoionization cross sections ( $v$ -ratios) exhibit pronounced oscillations as a function of photon energy, which is the fingerprint of electron diffraction by the surrounding atomic centers. This interpretation is supported by the excellent agreement between first-principles static-exchange and time-dependent density functional theory calculations and high resolution measurements, as well as by qualitative agreement at high energies with a model in which atomic displacements are treated to first order of perturbation theory. The latter model allows us to rationalize the results for all the  $v$ -ratios in terms of a *generalized  $v$ -ratio*, which contains information on the structure of the above three molecules and the corresponding molecular cations. A fit of the measured  $v$ -ratios to a simple formula based on this model suggests that the method could be used to obtain structural information of both neutral and ionic molecular species.

© 2013 AIP Publishing LLC. [<http://dx.doi.org/10.1063/1.4820814>]

### I. INTRODUCTION

X-ray light efficiently ionizes the inner and valence shells of atoms and molecules, leading to short-wavelength electrons that can be scattered coherently (or diffracted) by the surrounding atomic constituents. Thus, scattered photoelectrons carry information about the structure of the system, which could in principle be extracted by fitting the measured photoelectron spectra to different analytical formulas. The NEXAFS (near-edge X-ray absorption fine structure) or EXAFS (extended X-ray absorption fine structure) techniques are based on this principle<sup>1,2</sup> and are widely used to obtain structural information of crystals as well as bulk amorphous materials.<sup>3–9</sup>

Determining the structure of isolated molecules by photoelectron spectroscopy is more difficult due to the low density of the gas phase in comparison with that of bulk materials. Indeed, diffraction is clearly observed in the condensed phase because the relatively low intensity of the standard X-ray sources used in the above mentioned techniques is amply compensated by the large number of atoms or molecules present in the sample (which is of the order of Avogadro's number, i.e.,  $\sim 10^{23}$  atoms or molecules per mole). In contrast,

for structural determination of isolated molecules one has to work with gases at very low pressures, i.e., densities as low as  $10^{13}$ – $10^{15}$  molecules per  $\text{cm}^3$ . To overcome this difficulty, in addition to past and current developments in gas-phase EXAFS,<sup>10–12</sup> alternative methods are being explored. One of these takes advantage of the high brightness of x-ray free electron lasers, which should be ideal to obtain instantaneous and time-resolved pictures of molecular structure through the so-called photoelectron holography.<sup>13</sup> A more sophisticated strategy, already put in practice, consists in combining intense infrared femtosecond lasers<sup>14–16</sup> with laser-induced electron diffraction. In these experiments, the oscillating electric field of the laser forces a fraction of the tunneled electron to go back to the parent ion where it can diffract, thus conveying the necessary information to extract the structure of the molecule. Very recent experimental work has shown that this technique can provide sub-Å spatial resolution and sub-femtosecond temporal resolution. Another more traditional method consists in measuring molecular-frame photoelectron angular distributions (MFPAD) resulting from photoionization with synchrotron radiation.<sup>17,18</sup> In particular, it has been shown that, in some cases, MFPADs associated with very slow electrons provide a direct imaging of molecular structure.<sup>19,20</sup>

A common denominator in the above examples is that photoelectron spectra must be recorded (at least) as a function of the electron ejection angle. This requires the use of rather

<sup>a)</sup>Electronic mail: ueda@tagen.tohoku.ac.jp

<sup>b)</sup>Electronic mail: fernando.martin@uam.es

sophisticated coincidence setups with high angular resolution and high detection efficiency,<sup>21,22</sup> which are not always available or applicable. However, recent work on the photoionization of diatomic molecules by synchrotron radiation<sup>23,24</sup> has shown that, under some circumstances, photoelectron spectra integrated over electron ejection angle might also be a valuable tool for structural determination. In particular, experiments and theoretical calculations performed on H<sub>2</sub>, N<sub>2</sub>, and CO molecules have shown that the ratios of vibrationally resolved photoionization cross sections (hereafter called *v*-ratios) oscillate with photon energy and that this is due to the coherent electron emission from the two atomic centers.<sup>23</sup> The frequency of the oscillations depends on the internuclear distance, hence they necessarily convey information about molecular structure. Oscillations resulting from coherent electron emission have also been observed in acetylene.<sup>25</sup> There is recent evidence that electrons ejected from a very localized region of a molecule, such as the *1s* orbital of first-row atoms, also lead to oscillating patterns in the *v*-ratios as a result of electron scattering by the peripheral atomic centers of the molecule.<sup>26</sup>

In this paper, we unambiguously show that the *v*-ratios for photoionization of CF<sub>4</sub>, BF<sub>3</sub>, and CH<sub>4</sub> from the *1s* orbital of the central atom strongly oscillate as functions of photoelectron energy. The very good agreement between first-principles static-exchange and time-dependent density functional theory calculations and high resolution measurements, as well as the qualitative agreement at high energies with a simple model show that the origin of these oscillations is the diffraction by the surrounding H and F atoms. A sketch of the phenomenon is shown in Fig. 1 for the case of the BF<sub>3</sub>

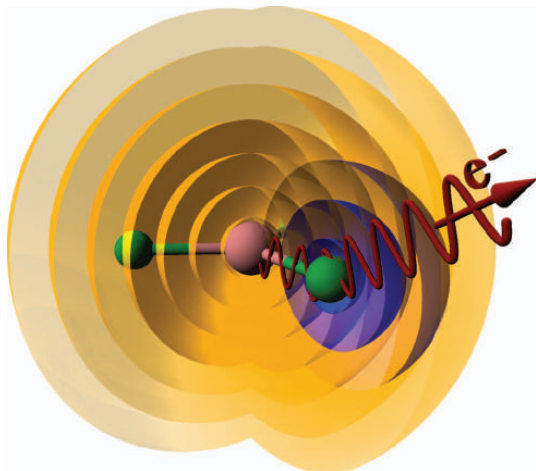


FIG. 1. Intramolecular electron diffraction in BF<sub>3</sub>. The *1s* electron of the central boron atom, which is localized around the boron nucleus, is ionized after absorption of an X-ray photon, leading, in a simplified picture to the yellow spherical wave. This wave is subsequently diffracted by the neighboring fluorine atoms, leading to secondary spherical waves as that plotted in blue around one of the fluorine atoms for an electron escaping along the direction represented by the red arrow. The combination of the yellow and blue waves leads to interferences that carry structural information about the parent neutral BF<sub>3</sub> molecule and the final BF<sub>3</sub><sup>+</sup> molecular ion.

molecule. From these results we have approximately determined the bond distances for the three molecules and their corresponding molecular cations. Thus, the present work provides an alternative and a complement to gas-phase electron diffraction (GED) techniques,<sup>27–30</sup> which have been successfully used to retrieve three-dimensional structural information from molecules in the gas phase but would be difficult to apply to molecular cations.

## II. METHODS

The experimental and theoretical methods have been explained in detail in previous work.<sup>26,31</sup> A brief summary is presented below.

The experiment was performed at the PLEIADES beamline<sup>32</sup> (70–1000 eV) for ultrahigh resolution spectroscopic studies<sup>33,34</sup> of isolated species at the 2.75 GeV French national synchrotron radiation laboratory SOLEIL. Linearly polarized light with the polarization vector at 54.7° with respect to the electron detection axis has been used with a spectral broadening of 55 meV or less. The electron spectrometer resolution was better than 40 meV. The *1s* photoelectron spectra have been analyzed through a least-squares fitting procedure by using macro package SPANCF for Igor Pro.<sup>35</sup>

For a given molecule, all spectra were fitted simultaneously. Post-collisional interaction (PCI) line shapes<sup>36</sup> were used in the fitting process with the Lorentzian width as a free parameter, but common for all the lines and spectra of the molecule. The Gaussian width representing the instrumental and translational Doppler broadenings was also kept as free parameter, but constrained to be the same to all peaks in the spectra. Rotational Doppler broadening<sup>37,38</sup> is absent in the present case, because the electron emission takes place from the center of mass of the molecules. As the initial guesses were obtained from the fitted Ar calibration data, only small variations from the initial values were observed. The asymmetry leading to the low energy tail due to the PCI effect was calculated by using the formula given in Ref. 39. The energy spacing of the symmetric stretching vibrational sub-levels was kept constant. In the data analysis, the recoil-induced excitations of asymmetric vibrations were taken into account by simultaneously fitting the asymmetric stretching and bending vibrational peaks with fixed energy separations for each mode, and their intensities were estimated following the method described in Ref. 40. In this way, individual vibrational progressions for the symmetric stretching, asymmetric bending, and asymmetric stretching modes could be obtained.

Vibrationally resolved photoionization cross sections were evaluated within the dipole and Born-Oppenheimer approximations. Bound and continuum electronic wave functions were calculated by using the static-exchange density functional theory (DFT) and the time-dependent density functional theory (TDDFT) as described in Refs. 26 and 31. In the latter works, the methods originally developed in, e.g., Refs. 41–44 to treat molecular photoionization in the fixed-nuclei approximation were extended to provide the electronic continuum wave functions and the corresponding potential energy surfaces over a wide range of nuclear positions. The electronic Kohn-Sham equations were solved by using a

representation in a basis of B-spline functions.<sup>45</sup> The vibrational wave function was written as a product of single-mode vibrational functions resulting from the solution of the vibrational Schrödinger equation in a basis of B-splines. As photoionization mainly leads to molecular cations with excitation in the symmetric stretching mode, calculations of the potential energy surfaces were restricted to this normal coordinate by keeping all the other normal coordinates frozen at their values of the equilibrium geometry. The method has been shown to provide accurate vibrationally resolved photoionization cross sections for N<sub>2</sub>, CO, and C<sub>2</sub>H<sub>2</sub>.<sup>23,25,31</sup>

### III. RESULTS

As an illustration, Fig. 2 shows the photoelectron spectra of BF<sub>3</sub> and CF<sub>4</sub> at photon energies 518 and 383 eV, respectively. The figure also shows the results of the least-squares fit. As discussed in earlier work,<sup>40,46</sup> the most prominent vibrational progression corresponds to the symmetric stretching mode. For this reason, all comparisons between experiment and theory reported below will be restricted to this mode. Recoil leads to a redistribution of the available energy

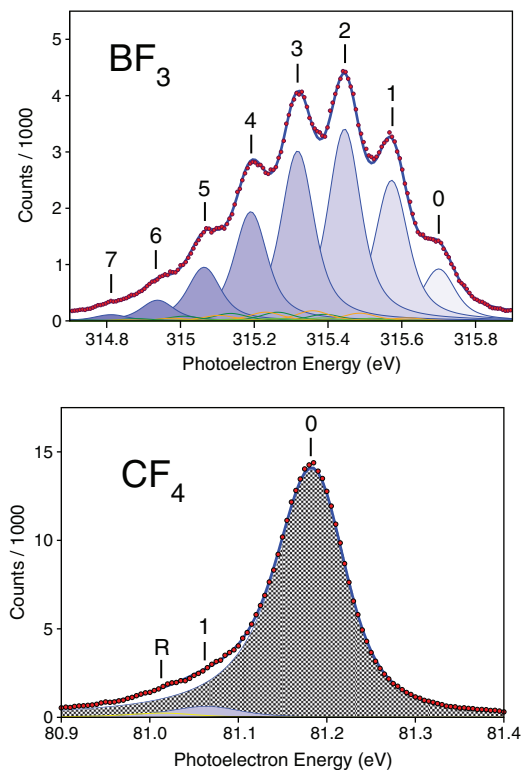


FIG. 2. Photoelectron spectra of BF<sub>3</sub> (left) and CF<sub>4</sub> (right) taken at  $h\nu = 518$  and 383 eV, respectively. Experimental results: circles. Thick blue line: fit of the experimental data. Thin blue lines enclosing shaded areas: vibrational progression associated with the symmetric stretching mode. Other thin lines: contribution of other modes resulting from recoil. Peak labels indicate the vibrational quantum number  $v$  in the BF<sub>3</sub><sup>+</sup> symmetric stretching mode.

even on symmetry-forbidden vibrational modes of the residual cation. For CF<sub>4</sub>, recoil leads to excitation of the asymmetric stretching and bending vibrations of the CF<sub>4</sub><sup>+</sup> ion, which superimpose to the  $v = 1$  symmetric stretching vibrational components.<sup>40</sup> A similar effect has been observed for CH<sub>4</sub> for the  $v = 1$  and  $v = 2$  components.<sup>47</sup> Figure 2 shows that vibrational excitations due to recoil effects are much less pronounced for BF<sub>3</sub> than for CF<sub>4</sub> (and CH<sub>4</sub><sup>47</sup>). As can be seen, BF<sub>3</sub> photoionization leads to a large progression of vibrational levels in its symmetric stretching mode. This is the consequence of the favorable Franck-Condon (FC) overlap between the initial and several final vibrational wave functions, which results from the fact that the B-F bond distances are significantly different in BF<sub>3</sub> and BF<sub>3</sub><sup>+</sup>. For CF<sub>4</sub> (CH<sub>4</sub>), the progression is limited to two (three) vibrational levels because the upper and the lower potential energy surfaces are very similar in the region close to the equilibrium geometry (in other words, the dominant FC overlap corresponds to the  $v' = 0 \rightarrow v = 0$  transition). For the three systems, the intensity of the measured peaks decreases very rapidly with photon energy. This rapid decrease usually washes out the oscillations arising from scattering effects as those sought for in this work. The problem is overcome in the  $v$ -ratios because the numerator and the denominator decrease with a similar rate. In spite of this, one cannot avoid long-time sample exposures due to the smallness of the cross sections at high photon energies.

Figure 3 shows the measured and calculated  $v$ -ratios as functions of photoelectron momentum for the symmetric stretching mode of BF<sub>3</sub>. The  $v$ -ratios exhibit pronounced oscillations superimposed to a nearly flat background. The agreement between theory and experiment is very good, even for the smallest  $v$ -ratios. In particular, the excellent agreement between the results from static-exchange DFT and the more elaborate TDDFT indicates that one can rely on the former to interpret the experimental findings. As can be seen in Fig. 3, the overall shape of the  $v$ -ratios is very similar for all  $v \geq 3$ ; for  $v = 0$  and  $v = 1$ , the oscillations are essentially identical but are perfectly out of phase from those with  $v \geq 3$ . For CH<sub>4</sub>, the  $v = 1/v = 0$  and  $v = 2/v = 0$  ratios reported in Ref. 26 are also very similar. For CF<sub>4</sub>, the present experiment can only provide the  $v = 1/v = 0$  ratio, but the various ones obtained from the static-exchange DFT and TDDFT calculations again resemble each other.

### IV. DISCUSSION

The above results suggest that, for a given molecule, all  $v$ -ratios carry the same structural information. As the amplitude of the oscillations is a small fraction of the vibrationally resolved cross section and, in particular, of the value that is obtained for this cross section within the FC approximation, one can assume that the variation of the transition dipole matrix element with the atomic displacements can be treated to first order in a Taylor expansion around the equilibrium geometry. Neglecting non-totally symmetric modes and assuming the validity of the harmonic approximation (which, as our calculations show, is a very good approximation for the low values of  $v$  populated in the present experiment), it can be

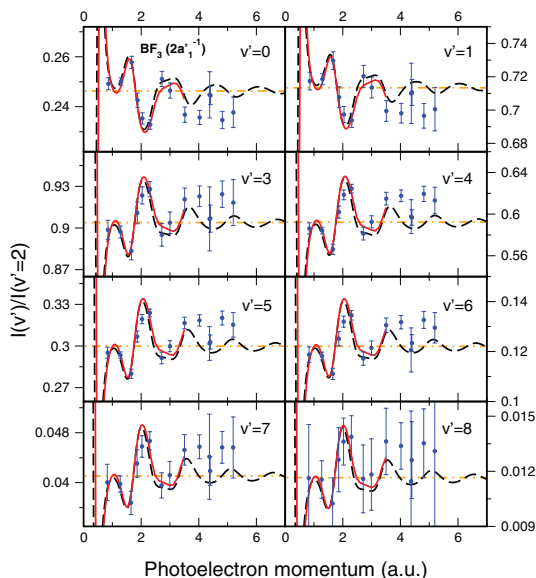


FIG. 3. Ratios between vibrationally resolved photoionization cross sections in B  $1s$  photoionization of  $\text{BF}_3$  in the symmetric stretching mode. The photoelectron momentum is defined with respect to the ground vibronic state of  $\text{BF}_3^+$ . All the ratios are referred to the  $v = 2$  cross section. Circles with error bars: experimental data including statistical errors. Red full lines: results of the TDDFT calculations. Black dashed lines: results from the static-exchange DFT calculations. Horizontal dashed-dotted lines: ratios predicted by the FC approximation.

easily shown that the vibrationally resolved photoionization cross section for the totally symmetric mode can be written as

$$\sigma_v(E) \simeq \text{FC}_v [\sigma_0(E) + v \sigma_1(E)], \quad (1)$$

where  $\text{FC}_v$  is the Franck-Condon factor  $\text{FC}_v = |\langle \chi_0 | \chi_v \rangle|^2$  with  $\chi_0$  and  $\chi_v$  the initial and final vibrational wave functions in the symmetric stretching mode,  $\sigma_0$  is the photoionization cross section of the rigid molecule at its equilibrium geometry, and  $\sigma_1$  is the first order correction due to the fact that the molecule is flexible. The total cross section is obviously given by

$$\sigma_{\text{Tot}} \simeq \sigma_0 + \bar{v} \sigma_1, \quad \bar{v} = \sum_v \text{FC}_v v. \quad (2)$$

The quantity  $(v - \bar{v})\sigma_1$ , which does not appear explicitly in the above expressions, describes the fluctuations of the barycenter of the photoelectron-peaks envelope with respect to the FC value. Hence, it is convenient to introduce a  $\mathcal{G}$  factor defined as

$$\mathcal{G} = \sigma_1 / \sigma_{\text{Tot}}, \quad (3)$$

with which the vibrationally resolved cross section and the corresponding  $v$ -ratio,  $\mathcal{R}$ , take on the form

$$\sigma_v(E) \simeq \sigma_{\text{Tot}}(E) \text{FC}_v [1 + (v - \bar{v}) \mathcal{G}(E)], \quad (4)$$

$$\mathcal{R}_{v,v_0}(E) \simeq (\text{FC}_v / \text{FC}_{v_0}) [1 + (v - v_0) \mathcal{G}(E)]. \quad (5)$$

From Eq. (5), it is apparent that the oscillatory behavior observed in the  $v$ -ratios is entirely contained in the universal function  $\mathcal{G}(E)$ , which in addition does not include the fast decrease of the total cross section.

By using the measured and DFT-calculated  $v$ -ratios in Eq. (5), we can extract experimental and theoretical values of  $\mathcal{G}$ . They are shown in Fig. 4. As for the  $v$ -ratios shown in Fig. 3, the agreement between theory and experiment is good for the three molecules. It is important to note that, since the  $\mathcal{G}$  factor contains information from all the measured  $v$ -ratios, statistical errors are substantially reduced with respect to those of the individual  $v$ -ratios, especially for  $\text{BF}_3$ . It can be seen that oscillations are quite apparent and have the characteristic momentum periodicity  $\Delta k = \pi / R_0^{\text{AB}_n}$ , where  $R_0^{\text{AB}_n}$  is the bond distance of the  $\text{AB}_n$  molecule at equilibrium.

To prove without ambiguity that the observed oscillations are entirely due to diffraction of the ejected photoelectron, we have also used a simple analytical model to evaluate  $\mathcal{G}(E)$ .<sup>48</sup> The model is based on a one-particle description of  $\text{AB}_n$  photoionization in which the interaction between photoelectron and ion is approximated by a sum of atomic Yukawa potentials, the initial electronic wave function is represented by a purely hydrogenic  $1s$  orbital, and the final wave function  $|\psi_{\vec{k}}^-\rangle$  is described within the first Born approximation:

$$|\psi_{\vec{k}}^-\rangle = |\vec{k}\rangle + G_0^-(E)V|\vec{k}\rangle, \quad (6)$$

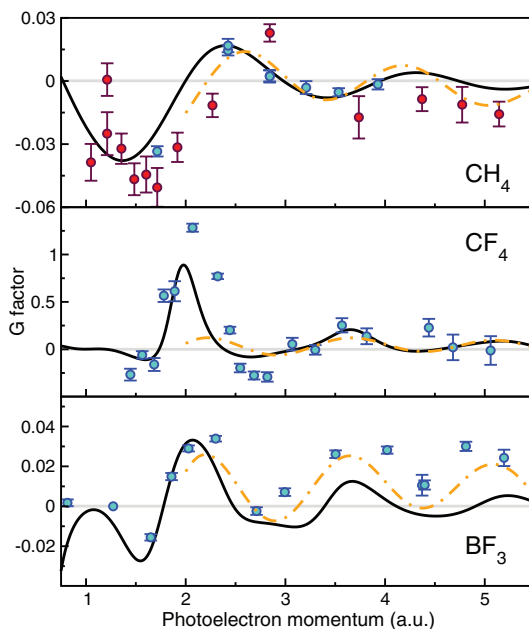


FIG. 4. Generalized  $v$ -ratio ( $\mathcal{G}$  factor) for  $\text{CH}_4$ ,  $\text{CF}_4$ , and  $\text{BF}_3$  as a function of photoelectron momentum. Circles with error bars: experimental results including statistical errors. Black full lines: results from the static-exchange DFT calculations. Orange dashed-dotted lines: results of the simple analytical model explained in the text. For  $\text{CH}_4$ , the  $\mathcal{G}$  factor has been evaluated from the experimental and theoretical data of Ref. 26 and the experimental data of Ref. 47 (red circles).

where  $|\vec{k}\rangle$  is a plane wave,  $G_0^-$  is the corresponding Green's function, and  $V$  is the electron-ion potential. Under these assumptions, all structural information is contained in the scattering term  $G_0^-(E)V|\vec{k}\rangle$ . Neglecting non-totally symmetric modes and averaging over all molecular orientations, Eq. (3) leads to<sup>48</sup>

$$\begin{aligned} \mathcal{G}(E, \vec{R}_0, Z_B, \phi) &= \frac{2Z_B}{\omega \Delta R M_B} \left[ 2 \cos \phi \int_0^\infty dq \frac{q^2 J(q, k)}{q^2 + 1} j_1(q \vec{R}_0) \right. \\ &\quad \left. - \pi \sin \phi 1s(k) \int_{-1}^1 dx \frac{k^3 x \sqrt{2-2x}}{2k^2(1-x) + 1} j_1(\sqrt{2-2x} k \vec{R}_0) \right] \\ &\quad \times \left[ \pi k 1s(k) - 4Z_A \mathcal{P} \int_0^\infty dp \frac{1s(p) p^3}{k^2 - p^2} \int_{-1}^1 \frac{x dx}{p^2 + k^2 - 2pkx + 1} \right]^{-1}, \end{aligned} \quad (7)$$

where  $E = k^2/2$ ,  $\vec{R}_0 = (R_0^{A B_n} + R_0^{A B_n^+})/2$  is the average equilibrium distance,  $\Delta R = R_0^{A B_n} - R_0^{A B_n^+} = \sqrt{2\bar{v}/n\omega M_B}$  is the difference in bond length between the neutral molecule and the cation,  $\phi$  is the intramolecular scattering phase,  $1s(k)$  is the initial  $1s$  orbital in momentum representation,  $j_1$  is the spherical Bessel function of order one,  $Z_B$  and  $M_B$  are, respectively, the effective charge and the mass of atom B, and

$$J(q, k) = \int_{-1}^1 dx \frac{k + qx}{q + 2kx} 1s(\sqrt{k^2 + q^2 + 2kqx}). \quad (8)$$

Thus, Eq. (7) may be employed to determine  $\vec{R}_0$  (and also  $Z_B$  and  $\phi$ ) by a least-squares fit to the experimental data. The resulting values for the C-H and B-F bond lengths of the neutral (charged) CH<sub>4</sub> and BF<sub>3</sub> molecules are 1.08 (1.03) and 1.20 (1.13) Å, respectively, in reasonable agreement with the experimental values 1.09 (1.04) and 1.31 (1.25) Å.<sup>46,49</sup> A similar fit is not possible for CF<sub>4</sub> due to the failure of the first Born approximation up to relatively high  $k$ . It is worth noticing that a fit of Eq. (7) to the static-exchange DFT data, which contain hundreds of points, leads to an even better agreement with the experimental bond length values, including CF<sub>4</sub>. These results confirm the validity of the assumptions leading to the  $\mathcal{G}$  function and prove that the relevant structural information for the neutral molecule and the cation is contained in that function. Still, there is room to improve the accuracy of the fitted bond lengths, e.g., by removing some of the approximations used to derive Eq. (7).

## V. CONCLUSION

We have performed high resolution experiments and static-exchange density functional theory and time-dependent density functional theory calculations to determine K-shell vibrationally resolved photoionization spectra of CF<sub>4</sub>, BF<sub>3</sub>, and CH<sub>4</sub>. The results show that the ratios between vibrationally resolved cross sections, the so-called  $v$ -ratios, exhibit pronounced oscillations as a function of photoelectron energy. These oscillations are the fingerprint of electron diffraction by the peripheral atomic centers. The observation of this phenomenon has been possible due to (i) the significant

improvement in experimental resolution and statistics with respect to earlier experiments, (ii) the measurements and calculations performed for three different molecular systems containing quite different atomic species, and (iii) a new theoretical framework that allows one to analyze the observed diffraction patterns in a unified way irrespective of the molecule under consideration. The latter framework is based on a simple first-order treatment of atomic displacements and has been used to determine the bond lengths of neutral BF<sub>3</sub> and CH<sub>4</sub>, as well as of their corresponding cations with a reasonable accuracy. This is a surplus of photoelectron spectroscopy with respect to more conventional spectroscopic techniques, which usually can only provide structural information of neutral molecular species.

Vibrationally resolved photoelectron spectroscopy allows detecting intramolecular electron diffraction in an elegant and consistent way, because (i) the problem of the rapid decrease of the photoionization probability with photon energy can be avoided by monitoring the ratios between vibrationally resolved cross sections (as opposed to the unresolved total cross section), and (ii) the effect of diffraction interferences manifest differently in different final vibrational states. High-resolution third-generation synchrotron facilities have made it possible to resolve the photoelectron peaks corresponding to different vibrational states of the parent ion, thus demonstrating unambiguously and conclusively that the nuclear response to intramolecular electron diffraction is observable and therefore could be used to obtain structural information of neutral and ionic symmetric polyatomic molecules.

## ACKNOWLEDGMENTS

We thank Mare Nostrum BSC, Cineca, and CCC-UAM for allocation of computer time. Work supported by the Advanced Grant of the European Research Council XCHEM 290853, the MICINN Project Nos. FIS2010-15127, ACI2008-0777, and CSD 2007-00010 (Spain), the ERA-Chemistry Project No. PIM2010EEC-00751, the European GrantNos. MC-ITN CORINF and MC-RG ATTOTREND, the European COST Action CM0702, the MC-IEF CHICROCSX under Grant Agreement No. 252781 (OT) and I3 program, the MEXT and JSPS agencies (Japan), and the Academy of Finland. Data collection was performed at the PLEIADES beamline at SOLEIL Synchrotron, France (Proposal No. 20110781). We are grateful to T. D. Thomas for stimulating discussions, to the SOLEIL staff for smoothly running the facilities and to E. Robert for technical assistance.

<sup>1</sup>D. E. Sayers, E. A. Sternf, and F. W. Lytle, *Phys. Rev. Lett.* **27**, 1204 (1971).

<sup>2</sup>R. F. Pettifer, O. Mathon, S. Pascarelli, M. D. Cooke, and M. R. J. Gibbs, *Nature (London)* **435**, 78 (2005).

<sup>3</sup>S. A. Chambers, *Adv. Phys.* **40**, 357 (1991).

<sup>4</sup>P. Hofmann, K. M. Schindler, S. Bao, A. M. Bradshaw, and D. P. Woodruff, *Nature (London)* **368**, 131 (1994).

<sup>5</sup>P. Glatzel and U. Bergmann, *Coord. Chem. Rev.* **249**, 65 (2005).

<sup>6</sup>C. Bressler and M. Chergui, *Chem. Rev.* **104**, 1781 (2004).

<sup>7</sup>D. Woodruff, *Surf. Sci. Rep.* **62**, 1 (2007).

<sup>8</sup>A. Arcovito, M. Benfatto, M. Cianci, S. S. Hasnain, K. Nienhaus, G. U. Nienhaus, C. Savino, R. W. Strange, B. Vallone, and S. D. Longa, *Proc. Natl. Acad. Sci. U.S.A.* **104**, 6211 (2007).

- <sup>9</sup>M. Haumann, A. Grundmeier, I. Zaharieva, and H. Dau, *Proc. Natl. Acad. Sci. U.S.A.* **105**, 17384 (2008).
- <sup>10</sup>N. Pangher, H. M. Köppe, J. Feldhaus, and J. Haase, *Phys. Rev. Lett.* **71**, 4365 (1993).
- <sup>11</sup>R. Prešeren, A. Kodre, I. Arčon, and M. Borowski, *J. Synchrotron Radiat.* **8**, 279 (2001).
- <sup>12</sup>J. Söderström, N. Mårtensson, O. Travnikova, M. Patanen, C. Miron, L. J. Saethre, K. J. Børve, J. J. Rehr, J. J. Kas, F. D. Vila, T. D. Thomas, and S. Svensson, *Phys. Rev. Lett.* **108**, 193005 (2012).
- <sup>13</sup>F. Krasniqi, B. Najjari, L. Strüder, D. Rolles, A. Voitkov, and J. Ullrich, *Phys. Rev. A* **81**, 033411 (2010).
- <sup>14</sup>M. Meckel, D. Comtois, D. Zeidler, A. Staudte, D. Pavicic, H. C. Bandulet, H. Pépin, J. C. Kieffer, R. Dörner, D. M. Villeneuve, and P. B. Corkum, *Science* **320**, 1478 (2008).
- <sup>15</sup>M. Okunishi, H. Niikura, R. Lucchese, T. Morishita, and K. Ueda, *Phys. Rev. Lett.* **106**, 3 (2011).
- <sup>16</sup>C. I. Blaga, J. Xu, A. D. DiChiara, E. Sistrunk, K. Zhang, P. Agostini, T. A. Miller, L. F. DiMauro, and C. D. Lin, *Nature (London)* **483**, 194 (2012).
- <sup>17</sup>H. Fukuzawa, X.-J. Liu, T. Teranishi, K. Sakai, G. Prümper, K. Ueda, Y. Morishita, N. Saito, M. Stener, and P. Decleva, *Chem. Phys. Lett.* **451**, 182 (2008).
- <sup>18</sup>J. Adachi, M. Kazama, T. Teramoto, N. Miyauchi, T. Mizuno, M. Yamazaki, T. Fujikawa, and A. Yagishita, *J. Phys. B* **45**, 194007 (2012).
- <sup>19</sup>J. B. Williams, C. S. Trevisan, M. S. Schöffler, T. Jahnke, I. Bocharova, H. Kim, B. Ulrich, R. Wallauer, F. Sturm, T. N. Rescigno, A. Belkacem, R. Dörner, T. Weber, C. W. McCurdy, and A. L. Landers, *Phys. Rev. Lett.* **108**, 233002 (2012).
- <sup>20</sup>J. B. Williams, C. S. Trevisan, M. S. Schöffler, T. Jahnke, I. Bocharova, H. Kim, B. Ulrich, R. Wallauer, F. Sturm, T. N. Rescigno, A. Belkacem, R. Dörner, T. Weber, C. W. McCurdy, and A. L. Landers, *J. Phys. B* **45**, 194003 (2012).
- <sup>21</sup>R. Dörner, V. Mergel, O. Jagutzki, L. Spielberger, J. Ullrich, R. Moshhammer, and H. Schmidt-Böcking, *Phys. Rep.* **330**, 95 (2000).
- <sup>22</sup>C. Miron and P. Morin, *Nucl. Instrum. Methods Phys. Res. A* **601**, 66 (2009).
- <sup>23</sup>S. E. Canton, E. Plésiat, J. D. Bozek, B. S. Rude, P. Decleva, and F. Martín, *Proc. Natl. Acad. Sci. U.S.A.* **108**, 7302 (2011).
- <sup>24</sup>X.-J. Liu, N. A. Cherepov, S. K. Semenov, V. Kimberg, F. Gel'mukhanov, G. Prümper, T. Lischke, T. Tanaka, M. Hoshino, H. Tanaka, and K. Ueda, *J. Phys. B* **39**, 4801 (2006).
- <sup>25</sup>L. Argenti, T. D. Thomas, E. Plésiat, X.-J. Liu, C. Miron, T. Lischke, G. Prümper, K. Sakai, T. Ouchi, R. Püttner, V. Sekushin, T. Tanaka, M. Hoshino, H. Tanaka, P. Decleva, K. Ueda, and F. Martín, *New J. Phys.* **14**, 033012 (2012).
- <sup>26</sup>E. Plésiat, L. Argenti, E. Kukku, C. Miron, K. Ueda, P. Decleva, and F. Martín, *Phys. Rev. A* **85**, 023409 (2012).
- <sup>27</sup>I. Hargittai and M. Hargittai, *Stereochemical Applications of Gas-Phase Electron Diffraction* (VCH, New York, 1988), Vols. 1 and 2.
- <sup>28</sup>S. A. Hayes, A. Stuart, R. J. Berger, B. Neumann, N. W. Mitzel, J. Bader, and B. Hoge, *Dalton Trans.* **39**, 5630 (2010).
- <sup>29</sup>C. E. Knapp, D. A. Wann, A. Bil, J. T. Schirlin, H. E. Robertson, P. F. McMillan, D. W. H. Rankin, and C. J. Carmalt, *Inorg. Chem.* **51**, 3324 (2012).
- <sup>30</sup>C. J. Hensley, J. Yang, and M. Centurion, *Phys. Rev. Lett.* **109**, 133202 (2012).
- <sup>31</sup>E. Plésiat, P. Decleva, and F. Martín, *Phys. Chem. Chem. Phys.* **14**, 10853 (2012).
- <sup>32</sup>C. Miron, see [www.synchrotron-soleil.fr/Recherche/LignesLumiere/PLEIADES](http://www.synchrotron-soleil.fr/Recherche/LignesLumiere/PLEIADES) for complete information about the PLEIADES beamline at SOLEIL.
- <sup>33</sup>C. Miron, C. Nicolas, O. Travnikova, P. Morin, Y. Sun, F. Gel'mukhanov, N. Kosugi, and V. Kimberg, *Nature Phys.* **8**, 135 (2012).
- <sup>34</sup>A. Lindblad, V. Kimberg, J. Söderström, C. Nicolas, O. Travnikova, N. Kosugi, F. Gel'mukhanov, and C. Miron, *New J. Phys.* **14**, 113018 (2012).
- <sup>35</sup>E. Kukku, Spectral Analysis by Curve Fitting Macro Package SPANCF 2000; See [www.physics.utu.fi/en/departement/materials\\_research/materials\\_science/Fitting.html](http://www.physics.utu.fi/en/departement/materials_research/materials_science/Fitting.html) for details of the lcode used to carry out the least-squares fit of the experimental data.
- <sup>36</sup>P. van der Straten, R. Morgenstern, and A. Niehaus, *Z. Phys. D: At., Mol. Clusters* **8**, 35 (1988).
- <sup>37</sup>Y.-P. Sun, C.-K. Wang, and F. Gel'mukhanov, *Phys. Rev. A* **82**, 052506 (2010).
- <sup>38</sup>T. D. Thomas, E. Kukku, K. Ueda, T. Ouchi, K. Sakai, T. X. Carroll, C. Nicolas, O. Travnikova, and C. Miron, *Phys. Rev. Lett.* **106**, 193009 (2011).
- <sup>39</sup>B. Paripás, G. Vitéz, G. Víkor, K. Tökési, A. Caló, R. Sankari, M. Huttula, S. Aksela, and H. Aksela, *J. Phys. B* **37**, 4507 (2004).
- <sup>40</sup>T. D. Thomas, E. Kukku, R. Sankari, H. Fukuzawa, G. Prümper, K. Ueda, R. Püttner, J. R. Harries, Y. Tamenori, T. Tanaka, M. Hoshino, and H. Tanaka, *J. Chem. Phys.* **128**, 144311 (2008).
- <sup>41</sup>M. Stener, G. De Alti, and P. Decleva, *Theor. Chem. Acc.* **101**, 247 (1999).
- <sup>42</sup>M. Stener and P. Decleva, *J. Chem. Phys.* **112**, 10871 (2000).
- <sup>43</sup>M. Stener, G. Fronzoni, and P. Decleva, *Chem. Phys. Lett.* **351**, 469 (2002).
- <sup>44</sup>M. Stener, D. Toffoli, G. Fronzoni, and P. Decleva, *J. Chem. Phys.* **124**, 114306 (2006).
- <sup>45</sup>H. Bachau, E. Cormier, P. Decleva, J. E. Hansen, and F. Martín, *Rep. Prog. Phys.* **64**, 1815 (2001).
- <sup>46</sup>T. D. Thomas, R. Püttner, H. Fukuzawa, G. Prümper, K. Ueda, E. Kukku, R. Sankari, J. Harries, Y. Tamenori, T. Tanaka, M. Hoshino, and H. Tanaka, *J. Chem. Phys.* **127**, 244309 (2007).
- <sup>47</sup>E. Kukku, K. Ueda, U. Hergenhahn, X.-J. Liu, G. Prümper, H. Yoshida, Y. Tamenori, C. Makochekanwa, T. Tanaka, M. Kitajima, and H. Tanaka, *Phys. Rev. Lett.* **95**, 133001 (2005).
- <sup>48</sup>L. Argenti, E. Plésiat, P. Decleva, and F. Martín (unpublished).
- <sup>49</sup>T. X. Carroll, N. Berrah, J. Bozek, J. Hahne, E. Kukku, L. J. Saethre, and T. D. Thomas, *Phys. Rev. A* **59**, 3386 (1999).

## Appendix B

Vibrationally resolved B1s  
photoionization cross section of BF<sub>3</sub>

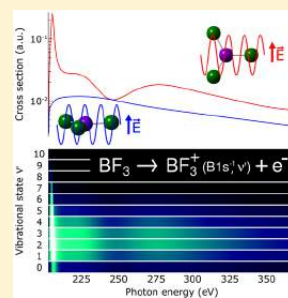




Vibrationally Resolved B 1s Photoionization Cross Section of BF<sub>3</sub>D. Ayuso,<sup>†</sup> M. Kimura,<sup>‡</sup> K. Kooser,<sup>§</sup> M. Patanen,<sup>||</sup> E. Plésiat,<sup>†</sup> L. Argenti,<sup>†</sup> S. Mondal,<sup>‡</sup> O. Travnikova,<sup>||</sup> K. Sakai,<sup>‡</sup> A. Palacios,<sup>†</sup> E. Kukk,<sup>§</sup> P. Decleva,<sup>⊥</sup> K. Ueda,<sup>‡</sup> F. Martín,<sup>\*,†,||,‡</sup> and C. Miron<sup>\*,||,∇</sup><sup>†</sup>Departamento de Química, Módulo 13, Universidad Autónoma de Madrid, 28049 Madrid, Spain<sup>‡</sup>Institute of Multidisciplinary Research for Advanced Materials, Tohoku University, Sendai 980-8577, Japan<sup>§</sup>Department of Physics and Astronomy, University of Turku, 20014 Turku, Finland<sup>||</sup>Synchrotron SOLEIL, L'Orme des Merisiers, Saint-Aubin, BP 48, 91192 Gif-sur-Yvette Cedex, France<sup>⊥</sup>Dipartimento di Scienze Chimiche e Farmaceutiche, Università di Trieste and CNR-Istituto Officina dei Materiali, 34127 Trieste, Italy<sup>||</sup>Instituto Madrileño de Estudios Avanzados en Nanociencia (IMDEA-Nanociencia), Cantoblanco, 28049 Madrid, Spain<sup>#</sup>Condensed Matter Physics Center (IFIMAC), Universidad Autónoma de Madrid, 28049 Madrid, Spain<sup>∇</sup>Extreme Light Infrastructure - Nuclear Physics (ELI-NP), "Horia Hulubei" National Institute for Physics and Nuclear Engineering, 30 Reactorului Street, RO-077125 Măgurele, Jud. Ilfov, Romania

## S Supporting Information

**ABSTRACT:** Photoelectron diffraction is a well-established technique for structural characterization of solids, based on the interference of the native photoelectron wave with those scattered from the neighboring atoms. For isolated systems in the gas phase similar studies suffer from orders of magnitude lower signals due to the very small sample density. Here we present a detailed study of the vibrationally resolved B 1s photoionization cross section of BF<sub>3</sub> molecule. A combination of high-resolution photoelectron spectroscopy measurements and of state-of-the-art static-exchange and time-dependent DFT calculations shows the evolution of the photon energy dependence of the cross section from a complete trapping of the photoelectron wave (low energies) to oscillations due to photoelectron diffraction phenomena. The diffraction pattern allows one to access structural information both for the ground neutral state of the molecule and for the core-ionized cation. Due to a significant change in geometry between the ground and the B 1s<sup>-1</sup> core-ionized state in the BF<sub>3</sub> molecule, several vibrational final states of the cation are populated, allowing investigation of eight different relative vibrationally resolved photoionization cross sections. Effects due to recoil induced by the photoelectron emission are also discussed.



## ■ INTRODUCTION

The availability of high brightness synchrotron radiation (SR) and ultrabright and ultrashort laser sources like Free Electron Lasers (FELs) and tabletop femto- and attosecond lasers has recently enabled imaging of the gas-phase molecules and their wave packets using photoelectron spectroscopy<sup>1,2</sup> to “shine the molecules from within”.<sup>3–7</sup> To capture in time the molecular dynamics, the laser-based studies often employ the widely spread pump–probe techniques, whereas the more conventional SR applications necessarily appeal to the natural times of light-induced molecular processes as a reference. For instance, a number of SR works use the “core–hole clock” method,<sup>8–13</sup> where the ultrashort lifetime of highly excited states offers a practical and relatively tunable time scale. The present work is, however, more focused on extracting structural information and analyzing the physical phenomena induced upon photoabsorption reaching up to a few hundreds of eV.

Recent applications of “photon in–electron out” methods using SR sources on isolated molecules include studies on photoelectron diffraction,<sup>14–17</sup> molecular potentials,<sup>18</sup> and structural characterization using Young double-slit interference.<sup>19–22</sup>

These phenomena and their origin are discussed here in detail. We investigate, both experimentally and theoretically, vibrationally resolved B 1s photoionization cross sections of the boron trifluoride (BF<sub>3</sub>) molecule. This study completes the preliminary results presented by Ueda *et al.*<sup>15</sup> and provides a detailed insight into the data analysis, theoretical modeling, and interpretation of the results using B-spline static-exchange and time-dependent DFT calculations. The present work shows that the oscillatory structure found in the relative cross sections is due to photoelectron diffraction, whereas very close to the photoionization threshold a complete trapping of the photoelectron is observed, manifesting itself as an emission angle dependent shape resonance feature. Finally, we discuss the existence of confinement effects that depend on the angular momentum of the ejected electron.<sup>23,24</sup>

**Special Issue:** Jean-Michel Mestdagh Festschrift

**Received:** November 14, 2014

**Revised:** March 11, 2015

**Published:** March 12, 2015



Atomic units are employed throughout the manuscript unless otherwise stated.

## ■ EXPERIMENT

The experiment was carried out at the PLEIADES beamline<sup>25–28</sup> at the SOLEIL national SR facility in Saint-Aubin, France. The experimental setup is described in the next subsection. It is followed by a detailed explanation of the methodology and software used to perform the analysis of the measured spectra, including a description of the six vibrational modes of the molecule. We finally discuss the procedure used to disentangle the contributions to the experimental spectra from each vibrational mode and from the recoil effect due to the ejection of a fast electron.

**Experimental Setup.** An Apple II-type permanent magnet HU80 (80 mm period) undulator was used to generate the linearly polarized SR, which was further monochromatized by a varied groove depth, varied line spacing, 2400 lines/mm plane grating monochromator. The B 1s photoelectrons were collected using a 30° wide angle lens VG-Scienta R4000 electron energy analyzer, whose detection axis is perpendicular to the storage ring plane containing the propagation axis of the SR. The angle between the polarization vector of the SR and the electron detection axis was selected to be 54.7° to exclude any photon energy dependent modulations of the cross section due to the photoelectron emission anisotropy. Even at the highest used photon energy (570 eV) the dipole approximation is valid.

The gaseous BF<sub>3</sub> sample (Sigma-Aldrich) had a purity of 99.99%. A gas cell equipped with a series of polarized electrodes (VG-Scienta) was used to compensate the plasma potentials present in the interaction region caused by the ion density gradient created along the SR beam. The sample gas pressure was increased as high as there was still a linear increase in the electron count rate; for pressures higher than  $1 \times 10^{-5}$  mbar in the spectrometer chamber, electron attenuation in the gas cell was observed. Therefore, the working pressure was set to  $7 \times 10^{-6}$  mbar inside the spectrometer chamber. The pressure in the gas cell is approximately 2 orders of magnitude higher.

The total instrumental electron energy resolution was  $\approx 30$ –65 meV for the whole set of photon energies used (212–570 eV), determined by the exit slit of the monochromator (photon bandwidth), as well as by the entrance slit and the pass energy of the electron energy analyzer (electron analysis resolution). The electron energy analyzer's curved entrance slit had a fixed value of 0.3 mm during all measurements, but the pass energy of the electron analyzer (either 20 or 50 eV) and the width of the exit slit of the monochromator (between 30 and 100  $\mu\text{m}$ ) were adjusted to achieve the desired resolution. Typically, the instrumental resolution was the highest at low photon energies and it had to be compromised a bit to keep the data collection time reasonable at higher photon energies due to the lower photoionization cross section and the slightly reduced photon flux. The translational Doppler effect broadens the measured spectra, and for BF<sub>3</sub> it was estimated to be at room temperature  $\approx 5$ –29 meV depending on the photoelectron kinetic energy. The Ar 2p<sub>3/2</sub> photoelectron line was recorded with the same settings as the BF<sub>3</sub> spectra at all photon energies used to obtain accurate information about the instrumental broadening, taking into account the lifetime broadening of this atomic line (119 meV<sup>29</sup>).

**Data Analysis.** The B 1s photoelectron spectra were fitted using the Igor Pro data analysis software from WaveMetrics Inc. and the SPANCF fitting macros by Kukk.<sup>30,31</sup> All spectra were

fitted simultaneously. Post-collisional interaction (PCI) line shapes<sup>32</sup> were used in the fitting process with a fixed Lorentzian width, corresponding to the B 1s lifetime broadening of 72 meV reported by Thomas et al.<sup>33</sup> The Gaussian width, representing the instrumental and the translational Doppler broadenings, was kept as a free parameter but was constrained to be the same for all peaks within one spectrum. As the initial guesses for the Gaussian broadening were obtained from the fitted Ar calibration data, only small variations from the initial values were observed. The asymmetry coefficients modeling the low energy tail caused by the PCI effect were calculated from the average Auger electron kinetic energy of  $\approx 160$  eV.<sup>34</sup>

BF<sub>3</sub> molecule has six vibrational modes, two of which are doubly degenerate: the totally symmetric stretching mode (TSSM) A<sub>1</sub>, the “umbrella” bending mode A<sub>2</sub><sup>g</sup>, two asymmetric stretching modes E<sub>2</sub><sup>g</sup>, and two asymmetric bending modes E<sub>2</sub><sup>g</sup>.

The boron atom has two stable isotopes <sup>10</sup>B and <sup>11</sup>B, so that the sample studied was a 1:4 mixture of <sup>10</sup>BF<sub>3</sub> and <sup>11</sup>BF<sub>3</sub> isotopologues. The vibrational frequencies of these two molecular species are slightly different, except for the TSSM. The harmonic frequencies and anharmonicity of the TSSM were determined from a Morse potential fit to the energy spacing of the B 1s photoelectron peaks determined from a low photon energy, high-resolution measurement. The constants derived from the fit for the B 1s core-ionized state of BF<sub>3</sub> molecule are  $\omega_e = 1031.1 \text{ cm}^{-1} = 128 \pm 1 \text{ meV}$ , and  $\omega_e x_e = -1.2 \text{ cm}^{-1} = -0.1 \pm 0.1 \text{ meV}$ , in line with the values reported by Thomas et al.<sup>33</sup> Therefore, the obtained energy spacings between the symmetric stretching vibrational peaks  $\nu' = 0$ –8 were kept fixed during the simultaneous fit of all spectra.

In the first approximation, only the TSSM should be active in B 1s photoionization. However, the recoil-induced momentum transfer between the boron atom and the emitted core photoelectron leads to a displacement of the central B atom, thus leading to a situation where the umbrella mode, the asymmetric stretching and the bending modes also become active. In practice, this means that in a photoelectron spectrum a given symmetric stretching vibrational peak is accompanied by six other (much smaller) vibrational peaks (A<sub>2</sub><sup>g</sup>, E<sub>2</sub><sup>g</sup>, and E<sub>2</sub><sup>g</sup> modes of <sup>10</sup>BF<sub>3</sub> and <sup>11</sup>BF<sub>3</sub> isotopologues).

**Estimation of the Signal Intensity for the Recoil-Activated Vibrational Modes.** To be able to fit the studied photoelectron spectra one has to know the relative intensities of the peaks associated with the recoil excitation with respect to the symmetric stretching peaks, which are much more intense and can be fitted in the spectrum unambiguously.

We now report how the contribution of the recoil-excited vibrational modes was taken into account in the data analysis. It is reasonable to assume that because the photoelectron is emitted from the core-shell of the B atom, the momentum exchange solely takes place between the photoelectron and the B atom. The recoil generates a displacement of the B atom from its equilibrium position, and the specific emission direction of the photoelectron (in the molecular plane/perpendicular to the plane) leads to the activation of specific vibrational modes. Consequently, to extract the signal associated with a given vibrational mode from the measured photoelectron spectra, we first need to know the relative intensities of the peaks associated with the recoil excitation compared to the symmetric stretching vibrational peaks that are directly observable owing to their much higher intensity and can be fitted in the spectrum unambiguously. On the one hand, the recoil-activated peaks are so small and overlapped by the much more intense TSSM peaks that they

cannot be fitted freely without making sophisticated assumptions concerning their relative intensities and energy positions, but on the other hand, at higher energies their modeling is necessary to produce a reasonable fit of the TSSM peaks (see Figure 1 for a demonstration of the recoil contributions at low (225 eV, panel a) and high (570 eV, panel b) photon energies).

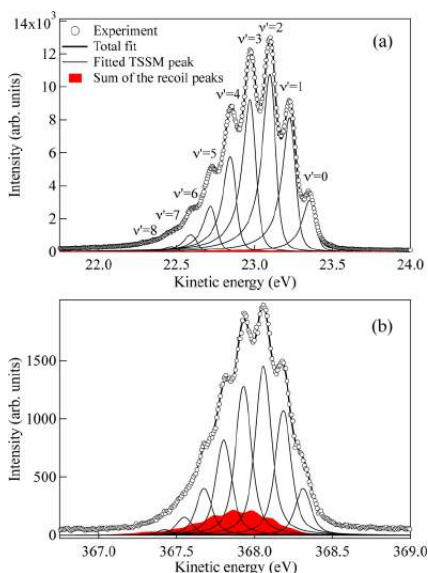


**Figure 1.** B 1s photoelectron spectrum of BF<sub>3</sub> measured with (a)  $\hbar\omega = 225$  eV (b)  $\hbar\omega = 570$  eV: experimental data points (circles), fit result (thick solid line), individual fitted TSSM peaks (thin solid lines), and sum of all the fitted peaks of the recoil-activated vibrations (filled area). The vibrational quantum numbers of the TSSM peaks are given in panel a.

The umbrella mode  $A_2''$  is activated when the electron is emitted out-of-plane, and the in-plane modes,  $E_4'$  and  $E_6'$ , are active when the photoelectron is emitted parallel to the molecular plane. When considering the relative transition probabilities for a given vibrational state, one has to perform orientational averaging to properly describe the randomly oriented sample studied here. We used the DALTON2011 code<sup>35</sup> to compute the vibrational frequencies and the atomic displacements at the Hartree–Fock level with the 6-311++G\*\* basis set.<sup>36</sup> It has been assumed that the vibrational frequencies are the same in the ground and the core-ionized states (linear-coupling model). The transition probabilities  $P_{V,\nu'}$  from ground state  $\chi_{V,0}^{\text{BF}_3}$  to an ionized state with recoil-activated vibrational modes  $\chi_{V,\nu'}^{\text{BF}_3^+}$ ,  $V = \{A_2'', E_4', E_6'\}$ , are due to the momentum exchange  $\Delta P$  between the photoelectron of momentum  $k_{\perp/\parallel}$  and the B atom and can be calculated as follows:

$$P_{V,\nu'} = |\langle \chi_{V,\nu'}^{\text{BF}_3^+} | \hat{T}_V(k_{\perp/\parallel}) | \chi_{V,0}^{\text{BF}_3} \rangle|^2 = |\langle \nu' | e^{-i\Delta P \hat{Q}} | 0 \rangle|^2 = \left| \frac{e^{\Delta P^2/4}}{\sqrt{\nu'!}} \left( \frac{-i\Delta P}{\sqrt{2}} \right)^{\nu'} \right|^2 \quad (1)$$

$$\Delta P = k_{\perp/\parallel} \Delta R_B / Q_V = k_{\perp/\parallel} \frac{U_{B_{\perp/\parallel}V}}{\sqrt{\omega_V M_B}} \quad (2)$$

where the displacement  $U_{B_{\perp/\parallel}V}$  of the B atom (mass  $M_B = 18252$  au,  $M_B = 200269$  au) in a specific mode with the frequency  $\omega_V$  to the direction perpendicular/parallel to the molecular plane is expressed in normal coordinates  $Q$ . We have calculated the following values for  $U_{B_{\perp/\parallel}V}$ :  $U_{B_{\perp/\parallel}A_2''} = 0.9223$ ,  $U_{B_{\perp/\parallel}E_4''} = 0.9154$ ,  $U_{B_{\perp/\parallel}E_6''} = 0.8769$ ,  $U_{B_{\perp/\parallel}E_4'} = 0.8661$ ,  $U_{B_{\perp/\parallel}E_6'} = 0.2966$ , and  $U_{B_{\perp/\parallel}E_6''} = 0.2857$ . From these values one can immediately notice that in the mode  $E_6'$  the B atom barely moves, and its contribution will be negligible. The computed vibrational frequencies used in the simulation for  $^{10}\text{BF}_3$  ( $^{11}\text{BF}_3$ ) were the following:  $\omega_{A_2''} = 0.00327$  (0.00315) au,  $\omega_{E_4'} = 0.0686$  (0.00663) au, and  $\omega_{E_6'} = 0.00220$  (0.00219) au.

Using eqs 1 and 2, we obtain the ratio

$$\frac{P_{V,1}}{P_{V,0}} = \frac{|\langle 1 | e^{-i\Delta P \hat{Q}} | 0 \rangle|^2}{|\langle 0 | e^{-i\Delta P \hat{Q}} | 0 \rangle|^2} = \frac{\Delta P^2}{2} \quad (3)$$

Applying the values listed above to estimate  $\Delta P$  in eq 3 and taking the orientational average (1/3 in case of  $A_2''$  mode and 2/3 in case of  $E$  modes) into account, we obtain the following relations for the probabilities  $P_{V,1}$  and  $P_{V,0}$  with a linear dependence on the kinetic energy of the photoelectron  $\varepsilon$ :

$$\begin{aligned} ^{10}\text{BF}_3: P_{A_2'',1} &= 0.00472 \cdot P_{A_2'',0} \cdot \varepsilon, P_{E_4',1} = 0.00410 \cdot P_{E_4',0} \cdot \varepsilon, P_{E_6',1} = \\ &0.00146 \cdot P_{E_6',0} \cdot \varepsilon \\ ^{11}\text{BF}_3: P_{A_2'',1} &= 0.00441 \cdot P_{A_2'',0} \cdot \varepsilon, P_{E_4',1} = 0.00376 \cdot P_{E_4',0} \cdot \varepsilon, P_{E_6',1} = \\ &0.00124 \cdot P_{E_6',0} \cdot \varepsilon \end{aligned}$$

These ratios were further weighted by the abundance of the corresponding isotope. Even at the highest studied photon energies the intensities of the recoil-excited peaks represented at most around 5% of the main TSSM peak. During the fitting process, the energy spacings were kept fixed, and the peak shapes were kept the same for all the peaks, so in the end the optimized fitting parameters were the energy positions and the intensities of the TSSM peaks, the Gaussian line width of the highest intensity peak (to which all the other peaks were linked), and a linear background.

## THEORY

Vibrationally resolved cross sections have been evaluated to first order of perturbation theory within the Born–Oppenheimer and the dipole approximations:<sup>37</sup>

$$\sigma_{\alpha}(\nu, \nu', \omega) = \frac{4\pi^2 \omega}{3c} \sum_{lh} |\langle \chi_{\nu'}(R) | \mu_{\text{ath}}(\varepsilon, R) | \chi_{\alpha, \nu}(R) \rangle|^2 \quad (4)$$

where  $\mu_{\text{ath}}(\varepsilon, R)$  is the electronic dipole-transition matrix element,  $\alpha$  denotes the electronic state of the residual ion, the indexes  $lh$  define the final symmetry of the photoelectron,  $l$  being its angular quantum number,  $\omega$  and  $\varepsilon$  are the photon and the photoelectron energies, which are related through the equation  $\varepsilon = \hbar\omega - E_{\alpha}^{\nu'}$ , where  $E_{\alpha}^{\nu'} = E_{\alpha\nu'} - E_{0\nu}$  is the energy required to produce the ion in the  $\alpha\nu'$  vibronic state,  $\nu$  and  $\nu'$  being the vibrational quantum numbers of the neutral and the ionized species, respectively, in the TSSM, and  $\chi_{\nu}(R)$  and  $\chi_{\alpha, \nu'}(R)$  are the corresponding vibrational wave functions, depending on the TSSM coordinate  $R$ , i.e., the internuclear boron–fluorine distance.

Electronic states have been evaluated using the static-exchange density functional theory (DFT) method developed by Declewa and collaborators,<sup>38,39</sup> which makes use of the Kohn–Sham DFT

to describe molecular states and of the Galerkin approach to evaluate continuum electron wave functions in the field of the corresponding Kohn–Sham density. A more sophisticated time-dependent version (TDDFT),<sup>40,41</sup> which takes into account the coupling between photoionization channels, has also been employed. Both methods have been shown to provide accurate results for the total cross sections of small molecules as well as for medium and large size systems within the fixed nuclei approximation (see ref 38 and references therein). To evaluate vibrationally resolved cross sections, we have computed  $\mu_{\text{clh}}(E, R)$  for different values of  $R$ , corresponding to the positions adopted by the nuclei along their vibration in the TSSM, which is the most relevant vibrational mode in core ionization, as clearly shown by the experimental data. In particular, around the Franck–Condon (FC) region we carried out the calculations for 41 different molecular geometries.

Bound and continuum electronic states were expanded in a multicentric basis set of B-splines and symmetry adapted<sup>42</sup> linear combinations of real spherical harmonics with origin over different positions in the molecule:

- A large one-center expansion (OCE) over the center of mass, which provides an accurate description of the long-range behavior of the continuum states. For our specific target, the TSSM in  $\text{BF}_3$ , it matches the position of the B atom.
- Small expansions, called off-centers (OC), located over the nonequivalent nuclei. They improve dramatically the convergence of the calculation, allowing us to reduce the angular expansion in the OCE, because they can effectively describe the Kato cusps<sup>43</sup> at the nuclear positions. In this case, only one nonequivalent expansion over the fluorine atoms was required. Because the OCE is already placed at the B atom, no additional OC is required.

The elements of the basis set may be written as

$$\xi_{nlh\lambda\mu}^p = \sum_{q \in \Lambda_p} \frac{1}{r_q} B_n^{\kappa}(r_q) \sum_m b_{mlh\lambda\mu}^q Y_{lm}(\theta_q, \varphi_q) \quad (5)$$

where  $\Lambda_p$  represents a shell of equivalent centers ( $p = 0$  refers to the OCE),  $q$  runs over the centers in the shell,  $n$  is an index over the B-spline functions  $B_n^{\kappa}$ , whose order is  $\kappa = 10$ ,  $\lambda\mu$  are the indexes of the irreducible representation (see ref 39),  $h$  runs over the linearly independent angular functions, which are constructed as linear combinations of real spherical harmonics associated with a fixed angular quantum number  $l$ , and the coefficients  $b_{mlh\lambda\mu}^q$  are determined by symmetry.<sup>42</sup>

The parameters employed in this work for the electronic structure calculations are shown in Table 1. A large amount of

**Table 1. Computational Parameters of the Basis Set Employed in the Expansion of the Electronic Wave Functions: Maximum Distance from the Origin  $R_{\text{max}}$ , Number of B-Spline Functions  $N_{\text{max}}$ , and Highest Angular Momentum  $l_{\text{max}}$**

Expansion	Origin	$R_{\text{max}}$ (au)	$N_{\text{max}}$	$l_{\text{max}}$
OCE	B atom	30.0	150	20
OC	F atoms	0.6	10	2

computational effort was saved by dividing the 3-dimensional space into 12 equivalent regions because the molecule belongs to the  $D_{3h}$  point group. Electronic exchange and correlation effects were described using the VWN<sup>44</sup> local density approximation functional, and the Amsterdam Density Functional<sup>45,46</sup> (ADF) package was employed to generate the initial guess of the

electronic density with a double  $\zeta$ -polarization plus basis set (taken from the ADF library).

The relevant vibrational eigenstates of the neutral and the ionized species (Figure 2) were obtained by solving the

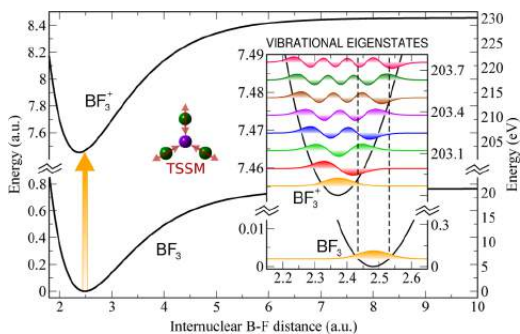


**Figure 2.** Morse potential energy curves along the TSSM coordinate of the electronic ground state of  $\text{BF}_3$  and of the core-hole species generated upon B 1s ionization (black lines), constructed from reliable spectroscopic parameters.<sup>33,47–50</sup> The relevant vibrational eigenstates are shown: the ground state of the neutral molecule (orange) and the low-lying states of the ion (different colors), as well as the FC region (dashed black lines).

corresponding eigenvalue problems in the TSSM coordinate  $R$ , using a basis set of 500 B-splines in a box of 15 au. The required potential energy curves (also shown in Figure 2) were constructed within the Morse approximation from reliable spectroscopic parameters available in the literature ( $\text{BF}_3$ :  $R_{\text{eq}} = 2.481$  au,<sup>47</sup>  $\omega_e = 888$   $\text{cm}^{-1}$ ,<sup>48</sup>  $\omega_e x_e = 1.201$ ;<sup>49</sup>  $\text{BF}_3^+$ :  $R_{\text{eq}} = 2.371$  au,<sup>33</sup>  $\omega_e = 1033$   $\text{cm}^{-1}$ ,<sup>33</sup>  $\omega_e x_e = 1.2$   $\text{cm}^{-1}$ ,<sup>33</sup> ionization energy = 202.8 eV<sup>50</sup>).

## RESULTS AND DISCUSSION

**Vibrational Branching Ratios.** The comparison between experiment and theory for the vibrational branching ratios ( $\nu$ -ratios)  $I(\nu')/I(\nu'=2)$ , for  $\nu' = 0-8$  is shown in Figure 3. Experimentally, presenting the cross sections as  $\nu$ -ratios is advantageous because certain calibration problems that one would face in the case of absolute cross section can be avoided. The rapid decrease of the photoionization cross section as a function of photon energy increases the acquisition times at high photon energies but does not affect the cross section oscillations when the  $\nu$ -ratios are shown, because this decrease is of atomic origin and will thus be the same for each vibrational component. We have chosen  $\nu' = 2$  as the common denominator because it represents the largest contribution at most photon energies. All  $\nu$ -ratios exhibit pronounced oscillations as a function of the photoelectron momentum, and near the ionization threshold the theoretical curve shows a very sharp structure. Obviously, the absolute, vibrationally resolved cross sections change with photon energy for all vibrational channels and the structures found in the  $\nu$ -ratios are a consequence of the different modulations. The oscillations found in the high-energy region are due to intramolecular scattering and their periodicity is  $2k_e R$ , where  $k_e$  is the photoelectron momentum and  $R$  the distance between the emitting (B) and the diffracting (F) atoms. The same periodicity appears in the well-known EXAFS equation,<sup>51</sup> where each  $\sin(2R_n k_e + \delta)$  term accounts for the diffraction from the  $n^{\text{th}}$  shell of surrounding atoms in a crystalline solid.

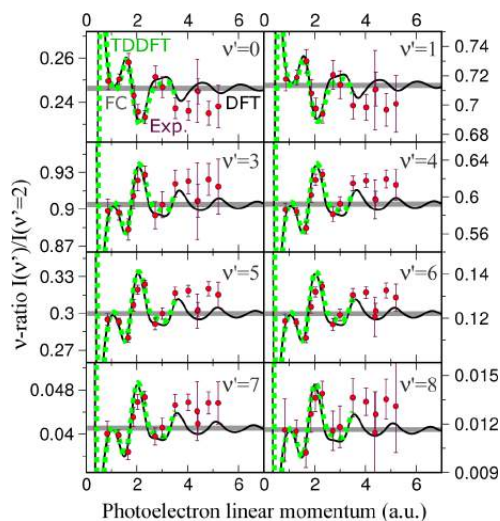


**Figure 3.**  $\nu$ -ratios corresponding to B 1s photoionization of  $\text{BF}_3$  in the totally symmetric stretching mode.  $\nu' = 2$  has been chosen as the common denominator because it represents the larger contribution to the total cross section at most energies. The momentum of the photoelectron is defined with respect to the vibrational ground state of the core-hole species. Key: green squares, TDDFT results; black lines, static-exchange DFT results; circles with error bars, experimental data including statistical errors; gray thick lines, ratios between the FC factors.

Such patterns, which are difficult to observe in the absolute spectra, are magnified in the  $\nu$ -ratios. It has been recently demonstrated<sup>15</sup> that, for a given molecule, all  $\nu$ -ratios carry the same information. In fact, their overall shape is essentially the same for  $\nu' \geq 3$ ; in the case  $\nu' = 0$  and  $\nu' = 1$ , they also seem very similar but inverted. A unified way of presenting the results for all vibrational levels through the so-called generalized  $\nu$ -ratio is discussed in the Supporting Information. In the present case the vibrational contributions are referred to  $\nu' = 2$ , but if we had chosen  $\nu' = 4$  instead, then the first four  $\nu$ -ratios would have been inverted. Figure 4 shows the theoretical, vibrationally resolved

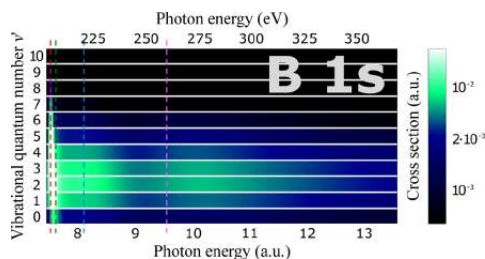


**Figure 4.** Vibrationally resolved B 1s photoionization cross section of  $\text{BF}_3$  in the totally symmetric stretching mode. They have been computed using the TDDFT method. Cuts of the 2D spectra are shown in Figure 5.

B 1s photoionization cross sections of  $\text{BF}_3$ , computed using the TDDFT methodology and plotted now as a function of the photon energy for analysis purposes. In good agreement with the experimental spectra shown in Figure 1, we observe a large

progression of vibrational states reaching up to  $\nu' = 8$ ;  $\nu' = 2$  and  $\nu' = 3$  are the dominant contributions at any photoelectron energy. This is a consequence of the favorable FC overlap between the initial  $\chi_i(R)$  and several final-state vibrational wave functions  $\chi_{i\nu'}(R)$  due to the large bond contraction accompanying core-ionization ( $\Delta R_{\text{BF}} = -0.110 \text{ \AA}$ ).<sup>33</sup> Cuts of the theoretical 2-dimensional vibrationally resolved cross section (Figure 4) at selected photon energies are shown in Figure 5 as a function

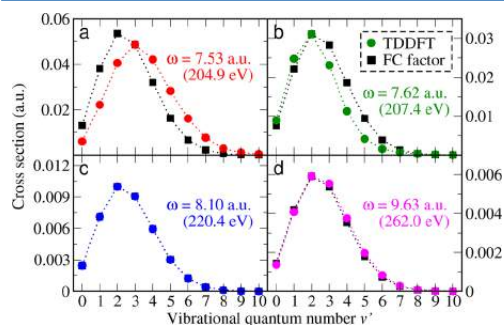


**Figure 5.** Vibrationally resolved B 1s photoionization cross section of  $\text{BF}_3$  in the totally symmetric stretching mode at selected photon energies (colored circles) corresponding to the vertical cuts indicated in Figure 3. The FC factors (black squares), scaled to the maximum value of the cross section in each case, are shown for comparison.

of the vibrational quantum number  $\nu'$  together with the calculated FC factors, i.e., the overlap between the corresponding vibrational wave functions (scaled in each case to the larger value of the cross section for a clearer comparison). The deviations from the FC predictions are rather apparent (Figure 5a,b).

To decipher the structures in the  $\nu$ -ratios, and the deviation from the FC predictions, we have analyzed the partial and total cross sections in detail.

**Total Cross Section.** Figure 6 presents the total B 1s photoionization cross sections of  $\text{BF}_3$  in the photon energy range 7.45–32 au, obtained by summing over all the vibrational contributions provided by the static-exchange and the time-dependent DFT methods, as explained above. Although the latter introduces the coupling between ionization channels and therefore is expected to be more accurate, we have found that both approaches provide equivalent results: the curves are slightly shifted in energy near the ionization threshold, but they reproduce the same structures and become indistinguishable at higher energies. This implies that interchannel coupling does not play an important role in the description of this process and that therefore one can rely on the computationally less expensive DFT to analyze the features appearing in the high-energy region.

We have performed calculations with different orientations of the molecule with respect to the polarization vector of the synchrotron radiation (SR). The photoelectron is ejected with  $E'$  symmetry when the molecular plane is parallel to the  $\vec{E}$  vector and with  $A_2''$  when it is perpendicular. In the case of randomly oriented molecules, the total cross section can be easily retrieved by combining all available symmetries and the weight of each contribution can be obtained by symmetry considerations. In the parallel case (Figure 6) we find a sharp structure near the ionization threshold, which is due to a shape resonance.<sup>52,53</sup> This sharp feature, also visible in the  $\nu$ -ratios, does not follow the

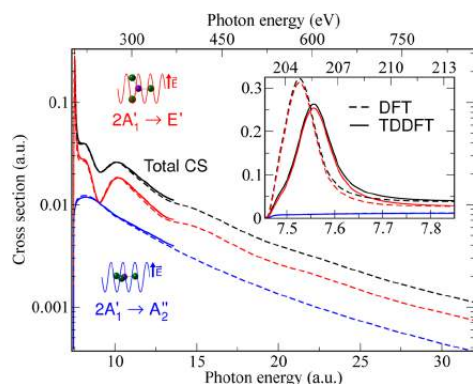


**Figure 6.** B 1s photoionization cross section of  $\text{BF}_3$  computed using the static-exchange DFT (dashed lines) and the TDDFT (full lines) methods. The total cross section is shown for the case of randomly oriented molecules (black lines) and for the molecular plane being parallel (red lines) and perpendicular (blue lines) to the polarization vector  $\vec{E}$  of the synchrotron radiation. The nuclear motion has been taken into account as explained in the text. Main figure: full energy-range (logarithmic scale). Right upper panel: magnified low energy region (linear scale).

intramolecular scattering patterns and depends on the electronic molecular potential. The origin of these structures can be understood in terms of a quasi-bound state embedded in the electronic continuum due to the presence of a small barrier in the electronic potential. A thorough analysis of the Kohn–Sham term in the Hamiltonian revealed that in this case the barrier was not entirely due to the electrostatic potential but to the interplay with the centrifugal forces. There are two additional peaks appearing at 8 and 10.1 au (218 and 275 eV) of photon energy (B 1s ionization threshold is 202.8 eV<sup>50</sup>) that are due to an intramolecular scattering effect: in its way out from the molecule, the photoelectron is diffracted by the surrounding atomic centers giving rise to constructive and destructive interferences between the different ionization paths. However, as the photon energy increases, the presence of these structures is less apparent in the total cross sections due to their rapid decay. As already indicated, a better analysis can be performed by calculating the  $\nu$ -ratios (Figure 3), where the diffraction patterns are imprinted as clear oscillations as a function of the photoelectron momentum also in the high energy range. This phenomenon has been recently observed in the  $\text{CH}_4$ ,<sup>37</sup>  $\text{CF}_4$ ,<sup>54</sup> and  $\text{CO}$ <sup>17</sup> molecules. In the case of  $\text{CH}_4$  the magnitude of the cross section oscillation is smaller due to the reduced size of the hydrogen atoms (scattering centers) and the effect was not so apparent in the total cross section. The  $\text{CF}_4$  C 1s cross section shows a behavior very similar to that for  $\text{BF}_3$ : the low energy region (photon energy about 0.3 au above the C 1s threshold) is dominated by the large shape resonance contribution, and the first photoelectron diffraction peak is observed at 2.7 au above the threshold.

Because the photoelectron's angular momentum is not well-defined due to the lack of spherical symmetry, we have performed an angular expansion of the electronic wave function (eqs 4 and 5). The contribution from each angular term to the total cross section, i.e., partial wave, is plotted in Figure 7 for both parallel (a) and perpendicular (b) orientations. As expected, only the lowest values of  $l$  contribute significantly to the cross sections near the threshold and as the energy increases higher angular

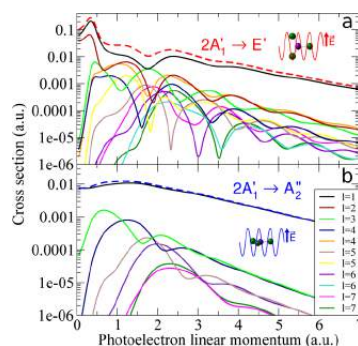


**Figure 7.** Total cross sections corresponding to B 1s photoionization of  $\text{BF}_3$  when the polarization vector  $\vec{E}$  of the SR is parallel (a) and perpendicular (b) to the molecular plane computed using the DFT method taking the nuclear motion into account. Colored solid lines present contributions from different angular momenta (partial waves), and the dashed line is the sum of these partial waves.

angular momenta become more important. In this work we have employed an expansion up to  $l = 20$  to ensure the convergence at high photoelectron energies. An angular momentum of  $l = 0$  for the ejected electron is forbidden by symmetry and  $l = 1$  represents the largest contribution in the entire energy range for the two available symmetries of the photoelectron. The shape resonance is seen as a large increase in the waves  $l = 1$  and  $l = 2$  near the ionization threshold when the molecular plane is parallel to the field (Figure 7a), and naturally, no such structure is observed when they are perpendicular (Figure 7b), because its origin is in the anisotropy of the molecular potential created by the fluorine atoms.

The most noteworthy feature in Figure 7 is probably that all partial waves show pronounced dips when the electron is ejected along the molecular plane, i.e., with  $E'$  symmetry (Figure 7a). The origin of these dips can be understood in terms of a confinement effect,<sup>23,24</sup> which is a consequence of the poor radial overlap between the initial wave function and a given angular component of the final one at some photoelectron energies. These structures<sup>55</sup> have been widely analyzed in  $\text{H}_2^+$  and  $\text{H}_2$ <sup>23,24</sup> using a one-dimensional particle-in-a-box model. The authors found that such minima are expected to arise when the photoelectron momentum  $k_e$  satisfies the relation  $k_e R_e = l\pi$ ,  $l$  being its angular momentum and  $R_e$  the equilibrium distance between the two nuclei. The minima predicted by this simple formula coincide with those of the transmission probability of an electron being scattered by two Dirac  $\delta$  distributions separated by a distance  $R_e$  at high energies, due to destructive interferences.<sup>24</sup> More recently, this confinement effect has been studied in other diatomic molecules ( $\text{Li}_2^+$ ,<sup>56</sup>  $\text{N}_2$ ,  $\text{CO}$ ,<sup>57</sup> and  $\text{F}_2$ <sup>58</sup>). Obviously, the situation is more complex in the case of a polyatomic molecule and a straightforward comparison is no longer valid. Nonetheless, the electrostatic potential created by the fluorine atoms can be idealized at low photoelectron energies as an equilateral billiard triangle, i.e., a triangular infinite well whose side is  $3^{1/2}R_{\text{eq}}$  where  $R_{\text{eq}}$  is the boron–fluorine equilibrium distance in the neutral molecule ( $R_{\text{eq}} = 2.481$  au<sup>47</sup>). The eigenfunctions of this triangle can be evaluated analytically using different approaches (see ref 59 and references therein). In particular, the energies of the low-lying eigenstates with  $E'$  symmetry are 3.32, 6.17, and 9.02 au,<sup>59</sup> which correspond to photoelectron linear momenta of

2.58, 3.51, and 4.25 au, respectively. Although the electrostatic potential created by the fluorine atoms is rather small compared to the energies discussed here, the qualitative agreement between these values and the minima appearing in the lowest wave ( $l = 1$  in Figure 7a) suggests that the photoelectron is confined within the molecular cage at some given energies. As already indicated, this partial wave is dominant in the entire energy range and, consequently, the dips shown in its profile are also imprinted in the total cross section.

## CONCLUSIONS

In this paper we have presented the vibrationally resolved B 1s photoionization cross section of the  $\text{BF}_3$  molecule. The accurate experimental determination of the relative cross sections ( $\nu$ -ratios) required the recoil effects to be taken into account. We observed that when the de Broglie wavelength of the photoelectron is comparable to the dimensions of the molecular target, i.e., for photon energies of the order of a few hundreds of electronvolts, the undulatory nature of the electron manifests through diffraction by the surrounding atomic centers, whereas at low photon energies the cross sections show a sharp feature due to a shape resonance. From the theoretical calculation, and its angular momentum decomposition, one can also confirm the existence of confinement effects as those previously described for diatomic molecules. In the future,  $\text{BF}_3$  ( $\text{CH}_4$ ,  $\text{CF}_4$ ,  $\text{CO}$ , ...) could provide an interesting workbench to study the photoelectron scattering phenomenon in a time-resolved (pump–probe) scheme at new monochromatic ultrahigh intensity photon sources like seeded FELs, which now become available.

## ASSOCIATED CONTENT

### Supporting Information

Discussion of the Generalized  $\nu$ -ratios and G factor. This material is available free of charge via the Internet at <http://pubs.acs.org>.

## AUTHOR INFORMATION

### Corresponding Authors

\*C. Miron. E-mail: [catalin.miron@synchrotron-soleil.fr](mailto:catalin.miron@synchrotron-soleil.fr).

\*F. Martin. E-mail: [fernando.martin@uam.es](mailto:fernando.martin@uam.es).

### Notes

The authors declare no competing financial interest.

## ACKNOWLEDGMENTS

Data collection was performed at the PLEIADES beamline at the SOLEIL Synchrotron, France (proposal no. 20110781). We are grateful to E. Robert, X.-J. Liu, and C. Nicolas for technical assistance, and to the SOLEIL staff for stable operation of the equipment and storage ring during the experiments. We thank Mare Nostrum BSC, Cineca, and CCC-UAM for allocation of computer time. Work supported by the Advanced Grant of the European Research Council XCHEM 290853, the MICINN project Nos. FIS2010-15127 and FIS2013-42002-R (Spain), the ERA-Chemistry project PIM2010EEC-00751, the European grants MC-ITN CORINF and MC-RG ATTOTREND, the European COST Actions CM0702 (CUSPFEL) and CM1204 (XLIC), the MC-IEF CHICROCSX under the grant agreement no. 252781 (OT) and the I3 program, the MEXT, and JSPS agencies (Japan), and the Academy of Finland.

## REFERENCES

(1) Vrakking, M. J. J. Attosecond Imaging. *Phys. Chem. Chem. Phys.* **2014**, *16*, 2775–2789.

(2) Miron, C.; Patanen, M. Synchrotron-Radiation-Based Soft X-Ray Electron Spectroscopy Applied to Structural and Chemical Characterization of Isolated Species, from Molecules to Nanoparticles. *Adv. Mater.* **2014**, *26*, 7911–7916.

(3) Haessler, S.; Caillat, J.; Boutu, W.; Giovanetti-Teixeira, C.; Ruchon, T.; Auguste, T.; Diveki, Z.; Breger, P.; Maquet, A.; Carre, B.; et al. Attosecond Imaging of Molecular Electronic Wavepackets. *Nat. Phys.* **2010**, *6*, 200–206.

(4) Rouzée, A.; Johnsson, P.; Rading, L.; Hundertmark, A.; Siu, W.; Huismans, Y.; Duesterer, S.; Redlin, H.; Tavella, F.; Stojanovic, N.; et al. Towards Imaging of Ultrafast Molecular Dynamics Using FELs. *J. Phys. B: At, Mol. Opt. Phys.* **2013**, *46*, 164029.

(5) Poisson, L.; Nandi, D.; Soep, B.; Hochlaf, M.; Boggio-Pasqua, M.; Mestdagh, J.-M. A Roaming Wavepacket in the Dynamics of Electronically Excited 2-hydroxypyridine. *Phys. Chem. Chem. Phys.* **2014**, *16*, 581–587.

(6) Boll, R.; Anielski, D.; Bostedt, C.; Bozek, J. D.; Christensen, L.; Coffee, R.; De, S.; Declava, P.; Epp, S. W.; Erk, B.; et al. Femtosecond Photoelectron Diffraction on Laser-Aligned Molecules: Towards Time-Resolved Imaging of Molecular Structure. *Phys. Rev. A* **2013**, *88*, 061402 (1–5).

(7) Landers, A.; Weber, T.; Ali, I.; Cassimi, A.; Hattass, M.; Jagutzki, O.; Nauert, A.; Osipov, T.; Staudte, A.; Prior, M. H.; et al. Photoelectron Diffraction Mapping: Molecules Illuminated from Within. *Phys. Rev. Lett.* **2001**, *87*, 013002.

(8) Morin, P.; Nenner, I. Atomic Autoionization Following Very Fast Dissociation of Core-Excited HBr. *Phys. Rev. Lett.* **1986**, *56*, 1913–1916.

(9) Björnehölm, O.; Sundin, S.; Svensson, S.; Marinho, R. R. T.; Naves de Brito, A.; Gel'mukhanov, F.; Ågren, F. Femtosecond Dissociation of Core-Excited HCl Monitored by Frequency Detuning. *Phys. Rev. Lett.* **1997**, *79*, 3150–3153.

(10) Gel'mukhanov, F.; Ågren, H. Resonant X-ray Raman Scattering. *Phys. Rep.* **1999**, *312*, 87–330.

(11) Kitajima, M.; Ueda, K.; de Fanis, A.; Furuta, T.; Shindo, H.; Tanaka, H.; Okada, K.; Feifel, R.; Sorensen, S. L.; Gel'mukhanov, F.; et al. Doppler Effect in Resonant Photoemission from  $\text{SF}_6$ : Correlation between Doppler Profile and Auger Emission Anisotropy. *Phys. Rev. Lett.* **2003**, *91*, 213003.

(12) Miron, C.; Morin, P. *Handbook of High-resolution Spectroscopy*; John Wiley & Sons, Ltd.: New York, 2011.

(13) Morin, P.; Miron, C. Ultrafast Dissociation: An Unexpected Tool for Probing Molecular Dynamics. *J. Electron Spectrosc. Relat. Phenom.* **2012**, *185*, 259–266.

(14) Söderström, J.; Mårtensson, N.; Travnikova, O.; Patanen, M.; Miron, C.; Sæthre, L. J.; Børve, K. J.; Rehr, J. J.; Kas, J. J.; Vila, F. D.; et al. Nonstoichiometric Intensities in Core Photoelectron Spectroscopy. *Phys. Rev. Lett.* **2012**, *108*, 193005.

(15) Ueda, K.; Miron, C.; Plésiat, E.; Argenti, L.; Patanen, M.; Kooser, K.; Ayuso, D.; Mondal, S.; Kimura, M.; Sakai, K.; et al. Intramolecular Photoelectron Diffraction in the Gas Phase. *J. Chem. Phys.* **2013**, *139*, 124306 (1–6).

(16) Kazama, M.; Fujikawa, T.; Kishimoto, N.; Mizuno, T.; Adachi, J.-i.; Yagishita, A. Photoelectron Diffraction from Single Oriented Molecules: Towards Ultrafast Structure Determination of Molecules Using X-Ray Free-Electron Lasers. *Phys. Rev. A* **2013**, *87*, 063417.

(17) Kukk, E.; Ayuso, D.; Thomas, T. D.; Declava, P.; Patanen, M.; Argenti, L.; Plésiat, E.; Palacios, A.; Kooser, K.; Travnikova, O.; et al. Effects of Molecular Potential and Geometry on Atomic Core-Level Photoemission Over an Extended Energy Range: The Case Study of the CO Molecule. *Phys. Rev. A* **2013**, *88*, 033412 (1–7).

(18) Kimberg, V.; Miron, C. Molecular Potentials and Wave Function Mapping by High-Resolution Electron Spectroscopy and Ab Initio Calculations. *J. Electron Spectrosc. Relat. Phenom.* **2014**, *195*, 301–306.

(19) Liu, X.-J.; Cherepkov, N. A.; Semenov, S. K.; Kimberg, V.; Gel'mukhanov, F.; Prümper, G.; Lischke, T.; Tanaka, T.; Hoshino, M.; Tanaka, H.; et al. Young's Double-Slit Experiment Using Core-Level Photoemission from  $\text{N}_2$ : Revisiting Cohen-Fano's Two-Centre Interference Phenomenon. *J. Phys. B: At, Mol. Opt. Phys.* **2006**, *39*, 4801.

- (20) Canton, S. E.; Plésiat, E.; Bozek, J. D.; Rude, B. S.; Decleva, P.; Martín, F. Direct Observation of Young's Double-Slit Interferences in Vibrationally Resolved Photoionization of Diatomic Molecules. *Proc. Natl. Acad. Sci. U. S. A.* **2011**, *108*, 7302–7306.
- (21) Kushawaha, R. K.; Patanen, M.; Guillemin, R.; Journal, L.; Miron, C.; Simon, M.; Piancastelli, M. N.; Skates, C.; Decleva, P. From Double-Slit Interference to Structural Information in Simple Hydrocarbons. *Proc. Natl. Acad. Sci. U. S. A.* **2013**, *110*, 15201–15206.
- (22) Ilchen, M.; Glaser, L.; Scholz, F.; Walter, P.; Deinert, S.; Rothkirch, A.; Seltmann, J.; Viehhaus, J.; Decleva, P.; Langer, B.; et al. Angular Momentum Sensitive Two-Center Interference. *Phys. Rev. Lett.* **2014**, *112*, 023001 (1–5).
- (23) Fernández, J.; Fojón, O.; Palacios, A.; Martín, F. Interferences from Fast Electron Emission in Molecular Photoionization. *Phys. Rev. Lett.* **2007**, *98*, 043005 (1–4).
- (24) Fernández, J.; Fojón, O.; Martín, F. Double-slit, Confinement and non Franck-Condon Effects in Photoionization of H<sub>2</sub> at High Photon Energy. *Phys. Rev. A* **2009**, *79*, 023420 (1–12).
- (25) Travnikova, O.; Liu, J.-C.; Lindblad, A.; Nicolas, C.; Söderström, J.; Kimberg, V.; Gel'mukhanov, F.; Miron, C. Circularly Polarized X Rays: Another Probe of Ultrafast Molecular Decay Dynamics. *Phys. Rev. Lett.* **2010**, *105*, 233001 (1–4).
- (26) Söderström, J.; Lindblad, A.; Grum-Grzhimailo, A. N.; Travnikova, O.; Nicolas, C.; Svensson, S.; Miron, C. Angle-Resolved Electron Spectroscopy of the Resonant Auger Decay in Xenon with meV Energy Resolution. *New J. Phys.* **2011**, *13*, 073014.
- (27) Miron, C.; Nicolas, C.; Travnikova, O.; Morin, P.; Sun, Y.; Gel'mukhanov, F.; Kosugi, N.; Kimberg, V. Imaging Molecular Potentials Using Ultrahigh-Resolution Resonant Photoemission. *Nat. Phys.* **2012**, *8*, 135–138.
- (28) Lindblad, A.; Kimberg, V.; Söderström, J.; Nicolas, C.; Travnikova, O.; Kosugi, N.; Gel'mukhanov, F.; Miron, C. Vibrational Scattering Anisotropy in O<sub>2</sub> Dynamics Beyond the Born-Oppenheimer Approximation. *New J. Phys.* **2012**, *14*, 113018 (1–19).
- (29) Nicolas, C.; Miron, C. Lifetime Broadening of Core-Excited and -Ionized States. *J. Electron Spectrosc. Relat. Phenom.* **2012**, *185*, 267–272.
- (30) Kukkk, E.; Snell, G.; Bozek, J. D.; Cheng, W.-T.; Berrah, N. Vibrational Structure and Partial Rates of Resonant Auger Decay of the N 1s → 2π Core Excitations in Nitric Oxide. *Phys. Rev. A* **2001**, *63*, 062702 (1–9).
- (31) Kukkk, E.; Ueda, K.; Hergenhanh, U.; Liu, X.-J.; Prümper, G.; Yoshida, H.; Tamenori, Y.; Makochekanwa, C.; Tanaka, T.; Kitajima, M.; et al. Violation of the Franck-Condon Principle due to Recoil Effects in High Energy Molecular Core-Level Photoionization. *Phys. Rev. Lett.* **2005**, *95*, 133001 (1–4).
- (32) van der Straten, P.; Morgenstern, R.; Niehaus, A. Angular Dependent Post-Collision Interaction in Auger Processes. *Z. Phys. D* **1988**, *8*, 35–45.
- (33) Thomas, T. D.; Püttner, R.; Fukuzawa, H.; Prümper, G.; Ueda, K.; Kukkk, E.; Sankari, R.; Harries, J.; Tamenori, Y.; Tanaka, T.; et al. Boron 1s Photoelectron Spectrum of <sup>11</sup>BF<sub>3</sub>: Vibrational Structure and Linewidth. *J. Chem. Phys.* **2007**, *127*, 244309 (1–6).
- (34) Ueda, K.; Ohmori, K.; Okunishi, M.; Chiba, H.; Shimizu, Y.; Sato, Y.; Hayaishi, T.; Shigemasa, E.; Yagishita, A. Direct Observation of Correlation between Electron Emission and Fragmentation into Ions Following B 1s Excitation of the BF<sub>3</sub> Molecule. *Phys. Rev. A* **1995**, *52*, R1815–R1818.
- (35) DALTON2011, a Molecular Electronic Structure Program. <http://www.daltonprogram.org>, 2011.
- (36) Krishnan, R.; Binkley, J. S.; Seeger, R.; Pople, J. A. Self-Consistent Molecular Orbital Methods. XX. A Basis Set for Correlated Wave Functions. *J. Chem. Phys.* **1980**, *72*, 650–654.
- (37) Plésiat, E.; Argenti, L.; Kukkk, E.; Miron, C.; Ueda, K.; Decleva, P.; Martín, F. Intramolecular Electron Diffraction in Vibrationally Resolved K-Shell Photoionization of Methane. *Phys. Rev. A* **2012**, *85*, 023409 (1–7).
- (38) Bachau, H.; Cormier, E.; Decleva, P.; Hansen, J. E.; Martín, F. Applications of B-Splines in Atomic and Molecular Physics. *Rep. Prog. Phys.* **2001**, *64*, 1815.
- (39) Toffoli, D.; Stener, M.; Fronzoni, G.; Decleva, P. Convergence of the Multicenter B-spline DFT Approach for the Continuum. *Chem. Phys.* **2002**, *276*, 25–43.
- (40) Stener, M.; Decleva, P. Time-Dependent Density Functional Calculations of Molecular Photoionization Cross Sections: N<sub>2</sub> and PH<sub>3</sub>. *J. Chem. Phys.* **2000**, *112*, 10871–10879.
- (41) Stener, M.; Fronzoni, G.; Decleva, P. Time Dependent Density Functional Study of the Symmetry Resolved N 1s Photoionization in N<sub>2</sub>. *Chem. Phys. Lett.* **2002**, *351*, 469–474.
- (42) Burke, P. G.; Chandra, N.; Gianturco, F. A. Electron-Molecule Interactions. IV. Scattering by Polyatomic Molecules. *J. Phys. B: At. Mol. Opt. Phys.* **1972**, *5*, 2212.
- (43) Kato, T. On the Eigenfunctions of Many-Particle Systems in Quantum Mechanics. *Communications on Pure and Applied Mathematics* **1957**, *10*, 151–177.
- (44) Vosko, S. H.; Wilk, L.; Nusair, M. Accurate Spin-Dependent Electron Liquid Correlation Energies for Local Spin Density Calculations: A Critical Analysis. *Can. J. Phys.* **1980**, *58*, 1200–1211.
- (45) Baerends, E.; Ellis, D.; Ros, P. Self-Consistent Molecular Hartree-Fock-Slater Calculations I. The Computational Procedure. *Chem. Phys.* **1973**, *2*, 41–51.
- (46) Fonseca Guerra, C.; Snijders, J. G.; te Velde, G.; Baerends, E. J. Towards an Order-N DFT Method. *Theor. Chem. Acc.* **1998**, *99*, 391–403.
- (47) Kuchitsu, K.; Konaka, S. B-F Bond Distance of Boron Trifluoride Determined by Gas Electron Diffraction. *J. Chem. Phys.* **1966**, *45*, 4342–4347.
- (48) Shimanouchi, T. NIST Chemistry WebBook, NIST Standard Reference Database. *NIST Chemistry WebBook* **2005**, not-supplied.
- (49) Kirkpatrick, R.; Masiello, T.; Weber, A.; Nibler, J. W. Coherent Raman Spectra of the ν<sub>1</sub> Mode of <sup>10</sup>BF<sub>3</sub> and <sup>11</sup>BF<sub>3</sub>. *J. Mol. Spectrosc.* **2006**, *237*, 97–103.
- (50) Ueda, K.; Chiba, H.; Sato, Y.; Hayaishi, T.; Shigemasa, E.; Yagishita, A. Resonance-Auger-Electron-Photoion Coincidence Studies on State-to-State Dissociation Dynamics of Inner-Shell-Excited BF<sub>3</sub>. *Phys. Rev. A* **1992**, *46*, R5–R8.
- (51) Stern, E. A. Theory of the Extended X-Ray-Absorption Fine Structure. *Phys. Rev. B* **1974**, *10*, 3027–3037.
- (52) Dehmer, J. L.; Dill, D. Shape Resonances in K-Shell Photoionization of Diatomic Molecules. *Phys. Rev. Lett.* **1975**, *35*, 213–215.
- (53) Shimizu, Y.; Ueda, K.; Chiba, H.; Ohmori, K.; Okunishi, M.; Sato, Y.; Hayaishi, T. Angle-Resolved Photoelectron and Photoion Study on the Shape Resonance in the B 1s Ionization Region of BF<sub>3</sub>. *J. Chem. Phys.* **1997**, *107*, 2415–2418.
- (54) Patanen, M.; Kooser, K.; Argenti, L.; Ayuso, D.; Kimura, M.; Mondal, S.; Plésiat, E.; Palacios, A.; Sakai, K.; Travnikova, O.; et al. Vibrationally Resolved C 1s Photoionization Cross Section of CF<sub>4</sub>. *J. Phys. B: At. Mol. Opt. Phys.* **2014**, *47*, 124032.
- (55) Della Picca, R.; Fainstein, P. D.; Martiarena, M. L.; Dubois, A. Zeros in the Photoionization Partial Cross Sections of H<sub>2</sub><sup>+</sup>. *Phys. Rev. A* **2008**, *77*, 022702–(1–7).
- (56) Fernández, J.; Yip, F. L.; Rescigno, T. N.; McCurdy, C. W.; Martín, F. Two-Center Effects in One-Photon Single Ionization of H<sub>2</sub><sup>+</sup>, H<sub>2</sub>, and Li<sub>2</sub><sup>+</sup> with Circularly Polarized Light. *Phys. Rev. A* **2009**, *79*, 043409.
- (57) Plésiat, E.; Decleva, P.; Martín, F. Vibrational Branching Ratios in the Photoelectron Spectra of N<sub>2</sub> and CO: Interference and Diffraction Effects. *Phys. Chem. Chem. Phys.* **2012**, *14*, 10853–10871.
- (58) Ayuso, D.; Palacios, A.; Decleva, P.; Martín, F. Dissociative and Non-Dissociative Photoionization of Molecular Fluorine from Inner and Valence Shells. *J. Electron Spectrosc. Relat. Phenom.* **2014**, *195*, 320–326.
- (59) Li, W.-K.; Blinder, S. M. Solution of the Schrödinger Equation for a Particle in an Equilateral Triangle. *J. Math. Phys.* **1985**, *26*, 2784–2786.



# Vibrationally Resolved B 1s Photoionization

## Cross Section of $\text{BF}_3$

### – Supporting Information –

D. Ayuso,<sup>†</sup> M. Kimura,<sup>‡</sup> K. Kooser,<sup>¶</sup> M. Patanen,<sup>§</sup> E. Plésiat,<sup>†</sup> L. Argenti,<sup>†</sup> S. Mondal,<sup>‡</sup> O. Travnikova,<sup>§</sup> K. Sakai,<sup>‡</sup> A. Palacios,<sup>†</sup> E. Kukk,<sup>¶</sup> P. Declava,<sup>||</sup> K. Ueda,<sup>‡</sup> F. Martín,<sup>\*,†,#</sup> and C. Miron<sup>\*,§,@</sup>

*Departamento de Química, Módulo 13, Universidad Autónoma de Madrid, 28049 Madrid, Spain, Institute of Multidisciplinary Research for Advanced Materials, Tohoku University, Sendai 980-8577, Japan, Department of Physics and Astronomy, University of Turku, 20014 Turku, Finland, Synchrotron SOLEIL, L'Orme des Merisiers, Saint-Aubin, BP 48, 91192 Gif-sur-Yvette Cedex, France, and Dipartimento di Scienze Chimiche e Farmaceutiche, Università di Trieste, Via L. Giorgieri 1, I-34127 Trieste, Italy and CNR-Istituto Officina dei Materiali, 34127 Trieste, Italy*

E-mail: fernando.martin@uam.es; catalin.miron@synchrotron-soleil.fr

---

\*To whom correspondence should be addressed

<sup>†</sup>Departamento de Química, Módulo 13, Universidad Autónoma de Madrid, 28049 Madrid, Spain

<sup>‡</sup>Institute of Multidisciplinary Research for Advanced Materials, Tohoku University, Sendai 980-8577, Japan

<sup>¶</sup>Department of Physics and Astronomy, University of Turku, 20014 Turku, Finland

<sup>§</sup>Synchrotron SOLEIL, L'Orme des Merisiers, Saint-Aubin, BP 48, 91192 Gif-sur-Yvette Cedex, France

<sup>||</sup>Dipartimento di Scienze Chimiche e Farmaceutiche, Università di Trieste, Via L. Giorgieri 1, I-34127 Trieste, Italy and CNR-Istituto Officina dei Materiali, 34127 Trieste, Italy

<sup>‡</sup>Instituto Madrileño de Estudios Avanzados en Nanociencia (IMDEA-Nanociencia), Cantoblanco, 28049 Madrid, Spain

<sup>#</sup>Condensed Matter Physics Center (IFIMAC), Universidad Autónoma de Madrid, 28049 Madrid, Spain

<sup>@</sup>Extreme Light Infrastructure - Nuclear Physics (ELI-NP), “Horia Hulubei” National Institute for Physics

## Generalized $\nu$ -ratio, $G$ factor

In the study of C 1s photoionization cross section of CH<sub>4</sub>, Plésiat *et al.* (see Ref. 37 of the main manuscript) presented a simple analytical model based on a Born approximation that can be applied to B 1s cross section of BF<sub>3</sub> as well. This model gives a straightforward physical picture of the photoelectron scattering and provides a clear parametrization for the relative variation of the height of an individual vibrational peak observed in the photoionization spectrum. More specifically, according to the model, the intensity  $I_\nu(E)$  of any given peak in the totally symmetric stretching mode has the following form:

$$I_\nu(E) = FC_\nu[I^0(E) + I^1(E) + \nu I^2(E)] \quad (1)$$

where  $FC_\nu$  are energy-independent Franck-Condon parameters,  $I^0(E)$  is a smooth, atomic-like photoionization cross section,  $I^1(E)$  is an oscillating term, which is much smaller than  $I^0(E)$  and which does not depend on  $\nu$ , i.e., an oscillation of the total cross section which would be present even for a completely rigid molecule.  $I^2(E)$  is a second oscillating term which is one order of magnitude smaller than  $I^1(E)$  and is multiplied by the vibrational quantum number  $\nu$  of the parent ion. This term,  $\nu I^2(E)$ , is responsible for the oscillation in the vibrationally-resolved cross section ratio.

We define the ratio  $R_\nu(E)$  as an intensity ratio of a given vibrational peak  $I_\nu(E)$  to the total cross section at energy  $E$ ,  $I_{tot}(E) = \sum_\nu I_\nu(E)$ :

$$R_\nu(E) = FC_\nu[1 + (\nu - \nu_{av})J(E)] \quad (2)$$

where  $\nu_{av} = \sum_\nu FC_\nu \nu$  is the average vibrational quantum number of the parent ion, and  $J(E) = I^2(E)/[I^0(E) + I^1(E) + I^2(E)]$ .

If  $I^0(E)$  is much larger than  $I^1(E)$  and  $I^2(E)$ , then the function  $J(E)$  is an oscillatory

---

and Nuclear Engineering, 30 Reactorului Street, RO-077125 Măgurele, Jud. Ilfov, Romania

function similar to  $j_1(2kR)$  (see Ref. 37 of the main manuscript).

From the Eq. 2 we can see that the relative intensities can be approximated with a Taylor expansion with respect to  $(\nu - \nu_{av})$  truncated to the first order. This parametrization assumes that the deviations from Franck-Condon are small and smooth across the photoelectron signal, which is a reasonable assumption outside the resonant energies. Thus, the equation 2 provides a way to describe the fluctuation of the whole Franck-Condon envelope with one parameter during the fitting process of each spectrum. From a practical point of view it turned out to be better to modify Eq. 2 and express the FC parameters as a function of the actual ratios  $R_\nu(E_0)$  at a given reference energy  $E_0$ :

$$FC_\nu = R_\nu(E_0)/[1 + (\nu - \nu_{av})J(E_0)]. \quad (3)$$

Then, Eq. 2 can be rearranged as

$$R_\nu(E) = R_\nu(E_0)\{1 + (\nu - \nu_{av})[J(E) - J(E_0)]/[1 + (\nu - \nu_{av})J(E_0)]\} \quad (4)$$

At relatively high energy,  $J(E)$  is expected to be small. Accurate theoretical predictions estimate an amplitude below 0.01 above  $E=100$  eV. To a first approximation, therefore, If  $(\nu - \nu_{av}) J(E_0)$  is negligible when compared to 1, which allows one to write

$$R_\nu(E) \sim R_\nu(E_0)[1 + (\nu - \nu_{av})(J(E) - J(E_0))] \quad (5)$$

This expression provides a way to extract a single value  $G(E) = J(E) - J(E_0)$  representing the oscillations of the spectrum at a given energy  $E$  with respect to a chosen  $E_0$  value.  $E_0$  was chosen arbitrarily to be the point at 24 eV above threshold. This method ensures much better statistics for the experiment since all the individual TSSM peaks of a given spectrum contribute to the same fitting parameter.

To compare with the experimental data,  $G(E)$  can be obtained for the static-exchange

DFT calculations from  $J(E)$  by inverting Eq. 2:

$$J(E; \nu) = [R_\nu(E)/FC_\nu - 1]/(\nu - \nu_{av}). \quad (6)$$

Finally, a weighted average of all the different  $J(E, \nu)$  was taken to obtain the  $G$  factor from the calculations

$$G_{th}(E) = \sum_{\nu} J(E; \nu) FC_\nu. \quad (7)$$

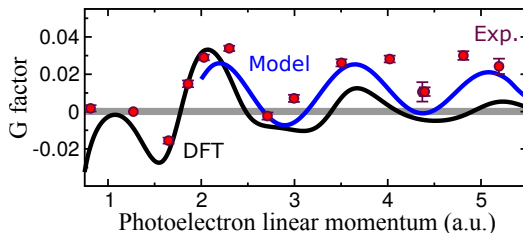


Figure 1: Generalized  $\nu$ -ratio ( $G$  factor) for  $\text{BF}_3$  as a function of photoelectron momentum. Circles with error bars: experimental results including statistical errors. Black line: results from the static-exchange DFT calculations. Blue line: results of the simple analytical model explained in the text.

Figure 1 presents the comparison between the experimental and theoretical generalized ratio  $G(E)$ . The agreement of the experimental data with the theoretical predictions is quite convincing (note that the second point is the one chosen as a reference). The Born approximation based scattering model catches nicely the three maxima between 2–5 a.u., but cannot be used to describe the data at very low electron momenta, where the static-exchange DFT calculations give a very good agreement with the experimental data. As already discussed in Ref. 15 of the main manuscript, the good agreement with the scattering model and the experiment at high energies proves the origin of these oscillations to be photoelectron diffraction.

## Appendix C

Vibrationally resolved C1s  
photoionization cross section of CF<sub>4</sub>



# Vibrationally resolved C 1s photoionization cross section of CF<sub>4</sub>

M Patanen<sup>1</sup>, K Kooser<sup>2</sup>, L Argenti<sup>3</sup>, D Ayuso<sup>3</sup>, M Kimura<sup>4</sup>, S Mondal<sup>4</sup>, E Plésiat<sup>3</sup>, A Palacios<sup>3</sup>, K Sakai<sup>4</sup>, O Travnikova<sup>1</sup>, P Decleva<sup>5</sup>, E Kukk<sup>2</sup>, C Miron<sup>1,7</sup>, K Ueda<sup>4</sup> and F Martín<sup>3,6</sup>

<sup>1</sup> Synchrotron SOLEIL, L'Orme des Merisiers, Saint-Aubin, BP 48, F-91192 Gif-sur-Yvette Cedex, France

<sup>2</sup> Department of Physics and Astronomy, University of Turku, FI-20014 Turku, Finland

<sup>3</sup> Departamento de Química, Módulo 13, Universidad Autónoma de Madrid, E-28049 Madrid, Spain

<sup>4</sup> Institute of Multidisciplinary Research for Advanced Materials, Tohoku University, Sendai 980-8577, Japan

<sup>5</sup> Dipartimento di Scienze Chimiche e Farmaceutiche, Università di Trieste, Via L. Giorgieri 1, I-34127 Trieste, Italy

<sup>6</sup> Instituto Madrileño de Estudios Avanzados en Nanociencia (IMDEA-Nanociencia), Cantoblanco, E-28049 Madrid, Spain

E-mail: [patanen@synchrotron-soleil.fr](mailto:patanen@synchrotron-soleil.fr), [catalin.miron@synchrotron-soleil.fr](mailto:catalin.miron@synchrotron-soleil.fr) and [fernando.martin@uam.es](mailto:fernando.martin@uam.es)

Received 1 December 2013, revised 2 January 2014

Accepted for publication 9 January 2014

Published 10 June 2014

## Abstract

The differential photoionization cross section ratio ( $\nu = 1$ )/( $\nu = 0$ ) for the symmetric stretching mode in the C 1s photoionization of CF<sub>4</sub> was studied both theoretically and experimentally. We observed this ratio to differ from the Franck–Condon ratio and to be strongly dependent on the photon energy, even far from the photoionization threshold. The density-functional theory computations show that the ratio is significantly modulated by the diffraction of the photoelectrons by the neighbouring atoms at high photon energies. At lower energies, the interpretation of the first very strong maximum observed about 60 eV above the photoionization threshold required detailed calculations of the absolute partial cross sections, which revealed that the absolute cross section has two maxima at lower energies, which turn into one maximum in the cross section ratio because the maxima appear at slightly different energies in  $\nu = 1$  and  $\nu = 0$  cross sections. These two strong, low-energy continuum resonances originate from the trapping of the continuum wavefunction in the molecular potential of the surrounding fluorine atoms and from the outgoing electron scattering by them.

Keywords: photoionization cross section, electron spectroscopy, DFT, electron diffraction, synchrotron radiation, PLEIADES

(Some figures may appear in colour only in the online journal)

## 1. Introduction

Atomic C 1s photoionization cross section is a monotonically decreasing curve as a function of the increasing photon energy [1], but when the C atom is brought into a molecular environment, the photoionization dynamics change, and the

cross section can be modulated due to several reasons. Close to the photoionization threshold the monotonic behaviour is disturbed by continuum resonances, such as shape resonances [2], modifying also for example the angular distributions of the emitted electrons [3–5], and leading to a non-Franck–Condon behaviour of vibrationally specific cross sections [6–8]. At higher photon energies, the photoelectron diffraction [9–11] as well as the Cohen–Fano type of an interference

<sup>7</sup> Author to whom any correspondence should be addressed.

phenomenon [12–16] lead to a (periodically) oscillating structure of the cross section. These oscillations in the cross section allow in principle the structural determination of the studied molecule, similarly to standard condensed matter characterisation methods, such as extended x-ray absorption fine structure (EXAFS) spectroscopy, based on the observation of the interference between the direct and the backscattered photoelectron waves [17]. Recently, Söderström *et al* [18] measured the C 1s cross section ratio between two chemically inequivalent carbon atoms in chlorinated ethanes in the gas phase. The cross section ratio was shown to be far from the stoichiometric ratio 1:1, having an oscillatory EXAFS-like behaviour [19] up to several hundred eVs above the photoionization thresholds. The observed oscillations in the intensity ratios of the photoelectron lines of chlorinated carbon and methyl group carbon mostly stem from the photoelectron scattering by the Cl atoms, and the amplitude of the oscillations was shown to be enhanced when more hydrogen atoms were progressively substituted with chlorine atoms.

The same photoelectron diffraction principle has been demonstrated to allow recovery of the molecular geometry by analysing the ratios of vibrationally resolved photoionization cross sections for the symmetric stretching mode in the C 1s photoionization of CH<sub>4</sub> [20].

Several theoretical and experimental studies of CF<sub>4</sub> photoionization cross sections were previously available. Toffoli *et al* [21] have theoretically studied the valence photoionization cross section and the electron angular distributions for CF<sub>4</sub>, up to a photon energy of 150 eV. Their computations were made in the framework of the time-dependent density-functional theory (TDDFT) and were based on a multicentric basis set expansion of the scattering wave function as a linear combination of atomic orbitals. The Schwinger variational method with Padé corrections has been used by Natalense *et al* [22] when they compared the cross sections and the angular dependence of the C 1s photoionization in CH<sub>4</sub>, CF<sub>4</sub> and CCl<sub>4</sub> close to the threshold. They showed that the cross sections and asymmetry parameters strongly depend on the fluorine and chlorine substitution in the studied energy range 300–360 eV. Their calculation was in good agreement with the experiments performed by Hitchcock and Mancini [23] and Truesdale *et al* [5].

In a recent study, Ueda *et al* studied a series of symmetric molecules, CH<sub>4</sub>, CF<sub>4</sub> and BF<sub>3</sub>, in an attempt to verify if photoelectron diffraction could be selected as a method to extract structural information from conventional photoemission measurements [24]. While for CH<sub>4</sub> and BF<sub>3</sub> the authors were able to obtain relatively good values for the internuclear distances, they pointed out that in the case of CF<sub>4</sub> it was not possible to accurately determine the molecular geometry by using this technique. The reasons that make CF<sub>4</sub> so special remained unclear [24]. Also, the vibrationally resolved C 1s photoionization cross section was studied in the case of CO [25], in a combined experimental and theoretical work demonstrating the applicability of DFT as a qualitative tool for structural analysis providing both dynamical and static molecular geometry parameters simultaneously.

In this paper we provide a more detailed analysis of the modulation of the photoionization cross section ratio

( $\nu = 1$ )/( $\nu = 0$ ) of the symmetric stretching mode in the C 1s photoionization of a polyatomic molecule, CF<sub>4</sub>. Our calculations show that, far from threshold, the oscillations in the  $\nu$ -ratios are indeed due to diffraction of the photoelectrons by the neighbouring atoms. In this energy region, they can be clearly distinguished from the features associated to the presence of continuum resonances, which are seen close to threshold. In the lower energy region, the observed structures result from a superposition of contributions due to the diffraction and due to the continuum resonance effects, preventing one from using simple physical models to interpret the experimental findings. However, the reasonable agreement between the experiment and the DFT calculations suggests that similarly to the case of CO [25], the DFT could be a tool of choice for structural determination of highly excited polyatomic molecules when theoretical models beyond the first Born approximation are needed.

## 2. Experiment

The experiment was carried out at the PLEIADES beamline [26–29] at the SOLEIL national synchrotron radiation (SR) facility in France. SR was generated using an Apple II type permanent magnet HU80 (80 mm period) undulator and monochromatized by varied groove depth, varied line spacing, 2400 nm<sup>-1</sup>, plane grating monochromator. The C 1s photoelectron spectra were recorded using a 30° wide angle lens VG-Scienta R4000 electron energy analyser, whose detection axis is perpendicular to the storage ring plane containing the propagation direction of the SR. The angle between the polarization vector of the SR and the electron detection axis was 54.7°, excluding the photon energy-dependent modulation of the cross section due to the photoelectron asymmetry  $\beta$  parameter in the dipole approximation.

The gaseous CF<sub>4</sub> sample had a purity of 99.995% and it was used as provided by Messer Schweiz AG. The gas was introduced in a gas cell equipped with a series of polarized electrodes, used to minimize the effect of plasma potentials caused by the ion density gradient created along the SR propagation axis. The pressure was  $4 \times 10^{-6}$  mbar inside the spectrometer, and approximately two or three orders of magnitude higher inside the gas cell in the interaction region.

The instrumental electron energy resolution is determined by the exit slit of the monochromator (photon bandwidth) and the entrance slit and the pass energy of the electron energy analyser. Also, the translational Doppler effect broadens the measured spectra. In order to trustworthily disentangle the overlapping vibrational peaks using a fitting method described in the next section, energy resolution had to be good, however bearing in mind that at high photon energies the data acquisition time increases rapidly due to a lower photoionization cross section and somewhat reduced photon flux. An acceptable compromise between good statistics and a reasonable acquisition time was to use an energy resolution of  $\approx 26$  meV for low photon energies (330–350 eV), and  $\approx 55$  meV for higher photon energies (360–500 eV). Exceptionally, at the photon energy of 335 eV the resolution



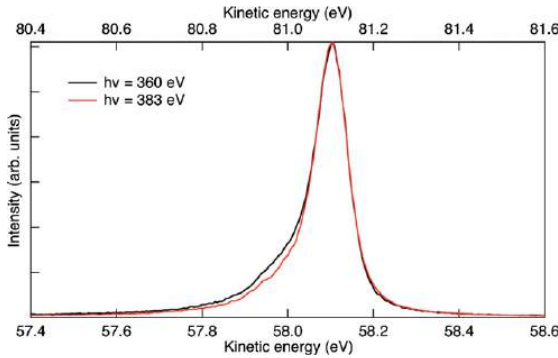


**Figure 1.** Comparison between two C 1s photoelectron spectra of CF<sub>4</sub> measured with 360 eV (black curve) and 383 eV (red curve) shows clear redistribution of intensity. The peaks have been normalized to have the same intensity at the highest point in order to achieve a better visual comparison.

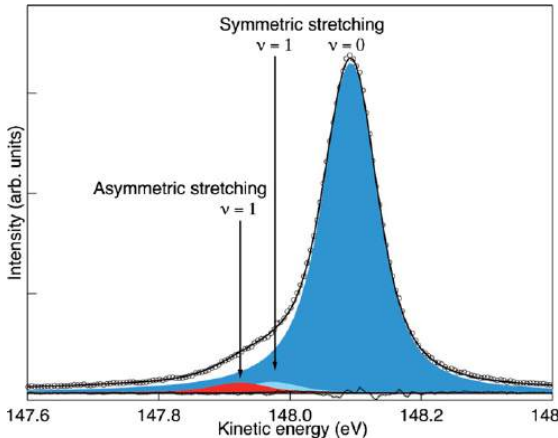


**Figure 2.** The C 1s photoelectron spectrum of CF<sub>4</sub> measured at 450 eV photon energy shows how the photoelectron line is divided into different components. Open circles are measured data points, the black solid curve is the total fitted spectrum. The fitted symmetric stretching vibrational components are shown as dark blue ( $\nu = 0$ ) and light blue ( $\nu = 1$ ) peaks, whereas the asymmetric stretching peak is shown in red. The dotted line shows the residual difference between the measured data points and the total fit.

of 52 meV was used and 570, 600 and 650 eV photon energy spectra were recorded with the total resolutions of 63 meV, 73 meV and 76 meV, respectively. The electron energy analyser's curved entrance slit had a fixed value of 0.3 mm during all the experiments, but the pass energy (either 20 or 50 eV) and the width of the exit slit of the monochromator (from 30 to 100  $\mu\text{m}$ ) were adjusted to achieve the desired resolution. The Ar 2p<sub>3/2</sub> photoelectron line was recorded with the same settings as the CF<sub>4</sub> spectra at all photon energies in order to get accurate information about the instrumental broadening, taking into account the lifetime broadening of this atomic line, 119 meV [30]. Spectra have been calibrated using the binding energy value of 301.898 eV reported by Myrseth *et al* [31].

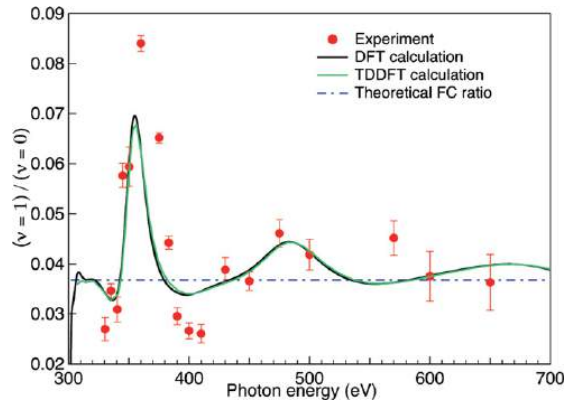


**Figure 3.** Vibrational branching ratio ( $\nu = 1$ )/( $\nu = 0$ ) for C 1s photoionization of CF<sub>4</sub> leading to excitation of the CF<sub>4</sub><sup>+</sup> symmetric stretching mode. Experimental data points compared with two DFT based theoretical models, time-independent (black solid line) and time-dependent (green solid line). The blue dash-dot line shows the theoretical Franck–Condon ratio (0.037).

### 3. Data analysis

The C 1s photoemission spectra were fitted using the Igor Pro data analysis software from WaveMetrics Inc. and the SPANCF fitting macros by Kukk [32]. All spectra were fitted simultaneously. Post-collisional interaction (PCI) line shapes [33] were used in the fitting process with the Lorentzian width as a free parameter, but common for all the lines and spectra. The optimized value is 70 meV, in satisfactory agreement with the  $67 \pm 2$  meV reported by Thomas *et al* [34]. The Gaussian width representing the instrumental and translational Doppler broadenings was also kept as a free parameter, but constrained to be the same to all peaks in the spectra. As the initial guesses were obtained from the fitted Ar calibration data, only small variations from the initial values were observed. The asymmetry leading to the low-energy tail due to the PCI effect was calculated from the average Auger electron kinetic energy of 250 eV and the photoelectron kinetic energy, using the formula from [35]. The energy spacing of the symmetric stretching vibrational sublevels was kept constant (119 meV) [34]. In the data analysis, the recoil-induced excitations of asymmetric vibrations were taken into account by simultaneously fitting the asymmetric stretching and bending vibrational peaks with the fixed energy separations of 169 meV and 77.6 meV, respectively. The relative intensity of the excited asymmetric peak with respect to the main  $\nu = 0$  symmetric stretching peak depends on the kinetic energy of the photoelectron  $E_e$ , and it was calculated for every spectrum measured at a different photon energy, using the formula given in [34]

$$I_i = \frac{m_e E_e}{m_A E_{\text{vib},i}} f_i, \quad (1)$$

where  $f_i$  is the fraction of the total recoil energy that ends up in the mode  $i$ ,  $m_e$  is the mass of the electron,  $m_A$  the mass of

the molecular constituent which takes the recoil energy (here the mass of C atom, 12 u), and  $E_{\text{vib},i}$  is the vibrational energy of the mode  $i$ .

The acquisition times varied remarkably as a function of the excitation energy owing to changes in the cross section and photon flux. The spectra with the highest statistics were collected in only 1 h (in total over 380 000 counts in the 3 eV region with  $h\nu = 335$  eV), whereas at the highest energy point recorded with 650 eV photon energy, the collection of 40 000 counts took nearly 10 h. This also implies that a lot of spectra had to be summed to achieve the final result. For instance, in the case of 650 eV photon energy, almost 200 individual spectra were recorded. Each spectrum was separately investigated in order to check for the possible energy shifts, then aligned and summed. Even though the procedure was carefully performed, there is always a possibility that for example plasma potentials correction was not perfect over time because the pressure decreased in the gas cell, leading to broader photolines. As a result, the data points measured with the highest photon energies have much larger error bars compared to the points measured with lower photon energies.

#### 4. Calculations

$\text{CF}_4$  molecule belongs to the  $T_d$  point group, and the symmetry of the C 1s orbital in this point group is  $a_1$ . The calculations have been performed using the dipole approximation, which limits the symmetry of continuum waves to  $T_2$ . Two sets of calculations were performed. The first one used time-independent static exchange DFT with inclusion of the nuclear motion [12, 20, 36] which, in general, leads to accurate values of the photoionization cross sections well above the ionization threshold, but, in some cases, may lead to a rather poor description just above it (see also [37] and references therein for calculations performed in the fixed nuclei approximation). The second, more elaborate, set of calculations were performed at TDDFT level of theory, with inclusion of the nuclear motion to account for interchannel coupling and a better description of electron correlation [36], effects that can be particularly important in the vicinity of the ionization threshold. It turned out that the static exchange DFT and TDDFT results for  $\text{CF}_4$  are practically undistinguishable.

The electronic Kohn–Sham equations were solved, obtaining bound and continuum eigenvectors in a basis of multicentric B-spline functions [38]. As in [12, 20, 36], calculations were performed within the Born–Oppenheimer approximation, and the vibrational wave functions were reduced to their symmetric stretching mode components, by using the values of the  $\text{CF}_4$  equilibrium geometry for all the other normal coordinates. These wave functions were obtained from the solution of the vibrational Schrödinger equation for the symmetric stretching mode in a B-spline basis. This approximation is justified because the excitation of the  $T_2$  vibrational mode can be accurately accounted for with simple semi-classical arguments. When such a recoil effect is removed, ionization mainly excites the symmetric stretching mode vibrations in the final state. In practice, the *ab initio* nuclear dynamics has been restricted along the symmetric

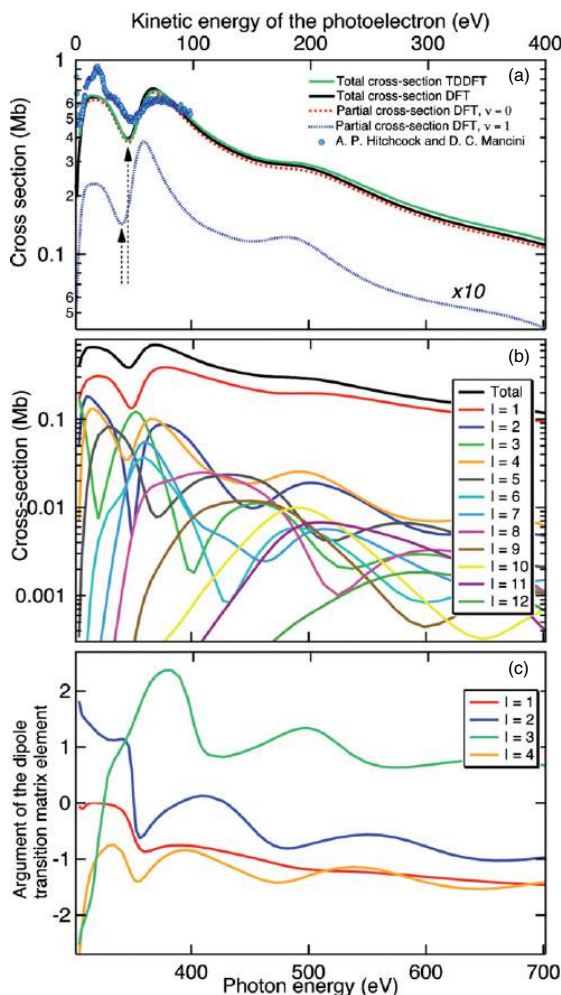


**Figure 4.** (a) Total (black solid curve) and partial  $\nu = 0$  (dashed red curve) and  $\nu = 1$  (dashed blue curve) cross sections calculated using time-independent static exchange DFT and total cross section calculated using the time-dependent DFT method (green solid curve). Spheres are experimental electron energy loss data from [23].  $\nu = 1$  cross section has been multiplied by 10 to have a better visual comparison of the energy shift and the changes between the  $\nu = 1$  and  $\nu = 0$  cross sections. The dashed arrows are drawn to emphasize the shifted positions of the minima. (b) Partial wave contributions of total cross section calculated using the time-dependent static exchange DFT method. (c) Argument of the dipole transition matrix element of each partial wave as a function of photoelectron energy.

stretching normal coordinate in both the initial molecule and the final cation. The symmetric stretching  $\nu = 0$  mode of the cation is predominantly excited due to a very small geometry change of the core-ionized state (the C–F bond contraction is only  $\sim 0.61$  pm [34]). The used method has provided accurate vibrationally resolved photoionization cross sections for  $\text{N}_2$ ,  $\text{CO}$ ,  $\text{C}_2\text{H}_2$ ,  $\text{BF}_3$  [12, 24, 36, 39]. Basically the same approach has been extensively employed by Lucchese and Poliakov

*et al* in their studies of vibrationally resolved photoionization spectra (see e.g. [40] and [41] and references therein).

## 5. Results and discussion

Figure 1 shows two examples of the measured spectra, demonstrating that the effect of the intensity redistribution at low photon energies can be seen directly from the spectra. The intensities of the asymmetric stretching peaks are 1.3% and 1.7%, and the intensities of the asymmetric bending peaks are 0.2% and 0.3% of the main peak at the photon energies 360 eV and 383 eV, respectively, thus having a very minor effect on the spectra in figure 1. At higher photon energies the recoil-induced peaks are more important, as demonstrated in figure 2 with a spectrum measured at  $h\nu = 450$  eV, where the intensities of the first asymmetric stretching and bending vibrations are 3.2% and 0.5% of the  $\nu = 0$  symmetric stretching peak, respectively.

Instead of extracting, for the vibrational components, absolute partial photoionization cross sections requiring very careful calibration with an external calibrant, the relative photoionization cross section is reported as the intensity ratio ( $\nu = 1$ )/( $\nu = 0$ ). Therefore, calibration problems are avoided and the natural decrease with photon energy of the photoionization cross sections is overcome, but the interpretation becomes slightly more complicated. Figure 3 shows the comparison between the experimental and the calculated  $\nu$ -ratio for the symmetric stretching mode. One has to bear in mind that when the intensity ratio shows a maximum, it typically indicates a minimum in C 1s  $\nu = 0$  cross section.

The experiment shows a strong maximum about 60 eV above the photoionization threshold, and the structure is confirmed by the calculations, which also show wider, but less pronounced maxima around 200 and 350 eV above the C 1s threshold and they are assigned to the signature of the scattering from the surrounding F atoms. The maximum at 200 eV above the threshold is supported by the experiment, but at higher energies the error bars of the experimental points are large due to the reduced resolution, poorer statistics and higher recoil peak contribution, thus the behaviour of the theoretical curve cannot be fully confirmed by the experiment.

In order to interpret the structures in the  $\nu$ -ratio curve, it is useful to look at the calculated absolute cross sections in detail. Figure 4 presents results from static exchange DFT and TDDFT calculations of the C 1s photoionization cross sections for the different final vibrational states of the symmetric stretching mode of  $\text{CF}_4^+$ . In figure 4(a) two maxima are observed in the cross sections at 20 and 70 eV above the photoionization threshold, in very good agreement with the experimental electron energy loss data from [23]. As expected from the Franck–Condon overlaps, the position of the dip is slightly different in the  $\nu = 0$  and  $\nu = 1$  cross sections (indicated by dashed arrows in figure 4(a)), and hardly manifests in the total cross sections fully dominated by  $\nu = 0$  contribution. Indeed this slight change and the strong slope of the cross section enhance the effect on the  $\nu$ -ratio giving rise to the very prominent peak observed. The contribution of different partial waves for the ejected

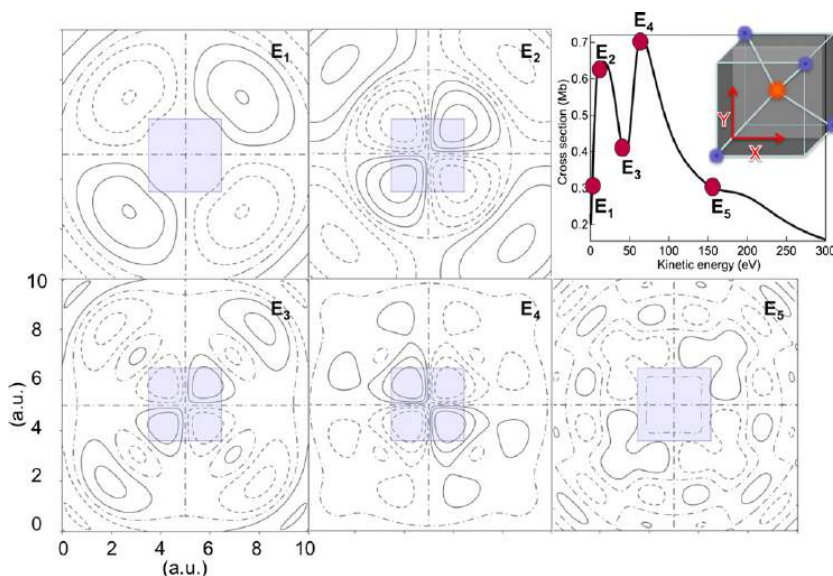
electron are plotted in figure 4(b), showing that the dominant one at any photon energy corresponds to the  $l = 1$  wave, except around the dip between the two maxima where the  $l = 3$  contribution is comparable.

Figure 4(c) presents the argument of the dipole transition matrix elements of the main partial waves. At the first maximum in the vibrationally resolved cross sections, observed experimentally already in 1974 by Wight and Brion [42], a sudden change of the argument of the dipole transition amplitude in the  $l = 3$  partial wave is identified. This kind of sudden change might be an indication of shape resonance. From 60 eV above the threshold and onwards, the argument of the dipole transition amplitude exhibits a rather smooth oscillatory behaviour without large sudden changes.

In order to understand the origin of the low-energy structures, the 2D projections of the ‘dipole prepared’ [ $d_z$  component] continuum orbitals were plotted for different planes at different energies (as an example, the contour plots on the XY-plane are shown in figure 5). It was found that at the energies where the cross section has a maximum, there exists a significant amplitude of the continuum wave inside the tetrahedral cage defined by the fluorine atoms; in particular the continuum waves  $l = 2$  and  $l = 4$  seem to be ‘trapped’ by the cage and resonances are observed in the cross section. Outside the resonances (for example between the two low-energy maxima) this kind of amplitude enhancement inside the cage is not observed, and at the highest plotted electron energy of 155 eV the fluorine atoms seem to become almost transparent to the continuum wave.

Somewhat similar continuum resonances at 30 and 60 eV above the S 1s threshold were observed in the photoabsorption cross section of  $\text{SF}_6$  [45]. The observed structures were well reproduced by multiple-scattering  $X\alpha$  calculations but not by single scattering plane wave EXAFS. The authors were not able to offer a definite interpretation for these structures and they concluded that the origin might be a combination of multiple-scattering effects and an interaction of the photoelectron with the molecular potential. Later, a theoretical work by Natalense and Lucchese confirmed the contribution of the resonant state around 60 eV above the threshold trapped by an  $l = 9$  angular momentum barrier [46].

In summary, from the above theoretical analysis of the partial vibrational cross sections we can deduce that the dominating maximum seen in  $\nu$ -ratio is a complex combination of intramolecular electron scattering and a non-diffractive confinement of the continuum wavefunction in the potential cage defined by the fluorine atoms, effective at low energies. Thus the latter effect is somewhat similar to that observed in the  $\text{H}_2$  [47] and  $\text{H}_2^+$  [48] molecules at higher photoelectron energies, although it is more pronounced for  $\text{CF}_4$  due to the three-dimensional character of the confining potential and the larger size of the peripheral atoms defining such potential. The maxima in the  $\nu = 0$  and  $\nu = 1$  cross sections are slightly shifted in energy with respect to each other, and thus the maximum in  $\nu = 1$  cross section overlaps with the dip of  $\nu = 0$  cross section, resulting in a maximum in their relative cross section.



**Figure 5.** Contour plots of the ‘dipole prepared’ ( $d_z$  component) continuum orbitals projected to the XY-plane at different electron kinetic energies  $E_1 = 1.08$  eV,  $E_2 = 7.62$  eV,  $E_3 = 40.82$  eV,  $E_4 = 62.58$  eV and  $E_5 = 155.10$  eV. The positions of these energies on the total cross section curve are shown with spheres. In the 2D plots the C atom is at  $(x, y) = (5.00, 5.00)$  au and the projections of the F atoms are located at  $(x, y) = (3.56, 3.56)$ ,  $(3.56, 6.44)$ ,  $(6.44, 3.56)$  and  $(6.44, 6.44)$  au, i.e. in the vertices of the blue square in the middle. The same plane is presented in the schematic shown in the upper right corner (a cube where F atoms are placed to the vertices and the C atom is in the centre).

## 6. Conclusions

We have performed a theoretical and experimental analysis of the C 1s photoionization cross sections of two vibrational levels of the symmetric stretching mode in  $\text{CF}_4$ . In order to avoid the complex calibration and significant decrease of the absolute experimental cross section as a function of the photon energy, we have studied the ratio of the  $\nu = 1$  and  $\nu = 0$  partial cross sections. The studied  $\nu$ -ratio shows a photon energy-dependent modulation, which has been interpreted using DFT calculations to originate from a confinement of the continuum wavefunction in the potential of the F atoms and from an electron diffraction from the surrounding fluorines. In particular, close to the threshold the continuum wave is sensitive to the details of the molecular potential and it is possible that the peculiar form of the cross section with two maxima and a deep minimum at low energy is due to an interplay between the ‘trapping’ of the continuum electron and the electron diffraction. The higher energy maximum at 200 eV above the threshold is the consequence of a pure electron diffraction by the surrounding fluorine atoms. Due to the described characteristic behaviour of the C 1s cross section in  $\text{CF}_4$ , dramatically exemplified by the dominant peak in the  $\nu$ -ratio at 60 eV, the determination of the molecular geometry requires theoretical models that go beyond a simple first Born approximation [24]. The static exchange DFT used in this work proved to be sufficiently accurate and computationally inexpensive to be considered as a viable candidate, even in the case of polyatomic molecules.

## Acknowledgments

Data collection was performed at the PLEIADES beamline at the SOLEIL Synchrotron, France (proposal no 20110781). We are grateful to E Robert, X-J Liu and C Nicolas for technical assistance, and to the SOLEIL staff for stable operation of the equipment and storage ring during the experiments. We thank Mare Nostrum BSC, Cineca and CCC-UAM for allocation of computer time. Work supported by the Advanced Grant of the European Research Council XCHEM 290853, the MICINN project nos FIS2010-15127 and CSD 2007-00010 (Spain), the ERA-Chemistry project PIM2010EEC-00751, the European grants MC-ITN CORINF and MC-RG ATTOTREND, the European COST Actions CM0702 (CUSPFEL) and CM1204 (XLIC), the MC-IEF CHICROCSX under grant agreement no 252781 (OT) and the I3 program, the MEXT and JSPS agencies (Japan), and the Academy of Finland.

## References

- [1] Yeh J J and Lindau I 1985 *At. Data Nucl. Data Tables* **32** 1
- [2] Piancastelli M N 1999 *J. Electron Spectrosc. Relat. Phenom.* **100** 167
- [3] Truesdale C M, Southworth S H, Kobrin P H, Becker U, Lindle D W, Kerkhoff H G and Shirley D A 1983 *Phys. Rev. Lett.* **50** 1265
- [4] Dill D, Swanson J R, Wallace S and Dehmer J L 1980 *Phys. Rev. Lett.* **45** 1393
- [5] Truesdale C M, Lindle D W, Kobrin P H, Becker U E, Kerkhoff H G, Heimann P A, Ferrett T A and Shirley D A 1984 *J. Chem. Phys.* **80** 2319

- [6] Dehmer J L, Dill D and Wallace S 1979 *Phys. Rev. Lett.* **43** 1005
- [7] Mistrov D A, De Fanis A, Kitajima M, Hoshino M, Shindo H, Tanaka T, Tamenori Y, Tanaka H, Pavlychev A A and Ueda K 2003 *Phys. Rev. A* **68** 022508
- [8] Lucchese R R, Söderström J, Tanaka T, Hoshino M, Kitajima M, Tanaka H, De Fanis A, Rubensson J-E and Ueda K 2007 *Phys. Rev. A* **76** 012506
- [9] Hitchcock A P and Brion C E 1978 *J. Electron Spectrosc. Relat. Phenom.* **14** 417
- [10] Yang B X, Kirz J and Sham T K 1987 *Phys. Rev. A* **36** 4298
- [11] Stöhr J and Bauchspiess K R 1991 *Phys. Rev. Lett.* **67** 3376
- [12] Canton S E, Plésiat E, Bozek J D, Rude B S, Decleva P and Martín F 2011 *Proc. Natl Acad. Sci. USA* **108** 7302
- [13] Liu X-J *et al* 2006 *J. Phys. B: At. Mol. Opt. Phys.* **39** 4801
- [14] Landers A L *et al* 2001 *Phys. Rev. Lett.* **87** 013002
- [15] Zimmermann B *et al* 2008 *Nature Phys.* **4** 649
- [16] Kushawaha R K, Patanen M, Guillemin R, Journel L, Miron C, Simon M, Piancastelli M N, Skates C and Decleva P 2013 *Proc. Natl Acad. Sci. USA* **110** 15201
- [17] Lee P A, Citrin P H, Eisenberger P and Kincaid B M 1981 *Rev. Mod. Phys.* **53** 769
- [18] Söderström J *et al* 2012 *Phys. Rev. Lett.* **108** 193005
- [19] Pangher N, Köppe H M, Feldhaus J and Haase J 1993 *Phys. Rev. Lett.* **71** 4365
- [20] Plésiat E, Argenti L, Kukuk E, Miron C, Ueda K, Decleva P and Martín F 2012 *Phys. Rev. A* **85** 023409
- [21] Toffoli D, Stener M, Fronzoni M G and Decleva P 2006 *J. Chem. Phys.* **124** 214313
- [22] Natalense A P P, Brescansin L M and Lucchese R R 2003 *Phys. Rev. A* **68** 032701
- [23] Hitchcock A P and Mancini D C 1994 *J. Electron Spectrosc. Relat. Phenom.* **67** 1
- [24] Ueda K *et al* 2013 *J. Chem. Phys.* **139** 124306
- [25] Kukuk E *et al* 2013 *Phys. Rev. A* **88** 033412
- [26] Travnikova O, Liu J C, Lindblad A, Nicolas C, Söderström J, Kimberg V, Gel'mukhanov F and Miron C 2010 *Phys. Rev. Lett.* **105** 233001
- [27] Söderström J, Lindblad A, Gvern-Grzhimailo A, Travnikova O, Nicolas C, Svensson S and Miron C 2011 *New J. Phys.* **13** 073014
- [28] Miron C, Nicolas C, Travnikova O, Morin P, Sun Y P, Gel'mukhanov F, Kosugi N and Kimberg V 2012 *Nature Phys.* **8** 135
- [29] Lindblad A, Kimberg V, Söderström J, Nicolas C, Travnikova O, Kosugi N, Gel'mukhanov F and Miron C 2012 *New J. Phys.* **14** 113018
- [30] Nicolas C and Miron C 2012 *J. Electron Spectrosc. Relat. Phenom.* **185** 267
- [31] Myrseth V, Bozek J D, Kukuk E, Sæthre L and Thomas T D 2002 *J. Electron Spectrosc. Relat. Phenom.* **122** 57
- [32] Kukuk E 2000 Macro package SPANCF
- [33] van der Straten P, Morgenstern R and Niehaus A 1988 *Z. Phys.* **D 8** 35
- [34] Thomas T D *et al* 2008 *J. Chem. Phys.* **128** 144311
- [35] Paripás B, Vitéz G, Víkor G, Tökési K, Caló A, Sankari R, Huttula M, Aksela S and Aksela H 2004 *J. Phys. B: At. Mol. Opt. Phys.* **37** 4507
- [36] Plésiat E, Decleva P and Martín F 2012 *Phys. Chem. Chem. Phys.* **14** 10853
- [37] Venuti M, Stener M and Decleva P 1998 *Chem. Phys.* **234** 95
- [38] Bachau H, Cormier E, Decleva P, Hansen J E and Martín F 2001 *Rep. Prog. Phys.* **64** 1601
- [39] Argenti L *et al* 2012 *New J. Phys.* **14** 033012
- [40] López-Domínguez J A, Hardy D, Das A, Poliakov E D, Aguilar A and Lucchese R R 2012 *J. Electron Spectrosc. Relat. Phenom.* **185** 211
- [41] Poliakov E D and Lucchese R R 2006 *Phys. Scr.* **74** C71
- [42] Wight G R and Brion C E 1974 *J. Electron Spectrosc. Relat. Phenom.* **4** 327
- [43] Loomba D, Wallace S, Dill D and Dehmer J L 1981 *J. Chem. Phys.* **75** 4546
- [44] Fronzoni G, Stener M, Furlan S and Decleva P 2001 *Chem. Phys.* **273** 117
- [45] Ferrett T A, Lindle D W, Heimann P A, Kerkhoff H G, Becker U E and Shirley D A 1986 *Phys. Rev. A* **34** 1916
- [46] Natalense A P P and Lucchese R R 1999 *J. Chem. Phys.* **111** 5344
- [47] Fernández J, Fojón O A, Palacios A and Martín F 2007 *Phys. Rev. Lett.* **98** 043005
- [48] Fernández J, Fojón O A and Martín F 2009 *Phys. Rev. A* **79** 023420



## **Appendix D**

Effects of molecular potential and geometry on atomic core-level photoemission over an extended energy range: The case study of the CO molecule





## Effects of molecular potential and geometry on atomic core-level photoemission over an extended energy range: The case study of the CO molecule

E. Kukk,<sup>1,\*</sup> D. Ayuso,<sup>2</sup> T. D. Thomas,<sup>3</sup> P. Declève,<sup>4,†</sup> M. Patanen,<sup>5</sup> L. Argenti,<sup>2</sup> E. Plésiat,<sup>2</sup> A. Palacios,<sup>2</sup> K. Kooser,<sup>1</sup> O. Travnikova,<sup>5</sup> S. Mondal,<sup>6</sup> M. Kimura,<sup>6</sup> K. Sakai,<sup>6</sup> C. Miron,<sup>5</sup> F. Martín,<sup>2,7</sup> and K. Ueda<sup>6,‡</sup>

<sup>1</sup>*Department of Physics and Astronomy, University of Turku, FIN-20014 Turku, Finland*

<sup>2</sup>*Departamento de Química, Módulo 13, Universidad Autónoma de Madrid, Cantoblanco 28049 Madrid, Spain*

<sup>3</sup>*Department of Chemistry, Oregon State University, Corvallis, Oregon 97331, USA*

<sup>4</sup>*Dipartimento di Scienze Chimiche, Università di Trieste, and CNR-IOM, 34127 Trieste, Italy*

<sup>5</sup>*Synchrotron SOLEIL, L'Orme des Merisiers, Saint-Aubin, B.P. 48, 91192 Gif-sur-Yvette Cedex, France*

<sup>6</sup>*Institute of Multidisciplinary Research for Advanced Materials, Tohoku University, Sendai 980-8577, Japan*

<sup>7</sup>*Instituto Madrileño de Estudios Avanzados en Nanociencia, Cantoblanco, 28049 Madrid, Spain*

(Received 26 April 2013; published 10 September 2013)

We report an experimental and theoretical study of single-molecule inner-shell photoemission measured over an extended range of photon energies. The vibrational intensity ratios  $I(v=1)/I(v=0)$  from the C 1s photoelectron spectra of carbon monoxide, although mostly determined by the bond length change upon ionization, are shown to be affected also by photoelectron recoil and by scattering from the neighboring oxygen atom. Static-exchange density functional theory (DFT) is used to encompass all these effects in a unified theoretical treatment. The *ab initio* calculations show that the vibrational ratio as a function of the photoelectron momentum is sensitive to both the ground-state internuclear distance and its contraction upon photoionization. We present a proof-of-principle application of DFT calculations as a quantitative structural analysis tool for extracting the dynamic and static molecular geometry parameters simultaneously.

DOI: [10.1103/PhysRevA.88.033412](https://doi.org/10.1103/PhysRevA.88.033412)

PACS number(s): 33.80.Eh, 32.80.Aa, 33.15.-e, 33.20.-t

### I. INTRODUCTION

Diatomic molecules in the gas phase have long been of fundamental scientific interest as the simplest quantum mechanical systems combining fast (electronic) and slow (nuclear) dynamics. Electronic structure studies of molecules ranging from the diatomics to complex organic molecules rely largely on energy- or wavelength-resolving spectroscopies. While the parameters of nuclear geometry of small molecules can be successfully derived using spectroscopic techniques, larger systems are probed mainly with scattering techniques in which either an electromagnetic or a matter wave is perturbed by atoms, creating new emission centers of scattered waves. Continuum waves from various sources then overlap and interfere, creating a characteristic pattern of intensity modulations. The suitability of scattering techniques for molecular structure determination in the gas phase was established in 1915 by Debye, who showed that, contrary to what might be assumed, averaging over the random orientations of free molecules containing the scattering atoms does not destroy the interference patterns [1]. Instead, pronounced oscillations of the outgoing wave intensity as a function of the detection angle are expected, with a period that depends on the structural parameters of the molecule such as its bond lengths, and on the wavelength of the scattered wave.

The scattering techniques can employ a variety of particles to form the wave to be scattered: electrons, photons, and neutrons. Due to the strong interaction of charged particles

with matter, electron scattering has become a standard technique in the gas phase, where it can determine structural parameters of free molecules with high accuracy [2]. X-ray and neutron diffraction, on the other hand, are the methods of choice for solid targets. There is also a choice between the origin of the wave to be scattered: external, as in the methods mentioned above, or internal. In the latter, electrons emitted by one of the atoms in the system form the initial wave that is subsequently scattered by neighboring atoms. In this case, the photoemission cross section  $\sigma(k)$  is modified by interference terms that oscillate as a function of the electron momentum  $k$  as  $\sim \sin(2kR_0)$ , where  $R_0$  is the distance between the emitter and the scatterer. This effect is at the basis of EXAFS (extended x-ray absorption fine structure) [3], a technique broadly employed in solids, and in which the short-range neighborhood structure is revealed by oscillations in the x-ray absorbance. In the less broadly employed technique of XPD (x-ray photoelectron diffraction), structural information of surfaces is extracted directly from photoemission intensity distributions, either angle or momentum resolved [4,5].

In randomly oriented molecular targets, in contrast to solids, photoemission has not been the tool of choice to probe the *static* geometry of the emitter's neighborhood. Instead, core-level photoelectron spectroscopy was found to be an excellent means to elicit information on molecular *dynamics*: the disturbance to the electronic structure by core hole creation induces changes in equilibrium structural parameters, causing readjustment of atomic positions and resulting in vibrational excitations [6]. In the case of diatomics, for example, the change of the bond length  $\Delta R$  is derived from the analysis of the vibrational progression in the photoelectron spectrum via Franck-Condon factors [7,8].

\*edwin.kukk@utu.fi

†declève@units.it

‡ueda@tagen.tohoku.ac.jp

The derivation of static ( $R_0$ ) and dynamic ( $\Delta R$ ) structural parameters has thus been largely based on different and independent approaches. A number of recent studies of molecular photoemission over extended energy ranges (e.g., [9–11]), however, made apparent that these properties should not be treated separately in the first place. Firstly, the emission of a photoelectron with momentum  $k$  entails a corresponding nuclear recoil that induces vibrational and rotational excitations. Yet, the direction of the nuclear recoil depends on whether the electron leaves the molecule directly or scatters on neighboring atoms. Secondly, scattering and interference effects modulate the cross sections and also affect the ratios of the vibrational peaks in the spectrum [11]. Thus, a highly accurate determination of  $\Delta R$  from a photoelectron spectrum at any given energy requires that these effects, which depend on the static molecular geometry, be taken into account as well.

In this study, we analyze the extended range photoemission spectrum of carbon monoxide (CO), a simple diatomic system, using an advanced theoretical model that includes all of the aforementioned effects. The focus of the study is on the ratio of vibrational intensities in the C  $1s$  photoemission, ( $\nu = 1$ )/( $\nu = 0$ ), as obtained from the experiment and by *ab initio* methods. We will refer to these as the “ $\nu$ -ratios.” The  $\nu$ -ratios are primarily determined by the change ( $\Delta R$ ) of the internuclear equilibrium distance and are calculated by means of the Franck-Condon factors. In the present case, both the recoil and intramolecular photoelectron scattering modify the Franck-Condon  $\nu$ -ratios. This circumstance is to be contrasted with the case of core-photoionization of the central atom in symmetric  $AB_n$  molecules ( $\text{BF}_3$  [12],  $\text{CF}_4$  [10,12,13], and  $\text{CH}_4$  [9,11]), where the photoelectron is ejected from the center of mass (hence, there are no rotational excitations) and the recoil and Franck-Condon excitations affect different vibrational modes [9,10]. As a result, the analysis of a diatomic molecule as simple as CO is in fact more complex than that of some larger systems with many vibrational degrees of freedom.

We have employed static-exchange density functional theory to obtain *ab initio* vibrationally resolved cross-sections of the C  $1s$  photoemission for  $\nu = 0$  and  $\nu = 1$  levels. These molecular effects are superimposed on the atomic cross section, which falls off sharply with increasing photon energy. As a result, direct comparison of theoretical cross sections with experiment is a difficult task with uncertain outcome. For this reason we compare the  $\nu$ -ratios, which are relative values, instead. We show in a systematic approach how the bond contraction, intramolecular scattering ( $R_0$ -dependent effect), and recoil excitations together determine the  $\nu$ -ratios observed in the C  $1s$  photoelectron spectra. This work is also a proof of principle that such a theoretical approach can be used to determine both the static and dynamic structural properties of a molecule *at the same time*.

## II. C $1s$ PHOTOELECTRON SPECTRA: EXPERIMENTS AND DATA TREATMENT

The experimental values of the intensity ratios in the vibrational progression in C  $1s$  photoelectron spectra of gas-phase carbon monoxide molecules were extracted from spectra measured over several different experimental periods and at

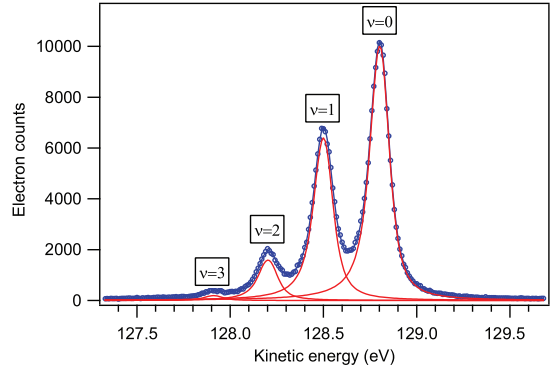


FIG. 1. (Color online) Carbon  $1s$  photoelectron spectrum, measured at  $h\nu = 425$  eV at SOLEIL. Circles: experiment; solid lines: least-squares fit of the vibrational progression.

two synchrotron radiation facilities, SPring-8 (Japan) and SOLEIL (France). The details for the experimental setups used at beamline BL27SU of SPring-8 and at beamline PLEIADES of SOLEIL are described in Refs. [14] and [15], respectively. In brief, Scienta 200-mm mean radius hemispherical electron energy analyzers were used in both experiments, while linearly polarized undulator radiation was used and the target gas was contained in a differentially pumped gas cell. The photon energy range covered by the PLEIADES dataset is from 320 to 525 eV and the electrons were detected at the “magic” emission angle of  $57.4^\circ$  from the polarization vector of linearly polarized light. The SPring-8 datasets from several experimental periods cover a wider photon energy range from 350 to 1500 eV. These spectra were recorded at  $0^\circ$  from the linear polarization vector. In order to compare the intensity ratios with the PLEIADES spectra taken at the magic angle, the following conversion should be applied:

$$R_{54.7} = \frac{R_0 + 2cR_{90}}{1 + 2c}, \quad c = \frac{1 - \beta/2}{1 + \beta}. \quad (1)$$

Here,  $\beta$  is the anisotropy parameter of C  $1s$  photoemission. At the photon energy of 330 eV, both the experimental ( $\beta = 1.79(5)$  [16]) and theoretical values ( $\beta = 1.7$  [17]) are already close to the maximum value of 2. As  $\beta$  asymptotically approaches the maximum value at higher energies,  $c \rightarrow 0$ . In the higher energy range of the present study, in a good approximation  $R_{54.7} \approx R_0$ . Therefore, in this work we compare the  $\nu$ -ratios obtained from  $0^\circ$  and magic-angle spectra directly. Figure 1 shows one example of the spectra analyzed for  $\nu$ -ratios, measured at the PLEIADES beamline. The instrumental broadening of the peaks arises as convolution of the spectrometer’s resolution (about 38 meV FWHM) and photon bandwidth (about 41 meV FWHM). Other experimental contributions to the line width in the spectra come from the translational and rotational [18] Doppler broadenings, which in the case of the spectrum shown in Fig. 1 are 28 and 25 meV, respectively. The spectra were decomposed into individual vibrational components by least-squares fitting using the SPANCF macro package for Igor Pro [19]. The experimental broadenings were represented by Gaussian profiles of adjustable width.

In the PLEIADES spectra that width ranged from 42 to 88 meV FWHM; in the SPring-8 spectra from 61 to 250 meV FWHM depending on the photon energy. These Gaussian profiles were convoluted with distorted Lorentzian shapes arising from the natural width of the C  $1s^{-1}$  core hole state. The asymmetric distortion is caused by post-collision interaction (PCI) between the photoelectron and the Auger electron and it was represented by analytical PCI lineshapes of van der Straten [20]. The PCI asymmetry appears only at photon energies  $h\nu \lesssim 550$  eV. The lifetime width was represented by a common value for each dataset analyzed; all datasets except one from Spring-8 converged to values within  $92.0 \pm 1.0$  meV, in good agreement with the value of  $95 \pm 5$  meV reported by Carroll *et al.* [8]. (The deviant value from one dataset was caused by a significant Lorentzian component in the instrumental broadening.) Energies (for  $\nu = 0$  peaks) and spacings  $\Delta E_{0,\nu}$  (from  $\nu > 0$  peaks to  $\nu = 0$  peak) were also given as adjustable fit parameters, but linked to be the same for each spectrum in a dataset. The spacings from the highest quality PLEIADES dataset are  $\Delta E_{0,1} = 302$ ,  $\Delta E_{1,2} = 298$ , and  $\Delta E_{2,3} = 288$  meV.

### III. THEORY

Vibrationally resolved cross sections are evaluated with first-order perturbation theory within the Born-Oppenheimer (BO) and the dipole approximations:

$$\sigma_{\alpha}(v, v', \omega) = \frac{4\pi^2\omega}{3\hbar c} a_0^2 \sum_{\eta} \sum_{l_{\eta}} |T_{\alpha\eta l_{\eta} v v'}(\varepsilon)|^2, \quad (2)$$

where  $v$  and  $v'$  are the vibrational quantum numbers for the neutral molecule and for the cation, respectively ( $v = 0$  since the initial state is the ground state of CO),  $\omega$  is the photon energy,  $\varepsilon$  is the photoelectron kinetic energy,  $\alpha$  denotes the electronic state of the residual cation,  $l$  is the angular momentum quantum number, and  $\eta$  stands for the symmetry of the final state. The BO approximation permits to write the transition element  $T_{\alpha\eta l_{\eta} v v'}(\varepsilon)$  as

$$T_{\alpha\eta l_{\eta} v v'}(\varepsilon) = \int \chi_{\text{CO},v}^*(R) \mu_{\alpha\eta l_{\eta}}(R) \chi_{\text{CO}^+,v'}(R) dR, \quad (3)$$

where  $\chi_{\text{CO},v}$  and  $\chi_{\text{CO}^+,v'}$  are the initial and the final vibrational wave functions and  $\mu_{\alpha\eta l_{\eta}}$  is the dipole coupling element between the initial electronic state,  $\phi_0$ , and the final one,  $\phi_{\alpha\eta l_{\eta}}$ , which in this case is obtained by promoting one electron from the  $2\sigma$  molecular orbital of CO to a continuum orbital. Electronic wave functions have been evaluated in a grid of 56 internuclear distances around the equilibrium geometry, as in previous work [21], employing the static-exchange density functional theory (DFT) method, developed by Decleva and co-workers [22,23]. This method makes use of the Kohn-Sham DFT to describe the molecular ionic states and the Galerkin approach to evaluate continuum electron wave functions in the field of the corresponding Kohn-Sham density. A standard local density approximation functional has been used to describe electronic exchange and correlation effects. Vibrational eigenfunctions have been obtained by solving the time-independent Schrödinger equation in a basis set of 256 B-splines within a box of 10 a.u. We have

employed the Morse approximation to construct potential energy curves from reliable spectroscopic parameters available in the literature [24]. The calculated  $\nu$ -ratios depend primarily on the equilibrium bond lengths in the neutral molecule and the cation, and especially on the difference in bond lengths,  $\Delta R$ . For instance, the  $\nu$ -ratios are modified approximately by 20% for a variation of 1% in  $\Delta R$ , whilst the effect of similar changes in  $\omega_e$  or in  $\omega_e x_e$  is only between 0.1% and 1%. This behavior is due to (1) the Franck-Condon overlap, which, without affecting the total cross section, changes dramatically the contribution from each vibrational excitation; and (2) the  $R$  dependence of the dipole elements [see Eq. (3)].

## IV. ANALYSIS

### A. Static-exchange DFT results

Before comparing the theoretical results with experimental data points, let us first consider the features of the theoretical curves in some detail. Figure 2 shows a set of static-exchange DFT calculations for the  $\nu$ -ratios in C  $1s$  photoemission spectra as a function of electron momentum, for several values of two crucial parameters, the ground state internuclear distance  $R_0$  and the contraction of that distance upon core ionization,  $\Delta R$ . The bold curves in both panels of Fig. 2 are from a calculation based on the literature values  $R_{\text{fit}} = 2.1322$  a.u. [25] and  $\Delta R_{\text{fit}} = -0.0932$  a.u. [7]. For comparison, the constant Franck-Condon  $\nu$ -ratio computed from the eigenfunctions of the Morse potentials is also reported. This value,  $I(\nu = 1)/I(\nu = 0) = 0.6110$ , is obtained from  $R_0 = 2.1322$  a.u.,  $\Delta R = -0.0932$  a.u., and the Morse curve parameters  $\omega_e = 269.0$  meV,  $\omega_e x_e = 1.648$  meV and  $\omega_e = 304.6$  meV,  $\omega_e x_e = 1.24$  meV for the ground and core-ionized states, respectively [24]. The set of curves in panel (a) of Fig. 2 is obtained by varying the ground-state internuclear distance in the range of  $R_0 = (0.95-1.05)R_{\text{fit}}$ . The effect of this variation is seen mainly as a change in the oscillation period, with shorter periods corresponding to larger internuclear distances. This is consistent with the picture where the oscillations are due to the interference between the electron emitted directly from the carbon atom and the same electron scattered by the oxygen atom. Indeed, a simplified analytical formulation of the interference pattern based on the interatomic scattering mechanism predicts that the period of the  $\nu$ -ratios' oscillations in the momentum scale is  $\Delta k = \pi/R_0$  [11]. This is also the period that appears in the well known EXAFS equation [3], where each  $\sin(2R_j k + \delta)$  term represents photoelectron scattering from the  $j$ th near-neighbor shell in crystalline solid.

Assuming an internuclear distance  $R_0$  of 2.1322 a.u., the static-exchange DFT calculation predicts an oscillation period of about  $\Delta k = 1.9$  a.u. in momentum units (Fig. 2, bold curves). But according to the relationship  $\Delta k = \pi/R_0$  mentioned above, this value should correspond to an internuclear distance  $R_0 = 1.64$  a.u. that is considerably smaller than the value provided as input. This discrepancy, which indicates how simplified analytical expressions are inadequate for quantitative structure determination, may have several causes. Firstly, the expression leading to the oscillation period of  $\pi/R_0$ , as in the EXAFS equation, is based on the assumption that only single-scattering events are relevant. As a rule

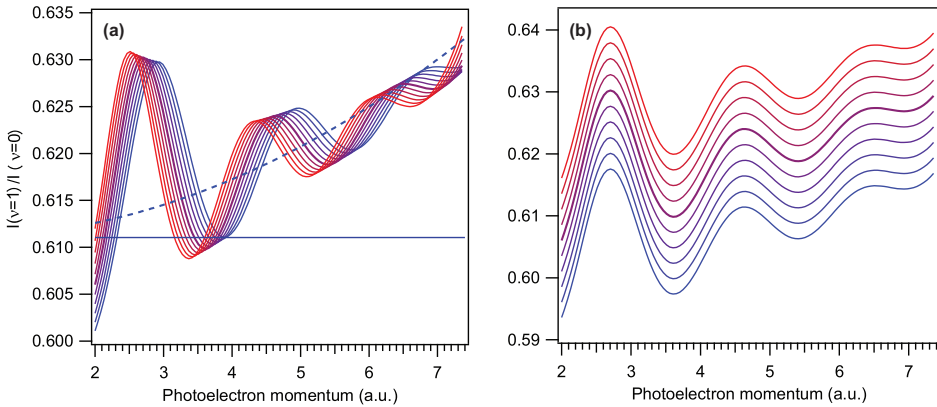


FIG. 2. (Color online) Static-exchange DFT calculations of vibrational ratios. Bold middle curves in both panels are obtained with  $R_0 = R_{lit}$  and  $\Delta R = \Delta R_{lit}$ . (a) Variations of  $R_0 = 0.95\dots 1.05R_{lit}$  (from blue to red) and (b)  $\Delta R = 0.99\dots 1.01\Delta R_{lit}$  (from blue to red). Horizontal line in panel a marks the value from Franck-Condon calculation and the dashed curve represents the photoelectron recoil effect.

of thumb, in EXAFS analysis this is considered a good assumption provided that  $k \gtrsim 1.5$  a.u. [3]. Since in this study we investigate the range of  $k > 2$  a.u., multiple scattering can be expected to have only minor effects. Secondly, as it is known also for the EXAFS equation, the phase  $\delta$  of the oscillation (or, equivalently, the oscillation frequency) is  $k$  dependent, while in the simplified analytical treatment it is considered constant.

One can see that, apart from the scattering-induced oscillations, the DFT prediction also systematically deviates from the Franck-Condon value as the photoelectron energy increases. This deviation is due to the photoelectron recoil effect, represented in Fig. 2(a) by a dashed curve, whose contribution to the  $v$ -ratio is estimated as follows: The Franck-Condon  $v$ -ratio provides the baseline for the recoil contribution. In the momentum scale, the photoelectron recoil excitation probability from  $\nu = 0$  to the  $\nu = 1$  level increases quadratically, and so does the corresponding  $v$ -ratio. The dashed line in Fig. 2(a) shows the photoelectron recoil contribution computed as

$$F(k) = F_{FC} + c_{rec}k^2, \quad (4)$$

where  $F_{FC}$  is the Franck-Condon baseline and the recoil coefficient  $c_{rec}$  is calculated following the semiclassical model given in Refs. [9,10]. The recoil coefficient also accounts for the recoil momentum partitioning between vibrational and rotational excitations and depends on the photoelectron angular distribution in the molecular frame (MFPAD). We made an approximation that, after averaging over the angles between the linear polarization vector of the x-rays and the random laboratory frame orientations of the molecular axis, MFPAD becomes isotropic and then

$$c_{rec} = 3.87 \times 10^{-4} \text{ a.u.}^{-2}.$$

On one hand, recent results using the COLTRIMS (cold target recoil ion momentum spectroscopy) technique have shown that at low photoelectron kinetic energies the MFPADs, even after averaging over the direction of the polarization vector, can be strongly anisotropic (e.g., photoemission preferentially

along the molecular bonds in methane) [26]. Indications of molecular frame anisotropy at low energies are given also by the occurrence of “knockout” secondary ionization processes induced by the primary photoelectron [27]. On the other hand, it was also observed that MFPAD rapidly approaches isotropic distribution with increasing electron energy [26] and we thus believe that in the range of strong recoil effects the approximation of isotropic orientationally averaged MFPAD is well justified, although the recoil model would benefit from more detailed information on MFPADs at the energies of interest.

As can be seen from Fig. 2(a), the recoil model reproduces well the average rising trend of the DFT calculation. Indeed, the calculation is expected to reproduce the recoil, provided that the coordinate system is set at the center of mass of the molecule (as was the case here). In Eq. (4), the Franck-Condon and recoil excitations probabilities are added incoherently. Using the generalized Franck-Condon factors [28,29], it can be shown that this approach is appropriate for the core-ionization from heteronuclear diatomics, where the core orbitals are well localized to a single atom. However, there is also the possibility that scattering of the outgoing photoelectron will cause the molecular frame angular distribution of the photoelectron to be other than isotropic. In this case, the coefficient  $c_{rec}$  in Eq. (4) would differ from the constant value indicated above and could depend on the kinetic energy as well. All these effects are included in the static-exchange DFT calculations; the near agreement between the trend of these calculations and the predictions of Eq. (4) confirms that, in the present case, these effects are small.

Panel (b) of Fig. 2 illustrates the changes in the  $v$ -ratios at fixed internuclear distance  $R_0 = R_{lit}$ , varying the bond contraction  $\Delta R$  upon core ionization in the range  $\Delta R = (0.99-1.01)\Delta R_{lit}$ . As seen from the figure, even a tiny variation of  $\Delta R$  results in large vertical excursion of the  $v$ -ratios' curves. These variations would be reflected also in the baseline Franck-Condon factors as the displacement along  $R$  of the initial and final state potential energy curves changes. Figure 2

thus demonstrates that the molecular  $v$ -ratios are sensitive probes for both the static and dynamic structure parameters. In the next section, these calculations are compared with the experimental results.

### B. Comparison with experiment and derivation of geometrical parameters

The ratios of the intensities of the  $v = 1$  and  $v = 0$  vibrational peaks in C 1s experimental photoelectron spectra, extracted by least-squares curve fitting, are shown in Fig. 3. The error bars of the SOLEIL data represent the statistical standard deviations obtained from the fitting. In the SPring-8 datasets it was observed that, when analyzing repeated electron energy scans at a particular energy, the  $v$ -ratios varied more than the error estimates based on counting statistics, most likely due to instabilities in electron detection. The error bars for this latter set take into account also this additional source of variation. In addition to the results from these experiments, the three data points with the lowest  $k$  values were extracted from the spectra published by Carroll *et al.* [8]. More values for the  $v$ -ratios in C 1s photoionization of CO are available in literature [30,31], but these were not included for comparison, because we did not have the possibility to reanalyze the original spectra consistently with the same methods.

The thin red line once again shows the DFT calculation based on the literature values  $R_{\text{lit}} = 2.1322$  a.u. [25] and  $\Delta R_{\text{lit}} = -0.0932$  a.u. [8]. Below  $k = 2$  a.u. the theory is in excellent agreement with the experimental data, representing also the major increase of the  $v$ -ratio due to the presence of the shape resonance near the threshold [11,32]. However, at  $k \geq 2$  a systematic discrepancy appears. This vertical offset of the theory is mostly influenced by the choice of the value of  $\Delta R$ . In considering this discrepancy, one should keep in mind that the literature value for  $\Delta R_{\text{lit}}$  has in fact been

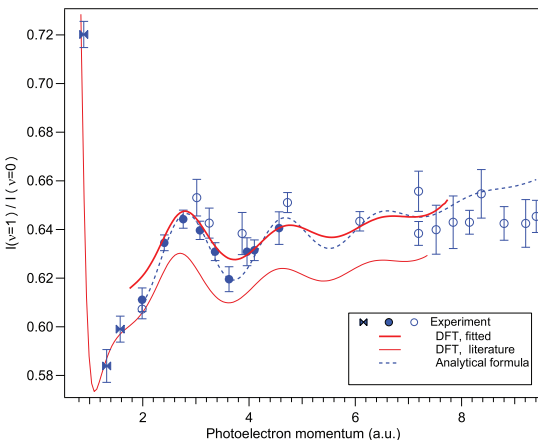


FIG. 3. (Color online) Experimental and calculated intensity ratios of the vibrational peaks in C 1s photoelectron spectra of CO. Open circles: measurements at SPring8; full circles: measurements at SOLEIL; double triangles: Ref. [8]. Bold solid red line: fit of the static-exchange DFT theory; thin red line: DFT theory with literature input values; dashed blue line: fit of analytical formula.

obtained from basic Franck-Condon analysis of photoelectron spectra such as the one depicted in Fig. 1. Yet Fig. 2 clearly shows that such an analysis does not properly take into account the modulation due to intramolecular scattering and photoelectron recoil, thus resulting in uncertain estimates of the internuclear bond contraction. Furthermore, the shape resonance in the C 1s photoionization of CO [32] affects the cross sections for the electrons with momenta up to  $\approx 1-2$  a.u. above threshold [11]. Since shape-resonance maxima occur at slightly different energies for different vibrationally resolved cross sections (by about 2 eV), the resonance also distorts the  $v$ -ratios close to threshold, rendering them unsuitable for accurate Franck-Condon analysis. In the energy range above the shape resonance, it is the scattering oscillations that modify the  $v$ -ratios. Finally, at high energy, where the oscillations are strongly damped, recoil excitations start to contribute significantly. It is therefore not surprising that calculations based on available literature data may fail to represent the experimental  $v$ -ratios across a broad electron momentum range.

In order to perform a consistent derivation of geometrical parameters from the experimental  $v$ -ratios, a least-squares fit of the DFT calculation to the experiment was performed. The result is shown in Fig. 3 as a bold red curve (also indicating the range of data points that were included in the fit). As the span over  $k$  of the fitted curve indicates, the data points for the lowest and highest momenta were not included since the purpose was the derivation of the geometrical parameters. The near-threshold values of the  $v$ -ratios are strongly influenced by multiple scattering and the shape resonance, while at large momentum values the characteristic oscillations become significantly damped. Also the near-threshold region is more sensitive to electron correlation and less accurately described by the static DFT calculations.

The fitting variables were  $R_0$  and  $\Delta R$ . The best agreement with the experimental data (as measured by  $\chi^2$  goodness-of-fit value) was obtained with  $R_0 = 2.09 \pm 0.05$  a.u. and  $\Delta R = -0.0945 \pm 0.0002$  a.u. The uncertainties are estimated from the fitting procedure and depend on the number of the experimental data points and their error bars; the uncertainties do not reflect any inaccuracies in the theoretical model. Such a quantitative procedure is feasible because, although the integral in Eq. (3) must be reevaluated at each step of the optimization procedure (the vibrational wave functions depend on the values of the Morse parameters), the dipole matrix elements  $\mu_{\alpha_0 l_0}(R)$  are computed once and for all at once. As a consequence, the fitting algorithm is actually very efficient from the computational point of view.

To get a better insight into the different contributions to the  $v$ -ratios, we added the oscillatory term of the simplified analytical model to the photoelectron recoil curve [Eq. (4)]:

$$F = F_{\text{FC}} + A \exp(-ck^2) \sin(2Rk + \delta) + c_{\text{rec}} k^2. \quad (5)$$

Once it was ascertained that Eq. (5) can match the fully theoretical curve with sufficient accuracy, the experimental data in Fig. 3 was fitted by freely varying the five parameters  $F_{\text{FC}}$ ,  $A$ ,  $c$ ,  $R$ , and  $\delta$ , while  $c_{\text{rec}}$  was kept at the fixed value of  $3.87 \times 10^{-4}$  a.u.<sup>-2</sup>, as explained above. As can be seen, the analytical formula follows the data well at  $k$  less than 7. However, it is notable that 7 out of 9 measured  $v$ -ratios at photon energies  $\geq 1000$  eV ( $k \gtrsim 7$ ) fall below the predicted

recoil curve. Based on the available data, we cannot tell whether this discrepancy is due to a deficiency of the recoil model or is an experimental artifact. For example, in the fitting we assumed a Gaussian instrumental profile. If, however, the true instrument function is skewed towards high kinetic energy, the  $v$ -ratios extracted using a symmetric profile are too low. A fitting conducted with asymmetric profiles would bring the high-energy results into better agreement with the theoretical predictions, but at this point any quantitative assumption about peak asymmetry would be unjustified.

This least-squares fit to the experiment converged with the essential geometry-related parameters  $F_{\text{FC}} = 0.627 \pm 0.001$  and  $R = 1.70 \pm 0.07$  a.u. As noted above, the analytical formula with EXAFS-like relationship between  $R$  and the oscillation period provides a value significantly lower than the true bond length, while the DFT fit result of  $R_0 = 2.09 \pm 0.06$  agrees well with the literature value of  $R_{\text{lit}} = 2.1322$  a.u. [25].

The literature values of  $\Delta R_{\text{lit}} = -0.0932$  a.u. [24] and  $-0.0917 \pm 0.0009$  a.u. from another source [8] are to be compared with the value of  $\Delta R = -0.0945 \pm 0.0002$  a.u. obtained by fitting the static-exchange DFT theory to the experiment. The less accurate empirical formula [Eq. (5)] gave a Franck-Condon ratio that corresponds to  $\Delta R = -0.096$  a.u.

We can see that employing the DFT theory allows for highly accurate determination of the dynamical parameter  $\Delta R$ , whereas the static ground state internuclear distance  $R_0$  is determined much less accurately, particularly in comparison with other available methods such as microwave spectroscopy [25]. It is a unique feature of this method, however, that these two quantities are obtained simultaneously. Also, current errors originate mostly from the uncertainty in the experimental data and therefore future improvements in experimental statistics and resolution at higher energies would significantly improve the accuracy of the fit.

## V. CONCLUSION

Vibrational intensity ratios ( $v$ -ratios) in the C 1s photoelectron spectra of CO were investigated by comparing a combined experimental dataset from several experiments with *ab initio* static-exchange DFT calculations, as well as with a simplified analytical model formula. The theoretical results included conventional Franck-Condon excitations, photoelectron recoil, and intramolecular scattering on the neighboring oxygen atom. It was demonstrated by a set of *ab initio* curves that the  $v$ -ratios are potentially a very sensitive means of determining both static (internuclear distance) and dynamic (bond length change) geometrical parameters *simultaneously*, although improvements particularly in experimental values will be needed to realize this potential.

It was also noted that simplified theoretical models for analytical expressions of  $v$ -ratios, although providing an excellent means for qualitative interpretation, can easily lead to erroneous quantitative results. For quantitative structural determinations from experimental data, comparison with fully *ab initio* theoretical descriptions is to be strongly preferred.

When theory and experiment are compared, it becomes apparent that bond lengths taken from the literature lead to a poor agreement. A least-squares fit of the full DFT calculation, varying  $R_0$  and  $\Delta R$ , considerably improves the agreement. From the fit, we extracted the new geometry values  $R_0 = 2.09$  a.u. and  $\Delta R = -0.0945$  a.u. and demonstrated the feasibility of using the DFT calculations for geometry determination in molecules. Even if equilibrium internuclear distances are often accurately known for many molecular systems already, the uniqueness of the approach described here lies in the ability to determine both static and dynamic geometrical values simultaneously. In fact, a separate determination of the dynamical values only—the bond length change—the usual means of Franck-Condon analysis of the vibrational structure is inevitably prone to systematic errors, since the scattering effects are neglected. Regarding the practical use of this method for determining the dynamic structure parameters, we point out the *local* nature of the scattering, probing mostly the nearest neighbor distances (akin to EXAFS). Therefore, using well localized core ionization, one can probe particular regions of large molecules with accuracy potentially better than that achievable by other methods.

## ACKNOWLEDGMENTS

We appreciate the help of the staff of SPring-8 (Japan) during the experiments there. At SOLEIL (France), data collection was performed at the PLEIADES beamline during beam time allotted under Proposal No. 20110781. SOLEIL staff are acknowledged for smoothly running the facilities and E. Robert for technical assistance. This work was supported by the FP7/2007-2013 Grant No. 252781 (OT) and Triangle de la Physique Contract No. 2007-010T (OT), and by the MEXT and JSPS agencies (Japan). We also thank Mare Nostrum BSC, Cineca and CCC-UAM for allocation of computer time. E.K. acknowledges financial support from the Academy of Finland. E.P., L.A., D.A., A.P., and F.M. acknowledge financial support from the Advanced Grant of the European Research Council XCHEM 290853, the MICINN Projects No. FIS2010-15127, No. ACI2008-0777, and No. CSD 2007-00010 (Spain), the ERA-Chemistry Project No. PIM2010EEC-00751, the European grants MC-ITN CORINF and MC-RG ATTOTREND, and the European COST Actions No. CM0702 (CUSPFEL) and No. CM1204 (XLIC).

- 
- [1] P. Debye, *Ann. Phys.* **46**, 809 (1915).  
 [2] I. Hargittai, *Electron Crystallogr.* **211**, 197 (2006).  
 [3] E. A. Stern, *Phys. Rev. B* **10**, 3027 (1974).  
 [4] D. P. Woodruff, *Appl. Phys. A* **92**, 439 (2008).  
 [5] F. Krasniqi, B. Najjari, L. Strüder, D. Rolles, A. Voitkiv, and J. Ullrich, *Phys. Rev. A* **81**, 033411 (2010).

- [6] Z. F. Liu, G. M. Bancroft, J. N. Cutler, D. G. Sutherland, K. H. Tan, J. S. Tse, and R. G. Cavell, *Phys. Rev. A* **46**, 1688 (1992).  
 [7] B. Kempgens, K. Maier, A. Kivimäki, H. M. Köppe, M. Neeb, M. N. Piancastelli, U. Hergenbahn, and A. M. Bradshaw, *J. Phys. B* **30**, L741 (1997).

- [8] T. X. Carroll, K. J. Børve, L. J. Sæthre, J. D. Bozek, E. Kukk, J. A. Hahne, and T. D. Thomas, *J. Chem. Phys.* **116**, 10221 (2002).
- [9] E. Kukk, K. Ueda, U. Hergenbahn, X.-J. Liu, G. Prümper, H. Yoshida, Y. Tamenori, C. Makochekanwa, T. Tanaka, M. Kitajima, and H. Tanaka, *Phys. Rev. Lett.* **95**, 133001 (2005).
- [10] T. D. Thomas, E. Kukk, R. Sankari, H. Fukuzawa, G. Prümper, K. Ueda, R. Püttner, J. Harries, Y. Tamenori, T. Tanaka, M. Hoshino, and H. Tanaka, *J. Chem. Phys.* **128**, 144311 (2008).
- [11] E. Plésiat, L. Argenti, E. Kukk, C. Miron, K. Ueda, P. Decleva, and F. Martín, *Phys. Rev. A* **85**, 023409 (2012).
- [12] K. Ueda *et al.*, *J. Chem. Phys.* (to be published).
- [13] M. Patanen *et al.* (private communication).
- [14] H. Ohashi, E. Ishiguro, Y. Tamenori, H. Kishimoto, M. Tanaka, M. Irie, T. Tanaka, and T. Ishikawa, *Nucl. Instrum. Methods A* **467**, 529 (2001); K. Ueda, *J. Phys. B* **36**, R1 (2003).
- [15] O. Travnikova, J.-C. Liu, A. Lindblad, C. Nicolas, J. Söderström, V. Kimberg, F. Gel'mukhanov, and C. Miron, *Phys. Rev. Lett.* **105**, 233001 (2010); J. Söderström, A. Lindblad, A. N. Grum-Grzhimailo, O. Travnikova, C. Nicolas, S. Svensson, and C. Miron, *New J. Phys.* **13**, 073014 (2011); C. Miron, C. Nicolas, O. Travnikova, P. Morin, Y. Sun, F. Gel'mukhanov, N. Kosugi, and V. Kimberg, *Nat. Phys.* **8**, 135 (2012).
- [16] O. Hemmers, S. B. Whitfield, N. Berrah, B. Langer, R. Wehlitz, and U. Becker, *J. Phys. B* **28**, L693 (1995).
- [17] E. Plésiat, P. Decleva, and F. Martín, *J. Phys. B* **45**, 194008 (2012).
- [18] T. D. Thomas, E. Kukk, K. Ueda, T. Ouchi, K. Sakai, T. X. Carroll, C. Nicolas, O. Travnikova, and C. Miron, *Phys. Rev. Lett.* **106**, 193009 (2011).
- [19] E. Kukk, spectral analysis by curve fitting macro package, SPANCF 2000, [http://www.physics.utu.fi/en/department/materials\\_research/materials\\_science/Fitting.html](http://www.physics.utu.fi/en/department/materials_research/materials_science/Fitting.html).
- [20] P. van der Straten, R. Morgenstern, and A. Niehaus, *Z. Phys. D* **8**, 35 (1988).
- [21] E. Plésiat, *Phys. Chem. Chem. Phys.* **14**, 10853 (2012).
- [22] M. Venuti, M. Stener, and P. Decleva, *Chem. Phys.* **234**, 95 (1998).
- [23] D. Toffoli, M. Stener, G. Fronzoni, and P. Decleva, *Chem. Phys.* **276**, 25 (2012).
- [24] U. Hergenbahn, *J. Phys. B* **37**, R89 (2004).
- [25] K. P. Huber and G. Herzberg, in *NIST Chemistry WebBook*, NIST Standard Reference Database Number 69, edited by P. J. Linstrom and W. G. Mallard (National Institute of Standards and Technology, Gaithersburg, MD), <http://webbook.nist.gov> (retrieved February 14, 2013).
- [26] J. B. Williams, *J. Phys. B* **45**, 194003 (2012).
- [27] T. Hartman, P. N. Juranić, K. Collins, B. Reilly, N. Appathurai, and R. Wehlitz, *Phys. Rev. Lett.* **108**, 023001 (2012).
- [28] P. Salek, F. Gel'mukhanov, H. Ågren, O. Björneholm, and S. Svensson, *Phys. Rev. A* **60**, 2786 (1999).
- [29] F. Gel'mukhanov, P. Salek, and H. Ågren, *Phys. Rev. A* **64**, 012504 (2001).
- [30] H. M. Köppe, A. L. D. Kilcoyne, J. Feldhaus, and A. M. Bradshaw, *J. Electron Spectrosc. Relat. Phenom.* **75**, 97 (1995).
- [31] M. Matsumoto, K. Ueda, E. Kukk, H. Yoshida, T. Tanaka, M. Kitajima, H. Tanaka, Y. Tamenori, K. Kuramoto, M. Ehara, and H. Nakatsuji, *Chem. Phys. Lett.* **417**, 89 (2006).
- [32] E. Shigemasa, J. Adachi, K. Soejima, N. Watanabe, A. Yagishita, and N. A. Cherepkov, *Phys. Rev. Lett.* **80**, 1622 (1998).





## **Appendix E**

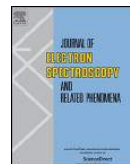
Dissociative and non-dissociative  
photoionization of molecular fluorine  
from inner and valence shells





Contents lists available at ScienceDirect

# Journal of Electron Spectroscopy and Related Phenomena

journal homepage: [www.elsevier.com/locate/elspec](http://www.elsevier.com/locate/elspec)

## Dissociative and non-dissociative photoionization of molecular fluorine from inner and valence shells

D. Ayuso<sup>a</sup>, A. Palacios<sup>a</sup>, P. Declava<sup>b,c</sup>, F. Martín<sup>a,d,\*</sup><sup>a</sup> Departamento de Química, Módulo 13, Universidad Autónoma de Madrid, Cantoblanco, 28049 Madrid, Spain<sup>b</sup> Dipartimento di Scienze Chimiche e Farmaceutiche, Università di Trieste, 34127 Trieste, Italy<sup>c</sup> CNR-IOM, Trieste, Italy<sup>d</sup> Instituto Madrileño de Estudios Avanzados en Nanociencia, Cantoblanco, 28049 Madrid, Spain

## ARTICLE INFO

## Article history:

Available online 5 December 2013

## Keywords:

Molecular fluorine  
Photoionization  
Cross section  
Cohen–Fano  
Static-exchange DFT

## ABSTRACT

We present a theoretical study of F<sub>2</sub> photoionization in the range 0–40 a.u. of photoelectron energy, where the undulatory behavior of the corresponding angle-integrated cross sections due to electron emission from equivalent centers is apparent. These double-slit type interferences are observed in both inner- and valence-shell ionization. We analyze confinement effects that appear at given energies when the electron is ejected parallel to the molecular axis. Since we account for the nuclear degrees of freedom, we evaluate and discuss the vibrationally resolved cross sections, including both dissociative and non-dissociative ionization channels. We also analyze the ratios between the latter cross sections and the relationship between the observed oscillations and the structure of the molecule.

© 2013 Elsevier B.V. All rights reserved.

### 1. Introduction

A large number of experimental studies on diatomic halogens has been performed to extract spectroscopic data of the ground state of both the neutral molecule and the corresponding cation [1,2]. The first photoelectron spectra were obtained more than twenty years ago [1–3], including the vibrational bands associated to the three lowest electronic states of the ion [2,3]. The lightest of the diatomic halogens, molecular fluorine, received particular attention over the years [3–5]. To our knowledge, photoionization measurements are only available in the literature for relatively low photon energies, comparable to the ionization potentials associated to the lowest electronic states (up to 22 eV) [3,5]. In the present work, we theoretically explore the photoionization cross sections of molecular fluorine scanning photon energies up to hundreds of eV and considering electron ejection from all valence and inner shells. We pay an especial attention to the interference effects that arise when energetic electrons are ejected from equivalent centers, similar to the interferences observed in Young's double-slit experiment, that leads to well-known oscillations in the photoelectron spectra as shown in previous experimental and theoretical works on other diatomic molecules such as H<sub>2</sub> [6], N<sub>2</sub> [7–10] or CO [9–11]. Our aim is to give a complete description of

F<sub>2</sub> photoionization. So we include the nuclear degrees of freedom in order to obtain vibrationally resolved cross sections. Photoionization experiments at these high photon energies are possible by using third-generation synchrotron radiation sources, which in combination with high-energy-resolution detection techniques have allowed for accurate measurements of vibrationally resolved photoionization spectra in the last few years (see Ref. [10] and references therein).

We evaluate both dissociative and non-dissociative ionization cross sections associated to the three lowest ionization thresholds. The bond-dissociation energy of fluorine is 0.059 a.u. [5], lower than for chlorine or bromine [12] and also than for other diatomic molecules made up of first row atoms (N<sub>2</sub>: 0.359 a.u. [13], CO: 0.408 a.u. [14], O<sub>2</sub>: 0.188 a.u. [14]; because of their multiple bonds). Therefore, from a chemical perspective, one would expect the F–F bond to easily break. Indeed, as we show in this work, in contrast with N<sub>2</sub> or CO [9,10], dissociative ionization is not negligible and therefore must be considered in a complete description of F<sub>2</sub> one-photon ionization.

In the following, we first introduce the theoretical approach employed to evaluate the electronic structure of both the neutral and the ion within the static-exchange density functional theory (DFT) method [15,16], as well as the methodological approach to include the nuclear degrees of freedom within the Born–Oppenheimer approximation. Then we present the photoionization cross sections for electron ejection from different molecular orbitals and compare with results obtained within the fixed nuclei approximation (FNA). Finally, we present the vibrationally resolved

\* Corresponding author at: Departamento de Química, Módulo 13, Universidad Autónoma de Madrid, Cantoblanco, 28049 Madrid, Spain. Tel.: +34 914974019.  
E-mail address: [fernando.martin@uam.es](mailto:fernando.martin@uam.es) (F. Martín).

photoionization cross sections. We end by summarizing the most relevant conclusions of our work.

## 2. Methodology

Vibrationally resolved cross sections have been evaluated using first order perturbation theory within the Born–Oppenheimer (BO) and the dipole approximations:

$$\sigma_{\alpha}(v, v', \omega) = \frac{4\pi^2\omega}{3\hbar c} a_0^2 \sum_{\eta} \sum_{l_{\eta}} T_{\alpha l_{\eta} v v'}(\epsilon) \quad (1)$$

where

$$T_{\alpha l_{\eta} v v'}(\epsilon) = \left| \int \chi_{F_2^*, v}(R) \mu_{\alpha l_{\eta}}(\epsilon, R) \chi_{F_2^+(\alpha), v'}(R) dR \right|^2 \quad (2)$$

$v$  and  $v'$  are the vibrational quantum numbers of the neutral molecule and of the residual ion, respectively, and  $\chi_{F_2^*, v}(R)$  and  $\chi_{F_2^+(\alpha), v'}(R)$  are corresponding wave functions,  $\mu_{\alpha l_{\eta}}(\epsilon, R)$  is the electronic dipole-transition matrix element,  $l_{\eta}$  is the photoelectron's ( $l, m$ ) angular momentum quantum numbers in a final state of symmetry  $\eta$ ,  $\alpha$  denotes the electronic state of the residual ion,  $\omega$  and  $\epsilon$  are the photon and the photoelectron energies, which are related through the equation  $\epsilon = \hbar\omega - IE_{\alpha}$ , where  $IE_{\alpha}$  is the energy required to produce the ion in the  $\alpha$  state.

For the inclusion of the vibrational structure, the dipole matrix elements need to be obtained in a grid of internuclear distances  $R$  around the equilibrium geometry, which makes most theoretical methods prohibitively expensive (see Ref. [10] and the references therein). In this sense, DFT-like methods have arisen as an excellent tool to treat molecular photoionization in medium size systems, providing a good compromise between accuracy and computational cost. In the following we introduce the most relevant characteristics of the methodology we have employed in this work (see Ref. [17] for a more complete description).

### 2.1. Static-exchange DFT

Electronic states have been evaluated using the static-exchange DFT method developed by Declava and collaborators [15,16]. In this method, the Kohn–Sham (KS) equations are solved to obtain an approximation for the initial (ground) state of the neutral molecule. The final continuum state is described as an antisymmetrized product of a continuum orbital and the wave function of the residual molecular cation. The latter is built by freezing the KS orbitals of the neutral molecule that remain occupied after ionization. The continuum orbital is evaluated in the field of the corresponding Kohn–Sham density by using the Galerkin approach. The method has been proven to provide accurate results for the total photoionization cross section of small molecules as well as for medium size systems within the fixed nuclei approximation (FNA) [15,18,19]. In order to evaluate vibrationally resolved cross sections, it was expanded to treat the non-equilibrium geometries adopted by the nuclei during the molecular vibration [9,10]. In this work we have considered 99 different internuclear distances around the Franck–Condon (FC) region. For each value, the following procedure was performed.

The first step consists in running a standard DFT calculation for the ground state of the neutral molecule. We have employed the Amsterdam Density Functional (ADF) [20,21] package using a double zeta plus polarization basis set (taken from the ADF library) and a LB94 functional [22] to describe the electronic exchange and correlation effects. The electronic ground state density provided by the self consistent field procedure was employed to build the Hamiltonian matrix in a multicentric basis set of B-splines of order 10

and symmetry adapted-spherical harmonics: (1) a large one-center (OCE) expansion over the center of the molecule, which provides an accurate description of asymptotic behavior of the continuum states; and (2) small off-centers (OC), located at the atomic positions, that improve the convergence of the calculation since they effectively describe the wave function cusps at the nuclei. For each expansion, the B-splines are defined over intervals  $[0, R_{max}]$ . A big value of  $R_{max}$  is required in the OCE in order to describe the long-range behavior of the continuum states. The local nature of the B-splines enables to control the overlap between the basis functions and it is possible to avoid running into numerical linear dependencies by keeping a small expansion over each off-center that is normally enough to describe of the bound states. In this work we have employed the following parameters for the OCE (for the OC): 250 B-splines (10 B-splines),  $l_{max} = 15$  (2) and  $R_{max} = 25$  a.u. (0.5 a.u.).

Since the off-center spheres do not intersect, the resulting Hamiltonian matrix can be partitioned into different blocks: (1) the diagonal ones, connecting basis functions that have the same origin in the multicentric expansion; and (2) the off-diagonals, involving basis with different origin. The largest computational cost corresponds to the calculation of the latter since the corresponding integrals do not have analytical resolution. However, they are computed using a three-dimensional Gauss-Legendre scheme and a substantial effort is saved using symmetry to divide the total space into equivalent subregions.

The initial state is represented as the Slater determinant of the Kohn–Sham orbitals obtained in the diagonalization of the Hamiltonian matrix in the new basis set. The description of the final states, however, is more complex since involves an electron in the continuum. In the present work we have made use of the Galerkin approach, which can yield the continuum wave function at any selected energy employing a fixed basis set without the need to change the box size. A detailed review on the Galerkin approach for our specific implementation is given in Ref. [17]. Within the static-DFT approach, final states are obtained by promoting one electron from a bound orbital to a continuum orbital.

### 2.2. The inclusion of the nuclear motion

The nuclear motion is taken into account at the Born–Oppenheimer level by including the vibrational eigenstates in Eq. (2), which are solutions of the corresponding eigenvalue problem [17]:

$$\left[ -\frac{1}{2\mu} \nabla_R^2 + E_{\alpha}(R) \right] \chi_{\alpha, v}(R) = E_{\alpha, v} \chi_{\alpha, v}(R) \quad (3)$$

where  $\mu$  is the reduced mass of the system,  $E_{\alpha}(R)$  is the potential energy curve of the neutral or the ionic species in the electronic state  $\alpha$ ,  $\chi_{\alpha, v}(R)$  are the vibrational wave functions and  $E_{\alpha, v}$  the corresponding vibronic energies. Eq. (3) was solved numerically in a basis set of 500 B-splines within a box of 15 a.u., which provided an orthonormal set of bound and discretized continuum states. The latter were renormalized a posteriori to the density of states in order to describe molecular dissociation [17]. The potential energy curves of the electronic ground state of molecular fluorine and of the 3 low-lying ionic states (Fig. 1) were constructed using reliable spectroscopic parameters available in the literature (see Table 1) within the Morse approximation. The dissociation of the ionic species  $F_2^+(^2\Pi_g)$  and  $F_2^+(^2\Pi_u)$  yields to the formation of the atomic fragments  $F(^2P_{3/2})$  and  $F^+(^3P_2)$ , both in the ground state, whereas the dissociation of  $F_2^+(^2\Sigma_g^+)$  produces  $F(^2P_{3/2})$  and the excited cation  $F^+(^1D_2)$  [2]. For simplicity, hereafter in the manuscript we will employ the following notation to name the electronic states of the ionized species:  $F_2^+(1\pi_g^{-1})$ ,  $F_2^+(1\pi_u^{-1})$  and  $F_2^+(3\sigma_g^{-1})$ , where the term in brackets designates the origin of the photoelectron in the neutral molecule.

**Table 1**  
Spectroscopic parameters employed to build the potential energy curves of the relevant electronic states of  $F_2$  and  $F_2^+$ : the internuclear equilibrium distance,  $R_{eq}$ , the harmonic frequency,  $\omega_e$ , the anharmonicity parameter,  $\omega_e x_e$ , and the adiabatic ionization potential, IP.

Electronic state	$R_{eq}$ (a.u.)	$\omega_e$ ( $\text{cm}^{-1}$ )	$\omega_e x_e$ ( $\text{cm}^{-1}$ )	IP (a.u.)
$F_2(^1\Sigma_g^+)$	2.66816 [23]	916.64 [23]	11.236 [23]	–
$F_2(^2\Pi_g)$	2.479 [2]	1104 [3]	9.84 [3]	0.57671 [3]
$F_2(^2\Pi_u)$	3.10 [2]	640 [3]	13.2 [3]	0.67251 [3]
$F_2(^2\Sigma_g^+)$	3.16 [2]	481 [2]	7.8 [2]	0.76200 [2]

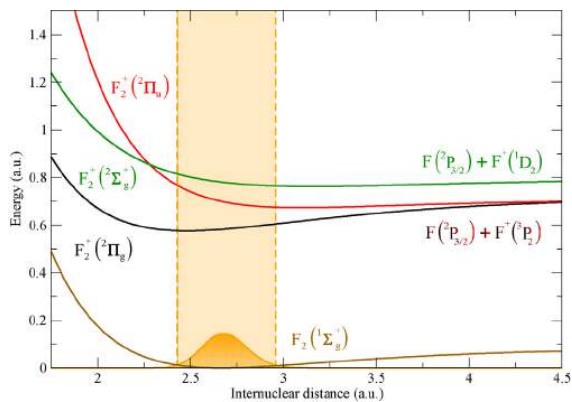


**Fig. 1.** Morse potential energy curves of the electronic ground state of  $F_2$  and of the three low-lying states of  $F_2^+$  constructed from the spectroscopic parameters shown in Table 1. The wave function of the vibrational ground state of  $F_2$  is represented in orange as well as the Franck-Condon region. (For interpretation of the references to color in this legend, the reader is referred to the web version of the article.)

### 3. Total photoionization cross section

We have computed the photoionization cross sections of  $F_2$  from the valence, the inner-valence and the core shells for photoelectron energies up to 40 a.u. Fig. 2 shows the cross sections as functions of photon energy for each molecular orbital of  $F_2$  (listed in the legend from the outer to the more inner shell), evaluated within the fixed nuclei approximation (FNA). We can see that for photon energies up to  $\approx 10$  a.u., photoionization leaves the ion in the two lowest electronic states. Only for photon energies larger than 10 a.u., inner valence ionization dominates, and at  $\approx 25$  a.u. one

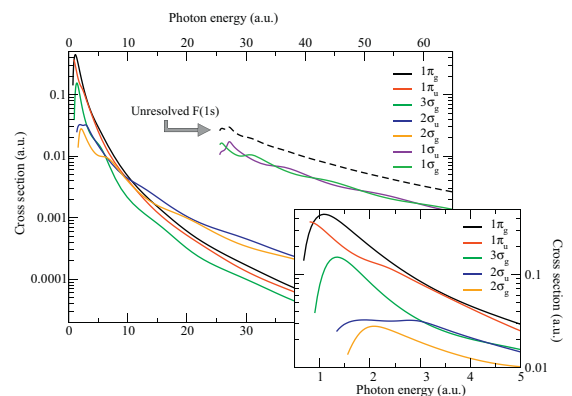


**Fig. 2.** Photoionization cross sections of  $F_2$  as a function of the photon energy obtained using the static DFT approach within the fixed nuclei approximation. The photoelectron's molecular orbital of origin is listed in the legend from the outer to the more inner shell.

reaches the ionization potential for K-shell electrons, thus becoming this core ionization the dominant contribution as expected. For  $F_2$ , the energy splitting between the  $1\sigma_g$  and  $1\sigma_u$  orbitals is extremely small,  $\sim 4$ – $30$  meV according to our DFT calculations performed with different basis sets. This splitting is much smaller than that found in other homonuclear diatomic molecules, as, e.g.,  $N_2$ , for which it is of the order of 100 meV. This is the consequence of the fact that the  $F_2$  bond is long and the  $1s$  orbitals of the F atoms are very concentrated around the corresponding nuclei, resulting in an almost zero overlap between them. The lifetimes of the  $F(1s)$  core-hole states are also very small and the corresponding widths are thus rather large, of the order of 200 meV [24], i.e., much larger than the energy splitting between the two states. Therefore, the peaks associated to ionization from the  $1\sigma_g$  and  $1\sigma_u$  orbitals will be very difficult to resolve experimentally. For the sake of comparison with future experimental work, the unresolved  $F(1s)$  total cross section is shown as a dotted line in Fig. 2.

In the bottom right panel in Fig. 2, valence and inner-valence shells photoionization cross sections are amplified for low photon energies. The sharp structures arising near the threshold in some photoionization channels can be understood in terms of shape resonances due to the existence of small potential barriers. Such features have been previously reported and explained for existing measurements in diatomic [10,25,26] and polyatomic molecules [27]. Note that the use of a single excitation approach prevents us from observing any possible signature coming from multiple (doubly, triply) excited electronic states of the molecule embedded in the ionization continua [28].

For larger photon energies, the cross sections in Fig. 2 show oscillations as functions of the photon energy. Although slightly obscured by the rapid exponential decay, these features are visible, mainly for the core and the inner valence, where the  $1\sigma_g(2\sigma_g)$  and the  $1\sigma_u(2\sigma_u)$  channels are out of phase because of the different bonding character. One can thus better explore these features by taking the ratios between the cross sections corresponding to those orbitals with different parity. The corresponding ratios are shown in Fig. 3, plotted now as functions of the photoelectron linear momentum for analysis purposes as explained in the following. The oscillations, which are now clearly distinguishable, are the fingerprint of the coherent photoelectron emission from two equivalent centers. Cohen and Fano [29] explained this phenomenon more than forty years ago for the photoionization of the hydrogen molecule by assuming that the photoelectron could be adequately described by a plane wave and by writing the  $\sigma_g$  and the  $\sigma_u$  molecular orbitals as:

$$1\sigma_{g/u} = \frac{1}{\sqrt{2}}(1s_a \pm 1s_b) \quad (4)$$

where  $1s_a$  and  $1s_b$  are atomic  $1s$  orbitals centered on each hydrogen atom. Under these assumptions, the photoionization cross section integrated over the ejection angle can be written as:

$$\sigma_{g/u}(\varepsilon) = \sigma_{g/u}^{(0)}(\varepsilon) \left( 1 \pm \frac{\sin k_e R}{k_e R} \right) \quad (5)$$

where  $\sigma^{(0)}(\varepsilon)$  is a decreasing background depending on the photon  $\omega$  or the photoelectron energy  $\varepsilon$ ,  $k_e$  is the photoelectron linear momentum and  $R$  is the internuclear distance. Eq. (5) can also

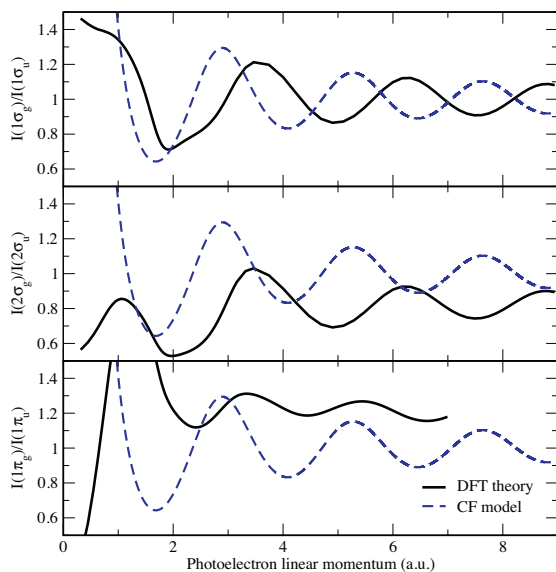


**Fig. 3.** Ratios between cross sections corresponding to photoionization from different molecular orbitals obtained within the fixed nuclei approximation. Black full line: DFT results; blue dashed line: results coming from the Cohen–Fano model explained in the text. (For interpretation of the references to color in this legend, the reader is referred to the web version of the article.)

provide qualitative values in more complex diatomic molecules, even when the electron is ejected from a valence shell, and it is possible to generalize it to the case of heteronuclear molecules [9]. When comparing values corresponding to  $\sigma_g/\sigma_u$  ionization in the same shell, the non-oscillatory terms will be very similar and one can assume  $\sigma_g^{(0)}(\varepsilon) = \sigma_u^{(0)}(\varepsilon)$  when taking the ratio:

$$\frac{\sigma(\varepsilon)_g}{\sigma(\varepsilon)_u} \simeq \frac{1 + \Gamma(k_e)}{1 - \Gamma(k_e)} \quad (6)$$

where

$$\Gamma(k_e) = \frac{\sin k_e R}{k_e R} \quad (7)$$

The good qualitative agreement between our DFT-like results and those coming from Eq. (6) (see Fig. 3) demonstrates that the oscillations found in the spectra are actually a manifestation of the coherent multicenter emission of photoelectrons as described by Cohen–Fano.

We note that although the previously discussed cross sections were obtained within the FNA, very similar results are obtained when including the nuclear motion. We have carried out calculations including the nuclear degrees of freedom for the photoionization from the three outer valence shells, for which reliable potential energy curves of the ion can be found in the literature. A comparison of the results obtained within the FNA and those computed including the nuclear motion is given in Fig. 4, for the photoionization ejecting an electron from an outer shell. We include the total cross section as a function of the photoelectron momentum, as well as the contributions from the different partial waves in which the electronic continuum wave function is expanded in our numerical description (see Section 2.1). For all total and partial cross sections, FNA results are indistinguishable from those including nuclear motion, except for a tiny difference in the relative minima, which are slightly smoothed when the nuclear motion is included. The origin of these minima, which are

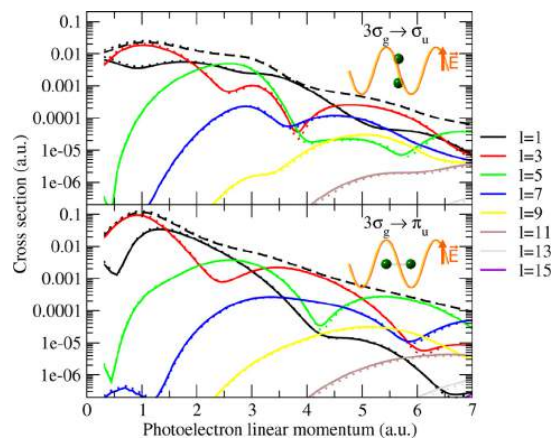


**Fig. 4.** DFT photoionization partial waves of the fluorine molecule from the  $3\sigma_g$  molecular orbital obtained including the nuclear motion in the calculations (lines) and within the fixed nuclei approximation (dots). Results are shown for the case of the molecule being parallel (upper panel) and perpendicular (lower panel) to the polarization vector of the electric field  $\vec{E}$ . Dashed line: total cross section.

more apparent in the individual partial waves, can be qualitatively explained in terms of a confinement effect, previously explained in other works with diatomic molecules [6]. In brief, a relative minimum is found for values of photoelectron momentum that satisfy the relation  $k_e R = l\pi$ , where  $R$  is the internuclear distance. This condition is similar to that satisfied by the eigenstates of a particle confined to move in a box of size  $R$ . The confinement condition implies that the electron moves preferentially along the molecular axis. The expression is thus expected to work better for  $\sigma \rightarrow \sigma$  transitions and for high photoelectron energies, when the molecular potential is negligible with respect to the electron kinetic energy. Considering the equilibrium internuclear distance of the neutral  $F_2$  ( $R = 2.668$  a.u.), one can predict the first dips to appear at around 1.2 a.u. of photoelectron momentum for the wave  $l = 1$  and at 3.5 a.u. for  $l = 3$ , which is in qualitative agreement with the values at which one sees the first minima in the corresponding cross sections. This is the case for all  $\sigma_g$  orbitals. Note that Fig. 4 also demonstrates the convergence of our calculations with respect to the electron angular momentum expansion ( $l_{max} = 15$ ), in both the FNA and in the calculations including the nuclear motion. The latter ones are widely discussed and analyzed in the next section.

#### 4. Vibrationally resolved cross section

We have computed the vibrationally-resolved cross section for the valence shells, i.e., for  $1\pi_g$ , the  $1\pi_u$  and  $3\sigma_g$  photoionization, and we seek to extract contributions from both dissociative and non-dissociative ionization channels. The vibrational structure has been separately obtained for each electronic state solving equation 3, where we use the Morse potential energy curves plotted in Fig. 1 and computed with the parameters given in Table 1. We obtain 56, 24 and 31 vibrational bound states associated to the  $F_2^+(1\pi_g^{-1})$ , the  $F_2^+(1\pi_u^{-1})$  and the  $F_2^+(3\sigma_g^{-1})$  electronic states, respectively.

The corresponding non-dissociative ionization cross sections are plotted in Fig. 5. We find quite distinct vibrational distributions for the bound molecular ion depending on the orbital from which the electron is ejected. When the electron is ejected from the outermost molecular orbital,  $1\pi_g$ , only the lowest vibrational states of the residual ion are significantly populated. This narrow and localized distribution has its maximum at  $v' = 1$ , since the maximum of the vibrational wave function located on the right of the node lies

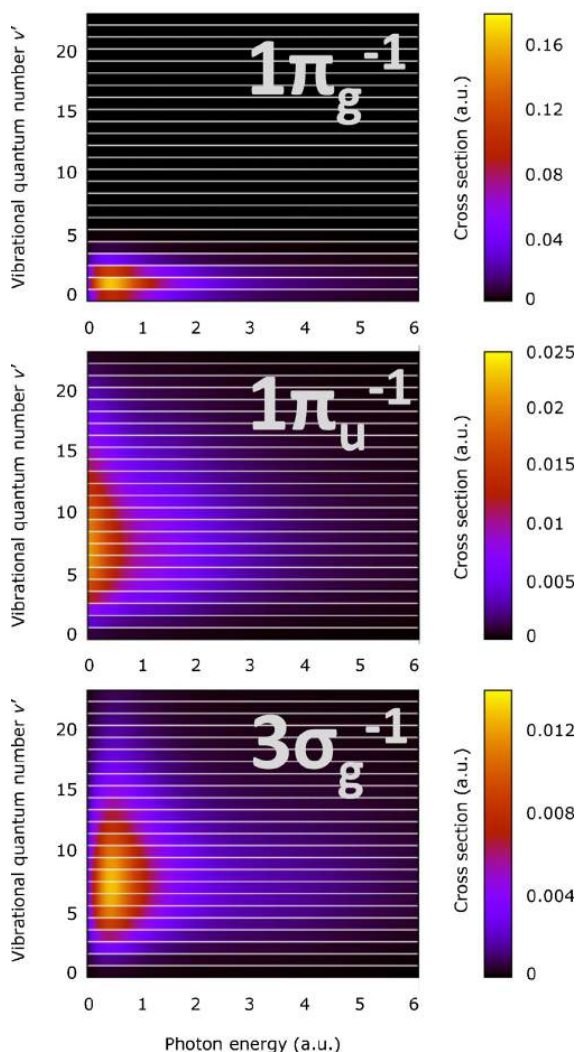


**Fig. 5.** Non-dissociative vibrational resolved cross section in atomic units corresponding to the photoionization of molecular fluorine from the  $1\pi_g$  (upper figure),  $1\pi_u$  (center figure) and  $3\sigma_g$  (lower figure) molecular orbitals.

in the middle of the Franck–Condon (FC) region, thus leading to a maximum overlap with the ground state vibrational state  $\nu=0$ . In the case of  $1\pi_u$  and  $3\sigma_g$  ionization, the large value of the bond length associated to the corresponding potential energy curves leads to a very unfavorable vibrational overlap with the ground state vibrational function of the parental ion. Instead, a large vibrational progression is observed and the  $\nu'=7$  excited state is found to be the most populated one in both cases.

The dissociative photoionization cross section,  $d\sigma/dE$ , differential in the nuclear kinetic energy  $E$  is given in Fig. 6, while the total, bound and dissociative ones, are reported in Fig. 7. As can be seen, dissociative ionization is negligible when the electron is removed from the  $1\pi_g$  orbital, which was expected because the non dissociative vibrational distribution is highly localized at low  $\nu'$ . Similar results are found for ionization of valence and inner shells of  $N_2$  or CO. However, an important contribution to

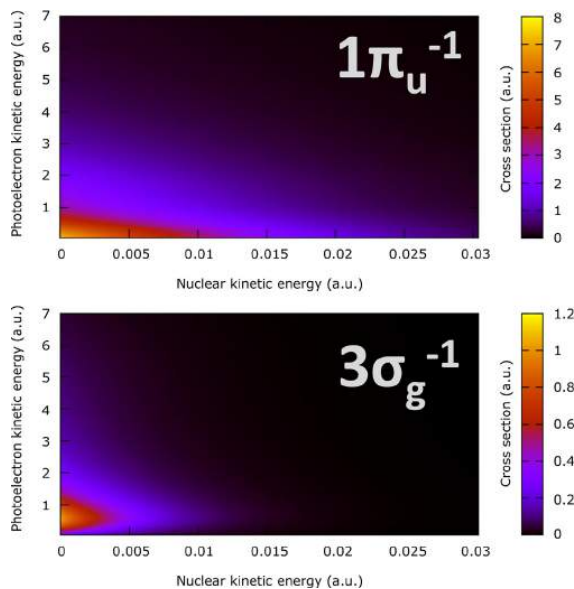


**Fig. 6.** Dissociative photoionization cross section in atomic units of molecular fluorine from the  $1\pi_u$  (upper figure) and the  $3\sigma_g$  (lower figure) molecular orbitals. Molecular dissociation is not observed when the electron is ejected from the  $1\pi_u$  orbital.

the total cross section comes from the dissociative path when the electron is ejected from the  $1\pi_u$  or the  $3\sigma_g$  molecular orbitals of  $F_2$ . Although the spectroscopic parameters (see Table 1) employed to set up the potential energy curve of the electronic species  $F_2^+(1\pi_u^{-1})$  [3] provide an accurate description of its vibrational structure, they overestimate the bond dissociation energy, which can be calculated precisely from the first ionization potential of the fluorine atom (0.640277 a.u. [30]), the corresponding adiabatic ionization potential of  $F_2(1^1\Sigma_g^+)$  (0.67251 a.u. [3]) and the bond energy of the neutral molecule (0.05902 a.u. [5]). For this reason, the dissociative contribution coming from this electronic state is expected to be even more important than shown in Fig. 7. In fact, if one forces the corresponding potential energy curve to

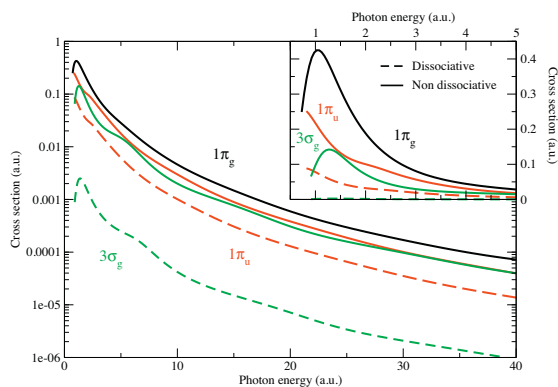


**Fig. 7.** Dissociative (dashed lines) and non-dissociative (continuous lines) photoionization cross sections in atomic units of molecular fluorine from the valence shells. They have been obtained by summing over all the vibrational contributions in the non-dissociative case (Fig. 5) and by integrating over the entire range of nuclear kinetic energies in the dissociative path (Fig. 6).

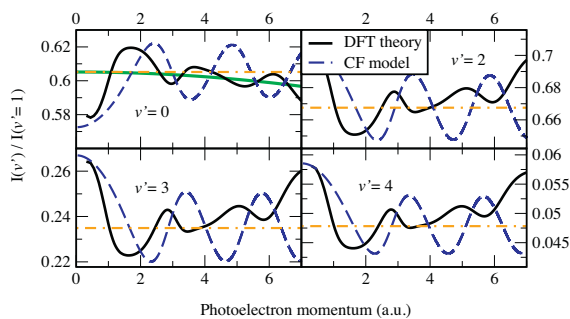


**Fig. 8.** Ratios between vibrationally resolved cross sections corresponding to  $1\pi_g$  photoionization of  $F_2$ . Black line: DFT theory; blue dashed line: Cohen–Fano model; orange dashed line: FC values; green line: FC values including the effect of the nuclear recoil [33]. (For interpretation of the references to color in this legend, the reader is referred to the web version of the article.)

the correct dissociation limit, the contribution from dissociative channel becomes half of the total  $1\pi_u^{-1}$  cross section.

As Fig. 6 shows, the cross section decreases with the nuclear kinetic energy ( $x$ -axis), due to the progressively smaller vibrational overlap. Indeed, the higher the vibrational state, the larger the internuclear distance at which the maximum near the outer classical turning point appears, hence the smaller the overlap with the vibrational ground state of the neutral. Similarly, the ionization cross section decreases dramatically as the photoelectron energy ( $y$ -axis in the figure) becomes higher due to the rapid decay of the electronic dipole coupling. For a better analysis of this high-energy region, where interesting effects due to the molecular structure may arise, we have also calculated the ratios between different vibrationally resolved cross sections. In doing so, one easily removes the rapid decrease of the absolute cross sections with photoelectron energy, thus magnifying all other possible effects [9]. A similar analysis has been performed in other works with diatomic and polyatomic molecules and has proven to be very useful for comparison with experimental data and extraction of structural information [31,32].

Figs. 8–10 show the vibrational branching ratios ( $\nu$ -ratios) corresponding to the ionization from the  $1\pi_g$ ,  $1\pi_u$  and the  $3\sigma_g$  molecular orbitals, respectively, as a function of the linear momentum of the ejected photoelectron. To make a clearer comparison, we have chosen the most populated state as the common denominator ( $\nu' = 1$  in the case of  $1\pi_g$  ionization and  $\nu' = 7$  for  $1\pi_u$  and for  $3\sigma_g$ ). The  $\nu$ -ratios show pronounced oscillations around the FC value as a function of the photoelectron linear momentum. These are the signature of the multicenter electron emission previously discussed. The features are now magnified in the vibrational branching ratios. To prove that the origin of the oscillations is multicenter electron emission we have extended the Cohen–Fano formula given in Eq. (5) to account for the vibrational motion. This simply requires the knowledge of the initial and final vibrational wave functions, which are trivial to obtain once the corresponding potential energy curves are known. The results of the model are included in Figs. 8–10.

In the case of  $3\sigma_g$  ionization (see Fig. 10), we find an excellent agreement between theory and the simple model. This is not the case for the electron ejection from the  $1\pi_g$  or the  $1\pi_u$  molecular orbitals (Figs. 8 and 9), which is not surprising since  $\pi$  orbitals concentrate most of the electron density outside the molecular axis (as illustrated by Eq. (4)), the Cohen–Fano model is only strictly valid for an initial electron density formed by the superposition of two spherical distribution). However, even in these cases, we observe oscillations in the  $\nu$ -ratios, with periodicity and amplitude that are

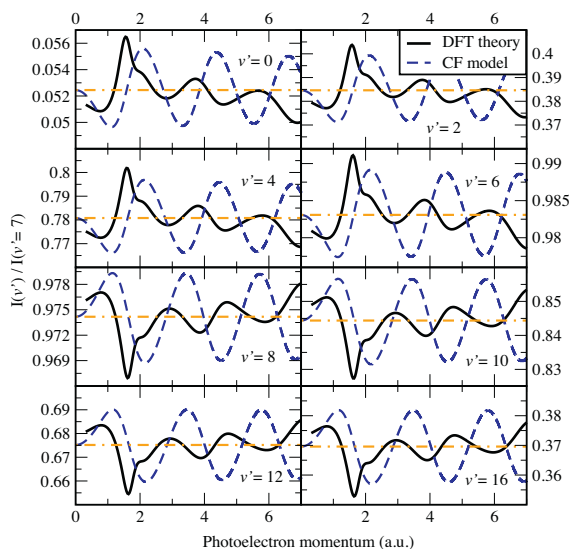


**Fig. 9.** Ratios between vibrationally resolved cross sections corresponding to  $1\pi_u$  photoionization of  $F_2$ . Black line: DFT theory; blue dashed line: Cohen–Fano model; orange dashed line: FC values. (For interpretation of the references to color in this legend, the reader is referred to the web version of the article.)

close to the actual ones. Only the phase of the oscillations is not properly described.

All  $\nu$ -ratios show an increase (a decrease if the vibrational level  $\nu'$  in the numerator is lower than in the denominator) with photon energy which is superimposed to their oscillatory trend. This behavior has its origin in the recoil effect suffered by the parent ion when the photoelectron's linear momentum is not negligible. In fact, using a semi-classical model [33], one can predict the values

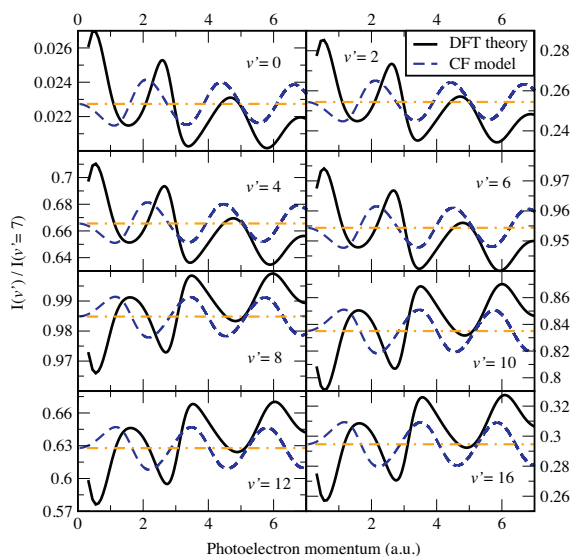


**Fig. 10.** Ratios between vibrationally resolved cross sections corresponding to  $3\sigma_g$  photoionization of  $F_2$ . Black line: DFT theory; blue dashed line: Cohen–Fano model; orange dashed line: FC values. (For interpretation of the references to color in this legend, the reader is referred to the web version of the article.)



of the  $\nu$ -ratios to increase linearly with photon energy, i.e., quadratically with photoelectron momentum. In Fig. 8 we have included the correction to the FC values due to the recoil for the lowest  $\nu$ -ratio to illustrate the effect, finding a good agreement with the our theoretical results.

## 5. Conclusion

We have theoretically explored photoionization of molecular fluorine for photon energies up to hundreds of eV, by considering electron ejection from different molecular orbitals. The photoionization cross sections have been obtained by using the DFT-like methodology described in Ref. [15,16]. For the outermost shells, we have also included the nuclear degrees of freedom as described in Ref. [9], which allows to describe dissociative and non-dissociative ionization channels. The photoionization cross sections show an oscillatory behavior as a function of the photoelectron momentum, which is the result of the coherent emission from two equivalent centers. The observed interference patterns are similar to those already explained by Cohen and Fano [29] in the early sixties. These interferences can be described by using very simple expressions that account for both the ratio between total photoionization cross sections associated to different orbitals and to the branching ratios between vibrationally resolved cross sections associated to the same electronic ionic state. Both effects were demonstrated in previous works [9,27] for other diatomic molecules, so the present work reinforces the general validity of those findings. Possible ways of extracting structural information from these ratios have been recently proposed in a similar study on CO [31]. The originality of molecular fluorine compared to all previously studied diatomic molecules (but molecular hydrogen) is that there is a non-negligible probability of dissociative ionization when the electron is ejected from the  $1\pi_u$  or the  $3\sigma_g$  molecular orbitals. This fact could be exploited experimentally to obtain molecular frame photoelectron angular distributions by using multi coincidence techniques, since detection of the charged atomic fragments provides information about the orientation of the molecule at the instant of ionization.

## Acknowledgements

This work was accomplished with an allocation of computer time from CCC-UAM and Mare Nostrum BSC, and was partially supported by the MICINN projects FIS2010-15127 CSD 2007-00010, the ERA-Chemistry project PIM2010EEC-00751, the European Grants MC-ITN CORINF and MC-IRG ATTOTREND, and the Advanced Grant of the European Research Council XCHEM 290853.

## References

- [1] A.B. Cornford, D.C. Frost, C.A. McDowell, J.L. Ragle, I.A. Stenhouse, *J. Chem. Phys.* 54 (1971) 2651–2657.
- [2] H. Van Lonkhuyzen, C.A. De Lange, *Chem. Phys.* 89 (1984) 313–322.
- [3] A.J. Cormack, A.J. Yencha, R.J. Donovan, K.P. Lawley, A. Hopkirk, G.C. King, *Chem. Phys.* 213 (1996) 439–448.
- [4] K.E. Banyard, D.J. Ellis, A.D. Tait, M. Dixon, *J. Phys. B: At. Mol. Opt. Phys.* 7 (1974) 1411.
- [5] J. Yang, Y. Hao, J. Li, C. Zhou, Y. Mo, *J. Chem. Phys.* 122 (2005) 134308.
- [6] J. Fernández, O. Fojón, A. Palacios, F. Martín, *Phys. Rev. Lett.* 98 (2007) 043005.
- [7] S.K. Semenov, N.A. Cherepkov, M. Matsumoto, K. Fujiwara, K. Ueda, E. Kukkk, F. Tahara, T. Sunami, H. Yoshida, T. Tanaka, K. Nakagawa, M. Kitajima, H. Tanaka, A.D. Fanis, *J. Phys. B: At. Mol. Opt. Phys.* 39 (2006) 375.
- [8] X.-J. Liu, N.A. Cherepkov, S.K. Semenov, V. Kimberg, F. Gel'mukhanov, G. Prümper, T. Lischke, T. Tanaka, M. Hoshino, H. Tanaka, K. Ueda, *J. Phys. B: At. Mol. Opt. Phys.* 39 (2006) 4801.
- [9] S.E. Canton, E. Plésiat, J.D. Bozek, B.S. Rude, P. Declève, F. Martín, *Proc. Natl. Acad. Sci. U. S. A.* 108 (2011) 7302–7306.
- [10] E. Plésiat, P. Declève, F. Martín, *Phys. Chem. Chem. Phys.* 14 (2012) 10853–10871.
- [11] M. Ehara, K. Kuramoto, H. Nakatsuji, M. Hoshino, T. Tanaka, M. Kitajima, H. Tanaka, A.D. Fanis, Y. Tamenori, K. Ueda, *J. Chem. Phys.* 125 (2006) 114304.
- [12] C.E. Housecroft, A.G. Sharpe, *Inorganic Chemistry*, Pearson Prentice Hall, Essex, England, 2005.
- [13] D.C. Frost, C.A. McDowell, *Proc. R. Soc. Lond. A* 236 (1956) 278–284.
- [14] D.D. Wagman, W.H. Evans, V.B. Parker, I. Halow, S.M. Bailey, R.H. Schumm, *Selected Values of Chemical Thermodynamic Properties, Part 3, Tables for the First Thirty-four Elements in the Standard Order of Arrangement*, National Bureau of Standards, U.S.A., 1967.
- [15] M. Stener, G. Fronzoni, P. Declève, *Chem. Phys. Lett.* 351 (2002) 469–474.
- [16] D. Toffoli, M. Stener, G. Fronzoni, P. Declève, *Chem. Phys.* 276 (2002) 25–43.
- [17] H. Bachau, E. Cormier, P. Declève, J.E. Hansen, F. Martín, *Rep. Prog. Phys.* 64 (2001) 1815.
- [18] M. Stener, P. Declève, *J. Chem. Phys.* 112 (2000) 10871–10879.
- [19] G. Frozoni, M. Stener, P. Declève, *Phys. Chem. Chem. Phys.* 1 (1999) 1405.
- [20] E.J. Baerends, D.E. Ellis, P. Ros, *Chem. Phys.* 2 (1973) 41–51.
- [21] C. Fonseca Guerra, J.G. Snijders, G. te Velde, E.J. Baerends, *Theor. Chem. Acc.* 99 (1998) 391–403.
- [22] R. van Leeuwen, E.J. Baerends, *Phys. Rev. A* 49 (1994) 2421–2431.
- [23] K.P. Huber, G. Herzberg, *Molecular Spectra and Molecular Structure, Vol. IV, Constants of Diatomic Molecules*, Van Nostrand, Princeton, 1979.
- [24] R. Guillemin, W.C. Stolte, M.N. Piancastelli, D.W. Lindle, *J. Phys. B: At. Mol. Opt. Phys.* 43 (2010) 215205.
- [25] J.L. Dehmer, D. Dill, *Phys. Rev. Lett.* 35 (1975) 213–215.
- [26] J.L. Dehmer, D. Dill, S. Wallace, *Phys. Rev. Lett.* 43 (1979) 1005–1008.
- [27] K. Ueda, C. Miron, E. Plésiat, L. Argenti, M. Patanen, K. Kooser, D. Ayuso, S. Mondal, M. Kimura, K. Sakai, O. Travnikova, A. Palacios, P. Declève, E. Kukkk, F. Martín, *J. Chem. Phys.* 139 (2013) 124306.
- [28] P. Bolognesi, G. Alberti, D.B. Thompson, L. Avaldi, G.C. King, *J. Phys. B: At. Mol. Opt. Phys.* 37 (2004) 4575.
- [29] H.D. Cohen, U. Fano, *Phys. Rev.* 150 (1966) 30–33.
- [30] K. Lidén, *Ark. Fys.* 1 (1949) 229.
- [31] E. Kukkk, D. Ayuso, T.D. Thomas, P. Declève, M. Patanen, L. Argenti, E. Plésiat, A. Palacios, K. Kooser, O. Travnikova, S. Mondal, M. Kimura, K. Sakai, C. Miron, F. Martín, K. Ueda, *Phys. Rev. A* 88 (2013) 033412.
- [32] R.K. Kushawaha, M. Patanen, R. Guillemin, L. Journel, C. Miron, M. Simon, M.N. Piancastelli, C. Skates, P. Declève, *Proc. Natl. Acad. Sci. U. S. A.* 110 (2013) 15201–15206.
- [33] E. Kukkk, K. Ueda, U. Hergenhanh, X.-J. Liu, G. Prümper, H. Yoshida, Y. Tamenori, C. Makochekanwa, T. Tanaka, M. Kitajima, H. Tanaka, *Phys. Rev. Lett.* 95 (2005) 133001.



## **Appendix F**

Ultrafast electron dynamics in  
phenylalanine initiated by attosecond  
pulses



## ATTOSECOND DYNAMICS

# Ultrafast electron dynamics in phenylalanine initiated by attosecond pulses

F. Calegari,<sup>1</sup> D. Ayuso,<sup>2</sup> A. Trabattoni,<sup>3</sup> L. Belshaw,<sup>4</sup> S. De Camillis,<sup>4</sup> S. Anumula,<sup>3</sup> F. Frassetto,<sup>5</sup> L. Poletto,<sup>5</sup> A. Palacios,<sup>2</sup> P. Decleva,<sup>6</sup> J. B. Greenwood,<sup>4</sup> F. Martín,<sup>2,7\*</sup> M. Nisoli<sup>1,3\*</sup>

In the past decade, attosecond technology has opened up the investigation of ultrafast electronic processes in atoms, simple molecules, and solids. Here, we report the application of isolated attosecond pulses to prompt ionization of the amino acid phenylalanine and the subsequent detection of ultrafast dynamics on a sub-4.5-femtosecond temporal scale, which is shorter than the vibrational response of the molecule. The ability to initiate and observe such electronic dynamics in polyatomic molecules represents a crucial step forward in attosecond science, which is progressively moving toward the investigation of more and more complex systems.

The investigation of ultrafast processes in atoms received a major stimulus with the introduction of attosecond pulses in the extreme ultraviolet (XUV) spectral region (1). Real-time observation of the femtosecond Auger decay in krypton was the first application of isolated attosecond pulses in 2002 (2). This demonstration was then followed by other important experimental results in the field of ultrafast atomic physics, such as the real-time observation of electron tunneling (3) and the measurement of temporal delays of the order of a few tens of attoseconds in the photoemission of electrons from different atomic orbitals of neon (4) and argon (5). The unprecedented time resolution offered by attosecond pulses has also allowed quantum mechanical electron motion and its degree of coherence to be measured in atoms by using attosecond transient absorption spectroscopy (6). Attosecond techniques have been applied in the field of ultrafast solid-state physics, with the measurement of delays in electron photoemission from crystalline solids (7) and the investigation of the ultrafast field-induced insulator-to-conductor state transition in a dielectric (8). In the past few years, attosecond pulses have also been used to measure ultrafast electronic processes in simple molecules (9). Sub-femtosecond electron localization after attosecond excitation has been observed in H<sub>2</sub> and D<sub>2</sub>

molecules (10), and control of photo-ionization of D<sub>2</sub> and O<sub>2</sub> molecules has been achieved by using attosecond pulse trains (APTs) (11, 12). More recently, an APT, in combination with two near-infrared fields, was used to coherently excite and control the outcome of a simple chemical reaction in a D<sub>2</sub> molecule (13). Although the study of more complex molecules is challenging, a formative measurement of the amino acid phenylalanine has shown that ionization by a short APT leads to dynamics on a temporal scale of a few tens of femtoseconds. This has been interpreted as the possible signature of ultrafast electron transfer inside the molecule (14).

The application of attosecond techniques to molecules offers the possibility of investigating primary relaxation processes, which involve electronic and nuclear degrees of freedom and their coupling. In the case of large molecules (e.g., biologically relevant molecules), prompt ioniza-

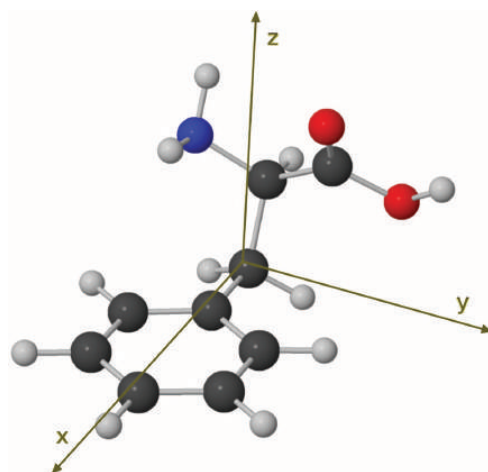
tion by attosecond pulses may produce ultrafast charge migration along the molecular skeleton, which can precede nuclear rearrangement. This behavior has been predicted in theoretical calculations by various authors (15–19), whose work was stimulated by pioneering experiments performed by Weinkauff, Schlag, and co-workers on fragmentation of peptide chains (20, 21). This electron dynamics, evolving on an attosecond or few-femtosecond temporal scale, can determine the subsequent relaxation pathways of the molecule (9). The process is induced by sudden generation of an electronic wave packet, which moves across the molecular chain and induces a site-selective reactivity, which is related to charge localization in a particular site of the molecule (15). Although picosecond and femtosecond pulses are suitable for the investigation of nuclear dynamics, the study of electronic dynamics with these pulses has been made possible by slowing down the dynamics through the use of Rydberg electron wave packets (22). However, in order to study the electron wave-packet dynamics in the outer-valence molecular orbitals relevant to most chemical and biological systems, attosecond pulses are required.

Here, we present experimental evidence of ultrafast charge dynamics in the amino acid phenylalanine after prompt ionization induced by isolated attosecond pulses. A probe pulse then produced a doubly charged molecular fragment by ejection of a second electron, and charge migration manifested itself as a sub-4.5-fs oscillation in the yield of this fragment as a function of pump-probe delay. Numerical simulations of the temporal evolution of the electronic wave packet created by the attosecond pulse strongly support the interpretation of the experimental data in terms of charge migration resulting from ultrafast electron dynamics preceding nuclear rearrangement.

The  $\alpha$ -amino acids consist of a central carbon atom ( $\alpha$  carbon) linked to an amine ( $-\text{NH}_2$ ) group, a carboxylic group ( $-\text{COOH}$ ), a hydrogen

**Fig. 1. Three-dimensional structure of phenylalanine.**

Molecular structure of the most abundant conformer of the aromatic amino acid phenylalanine. Dark gray spheres represent carbon atoms; light gray spheres, hydrogen atoms; blue sphere, nitrogen; and red spheres, oxygen. The molecular geometry has been optimized by using density functional theory (DFT) with a B3LYP functional.



<sup>1</sup>Institute of Photonics and Nanotechnologies (IFN)–Consiglio Nazionale delle Ricerche (CNR), Piazza Leonardo da Vinci 32, 20133 Milano, Italy. <sup>2</sup>Departamento de Química, Modulo 13, Universidad Autónoma de Madrid, Cantoblanco 28049 Madrid, Spain. <sup>3</sup>Department of Physics, Politecnico di Milano, Piazza Leonardo da Vinci 32, 20133 Milano, Italy. <sup>4</sup>Centre for Plasma Physics, School of Maths and Physics, Queen's University, Belfast BT7 1NN, UK. <sup>5</sup>IFN-CNR, Via Trasea 7, 35131 Padova, Italy. <sup>6</sup>Dipartimento di Scienze Chimiche e Farmaceutiche, Università di Trieste and CNR–Istituto Officina dei Materiali, 34127 Trieste, Italy. <sup>7</sup>Instituto Madrileño de Estudios Avanzados en Nanociencia, Cantoblanco, 28049 Madrid, Spain. \*Corresponding author. E-mail: fernando.martin@uam.es (F.M.); mauro.nisoli@polimi.it (M.N.)

atom, and a side chain (R), which in the case of phenylalanine is a benzyl group (Fig. 1). In our experiments, we used a two-color, pump-probe technique. Charge dynamics were initiated by isolated XUV sub-300-as pulses, with photon energy in the spectral range between 15 and 35 eV and probed by 4-fs, waveform-controlled visible/near infrared (VIS/NIR, central photon energy of 1.77 eV) pulses (see supplementary materials). A clean plume of isolated and neutral molecules was generated by evaporation of the amino acid from a thin metallic foil heated by a continuous wave (CW) laser. The parent and fragment ions produced by the interaction of the molecules with the pump and probe pulses were then collected by a linear time-of-flight device for mass analysis, where the metallic foil was integrated into the repeller electrode (23). Ionization induced by the attosecond pulse occurred in a sufficiently short time interval to exclude substantial electron rearrangement during the excitation process.

We measured the yield for the production of doubly charged immonium ions as a function of the time delay between the attosecond pump pulse and the VIS/NIR probe pulse (the structure of the immonium dication is  $^{++}\text{NH}_2\text{-CH-R}$ ). Figure 2A shows the results on a 100-fs time scale. The experimental data display a rise time of  $10 \pm 2$  fs and an exponential decay with time constant of  $25 \pm 2$  fs [this longer relaxation time constant is in agreement with earlier experi-

mental results reported in (14)]. Figure 2B shows a 25-fs-wide zoom of the pump-probe dynamics, obtained by reducing the delay step between pump and probe pulses from 3 to 0.5 fs. An oscillation of the dication yield is clearly visible. For a better visualization, Fig. 2C shows the same yield after subtraction of an exponential fitting curve. The data have been fitted with a sinusoidal function of frequency 0.234 PHz (corresponding to an oscillation period of 4.3 fs), with lower and upper confidence bounds of 0.229 and 0.238 PHz, respectively (see supplementary materials). The experimental data have been also analyzed by using a sliding-window Fourier transform, which, at the expense of frequency resolution, shows frequency and time information on the same plot. The result is shown in Fig. 3A. At short pump-probe delays, two frequency components are present, around 0.14 and 0.3 PHz. A strong and broad peak around 0.24 PHz forms in about 15 fs and vanishes after about 35 fs, with a spectral width that slightly increases upon increasing the pump-probe delay, in agreement with the frequency values obtained from best fitting of the data reported in Fig. 2C.

From these results, we can draw the following conclusions: (i) the ultrafast oscillations in the temporal evolution of the dication yield cannot be related to nuclear dynamics, which usually come into play on a longer temporal scale, ultimately leading to charge localization in a particular molecular fragment. Indeed, standard

quantum chemistry calculations in phenylalanine (see supplementary materials) show that the highest vibrational frequency is 0.11 PHz, which corresponds to a period of 9 fs, associated with X-H stretching modes, whereas skeleton vibrations are even slower, so that one can rule out that the observed beatings are due to vibrational motion. In any case, some influence of the nuclear motion cannot be completely excluded, because, for example, stretching of the order of a few picometers of carbon bonds can occur in a few femtoseconds, and this could modify the charge dynamics (24, 25). (ii) Clear oscillatory evolution of the dication yield is observed even without any conformer selection. It is well known that amino acids exist in many conformations as a result of their structural flexibility. Typically, the energy barrier to interconversion between different conformers is small, of the order of a few kcal/mol, so that, even at room temperature, thermal energy is sufficient to induce conformational changes. Theoretical investigations have shown that such changes can affect the charge migration process (26). In the case of phenylalanine, 37 conformers have been found by *ab initio* calculations (27), with a conformational distribution that depends on temperature. In our experiment, at an average temperature of about 430 K, only the six most stable conformers are substantially present, as discussed in the supplementary materials, with the most abundant configuration shown in Fig. 1.

To further investigate the measured dynamics, we also varied the photon energy and spectral width of the attosecond pump pulse by inserting an indium foil in the XUV beam path. The new XUV spectrum was characterized by a 3-eV (full width at half maximum) peak centered around 15 eV, followed by a broad and weak spectral component extending up to 25 eV. In this case, doubly charged immonium fragments were barely visible, suggesting that the dication formation involves relatively highly excited states of the cation. We have calculated the energy level diagram with all the states of singly charged phenylalanine generated by the XUV pump pulse and all the states of the dication (see supplementary materials). A number of transitions from excited states of the cation to the lowest states of the dication are possible, which involve the absorption of just a few VIS/NIR photons. These states cannot be accessed by low-energy excitation, as in the case of XUV pulses transmitted by the indium foil. In this case, transitions from cation states to the lowest dication states would require the less probable absorption of many VIS/NIR photons.

We also performed theoretical calculations to describe the hole dynamics induced by an attosecond pulse similar to that used in the experiment. Details of the method can be found in the supplementary materials. Because of the high central frequency and large spectral width of the pulse, a manifold of ionization channels is open, thus leading to a superposition of many one-hole (1h) cationic states, i.e., to an electronic wave packet. Ionization amplitudes for all 1h

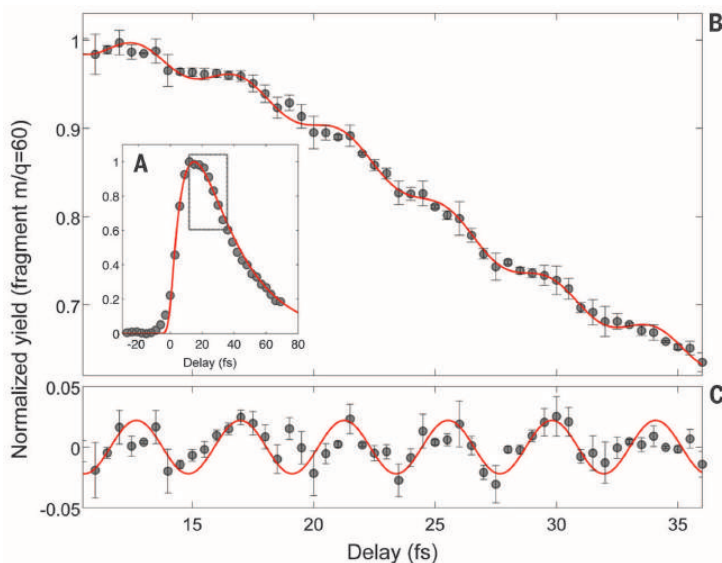


**Fig. 2. Pump-probe measurements.** (A) Yield of doubly charged immonium ion (mass/charge = 60) as a function of pump-probe delay, measured with 3-fs temporal steps. The red line is a fitting curve with an exponential rise time of 10 fs and an exponential relaxation time of 25 fs. (B) Yield of doubly charged immonium ion versus pump-probe delay measured with 0.5-fs temporal steps, within the temporal window shown as dotted box in (A). Error bars show the standard error of the results of four measurements. The red line is the fitting curve given by the sum of the fitting curve shown in (A) and a sinusoidal function of frequency 0.234 PHz (4.3-fs period). (C) Difference between the experimental data and the exponential fitting curve displayed in (A). Red curve is a sinusoidal function of frequency 0.234 PHz.

open channels (32 for a single conformer) were quantitatively determined by means of the static-exchange density functional theory (28–30), which has been thoroughly tested in systems of similar complexity, and first-order time-dependent perturbation theory. A calculated photoelectron spectrum at 45-eV photon energy is in very good agreement with that obtained at 100 eV in a synchrotron radiation experiment (31). From the ionization amplitudes, the actual electronic wave packet was calculated by using the experimental frequency spectrum of the attosecond pulse. The evolution of the electronic wave packet was then evaluated by using a standard time-dependent density matrix formalism (6), in which the system is described by a sum of single-particle Hamiltonians. This is a reasonable approximation when, as in the present case, changes in electronic density are mostly due to the coherent superposition of 1h cationic states induced by the XUV pulse (see supplementary materials). In other words, higher-order processes in which additional electrons are excited (e.g., correlation satellites) play a minor role in the observed dynamics. The hole-density was calculated as the difference between the electronic density of the neutral molecule, which does not depend on time, and the electronic density of the cation, from immediately after XUV excitation up to a 500-fs delay. Because, in the experiments, the molecules were not aligned, we calculated the charge dynamics resulting from excitation by pulses with the electric field polarized along three orthogonal directions (shown in Fig. 1). The results were then averaged assuming randomly oriented molecules. For a better analysis, we integrated the hole density around selected portions of the molecule: Beating frequencies were observed when the charge density was integrated around the amine group.

The six most populated conformers at 430 K were considered in the simulations. Although the precise frequencies of the relevant peaks in the calculated Fourier spectra depend on the particular conformer, the common characteristic is the presence of three dominant groups of Fourier peaks between 0.15 and 0.4 PHz. Our calculations show that the largest temporal modulation of the hole dynamics occurs around the amine group. Because of this fact, in Fig. 3C we only show the Fourier power spectrum of the calculated hole density around this group for the most abundant conformer. We have then analyzed the numerical results by using the same sliding-window Fourier transform procedure applied to the experimental data. Figure 3B shows the resulting spectrogram in a temporal window up to 45 fs, considering an experimental temporal resolution of about 3 fs. A dominant peak around 0.25 PHz is visible, which forms in about 15 fs and vanishes after about 35 fs, in close agreement with the results of the Fourier analysis of the experimental data. A higher frequency component is visible around 0.36 PHz in the delay intervals below ~15 fs and above ~30 fs. At short delays, this component favorably compares with the experimental observation of the

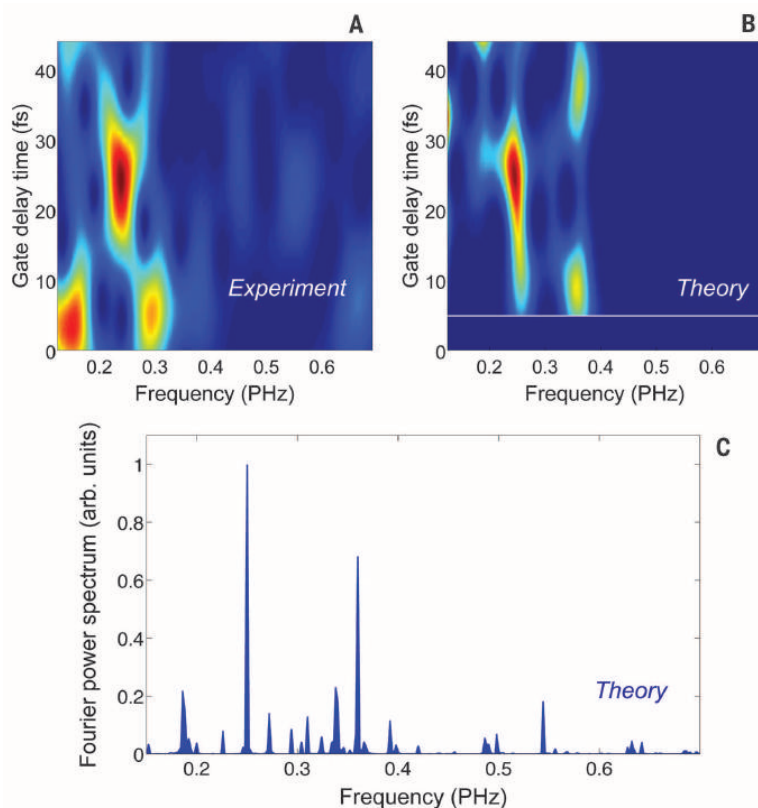


**Fig. 3. Fourier analysis of charge dynamics.** Spectrograms calculated for the measured data of Fig. 2C (A) and for the calculated hole density integrated over the amine group for the most abundant conformer (B). The sliding window Fourier transforms have been calculated by using a Gaussian window function  $g(t - t_d) = \exp[-(t - t_d)^2/t_0^2]$ , with  $t_0 = 10$  fs and peak at  $t_d$  (gate delay time). The spectrogram (B) was calculated considering an experimental temporal resolution of about 3 fs. (C) Fourier power spectrum of the calculated hole density integrated over the amine group for the most abundant conformer.

frequency peak around 0.30 PHz in the same window of pump-probe delays. The temporal evolution of the main Fourier components is a consequence of the complex interplay among several beating processes initiated by the broadband excitation pulse. Despite the agreement with the experimental results, we cannot exclude that the nuclear dynamics, which are not included in the simulations, also play a role in the temporal evolution of the measured oscillation frequencies. The good agreement between simulations and experimental results is rather remarkable in light of the fact that simulations do not take into account the interaction of the VIS/NIR probe pulse. The fact that the effects of the probe pulse are not included in the simulations can explain why the calculated intensities of the different beatings differ from the experimental ones. We note that the beating frequencies have been observed experimentally even though the initial hole density is highly delocalized. An important result of the simulations

is that the measured beating frequencies originate from charge dynamics around the amine group. This leads to the conclusion that the periodic modulations measured in the experiment are mainly related to the absorption of the probe pulse by the amine group. The mechanism that makes the probe pulse sensitive specifically to the charge density on this group is still not well understood, and therefore it will not be further discussed in the manuscript. Moreover, we observe that, in spite of the large number of potential frequency beatings associated to the wave packet motion induced by the attosecond pulse, only a few ones manifest in the experiment, thus reducing the impact of the modulations introduced by the probe pulse in the analysis of the wave packet motion. Figure 4 displays snapshots of the variation of the hole density with respect to the time-averaged hole density as a function of time for the most abundant conformer. In spite of the very delocalized nature of the hole-density resulting from the broadband XUV excitation, a

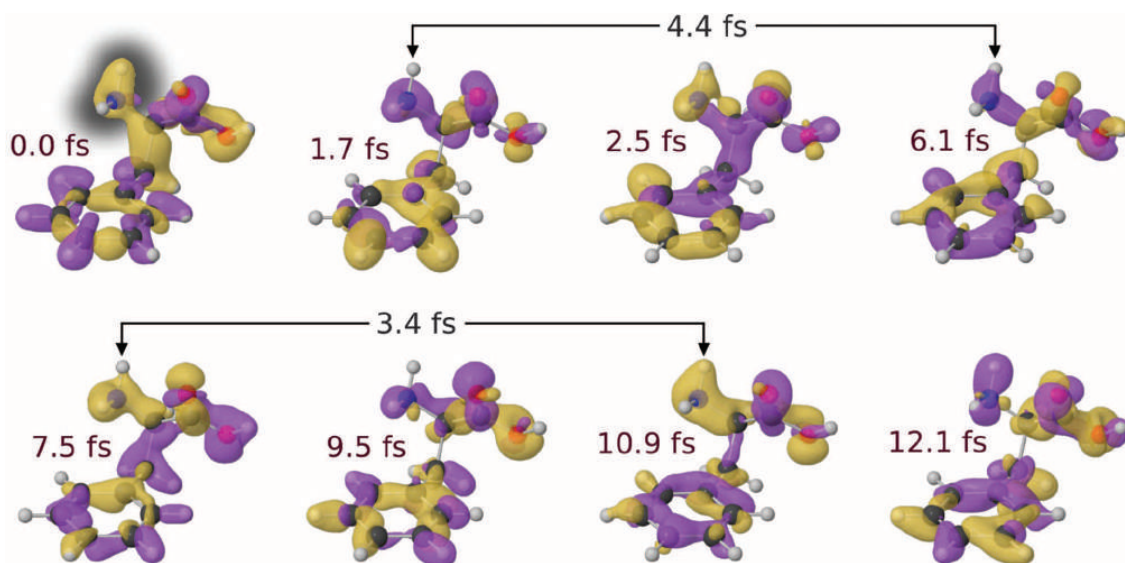


**Fig. 4. Snapshots of hole dynamics.** Relative variation of the hole density with respect to its time-averaged value as a function of time for the most abundant conformer. Isosurfaces of the relative hole density are shown for cutoff values of  $+10^{-4}$  arbitrary units (yellow) and  $-10^{-4}$  (purple). Time is with reference to the end of the XUV pulse (first snapshot). To guide the eye, time intervals between snapshots showing a similar accumulated density over the amine group are indicated. These time intervals are close to the dominant periods associated with the electronic wave-packet motion shown in Fig. 3. The location of the amine group is highlighted in the first snapshot with a shaded contour.

substantial redistribution of this density is observed on a sub-femtosecond scale. These charge dynamics cannot be associated with a simple migration from one side of the molecule to the other. Despite the complexity of the charge configuration calculated in a realistic (i.e., experimentally accessible) situation, the concept of charge migration is still valid. In particular, the snapshots shown in Fig. 4 evidence a notable and periodic variation of the charge density around the amine group. This is because the dominant beatings always involve delocalized orbitals with substantial localization around the amine group (see supplementary materials), thus showing that evolution of the hole density around this functional group provides a highly selective interaction with the probe pulse.

Direct measurement of the ultrafast charge dynamics in an amino acid, initiated by attosecond pulses, represents a crucial benchmark for the extension of attosecond methodology to complex systems. We have demonstrated that charge fluctuations over large regions of a complex molecule such as phenylalanine can be induced by attosecond pulses on a temporal scale much shorter than the vibrational response of the system. This result was achieved in spite of the broad bandwidth of the attosecond pulses and, therefore, their low frequency selectivity, thus showing that attosecond science offers the possibility to elucidate processes ultimately leading to charge localization in complex molecules. The latter has already been achieved in hydrogen molecules, where, after attosecond excitation, charge localization was induced by the probe

NIR pulse as a result of the coupling with the nuclear degrees of freedom at long time delays (10). A similar achievement can be envisaged in more complex molecules by performing more sophisticated experiments, e.g., as those of (10), combined with the extension of the existing theoretical methods to account for the nuclear motion.

#### REFERENCES AND NOTES

1. F. Krausz, M. Ivanov, *Rev. Mod. Phys.* **81**, 163–234 (2009).
2. M. Drescher *et al.*, *Nature* **419**, 803–807 (2002).
3. M. Uiberacker *et al.*, *Nature* **446**, 627–632 (2007).
4. M. Schultze *et al.*, *Science* **328**, 1658–1662 (2010).
5. K. Klünder *et al.*, *Phys. Rev. Lett.* **106**, 143002 (2011).
6. E. Goulielmakis *et al.*, *Nature* **466**, 739–743 (2010).
7. A. L. Cavalieri *et al.*, *Nature* **449**, 1029–1032 (2007).
8. A. Schiffrin *et al.*, *Nature* **493**, 70–74 (2013).
9. F. Lépine, M. Y. Ivanov, M. J. J. Vrakking, *Nat. Photonics* **8**, 195–204 (2014).
10. G. Sansone *et al.*, *Nature* **465**, 763–766 (2010).
11. F. Kelkensberg *et al.*, *Phys. Rev. Lett.* **107**, 043002 (2011).
12. W. Siu *et al.*, *Phys. Rev. A* **84**, 063412 (2011).
13. P. Ranitovic *et al.*, *Proc. Natl. Acad. Sci. U.S.A.* **111**, 912–917 (2014).
14. L. Belshaw *et al.*, *J. Phys. Chem. Lett.* **3**, 3751–3754 (2012).
15. F. Remacle, R. D. Levine, *Proc. Natl. Acad. Sci. U.S.A.* **103**, 6793–6798 (2006).
16. L. S. Cederbaum, J. Zobeley, *Chem. Phys. Lett.* **307**, 205–210 (1999).
17. H. Hennig, J. Breidbach, L. S. Cederbaum, *J. Phys. Chem. A* **109**, 409–414 (2005).
18. J. Breidbach, L. S. Cederbaum, *Phys. Rev. Lett.* **94**, 033901 (2005).
19. J. Breidbach, L. S. Cederbaum, *J. Chem. Phys.* **118**, 3983 (2003).
20. R. Weinkauf, P. Schanen, D. Yang, S. Soukara, E. W. Schlag, *J. Phys. Chem.* **99**, 11255–11265 (1995).
21. R. Weinkauf *et al.*, *J. Phys. Chem.* **100**, 18567–18585 (1996).

22. J. Wals *et al.*, *Phys. Rev. Lett.* **72**, 3783–3786 (1994).
23. C. R. Calvert *et al.*, *Phys. Chem. Chem. Phys.* **14**, 6289–6297 (2012).
24. S. Lünemann, A. I. Kuleff, L. S. Cederbaum, *Chem. Phys. Lett.* **450**, 232–235 (2008).
25. D. Mendive-Tapia, M. Vacher, M. J. Bearpark, M. A. Robb, *J. Chem. Phys.* **139**, 044110 (2013).
26. A. I. Kuleff, L. S. Cederbaum, *Chem. Phys.* **338**, 320–328 (2007).
27. H. Z. Huang, W. Yu, Z. Lin, *J. Mol. Struct. THEOCHEM* **758**, 195–202 (2006).
28. D. Toffoli, M. Stener, G. Fronzoni, P. Decleva, *Chem. Phys.* **276**, 25–43 (2002).
29. E. Plésiat, P. Decleva, F. Martín, *Phys. Chem. Chem. Phys.* **14**, 10853–10871 (2012).
30. S. E. Canton *et al.*, *Proc. Natl. Acad. Sci. U.S.A.* **108**, 7302–7306 (2011).

#### ACKNOWLEDGMENTS

We acknowledge support from the European Research Council under ERC grant nos. 227355 ELYCHE and 290853 XCHEM, LASERLAB-EUROPE (grant agreement no. 284464, European Commission's Seventh Framework Programme), European COST Action CM1204 XLIC, the Ministerio de Ciencia e Innovación project FIS2010-15127, the ERA-Chemistry project PIM2010EEC-00751, European grants MC-ITN CORINF and MC-RG ATTOTREND 268284, UK's Science and Technology Facilities Council Laser Loan Scheme, the Engineering and Physical Sciences Research Council (grant EP/J007048/1), the Leverhulme Trust (grant RPG-2012-735), and the Northern Ireland Department of Employment and Learning.

#### SUPPLEMENTARY MATERIALS

www.sciencemag.org/content/346/6207/336/suppl/DC1  
Materials and Methods  
Supplementary Text  
Figs. S1 to S11  
Tables S1 and S2  
References (31–53)  
Movie S1

28 March 2014; accepted 16 September 2014  
10.1126/science.1254061





## Supplementary Material for

### **Ultrafast electron dynamics in phenylalanine initiated by attosecond pulses**

F. Calegari, D. Ayuso, A. Trabattoni, L. Belshaw, S. De Camillis, S. Anumula, F. Frassetto, L. Poletto, A. Palacios, P. Decleva, J. Greenwood, F. Martín,\* M. Nisoli\*

\*Corresponding author. E-mail: fernando.martin@uam.es (F.M.); mauro.nisoli@polimi.it (M.N.)

Published 17 October 2014, *Science* **346**, 336 (2014)  
DOI: 10.1126/science.1254061

**This PDF file includes:**

Materials and Methods

Supplementary Text

Figs. S1 to S11

Tables S1 and S2

Full Reference List

**Other Supplementary Material for this manuscript includes the following:**  
(available at [www.sciencemag.org/content/346/6207/336/suppl/DC1](http://www.sciencemag.org/content/346/6207/336/suppl/DC1))

Movie S1

## Materials and Methods

### Experimental setup

For the experiments a Ti:sapphire laser system was used (Femtowatt PRO HE CEP, Femtolasers) delivering 6-mJ pulses, with 25-fs duration and 1-kHz repetition rate. The carrier-envelope phase (CEP) was stabilized by two feedback loops: a fast loop acting on the oscillator and a slow loop acting on a glass wedge placed in the stretcher before the preamplifier. The pulses used for the experiments present a residual CEP fluctuation of  $\sim 200$  mrad (rms), measured in-loop with a  $f$ - $2f$  interferometer using an integration time of 1 ms. We have first compressed the pulses using a hollow-fiber (32) with pressure gradient (33) and a broadband chirped-mirror dispersive delay line. We used a 1-m-long hollow fiber with an inner diameter of 320  $\mu\text{m}$ , filled with helium: the pressure at the input of the fiber was kept to  $<5$  mbar and 2 bar at the output. The beam position at the input of the hollow fiber was actively stabilized. A pulse energy of 3.3 mJ was obtained at the output with no gas in the fibre, and 2.3 mJ with gas. After 8 reflections on the chirped mirrors, pulses as short as 4 fs were achieved. The pulse duration was measured by using a single-shot Self-Referenced Spectral Interferometry method (34) implemented with Cross-Polarized Wave (XPW).

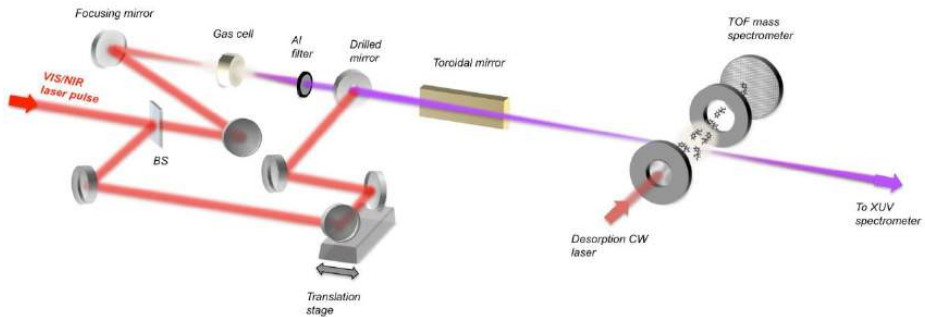


**Fig. S1.**

**Pump-probe experimental setup.** Experimental setup for the pump-probe measurements. BS is a broadband beam-splitter with 30% reflection; TOF mass spectrometer is a time of flight mass spectrometer. The focusing mirror has a 1-m radius of curvature.

The experimental setup used for the pump-probe measurements is shown in Fig. S1. The visible/near infrared (VIS/NIR) beam was divided into two parts using a beam splitter with 30% reflection. The transmitted portion of the beam was focused by a 1-m radius of curvature mirror into a 3-mm-thick cell filled with xenon at static pressure to produce extreme ultraviolet (XUV) radiation by high-order harmonic generation (HHG). Isolated attosecond pulses, with energy in the nanojoule range, were produced by employing the ionization gating technique (35). A 100-nm-thick aluminium filter was used to filter out the fundamental radiation and the low order harmonics. An indium foil has been also used in a few measurements described in the text. The temporal duration of

the XUV pulses ( $290\pm 20$  as) was measured by using the Frequency Resolved Optical Gating for Complete Reconstruction of Attosecond Bursts (FROG CRAB) technique (36-37). The remaining part of the VIS/NIR beam was collinearly recombined with the XUV beam by using a mirror with a central hole. The temporal delay between VIS/NIR and XUV pulses was adjusted with attosecond resolution by using a piezoelectric translation stage. The pump and probe pulses were collinearly focused into the mass spectrometer by using a gold-coated toroidal mirror, with unit magnification, which provided an almost aberration-free image of the XUV source with negligible temporal smearing of the attosecond pulses (38). The peak intensity of the VIS/NIR probe pulse in the sample was about  $5\times 10^{12}$  W/cm<sup>2</sup>. The spectrum of the XUV radiation was measured by using a high-resolution flat-field soft x-ray spectrometer consisting of a grating, followed by a phosphor screen, and a charge-coupled device (CCD) camera (38).

### Molecular Target Preparation

For the experiments, 99% DL-Phenylalanine was acquired from Sigma-Aldrich and used without further purification. It was rubbed directly onto the surface of a 301 stainless steel foil of 10- $\mu$ m thickness and 12-mm diameter and then clamped into the repeller electrode of a time of flight mass spectrometer (23). The distance from the foil, and hence the sample, to the focal point of the ionizing laser pulses was approximately 3 mm. To evaporate the sample, the reverse side of the foil was irradiated with a CW diode laser operating at a wavelength of 960 nm, with a spot diameter of 6 mm and power in the range 0.3 – 0.4 W.

The temperature of the sample was estimated by assuming equilibrium heat conduction along the foil to the repeller electrode (which acts as a room temperature heat sink) and that 30% of the incident radiation was absorbed by the foil at this wavelength (39). Radiative heat losses were negligible for the calculated temperatures. For the lowest laser power used, the temperature at the centre of the foil was estimated to be 430 K and about 410 K at a radius of 2 mm. As the sample depleted, to increase the evaporation at greater distances from the center, the diode laser power was increased to maintain a constant target gas density. While the evaporated target molecules were relatively hot, no fragmentation of the molecules was expected prior to interaction with the ionizing pulses. It was observed that using only the 4 fs VIS/NIR pulses to ionize the molecules produced predominantly parent ions in the mass spectrum. In other experiments using an even softer ionization method (near threshold single photon ionization), parent phenylalanine ions constituted more than 90% of the mass spectrum for a molecular temperature of 423 K (40). Therefore, we can conclude that the observed ultrafast dynamics can be attributed to the parent phenylalanine cation and that loss of the carboxyl group to form the immonium dication occurs after interaction with the pump and probe pulses.

### Fitting of the oscillations in the yield of immonium dication

The pump-probe measurement shown in Fig. 2A, acquired in the case of 3-fs temporal step for the delay between pump and probe pulses, has been fitted by the convolution,  $F(t)$ , of a Gaussian pulse of 4-fs full-width at half maximum (FWHM) corresponding to probe pulse duration, with the following function:

$$R(t) = A(e^{-t/\tau_1} - e^{-t/\tau_2}) \quad (1)$$

where  $\tau_1 = 10 \pm 2$  fs and  $\tau_2 = 25 \pm 2$  fs. In order to fit the temporal evolution of the oscillations in the yield of the doubly-charged immonium fragment, we have first subtracted the fitting curve  $F(t)$  (assuming  $\tau_1 = 10$  fs and  $\tau_2 = 25$  fs) from the experimental data acquired in the case of 0.5-fs delay-steps.

At short pump-probe delays ( $t < 10$  fs) Fourier analysis shows the presence of two main frequency components around 0.14 PHz and 0.3 PHz, as displayed in the spectrogram of Fig. 3A. Therefore, the experimental data have been fitted by the sum of two sinusoidal functions:

$$S(t) = A_1 \sin(2\pi\nu_1 t + \phi_1) + A_2 \sin(2\pi\nu_2 t + \phi_2) \quad (2)$$

The curve has been calculated by using the fitting tool of Matlab R2011a with a confidence level for the bounds of 95%. The result is displayed in Fig. S2. The calculated frequencies are: 0.14 PHz (lower and upper confidence bounds: 0.12 PHz and 0.158 PHz, respectively) and 0.293 PHz (lower and upper confidence bounds: 0.281 PHz and 0.304 PHz, respectively). The total deviation is 0.0063 PHz and the root-mean-square deviation is 0.0148 PHz.

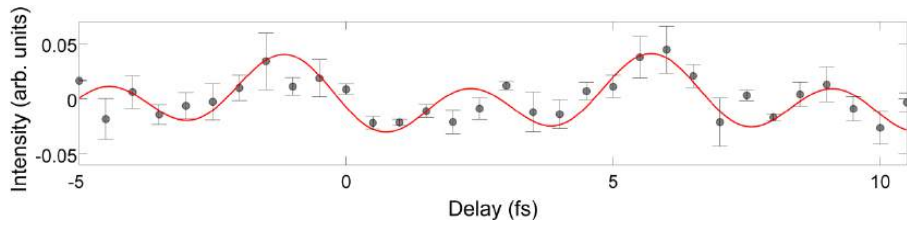


**Fig. S2**

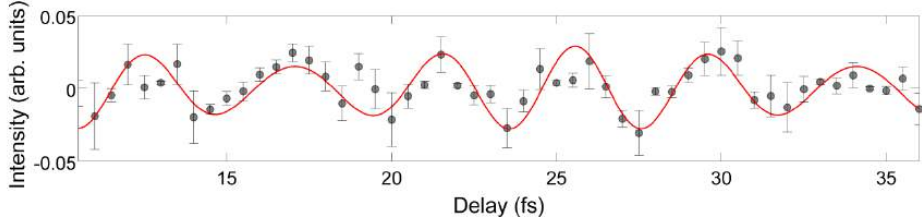
**Fitting curve: short pump-probe delays ( $t < 10$  fs).** Dots correspond to the difference between the experimental data and the exponential fitting curve  $F(t)$ . Error bars show the standard error of the results of four measurements. Red curve is the corresponding fitting curve calculated considering the sum of two sinusoidal functions of frequencies 0.14 PHz ( $A_1 = 0.016$ ,  $\phi_1 = 2.88$  rad) and 0.293 PHz ( $A_2 = 0.025$ ,  $\phi_2 = 3.62$  rad).

In the delay range between 10 fs and 40 fs a strong and broad peak around 0.24 PHz is visible in the spectrogram of Fig. 3A, with a spectral width which slightly increases upon increasing the pump-probe delay. We have first fitted the experimental data by using a single sinusoidal function. The result is shown in Fig. 2C. The calculated frequency is 0.234 PHz, with lower and upper confidence bounds of 0.229 PHz and 0.238 PHz, respectively. The total deviation is 0.0069 PHz and the root-mean-square deviation is 0.0119 PHz. The amplitude and phase of the fitting curve are  $A = 0.022$  and  $\phi = 1.75$  rad, respectively.

The same data can be also fitted by the sum of two sinusoidal functions. The result is displayed in Fig. S3. The resulting frequencies are: 0.234 PHz (lower and upper confidence bounds: 0.229 PHz and 0.239 PHz, respectively) and 0.292 PHz (lower and upper confidence bounds: 0.277 PHz and 0.307 PHz, respectively). The total deviation of

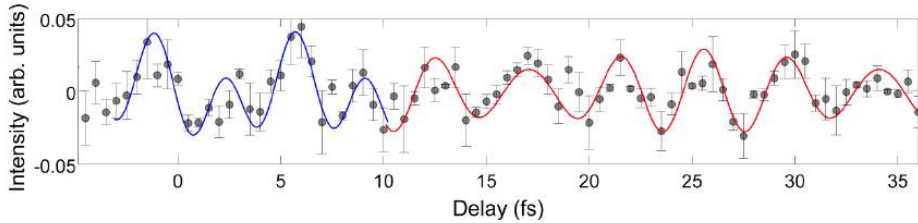
0.0059 PHz and the root-mean-square deviation of 0.0113 PHz are slightly reduced compared to the single-frequency fitting.

Figure S4 shows the experimental data, after subtraction of the fitting curve  $F(t)$ , in the whole temporal region of the pump-probe measurement. The fitting curve displayed in the figure is the composition of the curves shown in Fig. S2 and S3.



**Fig. S3**

**Fitting curve: delay range between 10 fs and 40 fs.** Dots correspond to the difference between the experimental data and the exponential fitting curve  $F(t)$ . Error bars show the standard error of the results of four measurements. Red curve is the corresponding fitting curve calculated considering the sum of two sinusoidal functions of frequencies 0.234 PHz ( $A_1 = 0.022$ ,  $\phi_1 = 1.61$  rad) and 0.292 PHz ( $A_2 = 0.007$ ,  $\phi_2 = 4.88$  rad).



**Fig. S4**

**Fitting curve: whole delay range.** Dots correspond to the difference between the experimental data and the exponential fitting curve  $F(t)$ . Error bars show the standard error of the results of four measurements. Blue curve is the fitting curve shown in Fig. S2, red curve is the fitting curve shown in Fig. S3.

### Theoretical method

As the XUV pulse is weak, we use time-dependent first-order perturbation theory to evaluate the ionization amplitudes at the end of the pulse  $t = T$ :

$$c_{\alpha l}(T) = -i \langle \Psi_{\alpha l}(\varepsilon, \vec{r}) | \vec{e} \cdot \vec{r} | \Psi_0(\vec{r}) \rangle \int_{-\infty}^T E(t) e^{i(E_{\alpha} + \varepsilon - E_0)t} dt \quad (3)$$

where  $\Psi_0$  is the all-electron (hereafter called  $N$ -electron) ground state of phenylalanine with energy  $E_0$ ,  $\Psi_{\alpha l}(\varepsilon)$  is the  $N$ -electron continuum state that describes a photoelectron ejected from the  $\alpha$  molecular orbital with kinetic energy  $\varepsilon$  and angular quantum number  $l$  (for simplicity in the notation, we have omitted the  $m$  quantum number),  $E_{\alpha}$  is the corresponding cationic energy and  $E(t)$  is the electric field associated with the XUV pulse polarized along the  $\vec{e}$  direction. This electric field is derived from the experimental measurements. The  $\Psi_0$  and  $\Psi_{\alpha l}(\varepsilon)$  wave functions have been evaluated in the framework

of the fixed-nuclei approximation by using the static-exchange density functional theory (DFT) and the LB94 functional for exchange and correlation (see reference (28)). A more accurate description of the corresponding energies has been obtained by using a local density approximation that includes the self-interaction correction term that ensures that the ionized electron sees the correct asymptotic charge. The electronic Kohn-Sham equations were solved by expanding the wave functions in a basis of multicentric B-spline functions. The static-exchange DFT method has been successfully used to study photoionization of a large number of diatomic and polyatomic molecules [see, e.g., (28-30, 41-50) and references therein].

Neglecting the interaction of the photoelectron with the remaining ( $N-1$ )-electron cation, the electronic density of the latter is given by (51, 52):

$$\rho_{\text{ion}}(\vec{r}, t) = \sum_{\alpha} \left( \sum_{\substack{\alpha' \\ \alpha' \neq \alpha}} \gamma_{\alpha'\alpha'}^{(\text{ion})} \right) \varphi_{\alpha}^2(\vec{r}) - \sum_{\substack{\alpha\alpha' \\ \alpha' \neq \alpha}} \gamma_{\alpha\alpha'}^{(\text{ion})} e^{i(E_{\alpha} - E_{\alpha'})t} \varphi_{\alpha}(\vec{r}) \varphi_{\alpha'}(\vec{r}) \quad (4)$$

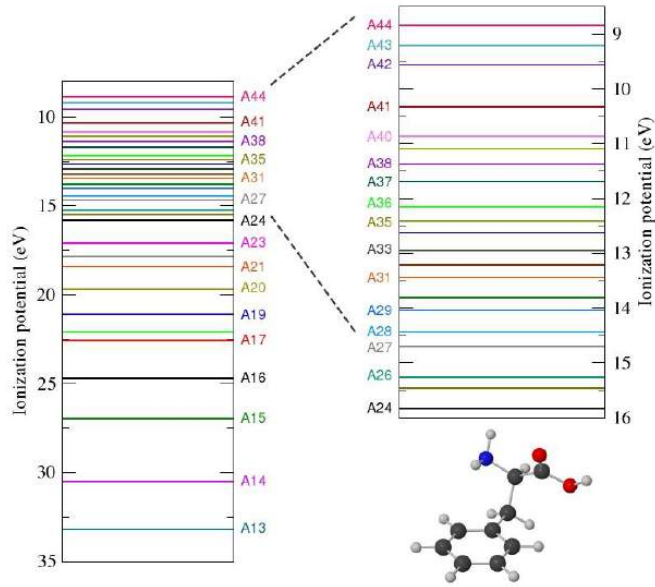


**Fig. S5.**

**Ionization potentials.** Ionization potentials for the most abundant conformer of the phenylalanine molecule obtained from static-exchange DFT-LDA calculations. The labels "An" denote the molecular orbital from which the electron is removed.

where  $\varphi_{\alpha}(\vec{r})$  is the  $\alpha$  molecular orbital and  $\gamma_{\alpha\alpha'}^{(\text{ion})}$  is the reduced density matrix element defined as :

$$\gamma_{\alpha\alpha'}^{(\text{ion})} = \sum_l \int c_{\alpha l}(\varepsilon) c_{\alpha' l}^*(\varepsilon) d\varepsilon \quad (5)$$

The hole density is given by the difference between the electronic density of the neutral molecule, which does not depend on time, and the electronic density of the cation:

$$\rho_{\text{hole}}(\vec{r}, t) = \rho_{\text{neutral}}(\vec{r}) - \rho_{\text{ion}}(\vec{r}, t) = \sum_{\alpha} \left( 1 - \sum_{\substack{\alpha' \\ \alpha' \neq \alpha}} \gamma_{\alpha'\alpha'}^{(\text{ion})} \right) \varphi_{\alpha}^2(\vec{r}) + \sum_{\substack{\alpha\alpha' \\ \alpha' \neq \alpha}} \gamma_{\alpha\alpha'}^{(\text{ion})} e^{i(E_{\alpha} - E_{\alpha'})t} \varphi_{\alpha}(\vec{r}) \varphi_{\alpha'}(\vec{r}) \quad (6)$$

where

$$\rho_{\text{neutral}}(\vec{r}) = \sum_{\alpha} \varphi_{\alpha}^2(\vec{r}) \quad (7)$$

## Supplementary Text

### Photoionization cross sections

Figure S5 shows the ionization energies of all open channels for the most abundant (according to Ref. (27)) conformer of phenylalanine. These energies are approximately given by the Kohn-Sham orbital energies resulting from the static-exchange DFT calculations. The blow-up shows the ionization energies for the highest channels.

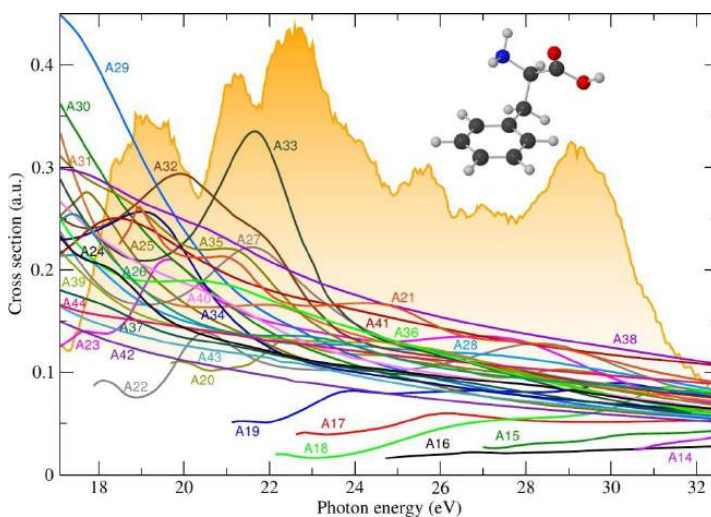


**Fig. S6.**

### Photoionization cross sections and spectrum of the attosecond pump pulse.

Photoionization cross sections of the phenylalanine molecule from different molecular orbitals provided by the static-exchange DFT method. Numbers and colors denote the same molecular orbitals as in Fig. S5. The frequency spectrum of the attosecond pulse used in the experiment and in the calculations of the transition amplitudes leading to the coherent superposition of the one-hole states is represented by a thick orange curve lying over a shaded area.

The corresponding photoionization cross sections are shown in Fig. S6 as a function of photon energy. The figure also shows the frequency spectrum of the XUV pulse. As can be seen, all open channels significantly contribute to the total ionization cross section in the whole energy range accessible by the XUV pulse.

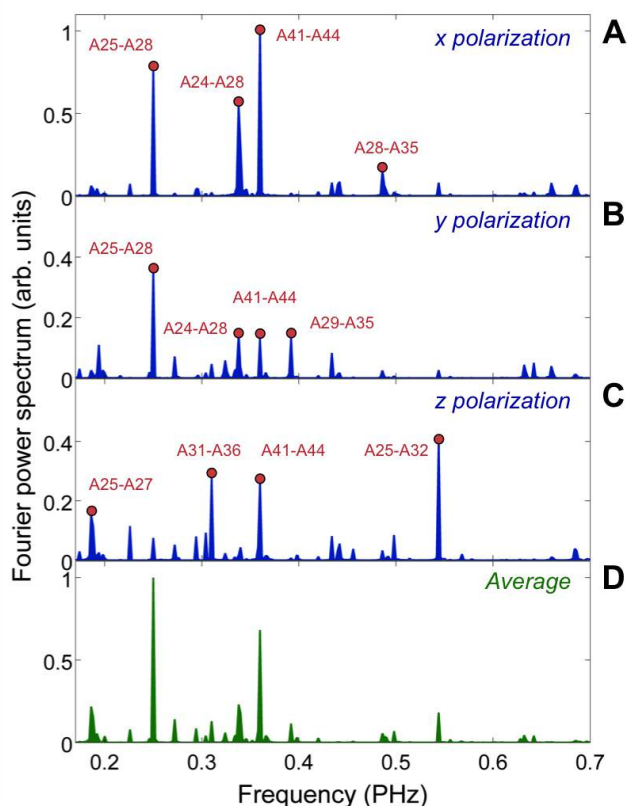


**Fig. S7.**

**Fourier analysis of hole dynamics: dependence on the polarization direction.** Fourier power spectra of the hole density integrated over the amine group for the most abundant conformer of phenylalanine for the three polarization directions defined in Fig. 1 of the manuscript and the average over all polarization directions (randomly oriented molecules). We have also identified the Kohn-Sham orbitals that are responsible for the most important beatings.

#### Analysis of the observed dynamics

We have evaluated the hole density (Eq. 6) at different values of time, from right after the interaction with the XUV pulse up to 500 fs. We seek to describe the interaction of



linearly polarized light with randomly oriented molecules, so we have considered the three polarization directions  $x$ ,  $y$  and  $z$  shown in Fig. 1 of the manuscript.

From the calculated evolution of the hole density it is clear that the largest variations of this density are observed around the amine group ( $-\text{NH}_2$ ). In order to perform a more quantitative analysis, we have integrated the hole density around the amine group. Figure S7 shows the results obtained in the case of the most abundant conformer of phenylalanine. The Fourier power spectra of the temporal evolution of the integrated hole densities are displayed for each orientation and the average over polarization direction, assuming randomly oriented molecules.

To better understand the observed dynamics, in Fig. S7 we have identified the Kohn-Sham orbitals that are responsible for the most important beatings. For completeness, the Kohn-Sham molecular orbitals are plotted in Fig. S8. As can be seen, the dominant beatings almost always involve two orbitals with significant density around the amine group, and at least one of these orbitals allows for delocalization over the whole molecule. This is the reason why the hole moves all over the molecule and the dynamics is better observed in the vicinity of the amine group. To further confirm that the observed dynamics can almost be entirely explained in terms of some of the cationic states that are initially populated by the XUV attosecond pulse, we have carried out calculations for the most abundant conformer in which only cationic states resulting from removing an electron from the A24, A25, A28, A29, A31, A32, A35, A36, A41, and A44 orbitals are included in the free propagation of the electronic wave packet.

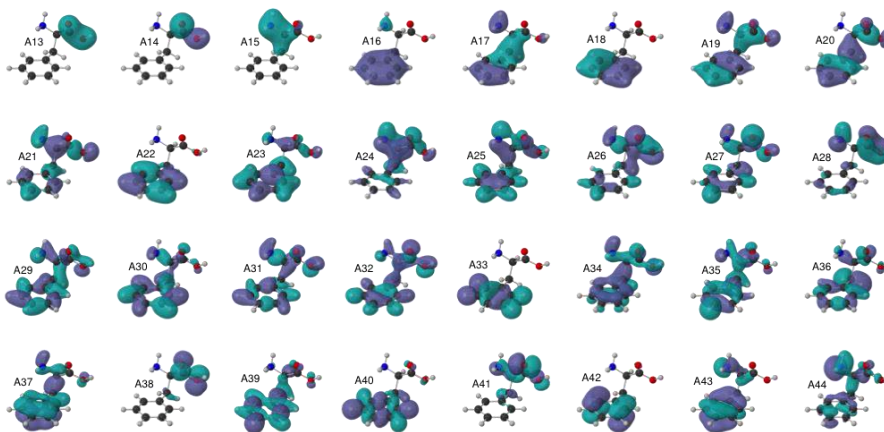


**Fig. S8.**  
**Kohn-Sham molecular orbitals.** Calculated Kohn-Sham orbitals of phenylalanine.

Conversely, we have also performed calculations in which all cationic states but the above mentioned ones are included. The results of these two calculations are shown and compared with the full calculations in Fig. S9. As can be seen, the full FT spectrum is almost entirely reproduced by only including the above ten states. In contrast, the dynamics resulting from excluding these states is almost inexistent.

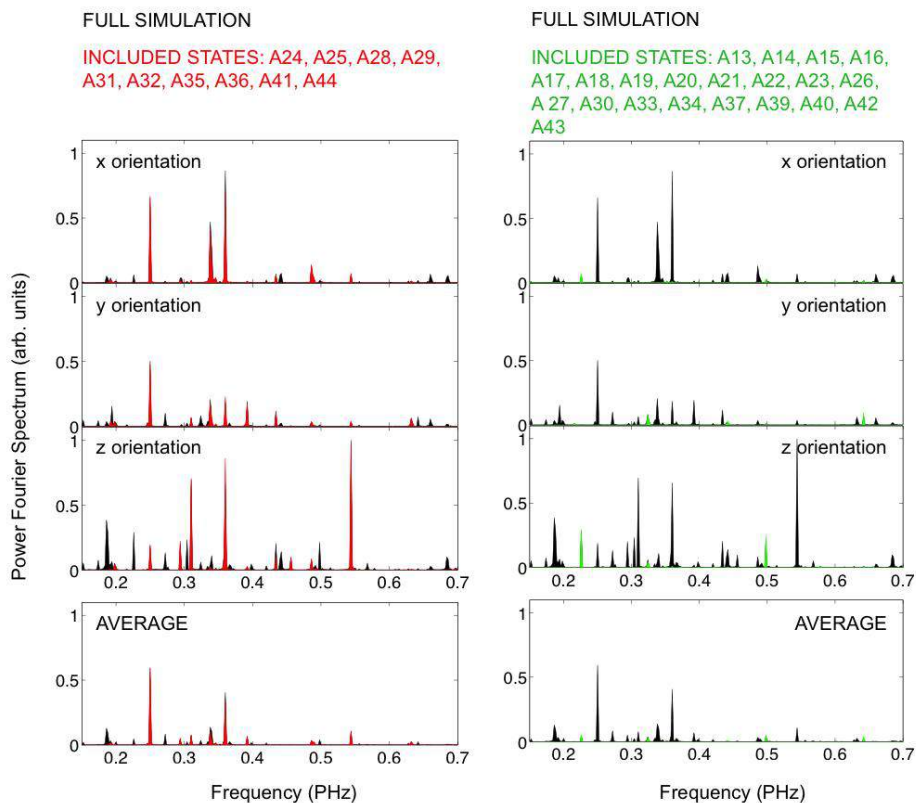


**Fig. S9.**

**Fourier power spectra.** Hole density integrated over the amine group for the most abundant conformer. Black curves: full calculation. Red curves: only cationic states resulting from removing an electron from the A24, A25, A28, A29, A31, A32, A35, A36, A41, and A44 orbitals are included. Green curves: all cationic states but the above mentioned ones are included.

The ultrafast temporal evolution of the wave packet generated by the attosecond pump pulse has also been calculated for the most stable six conformers of phenylalanine. While the precise frequencies of the relevant peaks in the calculated Fourier spectra depend on the particular conformer, the common characteristic is the presence of three dominant groups of Fourier peaks between 0.15 and 0.4 PHz. A thermal average of the various conformers has been calculated, on the basis of the estimated temperature of the phenylalanine molecules (~430 K), by using the ratios calculated by Huang *et al* (27), as given in Table S1.

These ratios were obtained by using statistical mechanics methods based on DFT B3LYP quantum chemistry calculations of the geometries, energies, vibrational frequencies and rotational constants of the 37 lowest conformers of phenylalanine.

**Table S1: Equilibrium distributions (%) of Phenylalanine conformers at T = 418 K.**  
Reported from Ref. (27).

Conformer	Eq. distribution (%) at T = 418 K
1	10.6
2	18.1
3	11.1
4	6.0
5	5.7
6	15.4

The corresponding Fourier power spectrum is given in Fig. S10B. The peaks around 0.25 PHz and 0.36 PHz, which dominate the corresponding Fourier power spectrum of the most abundant conformer (see Fig. S10A), are clearly visible. Likewise, the low-frequency component at 0.19 PHz is still evident.

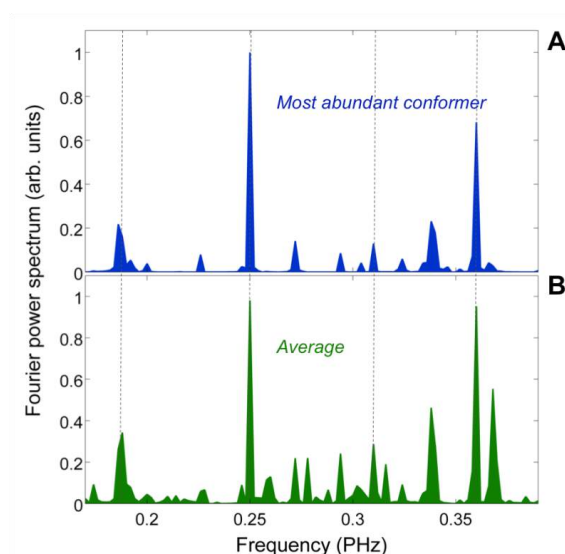


**Fig. S10.**

**Fourier analysis of hole dynamics: role of conformers.** Fourier power spectra of the calculated hole density integrated over amine group: (A) most abundant conformer; (B) average over the six mostly populated conformers.

We emphasize that the experiment and the calculations probe the specific dynamics generated by the initial pump pulse and go far beyond exclusively providing information about energy spacings between the different quantum states of the phenylalanine molecule. This is dramatically illustrated by Fig. S11, in which the calculated Fourier spectrum corresponding to the most abundant conformer is compared with a similar one containing all possible energy spacings with an equal weight. The dynamics of the

electronic wavepacket generation by the pump pulse is responsible for the fact that only a few beatings are observed. These depend on the dipole matrix elements (i.e., the ionizing transition induced by the XUV attosecond pulse) and the interference between the different amplitudes, which is a direct consequence of the time evolution of the hole density. Moreover, if all six conformers were considered, the bottom panel of Fig. S11 would appear as a quasi-continuum. This is a clear indication that the few beatings that are observed and their relative intensity carry the dynamical information about the ionization step and the subsequent evolution of the hole density.

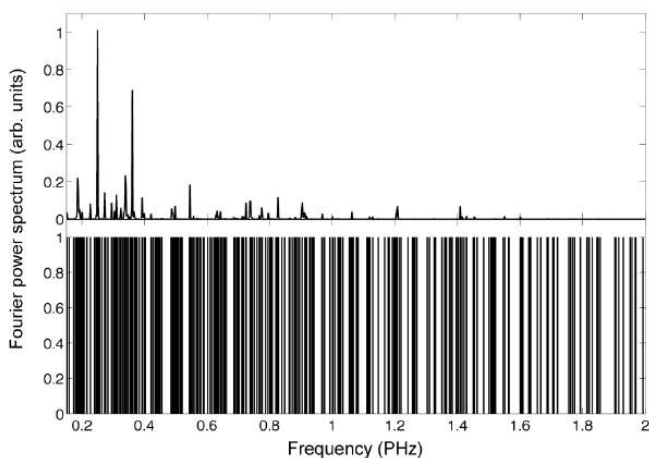


**Fig. S11.**

Fourier power spectra of the calculated hole density integrated over the amine group for the most abundant conformer of phenylalanine. Top: actual calculation. Bottom: results obtained by using an equal weight for all cationic states accessible by the XUV pulse.

#### Vibrational frequencies of phenylalanine

We have calculated the vibrational frequencies and corresponding vibrational periods of phenylalanine. These have been obtained from standard DFT-B3LYP quantum chemistry calculations. The results are given in Table S2. As can be seen, all the vibrational frequencies (periods) are much smaller (larger) than the frequency (period) of the slowest observed beating. Therefore, one can rule out that the observed beatings are due to vibrational motion.

**Table S2: Vibrational frequencies of phenylalanine.** Frequency ( $\text{cm}^{-1}$  and PHz) and corresponding periods (fs) of vibrational modes of phenylalanine.

Mode	Freq. ( $\text{cm}^{-1}$ )	Freq. (PHz)	Period (fs)
1	37.3	0.0011	894.8
2	45.0	0.0013	740.7
3	66.8	0.0020	499.2

4	104.3	0.0031	319.9
5	191.5	0.0057	174.2
6	229.6	0.0069	145.3
7	248.1	0.0074	134.5
8	292.9	0.0088	113.9
9	379.0	0.0114	88.0
10	408.8	0.0123	81.6
11	418.2	0.0125	79.8
12	487.6	0.0146	68.4
13	493.2	0.0148	67.6
14	565.8	0.0170	59.0
15	604.6	0.0181	55.2
16	635.6	0.0191	52.5
17	645.0	0.0193	51.7
18	714.6	0.0214	46.7
19	733.9	0.0220	45.5
20	773.4	0.0232	43.1
21	780.2	0.0234	42.8
22	855.2	0.0256	39.0
23	867.3	0.0260	38.5
24	885.8	0.0266	37.7
25	922.2	0.0276	36.2
26	945.6	0.0283	35.3
27	996.9	0.0299	33.5
28	1001.0	0.0300	33.3
29	1008.4	0.0302	33.1
30	1014.2	0.0304	32.9
31	1051.5	0.0315	31.7
32	1105.1	0.0331	30.2
33	1118.6	0.0335	29.8
34	1141.6	0.0342	29.2
35	1177.4	0.0353	28.3
36	1184.0	0.0355	28.2
37	1207.1	0.0362	27.6
38	1218.8	0.0365	27.4
39	1243.7	0.0373	26.8
40	1292.8	0.0388	25.8
41	1330.5	0.0399	25.1
42	1343.5	0.0403	24.8
43	1368.9	0.0410	24.4
44	1377.7	0.0413	24.2
45	1403.6	0.0421	23.8
46	1486.9	0.0446	22.4
47	1487.8	0.0446	22.4
48	1530.6	0.0459	21.8
49	1621.4	0.0486	20.6
50	1643.2	0.0493	20.3
51	1668.8	0.0500	20.0
52	1813.3	0.0544	18.4
53	3024.2	0.0907	11.0
54	3054.6	0.0916	10.9
55	3097.8	0.0929	10.8
56	3154.5	0.0946	10.6
57	3159.8	0.0947	10.6
58	3169.5	0.0950	10.5
59	3176.9	0.0952	10.5

60	3187.3	0.0956	10.5
61	3501.7	0.1050	9.5
62	3570.7	0.1070	9.3
63	3754.0	0.1125	8.9

### Accuracy of the time-propagation method

To verify the fidelity of our time-propagation method, we have performed theoretical calculations for the glycine molecule, which has been extensively studied by Kuleff *et al.* (53). In the latter reference, 2h1p states were explicitly included in the time propagation, so that a direct comparison with their results provides an unambiguous answer about the role played by such states not included in our time propagation scheme. Our results (to be published elsewhere) are in excellent agreement with those of Kuleff *et al.* (53). Therefore, in the range of photon energies leading to the cationic states relevant for the observed dynamics, we can safely conclude that 2h1p states do not play a significant role.

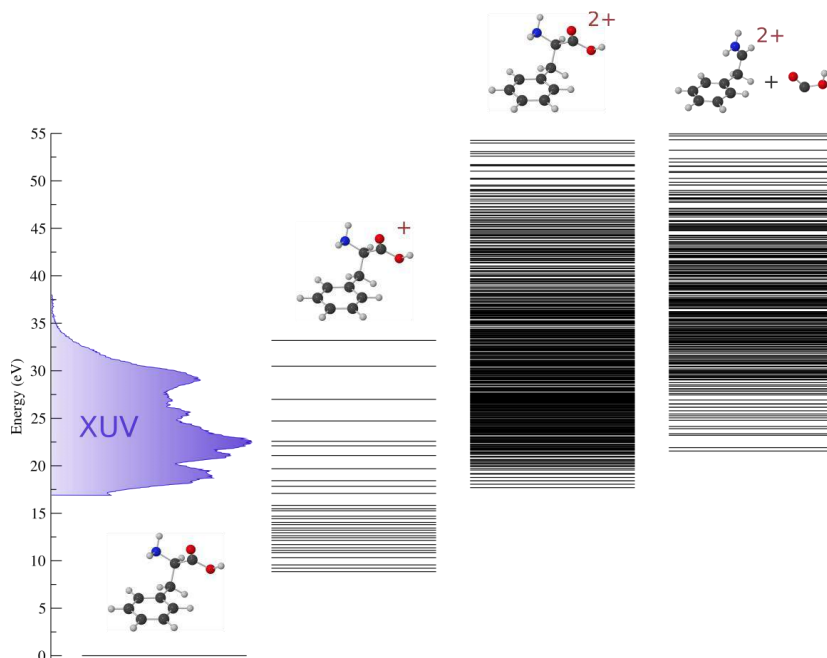


**Fig. S12.**

Energy level diagram containing all the states of singly charged phenylalanine created by the XUV pulse, all the states of doubly-charged phenylalanine and those for the system immonium<sup>++</sup> + COOH.

### Possible probe mechanisms

Figure S12 shows an energy-level diagram with all the states of singly charged phenylalanine (P<sup>+</sup>) created by the XUV pulse, all the states of doubly-charged phenylalanine (P<sup>++</sup>) and those for the system (immonium<sup>++</sup> + COOH) (for short I<sup>++</sup>). The

energies of the latter two systems have been generated by removing electrons from all molecular orbitals of  $P^+$  and immonium+, respectively. As can be seen, one can go from a highly excited state of  $P^+$  to the lowest states of  $P^{++}$  or  $I^{++}$  by absorbing just a few VIS/NIR photons (photon energy around 1.77 eV). Of course, one cannot know how likely this transition will be, but one can unambiguously say that the process only requires absorption of very few VIS/NIR photons. Even if these transitions were unlikely, e.g., due to unfavorable overlap between initial and final orbitals, the transition should be much more likely than others involving many photons even with favorable overlap.

### **Movie S1**

The movie depicts the calculated temporal evolution of the relative variation of the hole density with respect to its time-averaged value for the most abundant conformer of phenylalanine. Iso-surfaces of the relative hole density are shown for cutoff values of  $+10^{-4}$  a.u. (yellow) and  $-10^{-4}$  (purple). Time is referred to the end of the XUV pulse.

## References and Notes

1. F. Krausz, M. Ivanov, Attosecond physics. *Rev. Mod. Phys.* **81**, 163–234 (2009).  
[doi:10.1103/RevModPhys.81.163](https://doi.org/10.1103/RevModPhys.81.163)
2. M. Drescher, M. Hentschel, R. Kienberger, M. Uiberacker, V. Yakovlev, A. Scrinzi, T. Westerwalbesloh, U. Kleineberg, U. Heinzmann, F. Krausz, Time-resolved atomic inner-shell spectroscopy. *Nature* **419**, 803–807 (2002). [Medline doi:10.1038/nature01143](https://doi.org/10.1038/nature01143)
3. M. Uiberacker, T. Uphues, M. Schultze, A. J. Verhoef, V. Yakovlev, M. F. Kling, J. Rauschenberger, N. M. Kabachnik, H. Schröder, M. Lezius, K. L. Kompa, H. G. Muller, M. J. Vrakking, S. Hendel, U. Kleineberg, U. Heinzmann, M. Drescher, F. Krausz, Attosecond real-time observation of electron tunnelling in atoms. *Nature* **446**, 627–632 (2007). [Medline doi:10.1038/nature05648](https://doi.org/10.1038/nature05648)
4. M. Schultze, M. Fiess, N. Karpowicz, J. Gagnon, M. Korbman, M. Hofstetter, S. Neppl, A. L. Cavalieri, Y. Komninos, T. Mercouris, C. A. Nicolaides, R. Pazourek, S. Nagele, J. Feist, J. Burgdörfer, A. M. Azzeer, R. Ernstorfer, R. Kienberger, U. Kleineberg, E. Goulielmakis, F. Krausz, V. S. Yakovlev, Delay in photoemission. *Science* **328**, 1658–1662 (2010). [Medline doi:10.1126/science.1189401](https://doi.org/10.1126/science.1189401)
5. K. Klünder, J. M. Dahlström, M. Gisselbrecht, T. Fordell, M. Swoboda, D. Guénot, P. Johnsson, J. Caillat, J. Mauritsson, A. Maquet, R. Taïeb, A. L’Huillier, Probing single-photon ionization on the attosecond time scale. *Phys. Rev. Lett.* **106**, 143002 (2011).  
[Medline doi:10.1103/PhysRevLett.106.143002](https://doi.org/10.1103/PhysRevLett.106.143002)
6. E. Goulielmakis, Z. H. Loh, A. Wirth, R. Santra, N. Rohringer, V. S. Yakovlev, S. Zherebtsov, T. Pfeifer, A. M. Azzeer, M. F. Kling, S. R. Leone, F. Krausz, Real-time observation of valence electron motion. *Nature* **466**, 739–743 (2010). [Medline doi:10.1038/nature09212](https://doi.org/10.1038/nature09212)
7. A. L. Cavalieri, N. Müller, T. Uphues, V. S. Yakovlev, A. Baltuska, B. Horvath, B. Schmidt, L. Blümel, R. Holzwarth, S. Hendel, M. Drescher, U. Kleineberg, P. M. Echenique, R. Kienberger, F. Krausz, U. Heinzmann, Attosecond spectroscopy in condensed matter. *Nature* **449**, 1029–1032 (2007). [Medline doi:10.1038/nature06229](https://doi.org/10.1038/nature06229)
8. A. Schiffrin, T. Paasch-Colberg, N. Karpowicz, V. Apalkov, D. Gerster, S. Mühlbrandt, M. Korbman, J. Reichert, M. Schultze, S. Holzner, J. V. Barth, R. Kienberger, R. Ernstorfer, V. S. Yakovlev, M. I. Stockman, F. Krausz, Optical-field-induced current in dielectrics. *Nature* **493**, 70–74 (2013). [Medline doi:10.1038/nature11567](https://doi.org/10.1038/nature11567)
9. F. Lépine, M. Y. Ivanov, M. J. J. Vrakking, Attosecond molecular dynamics: Fact or fiction? *Nat. Photonics* **8**, 195–204 (2014). [doi:10.1038/nphoton.2014.25](https://doi.org/10.1038/nphoton.2014.25)
10. G. Sansone, F. Kelkensberg, J. F. Pérez-Torres, F. Morales, M. F. Kling, W. Siu, O. Ghafur, P. Johnsson, M. Swoboda, E. Benedetti, F. Ferrari, F. Lépine, J. L. Sanz-Vicario, S. Zherebtsov, I. Znakovskaya, A. L’huillier, M. Y. Ivanov, M. Nisoli, F. Martín, M. J. Vrakking, Electron localization following attosecond molecular photoionization. *Nature* **465**, 763–766 (2010). [Medline doi:10.1038/nature09084](https://doi.org/10.1038/nature09084)
11. F. Kelkensberg, W. Siu, J. F. Pérez-Torres, F. Morales, G. Gademann, A. Rouzée, P. Johnsson, M. Lucchini, F. Calegari, J. L. Sanz-Vicario, F. Martín, M. J. Vrakking,



- Attosecond control in photoionization of hydrogen molecules. *Phys. Rev. Lett.* **107**, 043002 (2011). [Medline doi:10.1103/PhysRevLett.107.043002](#)
12. W. Siu, F. Kelkensberg, G. Gademann, A. Rouzée, P. Johnsson, D. Doweck, M. Lucchini, F. Calegari, U. De Giovannini, A. Rubio, R. R. Lucchese, H. Kono, F. Lépine, M. J. J. Vrakking, Attosecond control of dissociative ionization of O<sub>2</sub> molecules. *Phys. Rev. A* **84**, 063412 (2011). [doi:10.1103/PhysRevA.84.063412](#)
  13. P. Ranitovic, C. W. Hogle, P. Rivière, A. Palacios, X. M. Tong, N. Toshima, A. González-Castrillo, L. Martín, F. Martín, M. M. Murnane, H. Kapteyn, Attosecond vacuum UV coherent control of molecular dynamics. *Proc. Natl. Acad. Sci. U.S.A.* **111**, 912–917 (2014). [Medline doi:10.1073/pnas.1321999111](#)
  14. L. Belshaw, F. Calegari, M. J. Duffy, A. Trabattoni, L. Poletto, M. Nisoli, J. B. Greenwood, Observation of ultrafast charge migration in an amino acid. *J. Phys. Chem. Lett.* **3**, 3751–3754 (2012). [doi:10.1021/jz3016028](#)
  15. F. Remacle, R. D. Levine, An electronic time scale in chemistry. *Proc. Natl. Acad. Sci. U.S.A.* **103**, 6793–6798 (2006). [Medline doi:10.1073/pnas.0601855103](#)
  16. L. S. Cederbaum, J. Zobeley, Ultrafast charge migration by electron correlation. *Chem. Phys. Lett.* **307**, 205–210 (1999). [doi:10.1016/S0009-2614\(99\)00508-4](#)
  17. H. Hennig, J. Breidbach, L. S. Cederbaum, Electron correlation as the driving force for charge transfer: Charge migration following ionization in N-methyl acetamide. *J. Phys. Chem. A* **109**, 409–414 (2005). [Medline doi:10.1021/jp046232s](#)
  18. J. Breidbach, L. S. Cederbaum, Universal attosecond response to the removal of an electron. *Phys. Rev. Lett.* **94**, 033901 (2005). [Medline doi:10.1103/PhysRevLett.94.033901](#)
  19. J. Breidbach, L. S. Cederbaum, Migration of holes: Formalism, mechanisms, and illustrative applications. *J. Chem. Phys.* **118**, 3983 (2003). [doi:10.1063/1.1540618](#)
  20. R. Weinkauff, P. Schanen, D. Yang, S. Soukara, E. W. Schlag, Elementary processes in peptides: electron mobility and dissociation in peptide cations in the gas phase. *J. Phys. Chem.* **99**, 11255–11265 (1995). [doi:10.1021/j100028a029](#)
  21. R. Weinkauff, P. Schanen, A. Metsala, E. W. Schlag, M. Bürgle, H. Kessler, Highly efficient charge transfer in peptide cations in the gas phase: threshold effects and mechanism. *J. Phys. Chem.* **100**, 18567–18585 (1996). [doi:10.1021/jp960926m](#)
  22. J. Wals, H. H. Fielding, J. F. Christian, L. C. Snoek, W. J. van der Zande, H. van Linden van den Heuvell, Observation of Rydberg wave packet dynamics in a Coulombic and magnetic field. *Phys. Rev. Lett.* **72**, 3783–3786 (1994). [Medline doi:10.1103/PhysRevLett.72.3783](#)
  23. C. R. Calvert, L. Belshaw, M. J. Duffy, O. Kelly, R. B. King, A. G. Smyth, T. J. Kelly, J. T. Costello, D. J. Timson, W. A. Bryan, T. Kierspel, P. Rice, I. C. Turcu, C. M. Cacho, E. Springate, I. D. Williams, J. B. Greenwood, LIAD-fs scheme for studies of ultrafast laser interactions with gas phase biomolecules. *Phys. Chem. Chem. Phys.* **14**, 6289–6297 (2012). [Medline doi:10.1039/c2cp23840c](#)

24. S. Lünemann, A. I. Kuleff, L. S. Cederbaum, Ultrafast charge migration in 2-phenylethyl-N,N-dimethylamine. *Chem. Phys. Lett.* **450**, 232–235 (2008).  
[doi:10.1016/j.cplett.2007.11.031](https://doi.org/10.1016/j.cplett.2007.11.031)
25. D. Mendive-Tapia, M. Vacher, M. J. Bearpark, M. A. Robb, Coupled electron-nuclear dynamics: Charge migration and charge transfer initiated near a conical intersection. *J. Chem. Phys.* **139**, 044110 (2013). [Medline](https://pubmed.ncbi.nlm.nih.gov/23711114/) [doi:10.1063/1.4815914](https://doi.org/10.1063/1.4815914)
26. A. I. Kuleff, L. S. Cederbaum, Charge migration in different conformers of glycine: The role of nuclear geometry. *Chem. Phys.* **338**, 320–328 (2007).  
[doi:10.1016/j.chemphys.2007.04.012](https://doi.org/10.1016/j.chemphys.2007.04.012)
27. H. Z. Huang, W. Yu, Z. Lin, Exploration of the full conformational landscapes of gaseous aromatic amino acid phenylalanine: An ab initio study. *J. Mol. Struct. THEOCHEM* **758**, 195–202 (2006). [doi:10.1016/j.theochem.2005.10.043](https://doi.org/10.1016/j.theochem.2005.10.043)
28. D. Toffoli, M. Stener, G. Fronzoni, P. Decleva, Convergence of the multicenter B-spline DFT approach for the continuum. *Chem. Phys.* **276**, 25–43 (2002). [doi:10.1016/S0301-0104\(01\)00549-3](https://doi.org/10.1016/S0301-0104(01)00549-3)
29. E. Plésiat, P. Decleva, F. Martín, Vibrational branching ratios in the photoelectron spectra of N<sub>2</sub> and CO: Interference and diffraction effects. *Phys. Chem. Chem. Phys.* **14**, 10853–10871 (2012). [Medline](https://pubmed.ncbi.nlm.nih.gov/22411114/) [doi:10.1039/c2cp40693d](https://doi.org/10.1039/c2cp40693d)
30. S. E. Canton, E. Plésiat, J. D. Bozek, B. S. Rude, P. Decleva, F. Martín, Direct observation of Young’s double-slit interferences in vibrationally resolved photoionization of diatomic molecules. *Proc. Natl. Acad. Sci. U.S.A.* **108**, 7302–7306 (2011).  
[doi:10.1073/pnas.1018534108](https://doi.org/10.1073/pnas.1018534108)
31. O. Plekan, V. Feyer, R. Richter, M. Coreno, K. C. Prince, Valence photoionization and photofragmentation of aromatic amino acids. *Mol. Phys.* **106**, 1143–1153 (2008).  
[doi:10.1080/00268970801974875](https://doi.org/10.1080/00268970801974875)
32. M. Nisoli, S. De Silvestri, O. Svelto, Generation of high energy 10 fs pulses by a new pulse compression technique. *Appl. Phys. Lett.* **68**, 2793 (1996). [doi:10.1063/1.116609](https://doi.org/10.1063/1.116609)
33. A. Suda, M. Hatayama, K. Nagasaka, K. Midorikawa, Generation of sub-10-fs, 5-mJ-optical pulses using a hollow fiber with a pressure gradient. *Appl. Phys. Lett.* **86**, 111116 (2005).  
[doi:10.1063/1.1883706](https://doi.org/10.1063/1.1883706)
34. T. Oksenhendler, S. Coudreau, N. Forget, V. Crozatier, S. Grabielle, R. Herzog, O. Gobert, D. Kaplan, Self-referenced spectral interferometry. *Appl. Phys. B* **99**, 7–12 (2010).  
[doi:10.1007/s00340-010-3916-y](https://doi.org/10.1007/s00340-010-3916-y)
35. F. Ferrari, F. Calegari, M. Lucchini, C. Vozzi, S. Stagira, G. Sansone, M. Nisoli, High-energy isolated attosecond pulses generated by above-saturation few-cycle fields. *Nature Phot.* **4**, 875–879 (2010). [doi:10.1038/nphoton.2010.250](https://doi.org/10.1038/nphoton.2010.250)
36. Y. Mairesse, F. Quéré, Frequency-resolved optical gating for complete reconstruction of attosecond bursts. *Phys. Rev. A* **71**, 011401(R) (2005). [doi:10.1103/PhysRevA.71.011401](https://doi.org/10.1103/PhysRevA.71.011401)
37. G. Sansone, E. Benedetti, F. Calegari, C. Vozzi, L. Avaldi, R. Flammini, L. Poletto, P. Villoresi, C. Altucci, R. Velotta, S. Stagira, S. De Silvestri, M. Nisoli, Isolated single-

- cycle attosecond pulses. *Science* **314**, 443–446 (2006). [Medline doi:10.1126/science.1132838](#)
38. L. Poletto, S. Bonora, M. Pascolini, P. Villoresi, Instrumentation for analysis and utilization of extreme-ultraviolet and soft x-ray high-order harmonics. *Rev. Sci. Instrum.* **75**, 4413 (2004). [doi:10.1063/1.1784563](#)
39. S. Boyden, J. Zhang, Temperature and wavelength-dependent spectral absorptivities of metallic materials in the infrared. *J. Therm. Heat Transfer* **20**, 9–15 (2006). [doi:10.2514/1.15518](#)
40. F. Gaie-Levrel, G. A. Garcia, M. Schwell, L. Nahon, VUV state-selected photoionization of thermally-desorbed biomolecules by coupling an aerosol source to an imaging photoelectron/photoion coincidence spectrometer: Case of the amino acids tryptophan and phenylalanine. *Phys. Chem. Chem. Phys.* **13**, 7024–7036 (2011). [Medline doi:10.1039/c0cp02798g](#)
41. M. Stener, P. Bolognesi, M. Coreno, P. O’Keeffe, V. Feyer, G. Fronzoni, P. Decleva, L. Avaldi, A. Kivimäki, Photoabsorption and S 2p photoionization of the SF<sub>6</sub> molecule: Resonances in the excitation energy range of 200–280 eV. *J. Chem. Phys.* **134**, 174311 (2011). [Medline doi:10.1063/1.3583815](#)
42. D. Catone, M. Stener, P. Decleva, G. Contini, N. Zema, T. Prospero, V. Feyer, K. C. Prince, S. Turchini, Resonant circular dichroism of chiral metal-organic complex. *Phys. Rev. Lett.* **108**, 083001 (2012). [Medline doi:10.1103/PhysRevLett.108.083001](#)
43. L. Argenti, T. D. Thomas, E. Plésiat, X.-J. Liu, C. Miron, T. Lischke, G. Prümper, K. Sakai, T. Ouchi, R. Püttner, V. Sekushin, T. Tanaka, M. Hoshino, H. Tanaka, P. Decleva, K. Ueda, F. Martín, Double-slit experiment with a polyatomic molecule: Vibrationally resolved C 1s photoelectron spectra of acetylene. *New J. Phys.* **14**, 033012 (2012). [doi:10.1088/1367-2630/14/3/033012](#)
44. S. Turchini, D. Catone, N. Zema, G. Contini, T. Prospero, P. Decleva, M. Stener, F. Rondino, S. Piccirillo, K. C. Prince, M. Speranza, Conformational sensitivity in photoelectron circular dichroism of 3-methylcyclopentanone. *ChemPhysChem* **14**, 1723–1732 (2013). [Medline doi:10.1002/cphc.201200975](#)
45. R. K. Kushawaha, M. Patanen, R. Guillemin, L. Journel, C. Miron, M. Simon, M. N. Piancastelli, C. Skates, P. Decleva, From double-slit interference to structural information in simple hydrocarbons. *Proc. Natl. Acad. Sci. U.S.A.* **110**, 15201–15206 (2013). [Medline doi:10.1073/pnas.1306697110](#)
46. K. Ueda, C. Miron, E. Plésiat, L. Argenti, M. Patanen, K. Kooser, D. Ayuso, S. Mondal, M. Kimura, K. Sakai, O. Travnikova, A. Palacios, P. Decleva, E. Kukk, F. Martín, Intramolecular photoelectron diffraction in the gas phase. *J. Chem. Phys.* **139**, 124306 (2013). [Medline doi:10.1063/1.4820814](#)
47. D. M. P. Holland, D. A. Shaw, S. Coriani, M. Stener, P. Decleva, A study of the valence shell electronic states of pyridazine by photoabsorption spectroscopy and time-dependent density functional theory calculations. *J. Phys. At. Mol. Opt. Phys.* **46**, 175103 (2013). [doi:10.1088/0953-4075/46/17/175103](#)

48. E. Plésiat, P. Decleva, F. Martín, Relationship between polarization-averaged molecular-frame photoelectron angular distributions and geometry. *Phys. Rev. A* **88**, 063409 (2013). [doi:10.1103/PhysRevA.88.063409](https://doi.org/10.1103/PhysRevA.88.063409)
49. R. Boll, D. Anielski, C. Bostedt, J. Bozek, L. Christensen, R. Coffee, S. De, P. Decleva, S. Epp, B. Erk, L. Foucar, F. Krasniqi, J. Küpper, A. Rouzée, B. Rudek, A. Rudenko, S. Schorb, H. Stapelfeldt, M. Stener, S. Stern, S. Techert, S. Trippel, M. Vrakking, J. Ullrich, D. Rolles, Femtosecond photoelectron diffraction on laser-aligned molecules: Towards time-resolved imaging of molecular structure. *Phys. Rev. A* **88**, 061402 (2013). [doi:10.1103/PhysRevA.88.061402](https://doi.org/10.1103/PhysRevA.88.061402)
50. M. Stener, P. Decleva, T. Mizuno, H. Yoshida, A. Yagishita, Off-resonance photoemission dynamics studied by recoil frame F1s and C1s photoelectron angular distributions of CH<sub>3</sub>F. *J. Chem. Phys.* **140**, 044305 (2014). [doi:10.1063/1.4862267](https://doi.org/10.1063/1.4862267)
51. K. Blum, *Density Matrix Theory and Applications* (Plenum, New York, 1996).
52. N. Rohringer, R. Santra, Multichannel coherence in strong-field ionization. *Phys. Rev. A* **79**, 053402 (2009). [doi:10.1103/PhysRevA.79.053402](https://doi.org/10.1103/PhysRevA.79.053402)
53. A. I. Kuleff, J. Breidbach, L. S. Cederbaum, Multielectron wave-packet propagation: General theory and application. *J. Chem. Phys.* **123**, 044111 (2005). [Medline](https://pubmed.ncbi.nlm.nih.gov/15711111/)  
[doi:10.1063/1.1961341](https://doi.org/10.1063/1.1961341)

## **Appendix G**

Ultrafast charge dynamics in an amino acid induced by attosecond pulses



# Ultrafast Charge Dynamics in an Amino Acid Induced by Attosecond Pulses

Francesca Calegari, David Ayuso, Andrea Trabattoni, Louise Belshaw, Simone De Camillis, Fabio Frassetto, Luca Poletto, Alicia Palacios, Piero Decleva, Jason B. Greenwood, Fernando Martín, and Mauro Nisoli

(Invited Paper)

**Abstract**—In the past few years, attosecond techniques have been implemented for the investigation of ultrafast dynamics in molecules. The generation of isolated attosecond pulses characterized by a relatively high photon flux has opened up new possibilities in the study of molecular dynamics. In this paper, we report on experimental and theoretical results of ultrafast charge dynamics in a biochemically relevant molecule, namely, the amino acid phenylalanine. The data represent the first experimental demonstration of the generation and observation of a charge migration process in a complex molecule, where electron dynamics precede nuclear motion. The application of attosecond technology to the investigation of electron dynamics in biologically relevant molecules represents a multidisciplinary work, which can open new research frontiers: those in which few-femtosecond and even subfemtosecond electron processes determine the fate of biomolecules. It can also open new perspectives for the development of new technologies, for example, in molecular electronics, where electron processes on an ultrafast

temporal scale are essential to trigger and control the electron current on the scale of the molecule.

**Index Terms**—Molecular physics, attosecond, femtosecond, extreme-ultraviolet (XUV) spectroscopy, high harmonics, ultrafast optics.

## I. INTRODUCTION

ULTRAFast dynamics in molecules is at the root of a number of physical, chemical and biological processes [1]–[3]. Indeed, chemical reactions are the result of bond breaking and formation, a dynamical process that is initiated by changes in the electronic structure. The study of the dynamics associated to the nuclear motion belongs to the realm of femtochemistry, a well-established field that for more than twenty years has been able to capture and even control the nuclear motion in chemical reactions and intramolecular processes [4]. The initial step, i.e., electron rearrangement, remains to be fully understood.

Time-resolved studies on electron dynamics can shed light on the underlying mechanisms in a variety of processes such as photosynthesis, cellular respiration or electron transport along large peptides and proteins [5], [6]. Electron dynamics of those processes are induced by absorption of photons in the ultraviolet (UV) and extreme UV (XUV) range and occur in the attosecond time scale. Experimental tools and techniques able to provide such time resolution in complex molecular targets are still in their infancy [7]. The first pump-probe experiment on molecules using an isolated attosecond pulse to launch electron dynamics was reported in 2010, where electron localization was then measured in H<sub>2</sub> and D<sub>2</sub> using an infrared (IR) probe pulse and recorded with attosecond time resolution [8]. One year later, trains of attosecond pulses were also used to investigate how a moderately intense IR field affects the electronic dynamics induced by the XUV photoionization of hydrogen molecules [9], or to demonstrate the possibility of controlling dissociative ionization of oxygen molecules [10]. Attosecond pulse trains have been also combined with two near-IR pulses to coherently excite and control the outcome of a simple chemical reaction in D<sub>2</sub> molecules [11].

Further applications of attosecond technology nowadays focus on larger and complex targets. Already in 2012, successful results have been reported on the use of a short train of attosecond pulses to explore the ultrafast dynamics in an amino acid [12]. In this paper, the evolution of various ionic fragments of phenylalanine was followed in time after prompt single-photon

Manuscript received November 28, 2014; revised March 27, 2015; accepted March 28, 2015. This work was supported by the European Research Council under the ERC Grants 227355 ELYCHE and 290853 XCHEM, by LASERLAB-EUROPE under Grant 284464, EC's Seventh Framework Program, by European COST Action CM1204 XLIC, the MICINN Project FIS2013-42002-R, the ERA-Chemistry Project PIM2010EEC-00751, the European Grants MC-ITN CORINF and MC-RG ATTOTREND 268284, the UK's STFC Laser Loan Scheme, the Engineering and Physical Sciences Research Council Grant EP/J007048/1, the Leverhulme Trust Grant RPG-2012-735, and the Northern Ireland Department of Employment and Learning. This work was accomplished with an allocation of computer time from CCC-UAM and Mare Nostrum BSC.

F. Calegari is with the Institute of Photonics and Nanotechnologies, National Research Council, Milano 20133, Italy (e-mail: francesca.calegari@polimi.it).

D. Ayuso and A. Palacios are with the Departamento de Química, Universidad Autónoma de Madrid, Cantoblanco 28049, Madrid, Spain (e-mail: david.ayuso@uam.es; alicia.palacios@uam.es).

A. Trabattoni is with the Department of Physics, Politecnico di Milano, Milano 20133, Italy (e-mail: andrea.trabattoni@polimi.it).

L. Belshaw, S. De Camillis, and J. B. Greenwood are with the Centre for Plasma Physics, School of Maths and Physics, Queen's University Belfast, Belfast BT7 1NN, U.K. (e-mail: lbelshaw01@qub.ac.uk; sdecamillis01@qub.ac.uk; J.Greenwood@qub.ac.uk).

F. Frassetto and L. Poletto are with the Institute of Photonics and Nanotechnologies, National Research Council, Padova 35131, Italy (e-mail: fabio.frassetto@pd.infn.cnr.it; poletto@dei.unipd.it).

P. Decleva is with the Dipartimento di Scienze Chimiche e Farmaceutiche, Università di Trieste, CNR-IOM, Trieste 34127, Italy (e-mail: decleva@uni.trieste.it).

F. Martín is with Instituto Madrileño de Estudios Avanzados en Nanociencia, Departamento de Química, Universidad Autónoma de Madrid, Cantoblanco, 28049 Madrid, Spain (e-mail: fernando.martin@uam.es).

M. Nisoli is with the Department of Physics, Politecnico di Milano, Milano 20133, Italy, and also with the Institute of Photonics and Nanotechnologies, National Research Council, Milano 20133, Italy (e-mail: mauro.nisoli@polimi.it).

Color versions of one or more of the figures in this paper are available online at <http://ieeexplore.ieee.org>.

Digital Object Identifier 10.1109/JSTQE.2015.2419218

ionization of the molecule by the XUV attosecond pulses. More recently, the authors of the present paper have reported the first experimental demonstration of charge migration in the same amino acid. It was found that this process is characterized by sub-4.5 fs oscillations appearing in the quantum yield of a specific doubly charged fragment [13].

Charge migration refers to a charge transfer mechanism occurring on a temporal scale that precedes notable nuclear motion [14], [15]. The first experimental glimpse of an extremely efficient and ultrafast charge transfer within polypeptide molecules, was reported by Schlag and co-workers [16], [17]. They showed that if an electron is selectively ionized from a chromophore at the C-terminal end of a peptide, the location of the charge can be probed by using the shift in absorption of the chromophore once charged. By employing this technique, they were able to observe a charge transfer over more than 10  $\sigma$ -bonds. They interpreted their experiments in terms of a very fast charge-transfer process, which can efficiently compete with fast intrachromophoric rates. They also showed that this charge transfer was directly correlated with the properties of individual amino acids.

The ultrafast dynamics of charge transfer processes initiated in complex biologically relevant molecules by sudden photoionization have been investigated in various theoretical papers [14], [15], [18], [19]. It was suggested that if an electron is suddenly removed from a molecular orbital, the molecule will be in a superposition of electronic states of the radical cation. The temporal evolution of this electronic wavepacket, producing charge oscillations, has been referred to as charge migration to distinguish it from charge transfer mediated by nuclear motion. For example, a hole generated by prompt ionization of the highest-occupied molecular orbital (HOMO) of the tetrapeptide Trp-Leu-Leu-Leu (Trp and Leu are the amino acids Tryptophan and Leucine, respectively) and localized on the Trp chromophore migrates to the N terminus (or amino-terminus) of the peptide in 0.75 fs [15]. Direct experimental access to such sub-femtosecond processes is mandatory to image electronic dynamics in complex molecules and requires of attosecond measurement techniques.

In this paper, we report experimental measurements and a detailed theoretical analysis of the first application of isolated attosecond pulses to phenylalanine. In Section II, the pump-probe experimental setup is described. Experimental results are discussed in Section III, where we first present the mass spectrum of phenylalanine produced upon photoionization by isolated attosecond pulses, followed by the pump-probe measurements that reveal the signature of ultrafast charge migration along the molecular skeleton. The theoretical data and interpretation are given in Section IV. Finally, Section V presents a summary of the most significant results.

## II. EXPERIMENTAL SETUP

For the experiments a Ti:sapphire laser system was used (Femtopower PRO HE CEP, Femtolasers) with the following characteristics: 6-mJ pulse energy, 25-fs pulse duration and 1-kHz repetition rate. The carrier-envelope phase (CEP) was

stabilized by two feedback loops: a fast loop acting on the oscillator and a slow loop acting on a glass wedge placed in the stretcher before the preamplifier. The residual CEP fluctuation was about 200 mrad (rms), measured in-loop with a  $f$ -to- $2f$  interferometer using an integration time of 1 ms. We have then compressed the pulses using the hollow-fiber compression technique [20], [21] in combination with a broadband chirped-mirror dispersive delay line. Due to the high energy of the laser pulses, the pressure gradient scheme has been employed [22]. We used a 1-m-long hollow fiber with an inner diameter of 320  $\mu\text{m}$ , filled with helium: the pressure at the input of the fiber was kept to  $<5$  mbar and 2 bar at the output. The beam position at the input of the hollow fiber was actively stabilized [23]. A pulse energy of 3.3 mJ was obtained at the output with no gas in the fibre, and 2.3 mJ with gas. After eight reflections on the chirped mirrors, pulses as short as 4 fs were achieved. The pulse duration was measured by using a single-shot self-referenced spectral interferometry method [24] implemented with cross-polarized wave (XPW). By using a novel single-shot interferometric technique, allowing *in situ* measurement of intensity-dependent phase changes experienced by ultrashort laser pulses upon nonlinear propagation, we have demonstrated that CEP stability is substantially preserved by the hollow fiber compression technique [25].

The visible/near infrared (VIS/NIR) beam was divided into two portions by using an ultrabroadband beam splitter with 30% reflection. The transmitted beam part was focused by a 1-m radius of curvature mirror into a 3-mm-thick cell filled with xenon at static pressure to produce extreme ultraviolet (XUV) radiation by high-order harmonic generation. Isolated attosecond pulses, with energy in the nanojoule range, were produced by employing the ionization gating technique, which is a temporal gating scheme based on sub-cycle ionization dynamics in a gas cell driven by few-optical-cycle pulses with above-saturation intensity and stable CEP [26], [27]. A 100-nm-thick aluminium filter was used to filter out the fundamental radiation and the low order harmonics. An indium foil has been also used in a few measurements described in the text. The temporal duration of the XUV pulses ( $290 \pm 20$  as) was measured by using the frequency resolved optical gating for complete reconstruction of attosecond bursts (FROG CRAB) technique [28], [29]. The remaining part of the VIS/NIR beam was collinearly recombined with the XUV beam by using a mirror with a central hole. The temporal delay between VIS/NIR and XUV pulses was adjusted with attosecond resolution by using a piezoelectric translation stage. The pump and probe pulses were collinearly focused into the mass spectrometer, as shown in Fig. 1, by using a gold-coated toroidal mirror, with unit magnification, which provided an almost aberration-free image of the XUV source with negligible temporal smearing of the attosecond pulses [30]. The peak intensity of the VIS/NIR probe pulse in the sample was about  $5 \times 10^{12}$  W/cm<sup>2</sup>. The spectrum of the XUV radiation was measured by using a high-resolution flat-field soft X-ray spectrometer [30].

Gas-phase molecules were produced by employing the laser induced thermal desorption method. Phenylalanine was deposited on a 10- $\mu\text{m}$ -thick stainless steel foil, mounted onto the repeller electrode of a time of flight (TOF) mass spectrometer



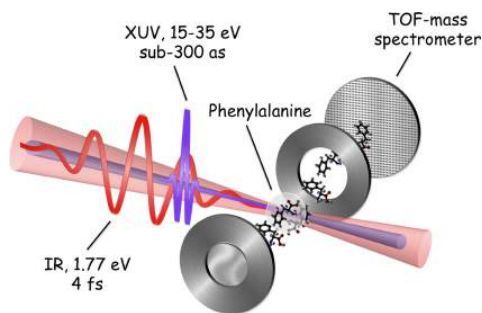


Fig. 1. Experimental setup for the pump-probe measurements showing the time-of-flight mass spectrometer used in the experiments.

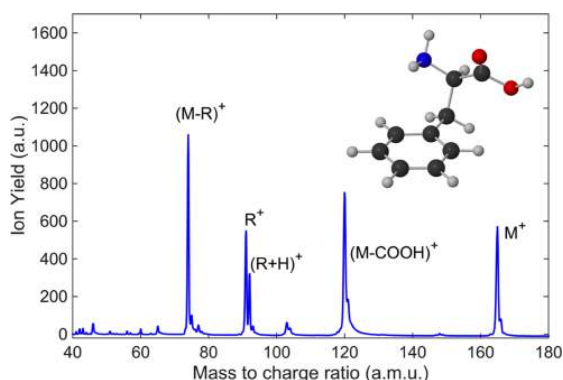


Fig. 2. Mass spectrum from ionization of phenylalanine by an XUV pulse. M stands for the parent ion and R for the side chain group. The inset displays the molecular structure of the most abundant conformer of phenylalanine; dark gray spheres represent carbon atoms, light gray spheres hydrogen atoms, blue sphere nitrogen and red spheres oxygen.

[31]. To evaporate the sample, the reverse side of the foil was irradiated with a CW diode laser operating at a wavelength of 960 nm, with a spot diameter of 6 mm and power in the range 0.3–0.4 W. The distance from the foil to the focal point of the ionizing laser pulses was approximately 3 mm.

The temperature of the sample was estimated by assuming equilibrium heat conduction along the foil to the repeller electrode and that 30% of the incident radiation was absorbed by the foil at this wavelength [32]. Radiative heat losses were negligible for the calculated temperatures. For the lowest laser power used, the temperature at the centre of the foil was estimated to be 430 K and about 410 K at a radius of 2 mm.

### III. EXPERIMENTAL RESULTS

#### A. Fragmentation Results

We investigated the phenylalanine molecule, one of the essential amino acids for human life, whose molecular structure is displayed in the inset of Fig. 2. It is an  $\alpha$ -amino acid, consisting in a central carbon atom ( $\alpha$  carbon), linked to an amine ( $-\text{NH}_2$ ) group, a carboxylic group ( $-\text{COOH}$ ), a hydrogen atom and a side chain ( $-\text{R}$ ). The side chain is specific for each amino

acid and for phenylalanine is formed by a methylene ( $-\text{CH}_2-$ ) group ( $\beta$  carbon) terminated by a phenyl ring. We have chosen it as a model molecule for charge migration because it contains two electron-acceptor sites with approximately the same binding energy located on the phenyl and amine groups, and separated by two singly bonded carbon atoms. The molecule was first irradiated with the XUV attosecond pulse which has a photon energy bandwidth of  $\sim 19$  eV, from 16 to 35 eV. The parent and fragment ions produced were then extracted into the TOF spectrometer for mass analysis. Fig. 2 shows the measured mass spectrum, where the main contributions correspond to the parent ion  $\text{M}^+$  (165 Da), loss of the carboxyl group yielding the immonium ion ( $\text{M}-\text{COOH}$  at 120 Da), and breakage of the  $\text{C}_\alpha-\text{C}_\beta$  bond with the charge residing on the amine ( $\text{M}-\text{R}$  at 74 Da) or phenyl groups ( $\text{R}$  at 91). We observe a small peak with a mass to charge ratio  $m/q = 60$ , which is due to the doubly charged immonium ion. The XUV pulse is capable of ionizing all valence and some inner shell orbitals, resulting in a wide range of fragment ions. It was observed that using only the 4-fs VIS/NIR pulses to ionize the molecule produced predominantly parent ions in the mass spectrum.

#### B. Pump-Probe Measurements

The temporal evolution of the ionic fragments produced in phenylalanine has been investigated by means of two-color pump-probe measurements, using attosecond pump pulses and 4-fs VIS/NIR probe pulses at a variable temporal delay. To obtain the zero of the experimental data we have removed the 100-nm-thick aluminium filter and we have measured as a function of time the fragment yields produced by the VIS/NIR-pump/VIS/NIR-probe interaction. This defines our zero time position to an accuracy better than 1 fs.

In a previous work [12] we observed dynamics in a number of fragments with a time constant of  $80 \pm 20$  fs, which we attributed to an internal conversion process. In this work, which has much better statistics, the fractional yields of nearly all the singly charged fragments vary as a function of pump-probe delay. However, there is a marked difference when the XUV beam is filtered with an aluminium foil, generating an XUV spectrum from 16 to 35 eV, compared to an indium foil, which produces a XUV spectrum with a 3-eV (full-width at half maximum) peak centred around 15 eV, followed by a broad and weak spectral component extending up to 25 eV. This is demonstrated in Fig. 3 for the fragment  $m/q = 28$  ( $\text{NH}_2\text{C}$ ). It can be seen that in the case of XUV pulses transmitted by the aluminium filter (see Fig. 3(a)), the fragment yield increases with pump-probe delay, with a time constant of  $80 \pm 2$  fs. Other fragments also increase with time constants in the range from 50 to 100 fs at the expense of the parent ( $m/q = 165$ ) and immonium ions ( $m/q = 120$ ) which decrease. By contrast, in the case of XUV pulses transmitted by the indium filter (see Fig. 3(b)), a sudden increase in the yield of the fragment  $m/q = 28$  can be observed with no subsequent dynamics. This result suggests that when only a valence electron can be ionized (XUV pulse filtered by indium), no temporal dynamics of the singly charged ions are observed, but the presence of hole in the valence shell allows the VIS/IR

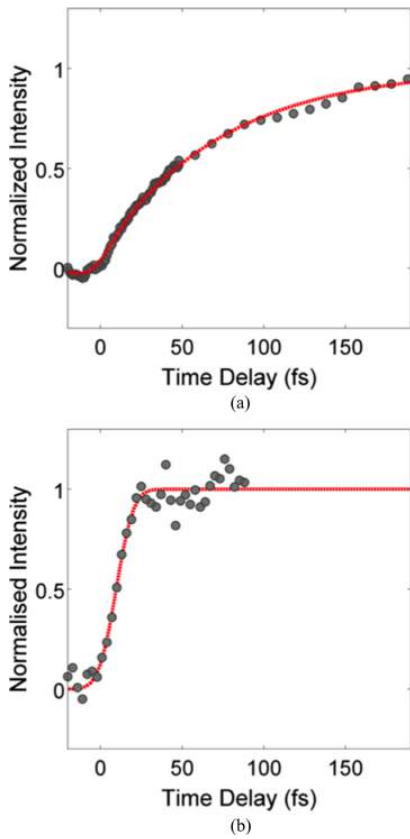


Fig. 3. Normalized yield of fragment  $m/q = 28$ , as a function of pump-probe delay for an XUV pump pulse transmitted by an aluminium foil (a) and an indium foil (b). In (a) the data has been fitted with the convolution of a Gaussian function (4-fs FWHM) with the function  $y = y_0 + b[1 - \exp(-t/\tau)]$ . In (b) the data has been fitted with the convolution of a Gaussian function with the step function.

pulse to be absorbed. For instance, it is known that absorption by the phenyl chromophore shifts from the ultraviolet to the green when there is a hole in the highest occupied molecular orbital [17]. This increases the yield of smaller fragments when the XUV pulse precedes the VIS/IR pulse with a concomitant reduction in parent and larger fragment ions. When an inner valence orbital is ionized (by the XUV pulse filtered with aluminium), there is initially no resonant absorption of the probe but an internal conversion to a lower electronic state generates a hole in the valence shell opening up absorption of the probe and hence further fragmentation. The measured timescale of 50–100 fs is compatible with an internal conversion mechanism as it is mediated by nuclear motion on potential energy surfaces.

On the other hand, the immonium dication ( $m/q = 60$ ) shows a faster temporal evolution, as shown in Fig. 4, where the data points have been acquired by using 3-fs step in pump-probe time delay. The experimental data has been fitted by the convolution,  $F(t)$ , of a Gaussian pulse of 4-fs full-width at half maximum

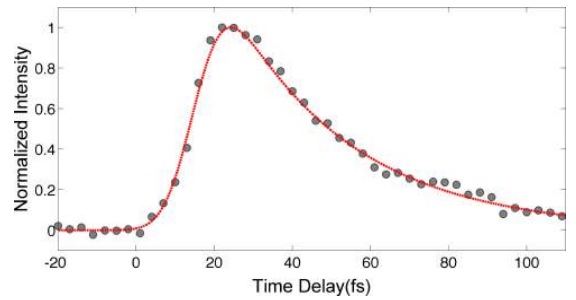


Fig. 4. Yield of doubly charged immonium ion ( $m/q = 60$ ) as a function of pump-probe delay. The dotted line is the convolution fitting function  $F(t)$  described in the text.

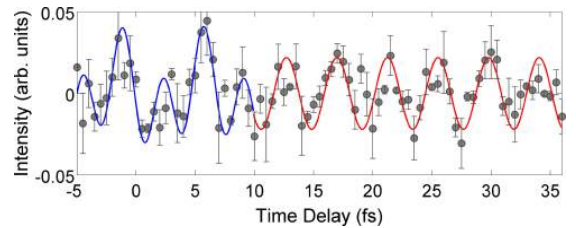


Fig. 5. Dots correspond to the difference between the experimental data and the fitting curve  $F(t)$ . Error bars show the standard error of the results of four measurements. Blue curve is a fitting curve obtained as the sum of two sinusoidal functions, red curve is a single sinusoidal fitting curve, as described in the text.

(FWHM), with the following function:

$$R(t) = A(e^{-t/\tau_1} - e^{-t/\tau_2}) \quad (1)$$

where  $\tau_1 = 10 \pm 2$  fs and  $\tau_2 = 25 \pm 2$  fs. Upon decreasing the delay-step between pump and probe pulses from 3 to 0.5 fs, an oscillation of the dication yield is clearly visible in the pump-probe measurement. Fig. 5 displays the measured data, acquired with delay-step between pump and probe pulses of 0.5 fs, after subtraction of the fitting curve  $F(t)$  (assuming  $\tau_1 = 10$  fs and  $\tau_2 = 25$  fs).

As reported in [13], we have performed a Fourier analysis of the experimental data. Time-dependent Fourier transforms have been calculated by using a sliding Gaussian window function

$$g(t - t_d) = \exp[-(t - t_d)^2/t_0^2] \quad (2)$$

with  $t_0 = 10$  fs and peak at  $t_d$  (gate delay time). As shown in Fig. 6 at short pump-probe delays ( $t < 10$  fs) two main frequency components are present, around 0.14 and 0.3 PHz. Therefore in this temporal window the pump-probe data have been fitted by the sum of two sinusoidal functions:

$$S(t) = A_1 \sin(2\pi\nu_1 t + \phi_1) + A_2 \sin(2\pi\nu_2 t + \phi_2). \quad (3)$$

The calculated frequencies are: 0.14 PHz (lower and upper confidence bounds: 0.12 and 0.158 PHz, respectively) and 0.293 PHz (lower and upper confidence bounds: 0.281 and 0.304 PHz, respectively). At longer pump-probe delays (in the range from 10 to 40 fs) a strong and broad peak around 0.24 PHz is visible in the Fourier spectrogram. For this reason the data have been fitted

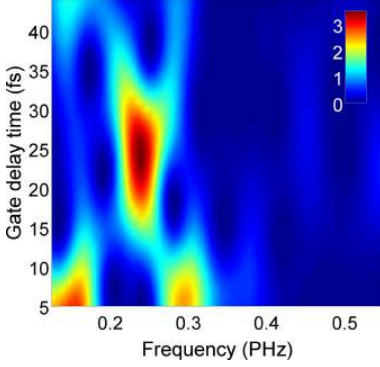


Fig. 6. Fourier sliding-window analysis of the experimental data.

with a sinusoidal function of frequency 0.234 PHZ (oscillation period of 4.3 fs), with lower and upper confidence bounds of 0.229 and 0.238 PHZ, respectively.

#### IV. THEORETICAL METHOD AND DISCUSSION

We have then performed numerical simulations in order to analyse the ultrafast charge evolution after attosecond excitation. Due to the low intensity of the attosecond pump pulses used in the experiment, time-dependent first-order perturbation theory has been employed for the calculation of the ionization amplitudes at the end of the pulse ( $t = T$ ):

$$c_{\alpha\epsilon lm}(T) = -i \langle \Psi_{\alpha lm}(\epsilon, \vec{r}) | \vec{e} \cdot \vec{r} | \Psi_0(\vec{r}) \rangle \times \int_{-\infty}^T E(t) e^{i(E_\alpha + \epsilon - E_0)t} dt \quad (4)$$

where  $\Psi_0$  is the all-electron (called  $N$ -electron) ground state of phenylalanine with energy  $E_0$ ,  $\Psi_{\alpha lm}(\epsilon)$  is the  $N$ -electron continuum state, describing a photoelectron ejected from the  $\alpha$  molecular orbital with kinetic energy  $\epsilon$  and angular quantum numbers  $l$  and  $m$  ( $|m| \leq l$ ),  $E_\alpha$  is the energy of the corresponding cationic species and  $E(t)$  is the electric field of the XUV pulse polarized along the  $\vec{e}$  direction. The  $\Psi_0$  and  $\Psi_{\alpha lm}(\epsilon)$  wave functions have been evaluated in the framework of the fixed-nuclei approximation by using the static-exchange density functional theory (DFT) [33] method, which makes use of the Kohn–Sham (KS) DFT to describe molecular bound states and of the Galerkin approach to evaluate continuum wave functions in the field of the corresponding KS density. The LB94 functional [34] has been employed to account for exchange and correlation effects. In order to obtain reliable values of the ionization energies  $E_\alpha$ , we have employed the VWN [35] local density approximation functional within the Slater transition state procedure [36] using the ADF commercial program [37], [38] with a TZP basis set (taken from the ADF library). Bound and continuum states are evaluated in a multicentric basis set built with products of B-splines and spherical harmonics, as widely described in previous works [39], [40]. We use a large one-center expansion (OCE) placed at the center of mass of the molecule to accurately describe the asymptotic behavior of

the continuum states. To improve the convergence of the calculation for the description of the more localized bound states, the OCE is supplemented with  $N$  (number of atoms) small non-overlapping off-center expansions located at the nuclear positions. For phenylalanine, we obtain converged results using as radial parameters a OCE with a 30 a.u. radius and 23 off-center expansions extended up to 1 a.u. of radius. Because of the large size and the lack of symmetry in the phenylalanine molecule, we have included an angular expansion of 484 spherical harmonics (equivalently, angular momentum  $l \leq 20$  in Eq. (4)). The initial guess for the electronic density was generated with ADF [37], [38], and the molecular geometries of the different conformers were optimized at the DFT-B3LYP [41], [42] level with the 6–311 + g(3df,2p) basis set employing Gaussian09 computational package [43].

The electronic density of the ( $N-1$ )-electron cation can be calculated as [44], [45]

$$\rho_{\text{ion}}(\vec{r}, t) = \sum_{\alpha} \left( \sum_{\substack{\alpha' \\ \alpha' \neq \alpha}} \gamma_{\alpha'\alpha'}^{(\text{ion})} \right) \varphi_{\alpha}^2(\vec{r}) + \sum_{\substack{\alpha\alpha' \\ \alpha' \neq \alpha}} \gamma_{\alpha\alpha'}^{(\text{ion})} e^{i(E_{\alpha'} - E_{\alpha})t} \varphi_{\alpha}(\vec{r}) \varphi_{\alpha'}(\vec{r}) \quad (5)$$

where  $\varphi_{\alpha}(\vec{r})$  is the  $\alpha$  molecular orbital and  $\gamma_{\alpha\alpha'}^{(\text{ion})}$  is the reduced density matrix element defined as:

$$\gamma_{\alpha\alpha'}^{(\text{ion})} = \sum_{l,m} \int c_{\alpha lm}(\epsilon) c_{\alpha' lm}^*(\epsilon) d\epsilon. \quad (6)$$

We have neglected the interaction of the photoelectron with the remaining ( $N-1$ )-electron cation. The hole density is given by the difference between the electronic density of the neutral molecule, which does not depend on time, and the electronic density of the ion,  $\rho_{\text{hole}}(\vec{r}, t) = \rho_{\text{neutral}}(\vec{r}) - \rho_{\text{ion}}(\vec{r}, t)$ , and can be written as follows:

$$\rho_{\text{hole}}(\vec{r}, t) = \sum_{\alpha} \left( 1 - \sum_{\substack{\alpha' \\ \alpha' \neq \alpha}} \gamma_{\alpha'\alpha'}^{(\text{ion})} \right) \varphi_{\alpha}^2(\vec{r}) + \sum_{\substack{\alpha\alpha' \\ \alpha' \neq \alpha}} \gamma_{\alpha\alpha'}^{(\text{ion})} e^{i(E_{\alpha'} - E_{\alpha})t} \varphi_{\alpha}(\vec{r}) \varphi_{\alpha'}(\vec{r}) \quad (7)$$

where

$$\rho_{\text{neutral}}(\vec{r}) = \sum_{\alpha} \varphi_{\alpha}^2(\vec{r}). \quad (8)$$

Fig. 7 shows the calculated ionization energies of all open channels for the most abundant conformer of phenylalanine, according to previous theoretical work [46]. These energies are approximately given by the KS orbital energies resulting from the VWN-transition state calculations. For a given photon energy, all channels below that energy will be populated. We are thus creating a wavepacket containing all ionic states with ionization potentials below 35 eV. As illustrated in Fig. 7, 35 eV is the largest photon energy contained within the bandwidth of the attosecond pulses used in the experiment. Their relative contributions to the total wavepacket are given by both the pulse

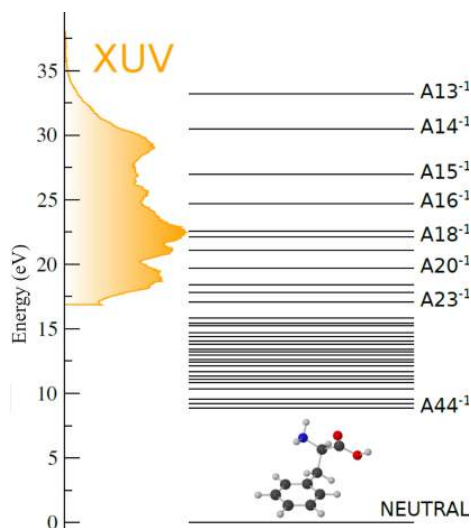


Fig. 7. Ionization potentials for the most abundant conformer of the phenylalanine molecule. The labels “An” denote the molecular orbital from which the electron is removed. The spectrum of the attosecond pulses used in the experiment and in the calculations is represented by a thick orange curve lying over a shaded area. All ionic states below the largest absorbed photon energy (35 eV) are being populated. Note, for instance, that for a photon of 25 eV all ionic states from A16<sup>-1</sup> to A44<sup>-1</sup> are accessible.

profile and the dipole couplings from the ground state of the neutral.

In order to test the validity of our description of the ionization process, we have first calculated the photoelectron spectra of phenylalanine for photon energies of 21.2 and 45 eV, by using the computed dipole transition matrix elements and ionization potentials, and we have compared our results with synchrotron [47] and He(I) [48], [49] radiation experiments. For the comparison with the experimental spectra available in the literature, we have convoluted our infinitely resolved lines with a Lorentzian function of 0.3-eV width at half maximum to account for the vibrational broadening and experimental energy resolution, which is rather limited in this and earlier experiments (the experiments cannot resolve the individual peaks). The comparison between theory and experiment is shown in Fig. 8. As can be seen, the agreement is reasonably good. We notice however that the experiment of Plekan *et al.* was performed at a photon energy of 100 eV, which is substantially higher than ours. Other two earlier experiments were performed at a photon energy of 21.2 eV [48], [49]. Our results are in better agreement with the most recent experiment, especially for binding energies below 15 eV, which includes the most relevant cationic states in the hole dynamics reported in the present work. The photoelectron spectra are expected to be more sensitive to the choice of photon energy as we approach the threshold. The ionization amplitudes can strongly vary with photon energy for values below 25–30 eV, while the variation becomes smoother for larger values [13]. This is most likely the reason to find a better agreement between the high-energy spectra.

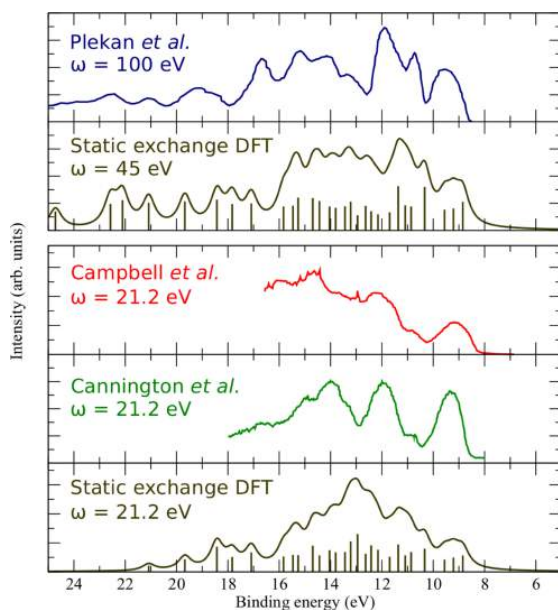


Fig. 8. Comparison between calculated and experimental photoelectron spectra of phenylalanine.

The electronic wavepacket generated by the attosecond pulse was then calculated from the ionization amplitudes, by using the experimental frequency spectrum of the pulse (shown in Fig. 7). Time zero in the simulation corresponds to the end of the attosecond pulse and the wavepacket evolution is calculated for positive times immediately after the prompt ionization. The evolution of the electronic wavepacket was then evaluated by using a standard time-dependent density matrix formalism [50], in which the system is described by a sum of single-particle Hamiltonians. Since in this work we consider ionization from the ground state, which has a pronounced single-determinant character, the effects related to 2-holes-1-particle (2h1p) states are expected to be much smaller. In ground state photoionization, 2h1p states are nevertheless not negligible in inner-valence shell ionization, as has been extensively studied by Breidbach and Cederbaum [51], but they are of minor importance in outer-valence ionization, which is the dominant process in our work. The latter conclusion is supported by photoelectron spectroscopy experiments in this and similar molecules, in which satellite lines associated to 2h1p states are always much weaker than those associated to 1h states. It is also supported by new theoretical calculations that we have carried out for glycine [52], in very good agreement with the results obtained by Kuleff *et al.* [53]. Therefore, in the range of photon energies leading to the cationic states relevant for the observed dynamics, we can safely conclude that 2h1p states do not play a significant role.

Every ionic state is related to a single Slater determinant with doublet spin multiplicity. However, this single determinant is not built from Hartree–Fock (HF) orbitals but from KS orbitals arising from DFT calculations. In complex non symmetric

molecules it often happens that there is a kind of “orbital rotation” upon ionization, expressed as a mixing of HF orbitals. This is reported, e.g., in the paper by Lünemann *et al.* [19]. However, this does not mean a breakdown of the one particle (1h) approximation for such states, just that the Dyson orbital, still of norm close to 1, is a linear combination of ground state HF orbitals. Since some correlation is built in the KS orbitals, they are generally closer to the correct Dyson orbitals than the HF ones. As mentioned above, this has been tested by reproducing the results by Kuleff *et al.* [53] for glycine outer valence ionizations [52]. The nature of the Dyson orbital can only be probed by evaluating dynamical properties, like photoionization cross sections, or electron momentum spectroscopy. This is additionally supported by the vast number of published studies of photoionization cross sections performed with the present approach, also in molecules of comparable complexity [54]–[63].

Due to the random orientation of the phenylalanine molecule, we calculated the hole dynamics resulting from excitation by pulses with the electric field polarized along three orthogonal directions, and the results were then averaged. Although no electron selection rules strictly apply, due the lack of global symmetry elements, of course approximate local symmetries will apply, depending on the localization of the initial orbital. For example, for an initial orbital of mainly  $\sigma$  ring character, a parallel polarization excites it to  $\sigma$  ring states, while a perpendicular one drives it to  $\pi$  final states, and similar considerations apply to initial orbitals mainly localized on other moieties ( $-\text{NH}_2$ ,  $-\text{COOH}$ , etc.). This explains why the results obtained for the different polarization directions,  $x$ ,  $y$  and  $z$ , are different.

We note that, in the particular case considered in this work, the Lebedev sampling method to average over molecular orientation [64], would lead to the same final result. Indeed, the reduced density matrix elements  $\gamma_{\alpha\alpha'}$  (reported in Eq. (6)) can be written as a function of the electron ejection direction ( $\Omega_e$ ) and the orientation of the molecule ( $\Omega_n$ ). For randomly oriented molecules and non-resolved electron ejection angles, one would have to integrate over both  $\Omega_e$  and  $\Omega_n$ . However, this integration would only affect the  $\gamma_{\alpha\alpha'}$  terms in Eq. (7), which contain products of amplitudes with the same angular momentum  $l$ , but different  $\alpha$  and  $\alpha'$ . So, if the symmetry of the channels  $\alpha$  and  $\alpha'$  is the same for all states (as in phenylalanine), the algebra to integrate the angular part of  $\gamma_{\alpha\alpha'}$  is exactly the same as the usual one to derive integrated cross sections (see [65] and references therein). This means that, in practice, it is enough to average the results obtained for three arbitrary but orthogonal orientations.

We have integrated the hole density around particular portions of the molecule. Fig. 9 shows the Fourier power spectra of the calculated hole density over various atoms of the molecule: the nitrogen atom of the amine group, the doubly bonded oxygen atom of the carboxylic group, two carbon atoms of the phenyl group and a non-aromatic carbon atom. Beating frequencies in agreement with the experimental observations were observed when the charge density was integrated around the amine group. The hole densities at different positions in the molecules do not show clear and clean frequency components (with the exception of the doubly bonded O atom in the carboxyl group, which however cannot be observed in the doubly-charged immonium fragment, which results from the loss of the carboxyl group).

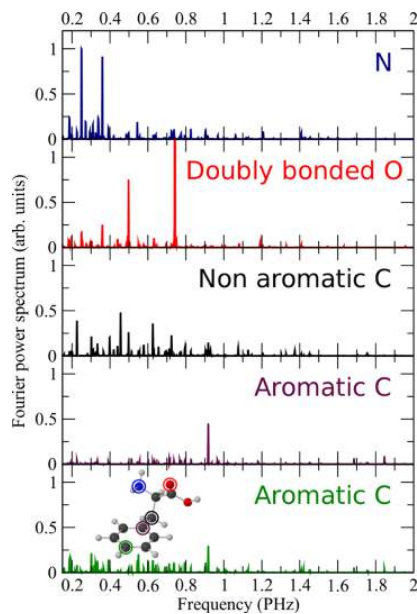


Fig. 9. Fourier power spectra of the calculated hole density integrated over various atoms of the phenylalanine molecule for the most abundant conformer.

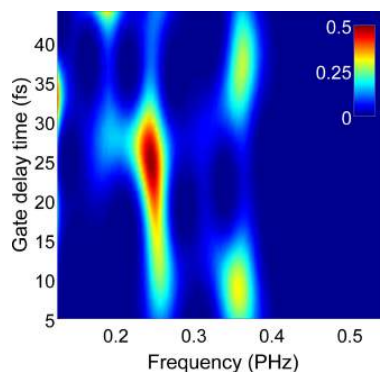


Fig. 10. Fourier sliding-window analysis of the calculated temporal evolution of hole density integrated over the amine group for the most abundant conformer of phenylalanine.

We note that the VIS/NIR probe pulse is not locally absorbed only by the amine group, but also by other sites of the molecule. However, the simulations indicate that the periodic modulations observed in the experiment are mainly related to the absorption of the probe pulse by the amine group. The charge dynamics around the amine group is then imprinted in the probe absorption. As shown in Fig. 9, a clear peak at 0.25 PHz is visible in Fourier power spectrum of the calculated hole density integrated around the amine group, in very good agreement with the pump-probe measurement. As discussed in [13], the sliding-window Fourier analysis of the numerical simulation, shown in Fig. 10, demonstrated that the main peak at 0.25 PHz forms in about 15 fs and disappears after about 35 fs, in agreement with the results of the Fourier analysis of the experimental data.

TABLE I  
VIBRATIONAL FREQUENCIES OF THE HOMO-1  
IONIC STATE OF PHENYLALANINE

Mode	Wavenumber ( $\text{cm}^{-1}$ )	Freq. (PHz)	Period (fs)
1	34.7	0.0010	961.5
2	55.2	0.0017	604.0
3	68.1	0.0020	489.7
4	92.6	0.0028	360.4
5	164.7	0.0049	202.5
6	218.5	0.0065	152.7
7	281.7	0.0084	118.4
8	339.8	0.0102	98.2
9	365.6	0.0110	91.2
10	384.7	0.0115	86.7
11	395.2	0.0118	84.4
12	409.4	0.0123	81.5
13	486.0	0.0146	68.6
14	503.6	0.0151	66.2
15	515.5	0.0155	64.7
16	554.4	0.0166	60.2
17	596.9	0.0179	55.9
18	631.1	0.0189	52.9
19	652.6	0.0196	51.1
20	676.3	0.0203	49.3
21	782.3	0.0235	42.6
22	791.3	0.0237	42.2
23	805.8	0.0242	41.4
24	833.5	0.0250	40.0
25	841.8	0.0252	39.6
26	913.8	0.0274	36.5
27	970.2	0.0291	34.4
28	999.9	0.0300	33.4
29	1015.9	0.0305	32.8
30	1026.7	0.0308	32.5
31	1032.0	0.0309	32.3
32	1070.2	0.0321	31.2
33	1090.9	0.0327	30.6
34	1109.3	0.0333	30.1
35	1149.9	0.0345	29.0
36	1172.1	0.0351	28.5
37	1188.6	0.0356	28.1
38	1207.6	0.0362	27.6
39	1245.9	0.0373	26.8
40	1286.9	0.0386	25.9
41	1294.8	0.0388	25.8
42	1341.3	0.0402	24.9
43	1362.7	0.0409	24.5
44	1370.8	0.0411	24.3
45	1437.8	0.0431	23.2
46	1470.8	0.0441	22.7
47	1490.9	0.0447	22.4
48	1509.2	0.0452	22.1
49	1542.7	0.0462	21.6
50	1610.1	0.0483	20.7
51	1621.0	0.0486	20.6
52	1832.2	0.0549	18.2
53	3077.5	0.0923	10.8
54	3093.9	0.0928	10.8
55	3150.0	0.0944	10.6
56	3173.8	0.0951	10.5
57	3178.7	0.0953	10.5
58	3188.6	0.0956	10.5
59	3200.2	0.0959	10.4
60	3206.1	0.0961	10.4
61	3524.4	0.1057	9.5
62	3674.4	0.1102	9.1
63	3730.9	0.1118	8.9

Wavenumber ( $\text{cm}^{-1}$ ), frequency (PHz) and corresponding periods (fs) of vibrational modes for the lowest cationic state of phenylalanine.

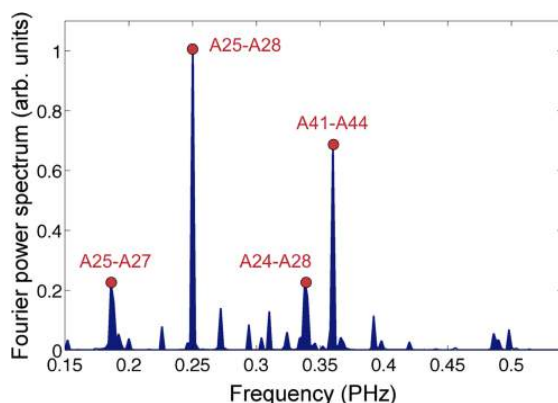


Fig. 11. Fourier power spectra of the hole density integrated over the amine group for the most abundant conformer of phenylalanine; we have identified the ionic states that are responsible for the most important beatings.

A higher frequency component is visible around 0.36 PHz in the delay intervals below 15 fs and above 30 fs. The temporal evolution of the main Fourier components is a consequence of the complex interplay among several beating processes initiated by the broad band excitation pulse. We note that the oscillation periods obtained from the experimental data and from the numerical simulations are shorter than the fastest vibrational period for the lowest cationic state of phenylalanine, which we have calculated by employing standard DFT-B3LYP quantum chemistry calculations (same procedure as for the geometry optimizations). The calculated vibrational frequencies are shown in Table I.

Of course we cannot claim that the relative intensities of the relevant beatings observed in the experiment can be explained by a theoretical calculation in which the probe step is not included (this may explain the discrepancies between measured and calculated peak intensities), but we can clearly identify that the observed beatings are unambiguously associated to charge fluctuations around the amine group, which in turn are associated to a small number of cationic states among all the accessible ones. Indeed, another important result of the numerical simulation is that it is possible to identify the ionic states that are responsible for the most important beatings. These are identified in Fig. 11, for the most abundant conformer. From the simulation it is possible to conclude that the main frequency peak around 0.25 PHz originates from a beating between two states that contain a hole in a molecular orbital that is highly delocalized (A25) and a second one that is more localized on the amine group (A28), shown in Fig. 12. Similarly, the frequency component around 0.36 PHz arises from an interference between two states (A41 and A44) that contain hole density on the amine and the carboxyl groups (see Fig. 12), which allows charge migration between the two sites. These interferences manifest as fluctuations in the electronic density on the amine group.

We have performed calculations for the six most populated conformers (see Fig. 13) at the temperature of the experiment (430 K), according to previous theoretical work [46]. The

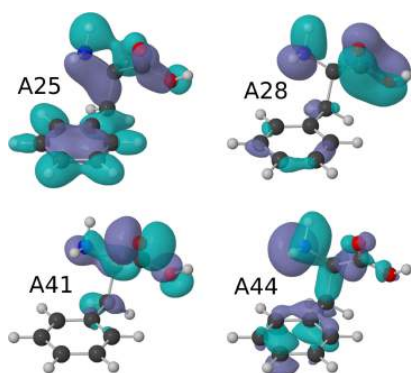


Fig. 12. Calculated KS orbitals of phenylalanine whose beating is mainly responsible of the Fourier peaks at 0.25 PHz (A25-A28) and 0.36 PHz (A41-A44).

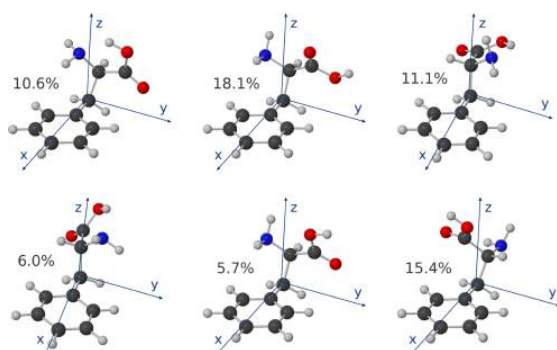


Fig. 13. Geometry of the most populated conformers of phenylalanine at the temperature of the experiment (430 K). Their relative populations are indicated as well as the 3 orthogonal orientations of the polarization vector of the electric field we have considered in the calculations.

corresponding Fourier spectra are shown in Fig. 14, together with the results for the thermal average (see bottom panel in Fig. 14) obtained by taking into account the relative populations given in [46]. For the most populated conformers (and therefore for the averaged results), the frequencies at which the dominant peaks appear are in good agreement with those observed experimentally.

From the pump-probe measurements and the numerical simulations it is possible to conclude that charge fluctuations moving across the molecular chain, which ultimately lead to charge localization, are extremely fast even for a molecule as large as phenylalanine; therefore, charge localization (spontaneous or forced by external factors) can occur in a similar or even shorter time scale. Moreover, we have demonstrated that these fluctuations, which are required for an ulterior localization of the charge, can be induced by an attosecond pulse in spite of its broad bandwidth and, therefore, its low selectivity. The consequence is that one does not need to start from a localized charge state to induce charge fluctuations over the whole molecule (as done in most previous theoretical works). All this shows that attosecond pulses not only have the appropriate temporal resolution to study charge transfer, but also induce the necessary

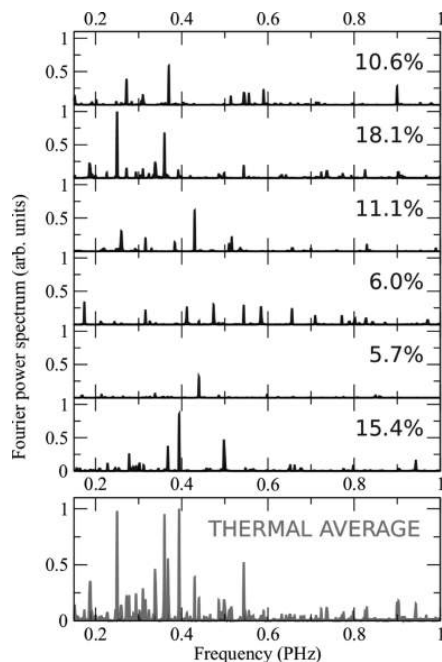


Fig. 14. Fourier power spectra of the hole density on the amine group for the most populated conformers, rescaled with their relative weights for a better illustration. The lower panel shows the averaged results.

charge fluctuations that are needed to force localization in a particular molecular site (e.g., by using an external electromagnetic field). The only remaining issue is how to extract more precise information about this last step (localization) by using a probe pulse as the one employed in the present work or others. Certainly this requires further investigations from the experimental and theoretical points of view.

## V. CONCLUSION

The observation of charge migration in complex molecular structures and, in particular, in biologically relevant molecules is one of the main targets of attosecond science. The investigation of charge evolution in these structures initiated by prompt ionization by attosecond pulses is important per se and for a better understanding of the interaction process between light and complex molecules. We adopted a novel methodology for the measurement of the charge migration process: we found that the yield of immonium dications is a particularly sensitive probe of charge location. Indeed, a clear ultrafast oscillation of the dication yield was measured, following the attosecond excitation, which we have unambiguously associated to the charge migration process within the investigated amino acid molecule. The results obtained in the case of phenylalanine can be seen as the first experimental confirmation that attosecond pulses and techniques are essential tools for understanding of dynamical processes on a temporal scale that is relevant for the evolution of crucial microscopic events at the heart of the macroscopic biological response of molecular complexes.

## REFERENCES

- [1] S. R. Leone *et al.*, "What will it take to observe processes in 'real time'?", *Nature Photon.*, vol. 8, no. 3, pp. 162–166, 2014.
- [2] F. Krausz and M. Ivanov, "Attosecond physics," *Rev. Mod. Phys.*, vol. 81, no. 1, pp. 163–234, 2009.
- [3] G. Sansone and M. Nisoli, "New frontiers in attosecond science," *Progr. Quantum Electr.*, vol. 33, no. 1, pp. 17–59, 2009.
- [4] A. H. Zewail, "Femtochemistry: Atomic-scale dynamics of the chemical bond," *J. Phys. Chem. A*, vol. 104, no. 24, pp. 5660–5694, 2000.
- [5] H. Gray and J. Winkler, "Electron tunneling through proteins," *Q. Rev. Biophys.*, vol. 36, pp. 341–372, 2003.
- [6] J. R. Winkler, H. B. Gray, T. R. Prytkova, I. V. Kurnikov, and D. N. Beratan, "Electron transfer through proteins," in *Bioelectronics*, I. Willner, E. Katz, Eds. Weinheim, Germany: Wiley-VCH Verlag, 2005, pp. 15–33.
- [7] F. Lépine, M. Y. Ivanov, and M. J. J. Vrakking, "Attosecond molecular dynamics: Fact or fiction?," *Nature Photon.*, vol. 8, no. 3, pp. 195–204, 2014.
- [8] G. Sansone *et al.*, "Electron localization following attosecond molecular photoionization," *Nature*, vol. 465, no. 7299, pp. 763–766, 2010.
- [9] F. Kelkensberg *et al.*, "Attosecond control in photoionization of hydrogen molecules," *Phys. Rev. Lett.*, vol. 107, no. 4, pp. 043002-1–043002-4, 2011.
- [10] W. Siu *et al.*, "Attosecond control of dissociative ionization of O<sub>2</sub> molecules," *Phys. Rev. A*, vol. 84, no. 6, pp. 063412-1–063412-4, 2011.
- [11] P. Ranitovic *et al.*, "Attosecond vacuum UV coherent control of molecular dynamics," *Proc. Nat. Acad. Sci. USA*, vol. 111, no. 3, pp. 912–917, 2014.
- [12] L. Belshaw *et al.*, "Observation of ultrafast charge migration in an amino acid," *J. Phys. Chem. Lett.*, vol. 3, no. 24, pp. 3751–3754, Dec. 2012.
- [13] F. Calegari *et al.*, "Ultrafast electron dynamics in phenylalanine initiated by attosecond pulses," *Science*, vol. 346, no. 6207, pp. 336–339, Oct. 2014.
- [14] L. S. Cederbaum and J. Zobeley, "Ultrafast charge migration by electron correlation," *Chem. Phys. Lett.*, vol. 307, no. 3/4, pp. 205–210, 1999.
- [15] F. Remacle and R. D. Levine, "An electronic time scale in chemistry," *Proc. Nat. Acad. Sci. USA*, vol. 103, no. 18, pp. 6793–6798, 2006.
- [16] R. Weinkauff, P. Schanen, D. Yang, S. Soukara, and E. W. Schlag, "Elementary processes in peptides: Electron mobility and dissociation in peptide cations in the gas phase," *J. Phys. Chem.*, vol. 99, no. 28, pp. 11255–11265, 1995.
- [17] R. Weinkauff *et al.*, "Highly efficient charge transfer in peptide cations in the gas phase: Threshold effects and mechanism," *J. Phys. Chem.*, vol. 100, no. 47, pp. 18567–18585, Nov. 1996.
- [18] S. Linnemann, A. I. Kuleff, and L. S. Cederbaum, "Charge migration following ionization in systems with chromophore-donor and amine-acceptor sites," *J. Chem. Phys.*, vol. 129, no. 10, pp. 104305-1–104305-12, 2008.
- [19] S. Linnemann, A. I. Kuleff, and L. S. Cederbaum, "Ultrafast charge migration in 2-phenylethyl-N,N-dimethylamine," *Chem. Phys. Lett.*, vol. 450, no. 4/6, pp. 232–235, 2008.
- [20] M. Nisoli, S. De Silvestri, and O. Svelto, "Generation of high energy 10 fs pulses by a new pulse compression technique," *Appl. Phys. Lett.*, vol. 68, no. 20, pp. 2793–2795, 1996.
- [21] M. Nisoli *et al.*, "Compression of high energy laser pulses below 5 fs," *Opt. Lett.*, vol. 22, no. 8, pp. 522–524, 1997.
- [22] A. Suda, M. Hatayama, K. Nagasaka, K. Midorikawa, "Generation of sub-10-fs, 5-mJ-optical pulses using a hollow fiber with a pressure gradient," *Appl. Phys. Lett.*, vol. 86, no. 11, pp. 111116-1–111116-3, 2005.
- [23] C. Vozzi *et al.*, "Advances in laser technology for isolated attosecond pulse generation," *Laser Phys. Lett.*, vol. 6, no. 4, pp. 259–267, 2009.
- [24] T. Oksenhendler *et al.*, "Self-referenced spectral interferometry," *Appl. Phys. B*, vol. 99, no. 1/2, pp. 7–12, 2010.
- [25] F. Lücking *et al.*, *Opt. Lett.*, vol. 39, no. 8, pp. 2302–2305, 2014.
- [26] F. Ferrari *et al.*, "High-energy isolated attosecond pulses generated by above-saturation few-cycle fields," *Nature Photon.*, vol. 4, pp. 875–879, no. 12, 2010.
- [27] G. Sansone, L. Poletto, and M. Nisoli, "High-energy attosecond light sources," *Nature Photon.*, vol. 5, no. 11, pp. 655–663, 2011.
- [28] Y. Mairesse and F. Quéré, "Frequency-resolved optical gating for complete reconstruction of attosecond bursts," *Phys. Rev. A*, vol. 71, no. 1, pp. 011401(R)-1–011401(R)-4, 2005.
- [29] G. Sansone *et al.*, "Isolated single-cycle attosecond pulses," *Science*, vol. 314, no. 5798, pp. 443–446, 2006.
- [30] L. Poletto, S. Bonora, M. Pascolini, and P. Villorosi, "Instrumentation for analysis and utilization of extreme-ultraviolet and soft x-ray high-order harmonics," *Rev. Sci. Instrum.*, vol. 75, no. 11, pp. 4413–4418, 2004.
- [31] C. R. Calvert *et al.*, "LIAD-fs scheme for studies of ultrafast laser interactions with gas phase biomolecules," *Phys. Chem. Chem. Phys.*, vol. 14, no. 18, pp. 6289–6297, 2012.
- [32] S. Boyden and J. Zhang, "Temperature and wavelength-dependent spectral absorptivities of metallic materials in the infrared," *J. Therm. Heat Transfer*, vol. 20, no. 1, pp. 9–15, 2006.
- [33] D. Toffoli, M. Stener, G. Fronzoni, and P. Decleva, "Convergence of the multicenter B-spline DFT approach for the continuum," *Chem. Phys.*, vol. 276, no. 1, pp. 25–43, 2002.
- [34] R. van Leeuwen and E. J. Baerends, "Exchange-correlation potential with correct asymptotic behavior," *Phys. Rev. A*, vol. 49, no. 4, pp. 2421–2431, 1994.
- [35] S. H. Vosko, L. Wilk, and M. Nusair, "Accurate spin-dependent electron liquid correlation energies for local spin density calculations: a critical analysis," *Can. J. Phys.*, vol. 58, no. 8, pp. 1200–1211, 1980.
- [36] J. C. Slater, "Statistical exchange-correlation in the self-consistent field," *Adv. Quantum Chem.*, vol. 6, pp. 1–92, 1972.
- [37] E. J. Baerends, D. E. Ellis, and P. Ros, "Self-consistent molecular Hartree-Fock-Slater calculations I. The computational procedure," *Chem. Phys.*, vol. 2, no. 1, pp. 41–51, 1973.
- [38] C. Fonseca Guerra, J. G. Snijders, G. te Velde, and E. J. Baerends, "Towards an order-N DFT method," *Theor. Chem. Acc.*, vol. 99, no. 6, pp. 391–403, 1998.
- [39] M. Stener, G. Fronzoni, P. Decleva, "Time dependent density functional study of the symmetry resolved N 1s photoionization in N<sub>2</sub>," *Chem. Phys. Lett.*, vol. 351, no. 5/6, pp. 469–474, 2002.
- [40] D. Toffoli, M. Stener, G. Fronzoni, and P. Decleva, "Convergence of the multicenter B-spline DFT approach for the continuum," *Chem. Phys.*, vol. 276, pp. 25–43, 2002.
- [41] C. Lee, W. Yang, and R. G. Parr, "Development of the Colle-Salvetti correlation-energy formula into a functional of the electron density," *Phys. Rev. B*, vol. 37, no. 2, pp. 785–789, 1988.
- [42] A. D. Becke, "Density-functional thermochemistry—Part III: The role of exact exchange," *J. Chem. Phys.*, vol. 98, no. 7, pp. 5648–5652, 1993.
- [43] M. J. Frisch *et al.*, Gaussian 09, Gaussian, Inc., Wallingford CT, Revised C01 edn., 2010.
- [44] K. Blum, *Density Matrix Theory and Applications*. (Springer Series in Atomic, Optical and Plasma Physics), Berlin, Germany: Springer-Verlag, vol. 64, 3rd ed., 2012.
- [45] N. Rohringer and R. Santra, "Multichannel coherence in strong-field ionization," *Phys. Rev. A*, vol. 79, no. 5, pp. 053402-1–053402-10, May 2009.
- [46] Z. Huang, W. Yu, and Z. Lin, "Exploration of the full conformational landscapes of gaseous aromatic amino acid phenylalanine: An ab-initio study," *J. Mol. Struct. (Theochem)*, vol. 758, no. 2/3, pp. 195–202, 2006.
- [47] O. Plekan, V. Feyer, R. Richter, M. Coreno, and K. C. Prince, "Valence photoionization and photofragmentation of aromatic amino acids," *Mol. Phys.*, vol. 106, no. 9/10, pp. 1143–1153, 2008.
- [48] S. Campbell *et al.*, "Proton affinities and photoelectron spectra of phenylalanine and N-Methyl- and N,N-Dimethylphenylalanine. Correlation of lone pair ionization energies with proton affinities and implications for N-Methylation as a method to effect site specific protonation of peptides," *J. Amer. Chem. Soc.*, vol. 116, no. 14, pp. 5257–5264, 1994.
- [49] P. H. Cannington and N. S. Ham, "He(I) and He(II) photoelectron spectra of glycine and related molecules," *J. Electron. Spectrosc. Relat. Phenom.*, vol. 32, no. 2, pp. 139–151, 1983.
- [50] E. Goulielmakis *et al.*, "Real-time observation of valence electron motion," *Nature*, vol. 466, no. 7307, pp. 739–743, Aug. 2010.
- [51] J. Breidbach and L. S. Cederbaum, "Migration of holes: Formalism, mechanisms, and illustrative applications," *J. Chem. Phys.*, vol. 118, no. 9, pp. 3983–3996, 2003.
- [52] F. Martín, private communication, Sep. 2014.
- [53] A. I. Kuleff, J. Breidbach, and L. S. Cederbaum, "Multielectron wavepacket propagation: General theory and application," *J. Chem. Phys.*, vol. 123, no. 4, pp. 044111-1–044111-10, 2005.
- [54] M. Stener *et al.*, "Photoabsorption and S 2p photoionization of the SF<sub>6</sub> molecule: Resonances in the excitation energy range of 200–280 eV," *J. Chem. Phys.*, vol. 134, no. 17, pp. 174311-1–174311-9, 2011.
- [55] D. Catone *et al.*, "Resonant circular dichroism of chiral metal-organic complex," *Phys. Rev. Lett.*, vol. 108, no. 8, pp. 083001-1–083001-5, 2012.
- [56] L. Argenti *et al.*, "Double-slit experiment with a polyatomic molecule: Vibrationally-resolved C 1s photoelectron spectra of acetylene," *New J. Phys.*, vol. 14, no. 3, p. 033012, 2012.
- [57] S. Turchini *et al.*, "Conformational sensitivity in photoelectron circular dichroism of 3-methylcyclopentanone," *Chem. Phys. Chem.*, vol. 14, no. 8, pp. 1723–1732, 2013.



- [58] R. K. Kushawaha *et al.*, "From double-slit interference to structural information in simple hydrocarbons," *Proc. Nat. Acad. Sci. USA*, vol. 110, no. 38, pp. 15201–15206, 2013.
- [59] K. Ueda *et al.*, "Intramolecular photoelectron diffraction in the gas phase," *J. Chem Phys.*, vol. 139, no. 12, pp. 124306-1–124306-6, 2013.
- [60] D. M. P. Holland, D. A. Shaw, S. Coriani, M. Stener, and P. Decleva, "A study of the valence shell electronic states of pyridazine by photoabsorption spectroscopy and time-dependent density functional theory calculations," *J. Phys. B, At. Mol. Opt. Phys.*, vol. 46, no. 17, pp. 175103-1–175103-15, 2013.
- [61] E. Plesiat, P. Decleva, and F. Martín, "Relationship between polarization-averaged molecular-frame photoelectron angular distributions and geometry," *Phys. Rev. A*, vol. 88, no. 6, pp. 063409-1–063409-5, 2013.
- [62] R. Boll *et al.*, "Femtosecond photoelectron diffraction on laser-aligned molecules: Towards time-resolved imaging of molecular structure," *Phys. Rev. A*, vol. 88, no. 6, pp. 061402-1–061402-5, 2013.
- [63] M. Stener, P. Decleva, T. Mizuno, H. Yoshida, and A. Yagishita, "Off-resonance photoemission dynamics studied by recoil frame FIs and CIs photoelectron angular distributions of CH<sub>3</sub>F," *J. Chem. Phys.*, vol. 140, no. 4, pp. 044305-1–044305-14, 2014.
- [64] V. I. Lebedev, "Values of the nodes and weights of ninth to seventeenth order gauss-markov quadrature formulae invariant under the octahedron group with inversion," *Zh. Vychisl. Mat. Mat. Fiz.*, vol. 15, no. 1, pp. 48–54, 1975.
- [65] D. Dill, "Fixed-molecule photoelectron angular distributions," *J. Chem. Phys.*, vol. 65, no. 3, pp. 1130–1133, 1976.



**Louise Belshaw** was born in Lisburn, Northern Ireland, in 1988. She received the M.Sci. degree in physics from the Queen's University Belfast, Belfast, U.K., in 2010 and the Ph.D. degree in "Ultrafast Molecular Dynamics" from the same institution in 2013. She is currently training to become a Clinical Scientist in the Medical Physics Department, the Belfast Health and Social Care Trust.



**Simone De Camillis** was born in Teramo, Italy, in 1988. He received the Master's degree in plasma physics from the University of Pisa, Pisa, Italy, in 2013, investigating the generation of plasma instabilities in the solar wind-magnetosphere interaction region. He is currently working toward the Ph.D. degree at Queen's University Belfast focusing on ultrafast intramolecular dynamics and charge transfers initiated by femtosecond or attosecond pulses.



**Francesca Calegari** was born in Milan, Italy, in 1981. She received the Master's degree (*cum laude*) from Università degli Studi di Milano, Milano, Italy, in 2005, and the Ph.D. degree from Politecnico di Milano, Milano, in 2009. She was a Postdoctoral Researcher with CNR-INFN until 2010 and with Politecnico di Milano until 2011. In 2010, she was a short-term Visiting Scientist at FOM Institute AMOLF, Amsterdam, The Netherlands. Since 2012, she has been a Researcher at CNR-IFN, Milan, and a Contract Professor of physics at Politecnico di Milano.

She is currently a Visiting Scientist at MPSD-CFEL, Hamburg, Germany. She is a co-author of more than 50 research papers in international journals. Her current research interests include attosecond science, ultrafast laser technology, control of electron dynamics in complex molecules. She received a European Research Council Starting Grant in 2014.



**Fabio Frassetto** was born in Treviso, Italy, in 1977. He received the Master's degree in physics in 2002, and the Ph.D. degree from the "Center of Studies and Activities for Space-G. Colombo" in 2006, both from Università di Padova, Padova, Italy. After some Postdoctoral positions at the National Research Council - Institute for Photonics and Nanotechnologies, CNR-IFN of Padova, he has currently a temporary position as Researcher at CNR-IFN. He is author/coauthor of more than 100 research papers/proceedings in international journals. His research activities include the design, realization, and characterization of diagnostic instrumentation for Free Electron Laser facilities and High Harmonic Generation beam lines for ultrafast experiments.



**David Ayuso** received the Graduate degree in chemistry from Universidad de Zaragoza, Zaragoza, Spain, in 2011, and the Master's degree in theoretical chemistry and computational modeling from Universidad Autónoma de Madrid, Madrid, Spain, in 2013, investigating the interaction of small molecules with synchrotron radiation. He is currently working toward the Ph.D. degree and his research is mainly focused on the theoretical description of vibrationally resolved photoionization processes and ultrafast electron dynamics in molecules initiated upon interaction with

synchrotron radiation and/or attosecond pulses.



**Andrea Trabattoni** was born in Saronno, Italy, in 1987. He received the Graduate degree in theoretical physics in 2011, investigating the symmetry properties of photonic quasicrystals. Since 2011, he has been working toward the Ph.D. degree at the Department of Physics - Politecnico di Milano, Milano, Italy. His research interests include the development of attosecond laser sources and the application of attosecond technology to the investigation of ultrafast electron dynamics in complex systems, such as nanoparticles and biologically relevant molecules.



**Luca Poletto** was born in Vicenza, Italy, in 1968. He received the Master's degree (*cum laude*) in 1993 and the Ph.D. degree from University of Padova, Padova, Italy, in 1996. From 1999 to 2006, he was a Research Scientist of the National Institute for the Physics of Matter, Italy. Since 2007, he has been Senior Research Scientist of the Institute of Photonics and Nanotechnologies, National Research Council, Italy. Since 2009, he has been the Director of the Division of Padova of the Institute. He is a co-author of more than 150 research papers in international

journals. His research activities include ultrafast optics in extreme-ultraviolet spectral region for synchrotron radiation, free-electron lasers and high-order laser harmonics, generation and handling of attosecond pulses, laser absorption spectroscopy for gas detection.



**Alicia Palacios** was born in Tomelloso, Spain, in 1979. She received the Graduate degree in chemistry in 2001 and the Ph.D. degree in 2006 both from the Universidad Autónoma de Madrid, Madrid, Spain. She completed her education with several stays in the Université Bordeaux I, and a long-term Postdoctoral fellowship (2006–2009) in Lawrence Berkeley National Lab, Berkeley, CA, USA. She is currently an Assistant Professor at the Universidad Autónoma de Madrid. She has published more than 40 peer-reviewed articles in international journals working

on atomic and molecular physics, in particular, developing new *ab initio* time-dependent treatments for the description of atoms and molecules subject to ultrashort intense laser pulses. She received the Marie Curie Integration Grant (ATTOTREND) as a Fellow Researcher.

**Piero Decleva** was at the Department of Chemistry, University of Trieste, where he became a Lecturer in theoretical chemistry in 1976, an Associate Professor of quantum chemistry from 1982 to 1994, and then a Full Professor of chemical physics till present. He is author of 240 research papers in international journals. His research covered theoretical description of many-body effects and electron cross sections in molecular photoionization, with many collaborations with leading experimental groups. A large molecular code for the calculation of dynamical photoionization observables has been developed in Trieste, with recent emphasis on ultrashort time dependent phenomena and strong field ionization.



**Jason B. Greenwood** was born in Belfast, Northern Ireland, in 1970. He received the Bachelor's degree from Oxford University, Oxford, U.K., in 1991 and the Ph.D. degree from Queen's University Belfast, Belfast, U.K., in 1995. After two years at NASA's Jet Propulsion Laboratory in Pasadena, CA, USA, he returned to Queen's for a lectureship in 1999, becoming a Senior Lecturer in 2006. He is author of more than 70 research papers in international journals in areas including electron-ion and ion-atom/molecule collisions, X-ray emission from solar wind-cometary

gas interactions, intense laser interactions with atoms and molecules, and ultrafast intramolecular dynamics.



**Fernando Martín** was born in Madrid, Spain, in 1961. He received the Graduate degree in chemistry in 1984 and physics from the Universidad Autónoma de Madrid, Madrid, in 1986, where he also received the Ph.D. degree in 1986. He completed his postdoctoral studies from the University of Bordeaux, Talence, France, in 1988, the Université de Paris VI from 1989 to 1990, and the University of Chicago from 1995 to 1996). He has been a Full Professor at the Universidad Autónoma de Madrid since 2005.

His research interests include theoretical modeling of photoexcitation and photoionization of atomic and molecular systems induced by synchrotron radiation and ultrashort laser pulses, as well as of complex molecular systems, isolated or deposited on surfaces. He has published more than 350 articles and, in 2011, he received Advanced Grant from the European Research Council.



**Mauro Nisoli** was born in Bergamo, Italy, in 1965. From 1990 to 2000, he was a Researcher of the National Research Council, Center of Quantum Electronic and Electronic Instrumentation. From 2001 to 2010, he was an Associate Professor with the Department of Physics, Politecnico di Milano, where he is currently a Full Professor. He is author of more than 170 research papers in international journals, 1 patent, several invited and tutorial communications at international meetings and schools. His research interests include attosecond science, ultrashortpulse

laser technology, control and real-time observation of electronic motion in atoms and molecules. He received European Research Council Advanced Grant in 2009.

# Bibliography

- [1] Ahmed H. Zewail. Femtochemistry: atomic-scale dynamics of the chemical bond. *The Journal of Physical Chemistry A*, 104(24):5660–5694, 2000.
- [2] Ahmed H. Zewail. *Pure and Applied Chemistry*, volume 72, chapter Femtochemistry: past, present, and future, page 2219. 2015 2000.
- [3] Nobelprize.org. Press release: The 1999 nobel prize in chemistry. 1999.
- [4] L. Lehr, T. Horneff, R. Weinkauff, and E. W. Schlag. Femtosecond dynamics after ionization: 2-phenylethyl-N,N-dimethylamine as a model system for nonresonant downhill charge transfer in peptides. *The Journal of Physical Chemistry A*, 109(36):8074–8080, 2005. PMID: 16834192.
- [5] M. Hentschel, R. Kienberger, Ch. Spielmann, G. A. Reider, N. Milosevic, T. Brabec, P. Corkum, U. Heinzmann, M. Drescher, and F. Krausz. Attosecond metrology. *Nature*, 414(6863):509–513, Nov 2001.
- [6] P. M. Paul, E. S. Toma, P. Breger, G. Mullot, F. Augé, Ph. Balcou, H. G. Muller, and P. Agostini. Observation of a train of attosecond pulses from high harmonic generation. *Science*, 292(5522):1689–1692, 2001.
- [7] A. McPherson, G. Gibson, H. Jara, U. Johann, T. S. Luk, I. A. McIntyre, K. Boyer, and C. K. Rhodes. Studies of multiphoton production of vacuum-ultraviolet radiation in the rare gases. *J. Opt. Soc. Am. B*, 4(4):595–601, Apr 1987.
- [8] M. Ferray, A. L’Huillier, X. F. Li, L. A. Lompre, G. Mainfray, and C. Manus. Multiple-harmonic conversion of 1064 nm radiation in rare gases. *Journal of Physics B: Atomic, Molecular and Optical Physics*, 21(3):L31, 1988.

- 
- [9] P. B. Corkum. Plasma perspective on strong field multiphoton ionization. *Physical Review Letters*, 71:1994–1997, Sep 1993.
- [10] Pierre Agostini and Louis F. DiMauro. The physics of attosecond light pulses. *Reports on Progress in Physics*, 67(6):813, 2004.
- [11] Ferenc Krausz and Misha Ivanov. Attosecond physics. *Reviews of Modern Physics*, 81:163–234, Feb 2009.
- [12] J. Itatani, F. Quéré, G. L. Yudin, M. Yu. Ivanov, F. Krausz, and P. B. Corkum. Attosecond streak camera. *Physical Review Letters*, 88:173903, Apr 2002.
- [13] G. Sansone, E. Benedetti, F. Calegari, C. Vozzi, L. Avaldi, R. Flammini, L. Poletto, P. Villoresi, C. Altucci, R. Velotta, S. Stagira, S. De Silvestri, and M. Nisoli. Isolated single-cycle attosecond pulses. *Science*, 314(5798):443–446, 2006.
- [14] E. Goulielmakis, M. Schultze, M. Hofstetter, V. S. Yakovlev, J. Gagnon, M. Uiberacker, A. L. Aquila, E. M. Gullikson, D. T. Attwood, R. Kienberger, F. Krausz, and U. Kleineberg. Single-cycle nonlinear optics. *Science*, 320(5883):1614–1617, 2008.
- [15] Kun Zhao, Qi Zhang, Michael Chini, Yi Wu, Xiaowei Wang, and Zenghu Chang. Tailoring a 67 attosecond pulse through advantageous phase-mismatch. *Optics Letters*, 37(18):3891–3893, Sep 2012.
- [16] P. B. Corkum and Ferenc Krausz. Attosecond science. *Nature Physics*, 3(6):381–387, Jun 2007.
- [17] Thomas Schultz and Marc Vrakking. *Attosecond and XUV Physics: Ultrafast Dynamics and Spectroscopy*. Wiley-VCH, 2013.
- [18] Alicia Palacios, José Luis Sanz-Vicario, and Fernando Martín. Theoretical methods for attosecond electron and nuclear dynamics: applications to the H<sub>2</sub> molecule. *Journal of Physics B: Atomic, Molecular and Optical Physics*, 48(24):242001, 2015.

- 
- [19] M. Drescher, M. Hentschel, R. Kienberger, M. Uiberacker, V. Yakovlev, A. Scrinzi, Th. Westerwalbesloh, U. Kleineberg, U. Heinzmann, and F. Krausz. Time-resolved atomic inner-shell spectroscopy. *Nature*, 419(6909):803–807, Oct 2002.
- [20] M. Uiberacker, Th. Uphues, M. Schultze, A. J. Verhoef, V. Yakovlev, M. F. Kling, J. Rauschenberger, N. M. Kabachnik, H. Schroder, M. Lezius, K. L. Kompa, H.-G. Muller, M. J. J. Vrakking, S. Hendel, U. Kleineberg, U. Heinzmann, M. Drescher, and F. Krausz. Attosecond real-time observation of electron tunnelling in atoms. *Nature*, 446(7136):627–632, Apr 2007.
- [21] M. Schultze, M. Fie, N. Karpowicz, J. Gagnon, M. Korbman, M. Hofstetter, S. Neppl, A. L. Cavalieri, Y. Komninos, Th. Mercouris, C. A. Nicolaides, R. Pazourek, S. Nagele, J. Feist, J. Burgdörfer, A. M. Azzeer, R. Ernstorfer, R. Kienberger, U. Kleineberg, E. Goulielmakis, F. Krausz, and V. S. Yakovlev. Delay in photoemission. *Science*, 328(5986):1658–1662, 2010.
- [22] K. Klünder, J. M. Dahlström, M. Gisselbrecht, T. Fordell, M. Swoboda, D. Guénot, P. Johnsson, J. Caillat, J. Mauritsson, A. Maquet, R. Taïeb, and A. L’Huillier. Probing single-photon ionization on the attosecond time scale. *Physical Review Letters*, 106:143002, Apr 2011.
- [23] Eleftherios Goulielmakis, Zhi-Heng Loh, Adrian Wirth, Robin Santra, Nina Rohringer, Vladislav S. Yakovlev, Sergey Zherebtsov, Thomas Pfeifer, Abdallah M. Azzeer, Matthias F. Kling, Stephen R. Leone, and Ferenc Krausz. Real-time observation of valence electron motion. *Nature*, 466(7307):739–743, Aug 2010.
- [24] A. L. Cavalieri, N. Muller, Th. Uphues, V. S. Yakovlev, A. Baltuska, B. Horvath, B. Schmidt, L. Blumel, R. Holzwarth, S. Hendel, M. Drescher, U. Kleineberg, P. M. Echenique, R. Kienberger, F. Krausz, and U. Heinzmann. Attosecond spectroscopy in condensed matter. *Nature*, 449(7165):1029–1032, Oct 2007.
- [25] Agustin Schiffrin, Tim Paasch-Colberg, Nicholas Karpowicz, Vadym Apalkov, Daniel Gerster, Sascha Muhlbrandt, Michael Korbman, Joachim Reichert, Martin Schultze, Simon Holzner, Johannes V. Barth, Reinhard

- 
- Kienberger, Ralph Ernstorfer, Vladislav S. Yakovlev, Mark I. Stockman, and Ferenc Krausz. Optical-field-induced current in dielectrics. *Nature*, 493(7430):70–74, Jan 2013.
- [26] G. Sansone, F. Kelkensberg, J. F. Perez-Torres, F. Morales, M. F. Kling, W. Siu, O. Ghafur, P. Johnsson, M. Swoboda, E. Benedetti, F. Ferrari, F. Lepine, J. L. Sanz-Vicario, S. Zherebtsov, I. Znakovskaya, A. L’Huillier, M. Yu Ivanov, M. Nisoli, F. Martín, and M. J. J. Vrakking. Electron localization following attosecond molecular photoionization. *Nature*, 465(7299):763–766, Jun 2010.
- [27] F. Kelkensberg, W. Siu, J. F. Pérez-Torres, F. Morales, G. Gademann, A. Rouzée, P. Johnsson, M. Lucchini, F. Calegari, J. L. Sanz-Vicario, F. Martín, and M. J. J. Vrakking. Attosecond control in photoionization of hydrogen molecules. *Physical Review Letters*, 107:043002, Jul 2011.
- [28] W. Siu, F. Kelkensberg, G. Gademann, A. Rouzée, P. Johnsson, D. Dowek, M. Lucchini, F. Calegari, U. De Giovannini, A. Rubio, R. R. Lucchese, H. Kono, F. Lépine, and M. J. J. Vrakking. Attosecond control of dissociative ionization of O<sub>2</sub> molecules. *Physical Review A*, 84:063412, Dec 2011.
- [29] Predrag Ranitovic, Craig W. Hogle, Paula Rivire, Alicia Palacios, Xiao-Ming Tong, Nobuyuki Toshima, Alberto González-Castrillo, Leigh Martin, Fernando Martín, Margaret M. Murnane, and Henry Kapteyn. Attosecond vacuum UV coherent control of molecular dynamics. *Proceedings of the National Academy of Sciences*, 111(3):912–917, 2014.
- [30] Franck Lepine, Misha Y. Ivanov, and Marc J. J. Vrakking. Attosecond molecular dynamics: fact or fiction? *Nature Photonics*, 8(3):195–204, Mar 2014. Review.
- [31] F. Remacle and R. D. Levine. An electronic time scale in chemistry. *Proceedings of the National Academy of Sciences*, 103(18):6793–6798, May 2006.
- [32] Lorenz S. Cederbaum and J. Zobeley. Ultrafast charge migration by electron correlation. *Chemical Physics Letters*, 307(3-4):205–210, 1999.

- 
- [33] J. Breidbach and L. S. Cederbaum. Migration of holes: formalism, mechanisms, and illustrative applications. *The Journal of Chemical Physics*, 118(9), 2003.
- [34] J. Breidbach and L. S. Cederbaum. Universal attosecond response to the removal of an electron. *Physical Review Letters*, 94:033901, Jan 2005.
- [35] Holger Hennig, Jörg Breidbach, and Lorenz S. Cederbaum. Electron correlation as the driving force for charge transfer: charge migration following ionization in N-methyl acetamide. *The Journal of Physical Chemistry A*, 109(3):409–414, 2005. PMID: 16833360.
- [36] R. Weinkauff, P. Aicher, G. Wesley, J. Grotemeyer, and E. W. Schlag. Femtosecond versus nanosecond multiphoton ionization and dissociation of large molecules. *The Journal of Physical Chemistry*, 98(34):8381–8391, 1994.
- [37] R. Weinkauff, P. Schanen, D. Yang, S. Soukara, and E. W. Schlag. Elementary processes in peptides: electron mobility and dissociation in peptide cations in the gas phase. *The Journal of Physical Chemistry*, 99(28):11255–11265, 1995.
- [38] R. Weinkauff, P. Schanen, A. Metsala, E. W. Schlag, M. Bürgle, and H. Kessler. Highly efficient charge transfer in peptide cations in the gas phase: threshold effects and mechanism. *The Journal of Physical Chemistry*, 100(47):18567–18585, 1996.
- [39] Louise Belshaw, Francesca Calegari, Martin J. Duffy, Andrea Trabattoni, Luca Poletto, Mauro Nisoli, and Jason B. Greenwood. Observation of ultrafast charge migration in an amino acid. *The Journal of Physical Chemistry Letters*, 3(24):3751–3754, 2012. PMID: 26291106.
- [40] J. Wals, H. H. Fielding, J. F. Christian, L. C. Snoek, W. J. van der Zande, and H. B. van Linden van den Heuvell. Observation of Rydberg wave packet dynamics in a coulombic and magnetic field. *Physical Review Letters*, 72:3783–3786, Jun 1994.
- [41] J. D. Jackson. *Classical electrodynamics*. Wiley, 1975.

- 
- [42] F. R. Elder, A. M. Gurewitsch, R. V. Langmuir, and H. C. Pollock. Radiation from electrons in a synchrotron. *Physical Review*, 71:829–830, Jun 1947.
- [43] Donald H. Bilderback, Pascal Elleaume, and Edgar Weckert. Review of third and next generation synchrotron light sources. *Journal of Physics B: Atomic, Molecular and Optical Physics*, 38(9):S773, 2005.
- [44] Gerard K. O’Neill. Storage-ring synchrotron: Device for high-energy physics research. *Physical Review*, 102:1418–1419, Jun 1956.
- [45] Ros Herman. Structure experiment ring is light on cash. *New Scientist*, 84(1171):357, November.
- [46] Ros Herman. Daresbury: tunable radiation for research. *New Scientist*, 87(1211):310, July.
- [47] D. J. Holder, P. D. Quinn, and N. G. Wyles. The SRS at Daresbury Laboratory: a Eulogy to the World’s First Dedicated High-energy Synchrotron Radiation Source. *11<sup>th</sup> European Particle Accelerator Conference*, 2008.
- [48] H. Baumgaertel. Bessy - the Berlin electron storage ring. 29(7):440–444, 1981.
- [49] Herman Winick, George Brown, Klaus Halbach, and John Harris. Wiggler and undulator magnets. *Physics Today*, 34:50–63, 1981.
- [50] Åke Kvik. Special issue synchrotron radiation and inorganic crystallography the european synchrotron radiation facility - an overview of planned diffraction capability. *Journal of Physics and Chemistry of Solids*, 52(10):1307–1312, 1991.
- [51] Freddy Adams. Opening ceremony of the European Synchrotron Radiation Facility (ESRF). *Journal of Analytical Atomic Spectrometry*, 10:12N–13N, 1995.
- [52] Y. Gohshi and H. Saisho. Preface. In H. Saisho and Y. Gohshi, editors, *Applications of Synchrotron Radiation to Materials Analysis*, volume 7 of *Analytical Spectroscopy Library*. Elsevier, 1996.



- 
- [53] R. Lewis. Medical applications of synchrotron radiation x-rays. *Physics in Medicine and Biology*, 42(7):1213, 1997.
- [54] R. Caciuffo, S. Melone, F. Rustichelli, and A. Boeuf. Monochromators for X-ray synchrotron radiation. *Physics Reports*, 152(1):1–71, 1987.
- [55] R. Stumm von Bordwehr. A history of X-ray absorption fine structure. *Annales de Physique*, 14(4):377–465, 1989.
- [56] Edward A. Stern. Musings about the development of XAFS. *Journal of Synchrotron Radiation*, 8(2):49–54, Mar 2001.
- [57] Irène Nenner and Paul Morin. Electronic and nuclear relaxation of core-excited molecules. In *VUV and Soft X-ray Photoionization*, Physics of Atoms and Molecules, pages 291–354. Springer US, 1996.
- [58] Renaud Guillemin, Wayne C. Stolte, and Dennis W. Lindle. Fragmentation of formic acid following photoexcitation around the carbon K edge. *Journal of Physics B: Atomic, Molecular and Optical Physics*, 42(12):125101, 2009.
- [59] E. Shigemasa, K. Ueda, Y. Sato, T. Sasaki, and A. Yagishita. Symmetry-resolved K-shell photoabsorption spectra of free N<sub>2</sub> molecules. *Physical Review A*, 45:2915–2921, Mar 1992.
- [60] T. X. Carroll, N. Berrah, J. Bozek, J. Hahne, E. Kukk, L. J. Sæthre, and T. D. Thomas. Carbon 1s photoelectron spectrum of methane: vibrational excitation and core-hole lifetime. *Physical Review A*, 59:3386–3393, May 1999.
- [61] T. X. Carroll, J. Hahne, T. D. Thomas, L. J. Sæthre, N. Berrah, J. Bozek, and E. Kukk. Carbon 1s core-hole lifetime in CO<sub>2</sub>. *Physical Review A*, 61:042503, Mar 2000.
- [62] M. Jurvansuu, A. Kivimäki, and S. Aksela. Inherent lifetime widths of Ar  $2p^{-1}$ , Kr  $3d^{-1}$ , Xe  $3d^{-1}$ , and Xe  $4d^{-1}$  states. *Physical Review A*, 64:012502, Jun 2001.

- 
- [63] K. J. Børve, L. J. Sæthre, T. D. Thomas, T. X. Carroll, N. Berrah, J. D. Bozek, and E. Kukk. Vibronic structure in the carbon  $1s$  photoelectron spectra of HCCH and DCCD. *Physical Review A*, 63:012506, Dec 2000.
- [64] Catalin Miron, Christophe Nicolas, Oksana Travnikova, Paul Morin, Yiping Sun, Faris Gel'mukhanov, Nobuhiro Kosugi, and Victor Kimberg. Imaging molecular potentials using ultrahigh-resolution resonant photoemission. *Nature Physics*, 8(2):135–138, Feb 2012.
- [65] R. Püttner, V. Pennanen, T. Matila, A. Kivimäki, M. Jurvansuu, H. Aksela, and S. Aksela. Refinement in the analysis of molecular Auger electron spectra: the  $2p^{-1} \rightarrow 3p\pi^{-2}$  spectra of HCl and DCl. *Physical Review A*, 65:042505, Mar 2002.
- [66] B. Kämmerling and V. Schmidt. Complete fragmentation pattern for two-step double photoionization in xenon. *Physical Review Letters*, 67:1848–1851, Sep 1991.
- [67] K. Ueda, Y. Shimizu, H. Chiba, Y. Sato, M. Kitajima, H. Tanaka, and N. M. Kabachnik. Experimental determination of Auger-decay amplitudes from the angular correlations in Auger cascade following the  $2p \rightarrow 4s$  photoexcitation in Ar. *Physical Review Letters*, 83:5463–5466, Dec 1999.
- [68] R. Wehlitz, L. S. Pibida, J. C. Levin, and I. A. Sellin. Observation of angular correlation between subsequently emitted Auger electrons. *Physical Review A*, 59:421–426, Jan 1999.
- [69] P. Lablanquie, F. Penent, R. I. Hall, H. Kjeldsen, J. H. D. Eland, A. Muehleisen, P. Pelicon, Z. Šmit, M. Zitnik, and F. Koike. Coster-Kronig decay of the Ar  $2s$  hole observed by Auger-threshold photoelectron coincidence spectroscopy. *Physical Review Letters*, 84:47–50, Jan 2000.
- [70] W. Eberhardt, S. Bernstorff, H. W. Jochims, S. B. Whitfield, and B. Crasemann. Photoelectron recapture through post-collision interaction. *Physical Review A*, 38:3808–3811, Oct 1988.
- [71] J. C. Levin, C. Biedermann, N. Keller, L. Liljeby, C. —S. O, R. T. Short, I. A. Sellin, and D. W. Lindle. Argon-photoion-Auger electron coincidence

- measurements following K-shell excitation by synchrotron radiation. *Physical Review Letters*, 65:988–991, Aug 1990.
- [72] Peter Puschnig, Stephen Berkebile, Alexander J. Fleming, Georg Koller, Konstantin Emtsev, Thomas Seyller, John D. Riley, Claudia Ambrosch-Draxl, Falko P. Netzer, and Michael G. Ramsey. Reconstruction of molecular orbital densities from photoemission data. *Science*, 326(5953):702–706, 2009.
- [73] A. V. Golovin, N. A. Cherepkov, and V. V. Kuznetsov. Photoionization of oriented molecules in a gas phase. *Zeitschrift für Physik D: Atoms, Molecules and Clusters*, 24(4):371–375, 1992.
- [74] R. Guillemin, E. Shigemasa, K. Le Guen, D. Ceolin, C. Miron, N. Leclercq, K. Ueda, P. Morin, and M. Simon. New setup for angular distribution measurements of Auger electrons from fixed in space molecules. *Review of Scientific Instruments*, 71(12), 2000.
- [75] R. Guillemin, E. Shigemasa, K. Le Guen, D. Ceolin, C. Miron, N. Leclercq, P. Morin, and M. Simon. Dynamical angular correlation in molecular Auger decay. *Physical Review Letters*, 87:203001, Oct 2001.
- [76] J. B. Williams, C. S. Trevisan, M. S. Schöffler, T. Jahnke, I. Bocharova, H. Kim, B. Ulrich, R. Wallauer, F. Sturm, T. N. Rescigno, A. Belkacem, R. Dörner, Th. Weber, C. W. McCurdy, and A. L. Landers. Imaging polyatomic molecules in three dimensions using molecular frame photoelectron angular distributions. *Physical Review Letters*, 108:233002, Jun 2012.
- [77] J. B. Williams, C. S. Trevisan, M. S. Schöffler, T. Jahnke, I. Bocharova, H. Kim, B. Ulrich, R. Wallauer, F. Sturm, T. N. Rescigno, A. Belkacem, R. Dörner, Th. Weber, C. W. McCurdy, and A. L. Landers. Probing the dynamics of dissociation of methane following core ionization using three-dimensional molecular-frame photoelectron angular distributions. *Journal of Physics B: Atomic, Molecular and Optical Physics*, 45(19):194003, 2012.

- 
- [78] Etienne Plésiat, Piero Decleva, and Fernando Martín. Relationship between polarization-averaged molecular-frame photoelectron angular distributions and geometry. *Physical Review A*, 88:063409, Dec 2013.
- [79] R. Dörner, V. Mergel, O. Jagutzki, L. Spielberger, J. Ullrich, R. Moshammer, and H. Schmidt-Böcking. Cold target recoil ion momentum spectroscopy: a momentum microscope to view atomic collision dynamics. *Physics Reports*, 330(2-3):95–192, 2000.
- [80] Catalin Miron and Paul Morin. High-resolution inner-shell coincidence spectroscopy. *Nuclear Instruments and Methods in Physics Research Section A: Accelerators, Spectrometers, Detectors and Associated Equipment*, 601(1-2):66–77, 2009. Special issue in honour of Prof. Kai Siegbahn.
- [81] S. E. Canton, E. Plésiat, J. D. Bozek, B. S. Rude, P. Decleva, and F. Martín. Direct observation of Cohen-Fano interferences in vibrationally resolved valence-shell photoionization spectra of H<sub>2</sub>, N<sub>2</sub> and CO. *Proceedings of the National Academy of Sciences*, 108:7302–7306, 2011.
- [82] E. Plésiat, L. Argenti, E. Kukk, C. Miron, K. Ueda, P. Decleva, and F. Martín. Intramolecular electron diffraction in vibrationally resolved K-shell photoionization of methane. *Physical Review A*, 85:023409, 2012.
- [83] Ackermann W., Asova G., Ayvazyan V., Azima A., Baboi N., Bahr J., Balandin V., Beutner B., Brandt A., Bolzmann A., Brinkmann R., Brovko O. I., Castellano M., Castro P., Catani L., Chiadroni E., Choroba S., Cianchi A., Costello J. T., Cubaynes D., Dardis J., Decking W., Delsim-Hashemi H., Delserieys A., Di Pirro G., Dohlus M., Dusterer S., Eckhardt A., Edwards H. T., Faatz B., Feldhaus J., Flottmann K., Frisch J., Frohlich L., Garvey T., Gensch U., Gerth Ch., Gorler M., Golubeva N., Grabosch H.-J., Grecki M., Grimm O., Hacker K., Hahn U., Han H. J., Honkavaara K., Hott T., Huning M., Ivanisenko Y., Jaeschke E., Jalmuzna W., Jezynski T., Kammering R., Katalev V., Kavanagh K., Kennedy E. T., Khodyachykh S., Klose K., Kocharyan V., Korfer M., Kollwe M., Koprek W., Korepanov S., Kostin D., Krassilnikov M., Kube G., Kuhlmann M., Lewis C. L. S., Lilje L., Limberg T., Lipka D., Lohl F., Luna H., Luong M., Mar-

tins M., Meyer M., Michelato P., Miltchev V., Moller W. D., Monaco L., Muller W. F. O., Napieralski O., Napoly O., Nicolosi P., Nolle D., Nunez T., Oppelt A., Pagani C., Paparella R., Pchalek N., Pedregosa-Gutierrez J., Petersen B., Petrosyan B., Petrosyan G., Petrosyan L., Pfluger J., Plonjes E., Poletto L., Pozniak K., Prat E., Proch D., Pucyk P., Radcliffe P., Redlin H., Rehlich K., Richter M., Roehrs M., Roensch J., Romaniuk R., Ross M., Rossbach J., Rybnikov V., Sachwitz M., Saldin E. L., Sandner W., Schlarb H., Schmidt B., Schmitz M., Schmuser P., Schneider J. R., Schneidmiller E. A., Schnepf S., Schreiber S., Seidel M., Sertore D., Shabunov A. V., Simon C., Simrock S., Sombrowski E., Sorokin A. A., Spanknebel P., Spesyvtsev R., Staykov L., Steffen B., Stephan F., Stulle F., Thom H., Tiedtke K., Tischer M., Toleikis S., Treusch R., Trines D., Tsakov I., Vogel E., Weiland T., Weise H., Wellhofer M., Wendt M., Will I., Winter A., Wittenburg K., Wurth W., Yeates P., Yurkov M. V., Zagorodnov I., and Zapfe K. Operation of a free-electron laser from the extreme ultraviolet to the water window. *Nature Photonics*, 1(6):336–342, Jun 2007.

- [84] Henry N. Chapman, Anton Barty, Michael J. Bogan, Sebastien Boutet, Matthias Frank, Stefan P. Hau-Riege, Stefano Marchesini, Bruce W. Woods, Sasa Bajt, W. Henry Benner, Richard A. London, Elke Plonjes, Marion Kuhlmann, Rolf Treusch, Stefan Dusterer, Thomas Tschentscher, Jochen R. Schneider, Eberhard Spiller, Thomas Moller, Christoph Bostedt, Matthias Hoener, David A. Shapiro, Keith O. Hodgson, David van der Spoel, Florian Burmeister, Magnus Bergh, Carl Caleman, Gosta Huldt, M. Marvin Seibert, Filipe R. N. C. Maia, Richard W. Lee, Abraham Szoke, Nicusor Timneanu, and Janos Hajdu. Femtosecond diffractive imaging with a soft-X-ray free-electron laser. *Nature Physics*, 2(12):839–843, Dec 2006.
- [85] Henry N. Chapman, Stefan P. Hau-Riege, Michael J. Bogan, Sasa Bajt, Anton Barty, Sebastien Boutet, Stefano Marchesini, Matthias Frank, Bruce W. Woods, W. Henry Benner, Richard A. London, Urs Rohner, Abraham Szoke, Eberhard Spiller, Thomas Moller, Christoph Bostedt, David A. Shapiro, Marion Kuhlmann, Rolf Treusch, Elke Plonjes, Florian Burmeister, Magnus Bergh, Carl Caleman, Gosta Huldt, M. Marvin Seibert, and Janos Ha-

---

jdu. Femtosecond time-delay X-ray holography. *Nature*, 448(7154):676–679, Aug 2007.

- [86] Stefano Marchesini, Sebastien Boutet, Anne E. Sakdinawat, Michael J. Bogan, Sasa Bajt, Anton Barty, Henry N. Chapman, Matthias Frank, Stefan P. Hau-Riege, Abraham Szoke, Congwu Cui, David A. Shapiro, Malcolm R. Howells, John C. H. Spence, Joshua W. Shaevitz, Joanna Y. Lee, Janos Hajdu, and Marvin M. Seibert. Massively parallel X-ray holography. *Nature Photonics*, 2(9):560–563, Sep 2008.
- [87] Allison Doerr. Diffraction before destruction. *Nature Methods*, 8(4):283–283, Apr 2011.
- [88] Henry N. Chapman, Petra Fromme, Anton Barty, Thomas A. White, Richard A. Kirian, Andrew Aquila, Mark S. Hunter, Joachim Schulz, Daniel P. DePonte, Uwe Weierstall, R. Bruce Doak, Filipe R. N. C. Maia, Andrew V. Martin, Ilme Schlichting, Lukas Lomb, Nicola Coppola, Robert L. Shoeman, Sascha W. Epp, Robert Hartmann, Daniel Rolles, Artem Rudenko, Lutz Foucar, Nils Kimmel, Georg Weidenspointner, Peter Holl, Mengning Liang, Miriam Barthelmess, Carl Caleman, Sebastien Boutet, Michael J. Bogan, Jacek Krzywinski, Christoph Bostedt, Sasa Bajt, Lars Gumprecht, Benedikt Rudek, Benjamin Erk, Carlo Schmidt, Andre Homke, Christian Reich, Daniel Pietschner, Lothar Struder, Gunter Hauser, Hubert Gorke, Joachim Ullrich, Sven Herrmann, Gerhard Schaller, Florian Schopper, Heike Soltau, Kai-Uwe Kuhnel, Marc Messerschmidt, John D. Bozek, Stefan P. Hau-Riege, Matthias Frank, Christina Y. Hampton, Raymond G. Sierra, Dmitri Starodub, Garth J. Williams, Janos Hajdu, Nicusor Timneanu, M. Marvin Seibert, Jakob Andreasson, Andrea Rocker, Olof Jonsson, Martin Svenda, Stephan Stern, Karol Nass, Robert Andritschke, Claus-Dieter Schroter, Faton Krasniqi, Mario Bott, Kevin E. Schmidt, Xiaoyu Wang, Ingo Grotjohann, James M. Holton, Thomas R. M. Barends, Richard Neutze, Stefano Marchesini, Raimund Fromme, Sebastian Schorb, Daniela Rupp, Marcus Adolph, Tais Gorkhover, Inger Andersson, Helmut Hirsemann, Guillaume Potdevin, Heinz Graafsma, Bjorn Nilsson, and John

- C. H. Spence. Femtosecond X-ray protein nanocrystallography. *Nature*, 470(7332):73–77, Feb 2011.
- [89] Lars Redecke, Karol Nass, Daniel P. DePonte, Thomas A. White, Dirk Rehders, Anton Barty, Francesco Stellato, Mengning Liang, Thomas R.M. Barends, Sébastien Boutet, Garth J. Williams, Marc Messerschmidt, M. Marvin Seibert, Andrew Aquila, David Arnlund, Sasa Bajt, Torsten Barth, Michael J. Bogan, Carl Caleman, Tzu-Chiao Chao, R. Bruce Doak, Holger Fleckenstein, Matthias Frank, Raimund Fromme, Lorenzo Galli, Ingo Grotjohann, Mark S. Hunter, Linda C. Johansson, Stephan Kassemeyer, Gergely Katona, Richard A. Kirian, Rudolf Koopmann, Chris Kupitz, Lukas Lomb, Andrew V. Martin, Stefan Mogk, Richard Neutze, Robert L. Shoeman, Jan Steinbrener, Nicusor Timneanu, Dingjie Wang, Uwe Weierstall, Nadia A. Zatsepin, John C. H. Spence, Petra Fromme, Ilme Schlichting, Michael Duszynski, Christian Betzel, and Henry N. Chapman. Natively inhibited Trypanosoma brucei cathepsin B structure determined by using an X-ray laser. *Science*, 339(6116):227–230, 2013.
- [90] Allaria E., Appio R., Badano L., Barletta W. A., Bassanese S., Biedron S. G., Borga A., Busetto E., Castronovo D., Cinquegrana P., Cleva S., Cocco D., Cornacchia M., Craievich P., Cudin I., D’Auria G., M. Dal Forno, Danailov M. B., R. De Monte, G. De Ninno, Delgiusto P., Demidovich A., S. Di Mitri, Diviacco B., Fabris A., Fabris R., Fawley W., Ferianis M., Ferrari E., Ferry S., Froehlich L., Furlan P., Gaio G., Gelmetti F., Giannessi L., Giannini M., Gobessi R., Ivanov R., Karantzoulis E., Lonza M., Lutman A., Mahieu B., Milloch M., Milton S. V., Musardo M., Nikolov I., Noe S., Parmigiani F., Penzo G., Petronio M., Pivetta L., Predonzani M., Rossi F., Rumiz L., Salom A., Scafuri C., Serpico C., Sigalotti P., Spampinati S., Spezzani C., Svandrlik M., Svetina C., Tazzari S., Trovo M., Umer R., Vascotto A., Veronese M., Visintini R., Zaccaria M., Zangrando D., and Zangrando M. Highly coherent and stable pulses from the fermi seeded free-electron laser in the extreme ultraviolet. *Nature Photonics*, 6(10):699–704, Oct 2012.
- [91] David Pile. X-rays: first light from SACLA. *Nature Photonics*, 5(8):456–457, Aug 2011.

- 
- [92] F. Calegari, D. Ayuso, A. Trabattoni, L. Belshaw, S. De Camillis, S. Anumula, F. Frassetto, L. Poletto, A. Palacios, P. Decleva, J. B. Greenwood, F. Martín, and M. Nisoli. Ultrafast electron dynamics in phenylalanine initiated by attosecond pulses. *Science*, 346(6207):336–339, 2014.
- [93] Alexander I. Kuleff, Jörg Breidbach, and Lorenz S. Cederbaum. Multielectron wave-packet propagation: general theory and application. *The Journal of Chemical Physics*, 123(4), 2005.
- [94] Alexander I. Kuleff and Lorenz S. Cederbaum. Charge migration in different conformers of glycine: the role of nuclear geometry. *Chemical Physics*, 338(2-3):320–328, 2007. Molecular Wave Packet Dynamics (in honour of Jörn Manz).
- [95] Siegfried Lünemann, Alexander I. Kuleff, and Lorenz S. Cederbaum. Ultrafast charge migration in 2-phenylethyl-N,N-dimethylamine. *Chemical Physics Letters*, 450(4-6):232–235, 2008.
- [96] Alexander I. Kuleff and Lorenz S. Cederbaum. Ultrafast correlation-driven electron dynamics. *Journal of Physics B: Atomic, Molecular and Optical Physics*, 47(12):124002, 2014.
- [97] F. Calegari, D. Ayuso, A. Trabattoni, L. Belshaw, S. De Camillis, F. Frassetto, L. Poletto, A. Palacios, P. Decleva, J.B. Greenwood, F. Martin, and M. Nisoli. Ultrafast charge dynamics in an amino acid induced by attosecond pulses. *Selected Topics in Quantum Electronics, IEEE Journal of*, 21(5):1–12, Sept 2015.
- [98] Bridgette Cooper, Premysl Kolorenc, Leszek J. Frasinski, Vitali Averbukh, and Jon P. Marangos. Analysis of a measurement scheme for ultrafast hole dynamics by few femtosecond resolution X-ray pump-probe Auger spectroscopy. *Faraday Discuss.*, 171:93–111, 2014.
- [99] B. Mignolet, R. D. Levine, and F. Remacle. Charge migration in the bifunctional PENNA cation induced and probed by ultrafast ionization: a dynamical study. *Journal of Physics B: Atomic, Molecular and Optical Physics*, 47(12):124011, June 2014.



- 
- [100] Nikolay V. Golubev and Alexander I. Kuleff. Control of charge migration in molecules by ultrashort laser pulses. *Physical Review A*, 91:051401, May 2015.
- [101] A. Marciniak, V. Despre, T. Barillot, A. Rouzee, M. C. E. Galbraith, J. Klei, C.-H. Yang, C. T. L. Smeenk, V. Lorient, S. Nagaprasad Reddy, A. G. G. M. Tielens, S. Mahapatra, A. I. Kuleff, M. J. J. Vrakking, and F. Lepine. XUV excitation followed by ultrafast non-adiabatic relaxation in PAH molecules as a femto-astrochemistry experiment. *Nature Communications*, 6, Aug 2015. Article.
- [102] David Mendive-Tapia, Morgane Vacher, Michael J. Bearpark, and Michael A. Robb. Coupled electron-nuclear dynamics: charge migration and charge transfer initiated near a conical intersection. *The Journal of Chemical Physics*, 139(4), 2013.
- [103] Morgane Vacher, Michael J. Bearpark, and Michael A. Robb. Communication: Oscillating charge migration between lone pairs persists without significant interaction with nuclear motion in the glycine and Gly-Gly-NH-CH<sub>3</sub> radical cations. *The Journal of Chemical Physics*, 140(20), 2014.
- [104] Morgane Vacher, David Mendive-Tapia, Michael J. Bearpark, and Michael A. Robb. The second-order Ehrenfest method. *Theoretical Chemistry Accounts*, 133(7), 2014.
- [105] V. Despré, a. Marciniak, V. Lorient, M. C. E. Galbraith, a. Rouzée, M. J. J. Vrakking, F. Lépine, and Alexander I. Kuleff. Attosecond hole migration in benzene molecules surviving nuclear motion. *The Journal of Physical Chemistry Letters*, 6(3):426–431, February 2015.
- [106] J. Caillat, J. Zanghellini, M. Kitzler, O. Koch, W. Kreuzer, and A. Scrinzi. Correlated multielectron systems in strong laser fields: a multiconfiguration time-dependent Hartree-Fock approach. *Physical Review A*, 71:012712, Jan 2005.
- [107] Tsuyoshi Kato and Hirohiko Kono. Time-dependent multiconfiguration theory for electronic dynamics of molecules in intense laser fields: a de-

- 
- scription in terms of numerical orbital functions. *The Journal of Chemical Physics*, 128(18), 2008.
- [108] Tsuyoshi Kato and Kaoru Yamanouchi. Time-dependent multiconfiguration theory for describing molecular dynamics in diatomic-like molecules. *The Journal of Chemical Physics*, 131(16), 2009.
- [109] Ofir E. Alon, Alexej I. Streltsov, and Lorenz S. Cederbaum. Many-body theory for systems with particle conversion: extending the multiconfigurational time-dependent Hartree method. *Physical Review A*, 79:022503, Feb 2009.
- [110] M. Nest. The multi-configuration electron-nuclear dynamics method. *Chemical Physics Letters*, 472(4-6):171–174, 2009.
- [111] D. J. Haxton, K. V. Lawler, and C. W. McCurdy. Multiconfiguration time-dependent Hartree-Fock treatment of electronic and nuclear dynamics in diatomic molecules. *Physical Review A*, 83:063416, Jun 2011.
- [112] D. J. Haxton and C. W. McCurdy. Ultrafast population transfer to excited valence levels of a molecule driven by X-ray pulses. *Physical Review A*, 90:053426, Nov 2014.
- [113] Daniel J. Haxton and C. William McCurdy. Two methods for restricted configuration spaces within the multiconfiguration time-dependent Hartree-Fock method. *Physical Review A*, 91:012509, Jan 2015.
- [114] E. Plésiat, P. Decleva, and F. Martín. Vibrational branching ratios in the photoelectron spectra of N<sub>2</sub> and CO: interference and diffraction effects. *Physical Chemistry Chemical Physics*, 14:10853–10871, 2012.
- [115] E. Plésiat, P. Decleva, and F. Martín. Vibrationally-resolved photoelectron angular distributions from randomly-oriented and fixed-in-space N<sub>2</sub> and CO molecules. *Journal of Physics B*, 45:194008, 2012.
- [116] E. Kukk, D. Ayuso, T. D. Thomas, P. Decleva, M. Patanen, L. Argenti, E. Plésiat, A. Palacios, K. Kooser, O. Travnikova, S. Mondal, M. Kimura, K. Sakai, C. Miron, F. Martín, and K. Ueda. Effects of molecular potential

- and geometry on atomic core-level photoemission over an extended energy range: the case study of the CO molecule. *Physical Review A*, 88:033412, 2013.
- [117] L. Argenti, T. D. Thomas, E. Plésiat, X. J. Liu, C. Miron, T. Lischke, G Prümper, K. Sakai, T. Ouchi, R. Püttner, V. Sekushin, T. Tanaka, M. Hoshino, H. Tanaka, P. Decleva, K. Ueda, and F. Martín. Double-slit experiment with a polyatomic molecule: vibrationally-resolved C 1s photoelectron spectra of acetylene. *New Journal of Physics*, 14:033012, 2012.
- [118] K. Ueda, C. Miron, E. Plésiat, L. Argenti, M. Patanen, K. Kooser, D. Ayuso, S. Mondal, M. Kimura, K. Sakai, O. Travnikova, A. Palacios, P. Decleva, E. Kukk, and F. Martín. Intramolecular photoelectron diffraction in the gas phase. *Journal of Chemical Physics*, 139:124306, 2013.
- [119] E. Plésiat, P. Decleva, and F. Martín. Vibrationally resolved K-shell photoionization cross sections of methane. *Central European Journal of Physics*, 11:1157, 2013.
- [120] M. Patanen, K. Kooser, L. Argenti, D. Ayuso, M. Kimura, S. Mondal, E. Plésiat, A. Palacios, K. Sakai, O. Travnikova, P. Decleva, E. Kukk, C. Miron, K. Ueda, and F. Martín. Vibrationally resolved C 1s photoionization cross section of CF<sub>4</sub>. *Journal of Physics B*, 47:124032, 2014.
- [121] D. Ayuso, A. Palacios, P. Decleva, and F. Martín. Dissociative and non-dissociative photoionization of molecular fluorine from inner and valence shells. *Journal of Electron Spectroscopy and Related Phenomena*, 195:320–326, 2014.
- [122] D. Ayuso, M. Kimura, K. Kooser, M. Patanen, E. Plésiat, L. Argenti, S. Mondal, O. Travnikova, K. Sakai, A. Palacios, E. Kukk, P. Decleva, K. Ueda, F. Martín, and C. Miron. Vibrationally resolved B 1s photoionization cross section of BF<sub>3</sub>. *The Journal of Physical Chemistry A*, 119(23):5971–5978, 2015. PMID: 25761399.
- [123] B. Diu C. Cohen-Tannoudji and F. Laloë. *Quantum mechanics*. Quantum Mechanics. Wiley, 1977.

- 
- [124] R. M. Potvliege C. J. Joachain, N. J. Kylstra. *Atoms in Intense Laser Fields*. Cambridge University Press, 2012.
- [125] André D. Bandrauk and Huizhong Lu. Exponential propagators (integrators) for the time-dependent Schrödinger equation. *Journal of Theoretical and Computational Chemistry*, 12(06):1340001, 2013.
- [126] A. Szabó and N. S. Ostlund. *Modern Quantum Chemistry: Introduction to Advanced Electronic Structure Theory*. Dover Books on Chemistry Series. Dover Publications, Incorporated, 1996.
- [127] M. Born and R. Oppenheimer. Zur quantentheorie der molekeln. *Annalen der Physik*, 389(20):457–484, 1927.
- [128] Hans Jo/rgen Aa. Jensen, Poul Jo/rghensen, and Hans Ågren. Efficient optimization of large scale MCSCF wave functions with a restricted step algorithm. *The Journal of Chemical Physics*, 87(1):451–466, 1987.
- [129] Alexandre B. Rocha and Carlos E. V. de Moura. The problem of hole localization in inner-shell states of N<sub>2</sub> and CO<sub>2</sub> revisited with complete active space self-consistent field approach. *The Journal of Chemical Physics*, 135(22), 2011.
- [130] Philip M. Morse. Diatomic molecules according to the wave mechanics. II. Vibrational levels. *Physical Review*, 34:57–64, Jul 1929.
- [131] Robert R. Lucchese and Vincent McKoy. Studies of differential and total photoionization cross sections of carbon dioxide. *Physical Review A*, 26:1406–1418, Sep 1982.
- [132] Theoretical study of the excited and continuum states in the NEXAFS region of Cl<sub>2</sub>. *Physical Chemistry Chemical Physics*, 1:1405, 1999.
- [133] M. Stener and P. Decleva. Time-dependent density functional calculations of molecular photoionization cross sections: N<sub>2</sub> and Ph<sub>3</sub>. *The Journal of Chemical Physics*, 112(24):10871–10879, 2000.
- [134] I. N. Levine. *Quantum Chemistry*. Pearson Education, Limited, 2013.

- 
- [135] Reiner M. Dreizler and Eberhard K. U. Gross. *Density Functional Theory. An Approach to the Quantum Many-Body Problem*. Springer-Verlag, 1990.
- [136] C. J. Cramer. *Essentials of Computational Chemistry: Theories and Models*. Wiley, 2002.
- [137] P. Hohenberg and W. Kohn. Inhomogeneous electron gas. *Physical Review*, 136:B864–B871, Nov 1964.
- [138] W. Kohn and L. J. Sham. Self-consistent equations including exchange and correlation effects. *Physical Review*, 140:A1133–A1138, Nov 1965.
- [139] M. Stener, A. Lisini, and P. Decleva. Accurate local density photoionization cross sections by LCAO stieltsjes imaging approach. *International Journal of Quantum Chemistry*, 53(2):229–244, 1995.
- [140] M. Stener, G. De Alti, and P. Decleva. Convergence of the density functional one-centre expansion for the molecular continuum:  $N_2$  and  $(CH_3)_3N$ . *Theoretical Chemistry Accounts*, 101:247–256, 1999.
- [141] M. Stener, S. Furlan, and P. Decleva. Density functional calculations of photoionization with an exchange-correlation potential with the correct asymptotic behaviour. *Journal of Physics B: Atomic, Molecular and Optical Physics*, 33(5):1081, 2000.
- [142] P. Decleva J. E. Hansen H. Bachau, E. Cormier and F. Martín. Applications of B-splines in atomic and molecular physics. *Reports on Progress in Physics*, 64(12):1815, 2001.
- [143] G. Fronzoni D. Toffoli, M. Stener and P. Decleva. Convergence of the multicenter B-spline DFT approach for the continuum. *Chemical Physics*, 276(1):25–43, 2002.
- [144] G. Fronzoni M. Stener, D. Toffoli and P. Decleva. Time dependent density functional study of the photoionization dynamics of  $SF_6$ . *The Journal of Chemical Physics*, 124(11):114306, 2006.

- 
- [145] D. Toffoli, M. Stener, G. Fronzoni, and P. Decleva. Photoionization cross section and angular distribution calculations of carbon tetrafluoride. *The Journal of Chemical Physics*, 124(21):–, 2006.
- [146] S. Korica, A. Reinköster, M. Braune, J. Viefhaus, D. Rolles, B. Langer, G. Fronzoni, D. Toffoli, M. Stener, P. Decleva, O.M. Al-Dossary, and U. Becker. Partial photoionization cross sections of C<sub>60</sub> and C<sub>70</sub>: a gas versus adsorbed phase comparison. *Surface Science*, 604(21-22):1940–1944, 2010.
- [147] Thomas X. Carroll, Maria G. Zahl, Knut J. Brve, Leif J. Sthre, Piero Decleva, Aurora Ponzi, Joshua J. Kas, Fernando D. Vila, John J. Rehr, and T. Darrah Thomas. Intensity oscillations in the carbon 1s ionization cross sections of 2-butyne. *The Journal of Chemical Physics*, 138(23):–, 2013.
- [148] Rajesh Kumar Kushawaha, Minna Patanen, Renaud Guillemin, Loic Journal, Catalin Miron, Marc Simon, Maria Novella Piancastelli, C. Skates, and Piero Decleva. From double-slit interference to structural information in simple hydrocarbons. *Proceedings of the National Academy of Sciences*, 110(38):15201–15206, 2013.
- [149] P G Burke, N Chandra, and F A Gianturco. Electron-molecule interactions. iv. scattering by polyatomic molecules. *Journal of Physics B: Atomic and Molecular Physics*, 5(12):2212, 1972.
- [150] Tosio Kato. On the eigenfunctions of many-particle systems in quantum mechanics. *Communications on Pure and Applied Mathematics*, 10(2):151–177, 1957.
- [151] C. Fonseca Guerra, J. G. Snijders, G. te Velde, and E. J. Baerends. Towards an order-N DFT method. *Theoretical Chemistry Accounts*, 99(6):391–403, 1998.
- [152] G. te Velde, F. M. Bickelhaupt, E. J. Baerends, C. Fonseca Guerra, S. J. A. van Gisbergen, J. G. Snijders, and T. Ziegler. Chemistry with ADF. *Journal of Computational Chemistry*, 22(9):931–967, 2001.

- [153] ADF2013 SCM. Theoretical Chemistry, Vrije Universiteit. Amsterdam, The Netherlands. <http://www.scm.com>.
- [154] S. H. Vosko, L. Wilk, and M. Nusair. Accurate spin-dependent electron liquid correlation energies for local spin density calculations: a critical analysis. *Canadian Journal of Physics*, 58(8):1200–1211, 1980.
- [155] R. van Leeuwen and E. J. Baerends. Exchange-correlation potential with correct asymptotic behavior. *Physical Review A*, 49:2421–2431, Apr 1994.
- [156] John Robert Taylor. *Scattering theory: the quantum theory on nonrelativistic collisions*. Wiley, 1972.
- [157] M. Stener, G. Fronzoni, and P. Decleva. Time-dependent density-functional theory for molecular photoionization with noniterative algorithm and multicenter B-spline basis set: CS<sub>2</sub> and C<sub>6</sub>H<sub>6</sub> case studies. *The Journal of Chemical Physics*, 122(23), 2005.
- [158] E. K. U. Gross and W. Kohn. Time-dependent density-functional theory. In Per-Olov Löwdin, editor, *Density Functional Theory of Many-Fermion Systems*, volume 21 of *Advances in Quantum Chemistry*, pages 255–291. Academic Press, 1990.
- [159] T. Darrah Thomas, R. Püttner, H. Fukuzawa, G. Prumper, K. Ueda, E. Kukk, R. Sankari, J. Harries, Y. Tamenori, T. Tanaka, M. Hoshino, and H. Tanaka. Boron 1s photoelectron spectrum of <sup>11</sup>BF<sub>3</sub>: vibrational structure and linewidth. *The Journal of Chemical Physics*, 127(24):244309, 2007.
- [160] T. D. Thomas, E. Kukk, R. Sankari, H. Fukuzawa, G. Prumper, K. Ueda, R. Püttner, J. Harries, Y. Tamenori, T. Tanaka, M. Hoshino, and H. Tanaka. Recoil excitation of vibrational structure in the carbon 1s photoelectron spectrum of CF<sub>4</sub>. *The Journal of Chemical Physics*, 128(14):144311, 2008.
- [161] Dale E. Sayers, Edward A. Stern, and Farrel W. Lytle. New technique for investigating noncrystalline structures: Fourier analysis of the extended X-ray absorption fine structure. *Physical Review Letters*, 27:1204–1207, Nov 1971.

- 
- [162] F. R. Pettifer, O. Mathon, S. Pascarelli, M. D. Cooke, and M. R. M. Gibbs. Measurement of femtometre-scale atomic displacements by X-ray absorption spectroscopy. *Nature*, 435:78–81, 2005.
- [163] Scott A. Chambers. Epitaxial film crystallography by high-energy Auger and X-ray photoelectron diffraction. *Advances in Physics*, 40(4):357–415, 1991.
- [164] Ph. Hofmann, K.-M. Schindler, S. Bao, A. M. Bradshaw, and D. P. Woodruff. Direct identification of atomic and molecular adsorption sites using photoelectron diffraction. *Nature*, 368(6467):131–132, Mar 1994.
- [165] Christian Bressler and Majed Chergui. Ultrafast X-ray absorption spectroscopy. *Chemical Reviews*, 104(4):1781–1812, 2004. PMID: 15080712.
- [166] Pieter Glatzel and Uwe Bergmann. High resolution 1s core hole X-ray spectroscopy in 3d transition metal complexes-electronic and structural information. *Coordination Chemistry Reviews*, 249(1-2):65–95, 2005. Synchrotron Radiation in Inorganic and Bioinorganic Chemistry.
- [167] D. P. Woodruff. Adsorbate structure determination using photoelectron diffraction: methods and applications. *Surface Science Reports*, 62(1):1–38, 2007.
- [168] Alessandro Arcovito, Maurizio Benfatto, Michele Cianci, S. Samar Hasnain, Karin Nienhaus, G. Ulrich Nienhaus, Carmelinda Savino, Richard W. Strange, Beatrice Vallone, and Stefano Della Longa. X-ray structure analysis of a metalloprotein with enhanced active-site resolution using in situ X-ray absorption near edge structure spectroscopy. *Proceedings of the National Academy of Sciences*, 104(15):6211–6216, 2007.
- [169] Michael Haumann, Alexander Grundmeier, Ivelina Zaharieva, and Holger Dau. Photosynthetic water oxidation at elevated dioxygen partial pressure monitored by time-resolved X-ray absorption measurements. *Proceedings of the National Academy of Sciences*, 105(45):17384–17389, 2008.
- [170] N. Pangher, H. M. Köppe, J. Feldhaus, and J. Haase. Determination of intramolecular bond lengths of low- $Z$  molecules in the gas phase, condensed,



- and chemisorbed states using extended X-ray absorption fine structure. *Physical Review Letters*, 71:4365–4368, Dec 1993.
- [171] Rok Prešeren, Alojz Kodre, Iztok Arčon, and Michael Borowski. Atomic background and EXAFS of gaseous hydrides of Ge, As, Se and Br. *Journal of Synchrotron Radiation*, 8(2):279–281, Mar 2001.
- [172] J. Söderström, N. Mårtensson, O. Travnikova, M. Patanen, C. Miron, L. J. Sæthre, K. J. Børve, J. J. Rehr, J. J. Kas, F. D. Vila, T. D. Thomas, and S. Svensson. Nonstoichiometric intensities in core photoelectron spectroscopy. *Physical Review Letters*, 108:193005, May 2012.
- [173] F. Krasniqi, B. Najjari, L. Strüder, D. Rolles, A. Voitkiy, and J. Ullrich. Imaging molecules from within: ultrafast Angström-scale structure determination of molecules via photoelectron holography using free-electron lasers. *Physical Review A*, 81:033411, Mar 2010.
- [174] H. Fukuzawa, X.-J. Liu, T. Teranishi, K. Sakai, G. Prümper, K. Ueda, Y. Morishita, N. Saito, M. Stener, and P. Decleva. Fluorine K-shell photoelectron angular distribution from CF<sub>4</sub> molecules in the molecular frame. *Chemical Physics Letters*, 451(4-6):182–185, 2008.
- [175] Jun-Ichi Adachi, Misato Kazama, Takahiro Teramoto, Naoya Miyauchi, Tomoya Mizuno, Masakazu Yamazaki, Takashi Fujikawa, and Akira Yagishita. C 1s photoelectron angular distributions from fixed-in-space CO molecules in the high-energy continuum  $\geq 50$  eV. *Journal of Physics B: Atomic, Molecular and Optical Physics*, 45(19):194007, 2012.
- [176] X.-J. Liu, N. A. Cherepkov, S. K. Semenov, V. Kimberg, F. Gel'mukhanov, G. Prümper, T. Lischke, T. Tanaka, M. Hoshino, H. Tanaka, and K. Ueda. Young's double-slit experiment using core-level photoemission from N<sub>2</sub>: revisiting Cohen-Fano's two-centre interference phenomenon. *Journal of Physics B: Atomic, Molecular and Optical Physics*, 39(23):4801, 2006.
- [177] PLEIADES Beamline. <http://www.synchrotron-soleil.fr/portal/page/portal/Recherche/LignesLumiere/PLEIADES>.

- 
- [178] B. Kempgens, K. Maier, A. Kivimäki, H. M. Köppe, M. Neeb, M. N. Piancastelli, U. Hergenhahn, and A. M. Bradshaw. Vibrational excitation in C 1s and O 1s photoionization of CO. *Journal of Physics B: Atomic, Molecular and Optical Physics*, 30(21):L741, 1997.
- [179] Uwe Hergenhahn. Vibrational structure in inner shell photoionization of molecules. *Journal of Physics B: Atomic, Molecular and Optical Physics*, 37(12):R89, 2004.
- [180] Thomas X. Carroll, Knut J. Børve, Leif J. Sæthre, John D. Bozek, Edwin Kukk, Jeffrey A. Hahne, and T. Darrah Thomas. Carbon 1s photoelectron spectroscopy of CF<sub>4</sub> and CO: search for chemical effects on the carbon 1s hole-state lifetime. *The Journal of Chemical Physics*, 116(23):10221–10228, 2002.
- [181] K. Ueda, H. Chiba, Y. Sato, T. Hayaishi, E. Shigemasa, and A. Yagishita. Resonance-Auger-electron-photoion coincidence studies on state-to-state dissociation dynamics of inner-shell-excited BF<sub>3</sub>. *Physical Review A*, 46:R5–R8, Jul 1992.
- [182] Kozo Kuchitsu and Shigehiro Konaka. B-F bond distance of boron trifluoride determined by gas electron diffraction. *The Journal of Chemical Physics*, 45(11), 1966.
- [183] T. Shimanouchi. NIST Chemistry WebBook, NIST Standard Reference Database. *NIST Chemistry WebBook*, (69), 2005.
- [184] Robynne Kirkpatrick, Tony Masiello, Alfons Weber, and Joseph W. Nibler. Coherent Raman spectra of the  $\nu_1$  mode of <sup>10</sup>BF<sub>3</sub> and <sup>11</sup>BF<sub>3</sub>. *Journal of Molecular Spectroscopy*, 237(1):97–103, 2006.
- [185] J. L. Dehmer and D. Dill. Shape resonances in K-shell photoionization of diatomic molecules. *Physical Review Letters*, 35:213–215, Jul 1975.
- [186] M. N Piancastelli. The neverending story of shape resonances. *Journal of Electron Spectroscopy and Related Phenomena*, 100(1-3):167–190, 1999.

- 
- [187] Y. Shimizu, K. Ueda, H. Chiba, K. Ohmori, M. Okunishi, Y. Sato, and T. Hayaishi. Angle-resolved photoelectron and photoion study on the shape resonance in the B1s ionization region of BF<sub>3</sub>. *The Journal of Chemical Physics*, 107(7):2415–2418, 1997.
- [188] Edward A. Stern. Theory of the extended X-ray-absorption fine structure. *Physical Review B*, 10:3027–3037, Oct 1974.
- [189] H. D. Cohen and U. Fano. Interference in the photo-ionization of molecules. *Physical Review*, 150:30–33, Oct 1966.
- [190] S. K. Semenov, N. A. Cherepkov, M. Matsumoto, K. Fujiwara, K. Ueda, E. Kukk, F. Tahara, T. Sunami, H. Yoshida, T. Tanaka, K. Nakagawa, M. Kitajima, H. Tanaka, and A. De Fanis. Vibrationally resolved photoionization of the  $1\sigma_g$  and  $1\sigma_u$  shells of N<sub>2</sub> molecule. *Journal of Physics B: Atomic, Molecular and Optical Physics*, 39(2):375, 2006.
- [191] M. Ehara, K. Kuramoto, H. Nakatsuji, M. Hoshino, T. Tanaka, M. Kitajima, H. Tanaka, A. De Fanis, Y. Tamenori, and K. Ueda. C1s and O1s photoelectron satellite spectra of CO with symmetry-dependent vibrational excitations. *The Journal of Chemical Physics*, 125(11), 2006.
- [192] J. Fernández, O. Fojón, A. Palacios, and F. Martín. Interferences from fast electron emission in molecular photoionization. *Physical Review Letters*, 98:043005, Jan 2007.
- [193] Stephan Eberhard, Giovanni Finazzi, and Francis-André Wollman. The dynamics of photosynthesis. *Annual Review of Genetics*, 42(1):463–515, 2008. PMID: 18983262.
- [194] Meike Cordes and Bernd Giese. Electron transfer in peptides and proteins. *Chemical Society Reviews*, 38:892–901, 2009.
- [195] David Becker, Amitava Adhikary, and Michael D. Sevilla. The role of charge and spin migration in DNA radiation damage. In Tapash Chakraborty, editor, *Charge Migration in DNA*, NanoScience and Technology, pages 139–175. Springer Berlin Heidelberg, 2007.

- 
- [196] Chengteh Lee, Weitao Yang, and Robert G. Parr. Development of the Colle-Salvetti correlation-energy formula into a functional of the electron density. *Physical Review B*, 37:785–789, Jan 1988.
- [197] Axel D. Becke. Density-functional thermochemistry. III. The role of exact exchange. *The Journal of Chemical Physics*, 98(7):5648–5652, 1993.
- [198] M. J. Frisch, G. W. Trucks, H. B. Schlegel, G. E. Scuseria, M. A. Robb, J. R. Cheeseman, G. Scalmani, V. Barone, B. Mennucci, G. A. Petersson, H. Nakatsuji, M. Caricato, X. Li, H. P. Hratchian, A. F. Izmaylov, J. Bloino, G. Zheng, J. L. Sonnenberg, M. Hada, M. Ehara, K. Toyota, R. Fukuda, J. Hasegawa, M. Ishida, T. Nakajima, Y. Honda, O. Kitao, H. Nakai, T. Vreven, J. A. Montgomery, Jr., J. E. Peralta, F. Ogliaro, M. Bearpark, J. J. Heyd, E. Brothers, K. N. Kudin, V. N. Staroverov, R. Kobayashi, J. Normand, K. Raghavachari, A. Rendell, J. C. Burant, S. S. Iyengar, J. Tomasi, M. Cossi, N. Rega, J. M. Millam, M. Klene, J. E. Knox, J. B. Cross, V. Bakken, C. Adamo, J. Jaramillo, R. Gomperts, R. E. Stratmann, O. Yazyev, A. J. Austin, R. Cammi, C. Pomelli, J. W. Ochterski, R. L. Martin, K. Morokuma, V. G. Zakrzewski, G. A. Voth, P. Salvador, J. J. Dannenberg, S. Dapprich, A. D. Daniels, . Farkas, J. B. Foresman, J. V. Ortiz, J. Cioslowski, and D. J. Fox. Gaussian 09 Revision D.01. <http://www.gaussian.com>. Gaussian Inc. Wallingford CT 2009.
- [199] Attila G. Csaszar. Conformers of gaseous glycine. *Journal of the American Chemical Society*, 114(24):9568–9575, 1992.
- [200] Zhijian Huang, Wenbo Yu, and Zijing Lin. Exploration of the full conformational landscapes of gaseous aromatic amino acid phenylalanine: an ab initio study. *Journal of Molecular Structure: THEOCHEM*, 758(2-3):195–202, 2006.
- [201] L. C. Snoek, R. T. Kroemer, M. R. Hockridge, and J. P. Simons. Conformational landscapes of aromatic amino acids in the gas phase: infrared and ultraviolet ion dip spectroscopy of tryptophan. *Physical Chemistry Chemical Physics*, 3:1819–1826, 2001.

- 
- [202] W. von Niessen, J. Schirmer, and L. S. Cederbaum. Computational methods for the one-particle green's function. *Computer Physics Reports*, 1(2):57–125, 1984.
- [203] John C. Slater. Statistical exchange-correlation in the self-consistent field. volume 6 of *Advances in Quantum Chemistry*, pages 1–92. Academic Press, 1972.
- [204] Oksana Plekan, Vitaliy Feyer, Robert Richter, Marcello Coreno, and Kevin C. Prince. Valence photoionization and photofragmentation of aromatic amino acids. *Molecular Physics*, 106(9-10):1143–1153, 2008.
- [205] Sherrie Campbell, Elaine M. Marzluff, M. T. Rodgers, J. L. Beauchamp, Margaret E. Rempe, Kimberly F. Schwinck, and D. L. Lichtenberger. Proton affinities and photoelectron spectra of phenylalanine and N-methyl- and N,N-dimethylphenylalanine. Correlation of lone pair ionization energies with proton affinities and implications for N-methylation as a method to effect site specific protonation of peptides. *Journal of the American Chemical Society*, 116(12):5257–5264, 1994.
- [206] P. H. Cannington and Norman S. Ham. He(I) and He(II) photoelectron spectra of glycine and related molecules. *Journal of Electron Spectroscopy and Related Phenomena*, 32(2):139–151, 1983.
- [207] John J. Neville, Y. Zheng, and C. E. Brion. Glycine valence orbital electron densities: comparison of electron momentum spectroscopy experiments with Hartree-Fock and density functional theories. *Journal of the American Chemical Society*, 118(43):10533–10544, 1996.